The
University
Of
Sheffield.

The development of micropillars and two-dimensional nanocavities that incorporate an organic semiconductor thin film.

By

Faleh Lafta Mater Al-Jashaam

A thesis submitted in partial fulfilment of the requirements for
the degree of Doctor of Philosophy

The University of Sheffield
Faculty of Science
Department of Physics and Astronomy

Supervised by

Professor David G. Lidzey

November 2019

Dedication

This thesis is dedicated to my beloved family
My parents for their patience and their supplications
My brother and sisters for their encouragement
My wife for her unlimited support
My sons and daughters
My friends

Acknowledgements

First of all, I would like to thank my God (Allah Almighty) who gave me strength and patience and guided me during my studies.

I would like also to express my deep gratitude and my great appreciation to my supervisor, Prof. David Lidzey, for his advice, feedback, unconditional support, generosity, help and time. Prof. Lidzey was always ready and able to give face-to-face discussions and keeping his office open when I need help. I would like to thank him again for opening my eyes to the world of photonic crystal research.

I would like to thank the Iraqi Ministry of Higher Education and Scientific Research, Tikrit University and the college of Science in the University for providing me a valuable Ph.D. scholarship that has supported me during my Ph.D. study. I would also like to thank the University of Sheffield, Physics Department for this opportunity.

Finally, I would like to thank Dr. Khalid Sediq for his help and advice in the C13 laboratory and in the Centre for Nanoscience and Technology at the University of Sheffield. Also I sincerely thank Dr. David Coles for his help and effort in the Sorby Centre and in simulation part of this thesis. I would like to thank my lab's team, Dr Kyriacos Georgiou, Dr. Rahul Jayaprakash and Dr. Andrew Musser who helped me a lot in the experimental part in this thesis and I would like to thank all EPMM group members in University of Sheffield for their help.

List of Abbreviations & Symbols

Chapter 1

$(\lambda/n)^3$	A cubic wavelength
FDTD	Finite Difference Time Domain
GaAs	Gallium Arsenide
Si	Silicon
OLED	Organic light emitting diode
SiN	Silicon nitride semiconductor

Chapter 2

PC	Photonic crystals
PBG	Photonic band gap
SEM	Scanning Electron Microscope
TiO2	Titanium oxide
PMMA	Polymethyl-methacrylate
PCF	Photonic crystal fibres
EBL	Electron-beam lithography
RIE	Reactive-ion-beam etching
ICP	Inductively Coupled Plasma
TIR	Total internal reflection
DBR	Distributed Bragg reflectors
ε	Dielectric constant
E	The electric field
H	The magnetic field
B	The magnetic flux density
D	The electric displacement
J	The electric current density
ρ	The electric charge density
P	Polarization
M	The magnetization field
$X_{e,m}$	The electric and the magnetic susceptibility
μ	Permeability
ω	Angular frequency
c	Speed of light
V(r)	Total potential energy
G	Reciprocal lattice vector
$\hbar$	Reduced Planck constant
k	Wave vector
n	Refractive index
1D	One-Dimensional
2D	Two-Dimensional
3D	Three-Dimensional
BZ	Brillouin zone
TE	Transverse electric field modes
TM	Transverse magnetic field modes
MPB	Plane wave basis method
GME	The guided mode expansion method
FF	Filling fraction
V	The mode volume
Q	Quality factor
τ	Photon storage lifetime
ν	Optical frequency
λo	The central wavelength of the cavity
FWHM	The full-width half-maximum
Γ	The emitter spontaneous emission rate
$\rho(\omega)$	The local density of optical states
HOMO	The highest occupied molecular orbital
LUMO	The lowest unoccupied molecular orbital
AR	Anti-Reflection mirror
HR	High Reflective mirror
R	The intensity reflectivity
$\emptyset$	The cavity round trip phase
L	Cavity length
F	The finesse of the planar cavity
FSR	The free spectral range
n_{eff}	The effective refractive index
λ_B	Bragg wavelength

Chapter 3

FIB	Focus ion beam
PL	The photoluminescence
IPA	Isopropyl alcohol
CSAR	Chemical semi amplified resist
ASCII	Triangular Lattice Photonic Crystal software
CAD	Computer-aided design
MIBK	Methyl- iso-butyl-ketone: Isopropyl alcohol
AFM	An atomic force microscope
NA	A numerical aperture
CCD	A nitrogen cooled charge coupled device
LMIS	A gallium liquid metal ion source

Chapter 4

PF	Purcell Factor
PFR	Red – F emitting conjugated polymer

Chapter 5

PCSs	Photonic crystal slabs
NIR	Near Infrared
CMOS	Complementary metal oxide semiconductor
TPA	Two-photon absorption
CPBG	Complete photonic band Gap
*L*3	Three missing holes nanocavity
h	Slab thickness
a	Lattice constant
S	Hole shift value
r	Hole radius
E^2	The field distribution

List of Figures

List of Tables

Abstract

Photonic crystals (PC) are periodic optical structures containing low and high refractive index layers that influence the propagation of electromagnetic waves. Photonic cavities can be created by inserting defects into a photonic crystal. Such structures have received significant attention due to their potential of confining light inside volumes (V) smaller than a cubic wavelength of light $(\lambda/n)^3$ which can be used to enhance light-matter interaction. Cavity quality factor (Q) is useful for many applications that depend on the control of spontaneous emission from an emitter such quantum optical communication and low-threshold lasing. High Q/V values can also result in an enhancement of the radiative rates of an emitter placed on the surface of the cavity by means of the Purcell effect.

This thesis concerns the fabrication and study of two types of optical cavity containing an organic-semiconductor material. The cavities explored are; (1) one-dimensional micropillar microcavities based on multilayer films of dielectric and organic materials, and (2) two-dimensional nanocavities defined into a photonic crystal slab.

Firstly, light emission from a series of optical micropillar microcavities containing a thin fluorescent, red-emitting conjugated polymer film is investigated. The photoluminescence emission from the cavities is characterized using a Fourier imaging technique and it is shown that emission is quantised into a mode-structure resulting from both vertical and lateral optical confinement within the pillar. We show that optical-confinement effects result in a blue-shift of the fundamental mode as the pillar-diameter is reduced, with a model applied to describe the energy and distribution of the confined optical modes.

Secondly, simulation, design, and analysis of two dimensional photonic crystal L3 nanocavities photonic crystal are presented. Nanocavities were then prepared from silicon nitride (SiN) as the cavity medium with the luminescence emitted from an organic material at red wavelengths that was coated on the cavity surface.

To improve the quality factor of such structures, hole size, lattice constant and hole shift are systematically varied with their effect as cavity properties determined. Finite Difference Time Domain (FDTD) modelling is used to support the experimental work and predict the optimum design for such photonic crystal nanocavity devices.

It is found that by fine-tuning the nearest neighbour air-holes close to the cavity edges, the cavity Q factor can be increased. As a result, we have obtained a single cavity mode having a Q-factor 938 at a wavelength of 652 nm. Here, the cavity Q factor then increases to 1100 at a wavelength of 687 nm as a result of coating a red-emitting conjugated polymer film onto the top surface of the nanocavity. We propose that this layer planarizes the dielectric surface and helps reduce optical losses as a result of scattering.

Contains

Chapter 3 74

Chapter 1
Introduction

1.1 Introduction

Controlling the emission and absorption of light by a quantum emitter in an optical cavity is considered a key technique in photonic quantum technology and is a fundamental technique used in nanoscale photonics. During the last twenty years, a wide range of new technologies have been developed that are based on the interaction between light and matter, in which light is confined in micro and nanostructured cavities having a volume that is much smaller than a cubic wavelength $(\lambda/n)^3$ [1-15]. The enhancement of light – matter interaction has allowed the size of photonic devices to be reduced compared to electronic devices [16]; a result that is used in a number of engineering applications such as ultra-small filters [17], single-photon sources [18], ultra-low threshold lasers [19], optical sensing [20], quantum sensing in quantum information applications [21-22], high-efficiency solar cells [23], optical biosensors [24], chemical sensor devices [25], and optical logic gates [26-27].

In this thesis the effect of two types of optical cavity containing organic-semiconductor are studied. Specifically the cavities explored are; (1) one-dimensional microcavities based on multilayer films of dielectric materials, and (2) two-dimensional nanocavities defined into a slab photonic crystal. To improve the quality factor of the two dimensional photonic crystal nanocavities the hole size, lattice constant and hole shift are systematically varied with their effect as cavity properties determined. Finite Difference Time Domain (FDTD) modelling is used to support the experimental work and predict the optimum design for such photonic crystal nanocavity devices.

The second type of structure explored is a micropillar microcavities such structures have previously been widely explored using semiconductors such as Gallium Arsenide

(GaAs) [28-30], Silicon (Si) [31-32] and (GaAs/AlGaAs) [33-34] and emit light at near infra-red wavelengths. Here however, we explore micropillar microcavities containing an organic semiconductor that emits light at visible wavelengths. We expect that such structures may potentially have interesting applications [35-38] such as single photon devices [39] or microscale lasers [40] working at visible wavelengths.

1.2 Thesis Plan

In this thesis, I have studied the interactions between the electromagnetic field in micropillar and nanostructured cavities in detail. A general description of each chapter in this thesis is as follows:

In chapter 2, I discuss the theoretical background, literature review and optical properties of one, two and three dimensional photonic crystals and optical nanocavities. The fundamentals of photonic crystals that work in the weak coupling regimes are discussed. I also describe the parameters that affect the optical properties of photonic crystals. The fundamental photophysics of organic molecular materials used in such structures are introduced and some applications are described.

Chapter 3 introduces the fabrication processes utilized to create one and two – dimensional photonic crystal and micropillars microcavities. The experimental techniques and operational principles of the equipment utilized in the samples characterisation are also presented. The deposition techniques and characterization of multilayer thin films and microcavity micropillars are also introduced in this chapter.

Chapter 4 discusses the optical properties of micropillar microcavities containing a fluorescent conjugated-polymer. The photoluminescence emission from the cavities are characterised using a Fourier imaging technique. Lumerical finite difference time domain (FDTD) modelling was also used to investigate the structure of the electromagnetic field in micropillar microcavities. Here, the Fourier imaging results were obtained in collaboration with Dr. Rahul Jayaprakash, and the measurement of the quantum efficiency of the Red- F fluorescent conjugated-polymer were obtained by collaboration with Dr Kyriacos Georgiou, both in the Department of Physics and Astronomy of the University of Sheffield.

Chapter 5 discusses the fabrication and design of two - dimensional photonic crystal nanocavities. The optical properties of silicon nitride semiconductor (SiN) L3 nanocavities are presented before and after coating with a thin film of a red- emitting organic semiconductor. Finite difference time domain (FDTD) computational modelling is again used to model the photonic crystals described in this thesis. This is utilized to investigate the effect of modifying the cavity structure on their resonant frequencies, field distribution and quality factors.

Chapter 6 contains conclusions and suggestions for future work.

References

[1] García, P.D. and Lodahl, P., ‘‘Physics of quantum light emitters in disordered photonic nanostructures’’. Annalen der Physik, 529, 1600351, (2017).

[2 Liberal, I. and Engheta, N., ‘‘Nonradiating and radiating modes excited by quantum emitters in open epsilon-near-zero cavities’’. Science advances, 2, 1600987, (2016).

[3] Lu, Y.W., Li, L.Y. and Liu, J.F., ‘‘Influence of Surface Roughness on Strong Light-Matter Interaction of a Quantum Emitter-Metallic Nanoparticle System’’. Scientific reports, 8, 7115, (2018).

[4] Diguna, L., Tjahjana, L., Darma, Y., Zeng, S., Wang, H. and Birowosuto, M., ‘‘Light–Matter Interaction of Single Quantum Emitters with Dielectric Nanostructures’’. In Photonics, Multidisciplinary Digital Publishing Institute 5, 14, (2018).

[5] Lee, J., Javed, T., Skeini, T., Govorov, A.O., Bryant, G.W. and Kotov, N.A., ‘‘Bioconjugated Ag Nanoparticles and CdTe Nanowires: Metamaterials with Field-Enhanced Light Absorption’’. Angewandte Chemie, 118, 4937-4941, (2006).

[6] Sorger, V.J., Pholchai, N., Cubukcu, E., Oulton, R.F., Kolchin, P., Borschel, C., Gnauck, M., Ronning, C. and Zhang, X., ‘‘Strongly enhanced molecular fluorescence inside a nanoscale waveguide gap’’. Nano Letters, 11, 4907-4911, (2011).

[7] Englund, D., Fattal, D., Waks, E., Solomon, G., Zhang, B., Nakaoka, T., Arakawa, Y., Yamamoto, Y. and Vučković, J., ‘‘Controlling the spontaneous emission rate of single quantum dots in a two-dimensional photonic crystal’’. Physical Review Letters, 95, 013904, (2005).

[8] Barth, M., Kouba, J., Stingl, J., Löchel, B. and Benson, O., ‘‘Modification of visible spontaneous emission with silicon nitride photonic crystal nanocavities’’. Optics Express, 15, 17231-17240, (2007).

[9] Adawi, A.M., Chalcraft, A.R.A., Whittaker, D.M. and Lidzey, D.G., ‘‘Refractive index dependence of L3 photonic crystal nano-cavities’’. Optics Express, 15, 14299-14305, (2007).

[10] Zeng, L., Bermel, P., Yi, Y., Alamariu, B.A., Broderick, K.A., Liu, J., Hong, C., Duan, X., Joannopoulos, J. and Kimerling, L.C., ‘‘Demonstration of enhanced absorption in thin film Si solar cells with textured photonic crystal back reflector’’. Applied Physics Letters, 93, 221105, (2008).

[11] Hashemi, M., Farzad, M.H., Mortensen, N.A. and Xiao, S., ‘‘Enhanced absorption of graphene in the visible region by use of plasmonic nanostructures’’. Journal of Optics, 15, 055003, (2013).

[12] Niu, W., Su, L.T., Chen, R., Chen, H., Wang, Y., Palaniappan, A., Sun, H. and Tok, A.I.Y., ‘‘3-Dimensional photonic crystal surface enhanced upconversion emission for improved near-infrared photoresponse’’. Nanoscale, 6,817-824, (2014).

[13] Friberg, A.T. and Dändliker, R., ‘‘Advances in information optics and photonics’’ Vol. 6, Society of Photo-Optical Instrumentation Engineers Press, USA, (2008).

[14] Lalanne, P., Velha, P., Lecamp, G., Sauvan, C. and Hugonin, J.P., ‘‘October. Light confinement in photonic-crystal microcavities: a Fabry-Perot point of view’’. In LEOS 2007-IEEE Lasers and Electro-Optics Society Annual Meeting Conference Proceedings, 194-195, IEEE, (2007).

[15] Lalanne, P., Sauvan, C. and Hugonin, J.P., ‘‘Photon confinement in photonic crystal nanocavities’’. Laser & Photonics Reviews, 2, 514-526, (2008).

[16] Vasa, P. and Lienau, C., ‘‘Strong light–matter interaction in quantum emitter/metal hybrid nanostructures’’. Acs Photonics, 5, 2-23, (2017).

[17] Akahane, Y., Asano, T., Song, B.S. and Noda, S., ‘‘Fine-tuned high-Q photonic-crystal nanocavity’’. Optics Express, 13, 1202-1214, (2005).

[18] Liu, S., Wei, Y., Su, R., Su, R., Ma, B., Chen, Z., Ni, H., Niu, Z., Yu, Y., Wei, Y. and Wang, X., ‘‘A deterministic quantum dot micropillar single photon source with> 65% extraction efficiency based on fluorescence imaging method’’ Scientific reports, 7, 13986, (2017).

[19] Wang, D., Zhu, T., Oliver, R.A. and Hu, E.L., ‘‘Ultra-low-threshold InGaN/GaN quantum dot micro-ring lasers’’. Optics letters, 43, 799-802, (2018).

[20] Li, L., Wang, W., Luk, T.S., Yang, X. and Gao, J., ‘‘Enhanced quantum dot spontaneous emission with multilayer metamaterial nanostructures’’. ACS Photonics, 4, 501-508, (2017).

[21] Peng, P., Liu, Y.C., Xu, D., Cao, Q.T., Lu, G., Gong, Q. and Xiao, Y.F., ‘‘Enhancing coherent light-matter interactions through microcavity-engineered plasmonic resonances’’. Physical Review Letters, 119, 233901, (2017).

[22] Albert, F., Sivalertporn, K., Kasprzak, J., Strauß, M., Schneider, C., Höfling, S., Kamp, M., Forchel, A., Reitzenstein, S., Muljarov, E.A. and Langbein, W., ‘‘Microcavity controlled coupling of excitonic qubits’’. Nature Communications, 4, 1747, (2013).

[23] Florescu, M., Lee, H., Puscasu, I., Pralle, M., Florescu, L., Ting, D.Z. and Dowling, J.P., ‘‘Improving solar cell efficiency using photonic band-gap materials’’. Solar Energy Materials and Solar Cells, 91, 1599-1610, (2007).

[24] Fan, X., White, I.M., Shopova, S.I., Zhu, H., Suter, J.D. and Sun, Y., ‘‘Sensitive optical biosensors for unlabeled targets: A review’’. Analytica Chimica Acta, 620 (1-2), 8-26, (2008).

[25] Deasy, K., Sediq, K.N., Brittle, S., Wang, T., Davis, F., Richardson, T.H. and Lidzey, D.G., ‘‘A chemical sensor based on a photonic-crystal L3 nanocavity defined in a silicon-nitride membrane’’. Journal of Materials Chemistry C, 2, 8700-8706, (2014).

[26] Notomi, M., Shinya, A., Mitsugi, S., Kira, G., Kuramochi, E. and Tanabe, T., ‘‘Optical bistable switching action of Si high-Q photonic-crystal nanocavities’’ Optics Express, 13, 2678-2687, (2005).

[27] Liu, Y., Qin, F., Meng, Z.M., Zhou, F., Mao, Q.H. and Li, Z.Y., ‘‘All-optical logic gates based on two-dimensional low-refractive-index nonlinear photonic crystal slabs’’. Optics Express, 19, 1945-1953, (2011).

[28] Chalcraft, A.R.A., Lam, S., O’Brien, D., Krauss, T.F., Sahin, M., Szymanski, D., Sanvitto, D., Oulton, R., Skolnick, M.S., Fox, A.M. and Whittaker, D.M., ‘‘Mode structure of the L 3 photonic crystal cavity’’. Applied Physics Letters, 90, 241117, (2007).

[29] Badolato, A., Hennessy, K., Atatüre, M., Dreiser, J., Hu, E., Petroff, P.M. and Imamoğlu, A., ‘‘Deterministic coupling of single quantum dots to single nanocavity modes’’. Science, 308, 1158-1161, (2005).

[30] Astratov, V.N., Yang, S., Lam, S., Jones, B.D., Sanvitto, D., Whittaker, D.M., Fox, A.M., Skolnick, M.S., Tahraoui, A., Fry, P.W. and Hopkinson, M., ‘‘Whispering gallery resonances in semiconductor micropillars’’. Applied Physics Letters, 91, 071115, (2007).

[31] Wu, Z., Mi, Z., Bhattacharya, P., Zhu, T. and Xu, J., ‘‘Enhanced spontaneous emission at 1.55 μ m from colloidal PbSe quantum dots in a Si photonic crystal microcavity’’. Applied Physics Letters, 90, 171105, (2007).

[32] Song, H.Z., Takemoto, K., Miyazawa, T., Takatsu, M., Iwamoto, S., Ekawa, M., Yamamoto, T. and Arakawa, Y., ‘‘High quality-factor Si/SiO 2-InP hybrid micropillar cavities with submicrometer diameter for 1.55-μm telecommunication band’’. Optics Express, 23, 16264-16272, (2015).

[33] Ho, Y.L., Gibson, R., Hu, C.Y., Cryan, M.J., Rarity, J.G., Heard, P.J., Timpson, J.A., Fox, A.M., Skolnick, M.S., Hopkinson, M. and Tahraoui, A., ‘‘Focused ion beam etching for the fabrication of micropillar microcavities made of III-V semiconductor materials’’. Journal of Vacuum Science & Technology B: Microelectronics and Nanometer Structures Processing, Measurement, and Phenomena, 25, 1197-1202, (2007).

[34] Stoltz, N.G., Rakher, M., Strauf, S., Badolato, A., Lofgreen, D.D., Petroff, P.M., Coldren, L.A. and Bouwmeester, D., ‘‘High-quality factor optical microcavities using oxide apertured micropillars’’. Applied Physics Letters, 87, 031105, (2005).

[35] Shim, Y.S., Kim, K.N., Hwang, J.H., Park, C.H., Jung, S.G., Park, Y.W. and Ju, B.K., ‘‘Spectral-distortion-free light extraction from organic light-emitting diodes using nanoscale photonic crystal’’. Nanotechnology, 28, 045301, (2016).

[36] Chakaroun, M., Diallo, A.T., Hamdad, S., Khadir, S., Fischer, A.P.A. and Boudrioua, A., ‘‘Experimental and Theoretical Study of the Optical Properties Optimization of an OLED in a Microcavity’’. IEEE Transactions on Electron Devices, 65, 4897-4904, (2018).

[37] Coburn, C., Jeong, C. and Forrest, S.R., ‘‘Reliable, all-phosphorescent stacked white organic light emitting devices with a high color rendering index’’. ACS Photonics, 5, 630-635, (2017).

[38] Jeon, S., Lee, S., Han, K.H., Shin, H., Kim, K.H., Jeong, J.H. and Kim, J.J., ‘‘High-Quality White OLEDs with Comparable Efficiencies to LEDs’’. Advanced Optical Materials, 6, 1701349, (2018).

[39] Polisseni, C., Major, K.D., Boissier, S., Grandi, S., Clark, A.S. and Hinds, E.A., ‘‘Stable, single-photon emitter in a thin organic crystal for application to quantum-photonic devices’’. Optics Express, 24, 5615-5627, (2016).

[40] Zhang, W., Yao, J. and Zhao, Y.S., ‘‘Organic micro/nanoscale lasers’’. Accounts of chemical research, 49, 1691-1700, (2016).

Chapter 2
Theoretical Background

2.1 Introduction

Moore's Law predicts that an exponential development in the complexity of electronic devices is expected and anticipates that problems will arise because of a reduction in the physical dimensions of electronic devices. These results from heating effects and electromagnetic interference in nanoscale transistor devices; a situation that will create a problem for the future of electronics. The science of photonics attempts to use light to carry out tasks that are conventionally performed by electronics. Nanophotonic devices have some similarities to conventional electronic circuits; for example they can act as optical delay lines, couplers and splitters, logical gates, optical memories, filters and multiplexers. Optical connectors also offer the promise of greater bandwidth, decreased power loss and optical memory system. Progress has been driven by semiconductor fabrication techniques that now make it possible to produce nanometre size photonic devices that can control light at the nanoscale [1-9].

Photonic crystals (PC) are periodic optical structures with low and high refractive index layers that can control the propagation of electromagnetic waves [10-11]. The term Photonic Crystal arises from the combination of a periodic crystalline material that has a length–scale that is defined at optical frequencies, allowing it to interact with light [12-13]. In a periodic dielectric material, light at a range of frequencies cannot propagate, thus creating a photonic band gap (PBG); an idea first suggested by Yablonovitch [14] and John [15]. If the structure of a photonic crystal prohibits the propagation of light in all directions, this means that the crystal possesses a complete photonic band gap [16-19]. Defects can be placed into the structure of such a photonic crystal, creating an optical nanocavity that can confine light inside a volume smaller than a cubic wavelength $(\lambda/n)^3$. Very high quality factor cavities can be formed from such structures, which lead to a strong localization of the optical field. This can be used in different applications that depend on the control of the spontaneous emission from a quantum emitter, such as thresholdless lasers [20]. This approach can also be used to improve the efficiency of organic light emitting diodes (OLED) [21-22]. The unusual optical properties of photonic crystals (such as anomalous reflection and negative refractive index) can also result as result of the interaction between periodic dielectric materials and light [23-26]. Artificial photonic crystals bear similarity to structures that appear in nature, such as the wings of certain butterflies [27-29] as in Figure 2.1

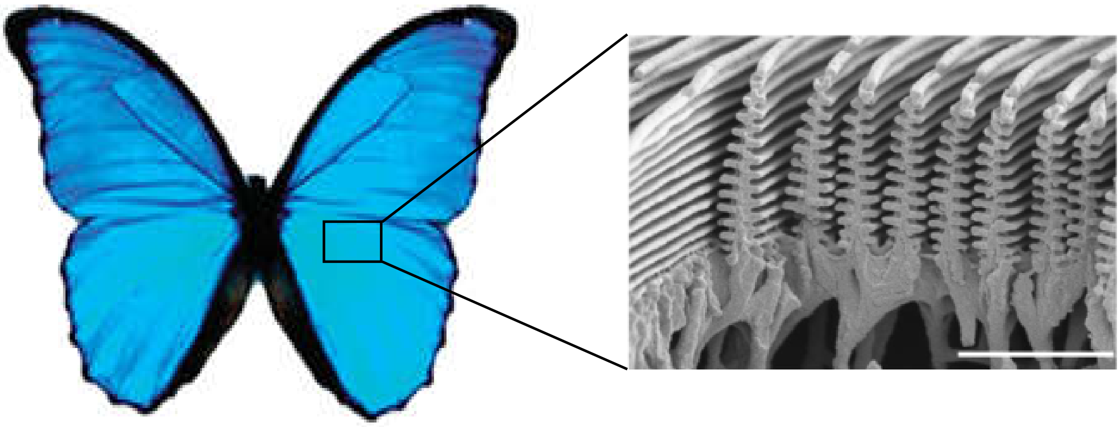

(a) (b)

Figure 2.1: (a) Photonic crystals found in nature. Here surface structure of butterfly wings leads to blue iridescence. (b) An SEM image of the cross-section of a butterfly wing. This Figure was taken from Ref [29]

2.2 General Literature review of photonic crystal-devices

The field of Photonic Crystals has been dominated by inorganic semiconductors for many years because such materials have a high refractive index, allowing the propagation of light that travels through a medium to be controlled with a high degree of precision. Inorganic and organic materials have been used to made photonic crystals. Inorganic materials have been used during the last decades in multiple microscale technology applications; for example GaAs/InGaAs microlenses, InAs/InGaAs/GaAs microdisks and microrings, InGaAs/GaAs microtube lasers and semiconductors containing GaAs/GaAlAs quantum dots [30-37].

Lord Rayleigh was the first person to consider forbidden stop-bands in one dimensional periodic media [38]**.** The idea of photonic bandgap or photonic crystal was then suggested by Eli Yablonovitch and Sajeev John who used the physics of solid state and classical electromagnetism to illustrate the principle of photonic band gaps in three dimensions [14-15]. Yablonovitch et al then introduced a new face-centred-cubic structure that solved two problems in photonic band structure: (i) he showed that the band gap of a full three-dimensional photonic crystal could exist in a dielectric structure and (ii) such structures could be made using the microfabrication techniques [39]. In 1991, Philip Russell introduced the concept of photonic crystal fibres (PCF). He suggested using a photonic bandgap to confine light in a hollow core fibre through engineering periodic, microscopic holes in a wavelength size lattice using Ge-doped silica semiconductors [40].

Practical applications, such as the first Vertical Cavity Surface-emitting Laser devices were produced by Iga et al. in the late 1970s. These consisted of GaAs layers of a few micrometres in thicknesses that were coated with dielectric mirrors [41]. The first low threshold lasing operation was then demonstrated using a GaInAsP/InP SE laser by Iga et al. in 1979 [42].

In 1991 Yablonovitch et al produced acceptor and donor modes in three-dimensional periodic dielectric structures using Si and GaAs semiconductors as evidenced a forbidden gap for electromagnetic wave propagation. The donor modes were produced by adding more dielectric material inside the photonic crystal. Conversely, acceptor modes were produced by the removal of dielectric material. This has led to the realization of high quality electromagnetic cavities of ~1 cubic wavelength operating at short wavelengths [43].

In 1992 Weisbuch, et al explored optical cavity devices in which quantum well excitons and the optical cavity are in resonance [44]. Rabi splitting behaviour was observed between the quantum well excitons and the electromagnetic field of the microcavity. Lasing at room temperature in strong- coupled inorganic GaN microcavities was first observed by Christopoulos et al in 2007, as a result of a high binding energy of Wannier-Mott excitons in GaN [45]. In 1976 Shyh Wang, et al invented an improved form of optical laser consisting of a two-dimensional distributed feedback periodic structure based on GaAs-GaAl-As semiconductors that supported controllable transverse modes [46]. In 1993 Wendt, et al explored the fabrication of two-dimensional photonic lattice structures in GaAs/AlGaAs using direct-write electron-beam lithography (EBL) and reactive-ion-beam etching (RIE) to etch features in size of 50 nm. Using such a technique, a hexagonal array of air cylinders were etched into a semiconductor surface having a high refractive index contrast to form the lattice of a photonic crystal [47].

Following this, Gruning, et al reported the creation of a two-dimensional photonic band structure in a square lattice of circular air rods in macroporous silicon, with individual gaps observed for both E- and H-polarized radiation in the infrared region between 20–40 μm [48]. Laser devices have been fabricated from a single defect in a two-dimensional photonic crystal using III-V based semiconductors. Here, two different mechanisms were used to confine light inside the microcavity; first, trapping photons in the vertical direction was achieved using a λ/2 high-index slab with total internal reflector at the air-slab interface to confine light in the cavity. Secondly, a 2D photonic crystal that was formed from a hexagonal array of air holes etched into the slab that was used to localize the light in plane [49]. In 1978 Ohtaka improved the formalism for photonic band structure calculations and discussed photonic crystals that exist in three-dimensions [50].

Strong coupling observed by Weisbuch et al introduced an important era in solid state physics [44]. Strong coupling between single photons and excitons was be first demonstrated in GaAs and AlAs micropillars [51]. Following this, GaAs/AlAs micropillar microcavities with 10 μm diameter and a Q factor of up to 30,000 was then demonstrated. Such Q-factors were up to three times higher than the Q factor of planar microcavity structures. Here, electron-beam lithography was used together with inductively coupled plasma to fabricate the micropillars [52]. Increases in quality factors up to 48,000 were achieved using an oxide aperture to confine optical modes in a micropillar structure that operated in the weak coupling regime prepared using a molecular-beam epitaxy on a semi-insulating GaAs substrate [53]. In this structure the spontaneous emission rate of an atom was enhanced as compared to outside the cavity [54].

Ho et al investigated the blue-shifts in GaAs/AlAs micropillar mode resonance as the micropillar diameter was decreased using 3-D finite difference time domain (FDTD) method [55]. Lecamp et al have also studied the effect of the oxide cladding and the corrugation of Bragg mirror on the quality factor of GaAs/AlGaAs micropillars with a Q-factor of 1,500 for a 600 nm diameter micropillar [56]. Reitzenstein et al fabricated micropillar microcavities having diameters between 1 μm and 4 μm. As a result a micropillar microcavity laser with a Q-factor of 23,000 from a weak coupling regime was demonstrated with a low lasing threshold [57]. One year later, the same authors designed AlAs/GaAs micropillar cavities with diameter up to 4 μm using a high reflectivity distributed Bragg reflectors DBRs to produce a high quality factors up to 165,000 [58]. Boulier, et al have also demonstrated a strong enhancement of a novel squeezed light source in semiconductor micropillars based on 15 pairs of GaAs–InGaAs [59].

Winkler et al demonstrated a new type of AlAs/GaAs micropillar microcavity containing InAs quantum dots embedded in its centre. This structure was able to confine the electromagnetic field in a horizontal direction without deep etching using a bullseye defect technique, allowing optical modes to be squeezed into a high Q factor cavity having a very small volume. As a result, a Q factor of up to 100,000 was obtained in a micropillar with a diameter less than 1.5 μm [60]. Stock et al observed an enhancement of emission from a weakly coupled microlaser that could operate as a light source to excite another microcavity structure [61]. Bonato et al studied the operation of quantum information schemes in a weak coupling regime. Here, a single electron charge confined in a quantum dot was imbedded in a micropillar microcavity. Such structure is used as a quantum CNOT gate [62].

Significant attention and an increasing number of studies have been directed toward the use of organic materials and hybrid organic-inorganic materials in photonics, due to the ability to customize their optical properties and the possibility of combining the properties both of inorganic materials such as high mobility, electrical pumping and band engineering with the properties of organic materials such as low cost and high luminescence quantum yield at room temperature. In 1997 a hybrid cavity combining inorganic and organic semiconductors was theoretically proposed [63-64]. One of the first studies of the physics of placing emitting molecules inside a cavity resonator explored its effect on spontaneous emission. Here, it was argued that the resonator's dimensions should be similar to the emission wavelength to control spontaneous emission [65]**.** Dodabalapur et al. demonstrated red, green, and blue emissive devices based on a single organic material using Fabry-Perot

Cavity effects to selectivity enhance the broad luminescence from an organic semiconductor [66].

In 1996 Tessler and co-workers demonstrated the first optically pumped organic microcavity laser. Organic lasers offer the prospect of wavelength tunability, low-cost production and mechanical flexibility [67]**.** Following this, Dirr et al. observed the effect of the position of a thin film in a cavity on its luminescence spectra, with the cavity consisting of an organic material such as Alq3 positioned in a planar Fabry-Perot microcavity [68-69]. The first observation of the strong coupling regime within an optical organic semiconductor microcavity was reported in 1998 [70]. In 1999, Tokito et al. designed a planar microcavity composed of three pairs of SiO2/TiO2 dielectric mirrors between an organic layer and a top metal layer working as a mirror [71]. The same year, Kozlov et al at demonstrated lasing action using an assortment of cavity designs containing thin films of organic semiconductors by optical pumping [72]. Lin et al. studied the optical characteristics of microcavity organic light-emitting devices based on two metal mirrors. The study showed that a high-reflectivity back mirror and a low-loss high-reflection exit mirror were essential to enhance the luminance from such microcavity devices [73].

Pisanello et al used two-dimensional photonic crystal fabricated resonators from silicon nitride as a platform to create photonic devices based on spontaneous emission technique of nanoemitters. As a result, spontaneous emission was observed in the visible spectral range [74]. Kitamura, et al used patterned SiO2 membranes to fabricate an organic semiconductor based two-dimensional photonic crystal nanocavity. The organic layer based on DCM2 doped into AlQ3 which was deposited on a SiO2 membrane to form an organic photonic crystal. Here, an increase in the intensity by more than ten times was observed at the resonant wavelength [75-76]. Adawi, et al have also fabricated light emitting diodes based on a conjugated polymer containing a two-dimensional photonic crystal (PC) placed between the

ITO anode and the glass substrate. It was observed that LEDs incorporating the PC had an increased electroluminescence external quantum efficiency by a factor of (2.3 ± 1.0) times [77]. Gourdon, et al fabricated and investigated a two-dimensional photonic crystal micro-cavity containing an organic gain material (Alq3: DCJTB) deposited on a planar Si_3N_4 photonic crystal microcavity. They illustrated lasing emission from the structure under optical pumping of the organic layer [78].

Dusel et al. have recently used thermal imprint technology to produce three-dimensional pillar microcavities with this technique forming hemispherical pillar geometries rather than cylindrical pillars. Hemispherical pillars were imprinted directly on top of dielectric mirrors from an organic semiconductor with the pillars then capped by a thin layer of gold [79]. Organic photonic crystals have also been used to enhance the efficiency and to improve the performance of photovoltaic cells [80-82].

2.3 Maxwell's Equations in a Periodic Structure

In order to understand and describe the behaviour of the electromagnetic waves that propagate in a uniform dielectric medium (dielectric constant ε) we need to use Maxwell's macroscopic equations [83-84]. In their differential form these are**:**

$$\nabla.\vec{\mathrm{B}} = 0 \qquad \text{2-1}$$

$$\nabla.\vec{D} = \rho \qquad \text{2-2}$$

$$\nabla \times \vec{E} + \frac{\partial \vec{B}}{\partial t} = 0 \qquad \text{2-3}$$

$$\nabla \times \vec{H} - \frac{\partial \vec{\mathrm{D}}}{\partial \mathrm{t}} = \vec{\mathrm{J}} \qquad \text{2-4}$$

Here, **E** is the electric field ($\mathrm{Vm^{-1}}$), **H** is the magnetic field ($\mathrm{Am^{-1}}$), **B** is the magnetic flux density (T), **D** is the electric displacement ($\mathrm{Cm^{-2}}$), **J** is the electric current density ($\mathrm{Am^{-2}}$) and **ρ** is the electric charge density ($\mathrm{Cm^{-3}}$) [85]**.** Inside a mixed dielectric medium where light propagates but there are no sources of light, we can consider $\rho = 0$ and $J = 0$ [84]**.** The auxiliary fields can be defined as:

$$\mathrm{D} = \varepsilon_o \mathrm{E} + \mathrm{P} \qquad \text{2-5}$$

$$\mathrm{H} = 1/\mu_o\, \mathrm{B} - \mathrm{M} \qquad \text{2-6}$$

$$\mathrm{P} = \varepsilon_o \overleftrightarrow{\chi_e}\, .\ \mathrm{E} \qquad \text{2-7}$$

$$\mathrm{M} = \overleftrightarrow{\chi_m}\, .\ \mathrm{H} \qquad \text{2-8}$$

Here, **P** is the "polarization field, **M** is the "magnetization field and χ is the electric and the magnetic susceptibility [86]. The above equations can be written for local, nonmagnetic, linear, isotropic, and homogeneous materials using [87-88]

$$\mathrm{D}\,(\mathrm{r}) = \varepsilon(\mathrm{r})\, \mathrm{E}(\mathrm{r}) \qquad \text{2-9}$$

$$\mathrm{B}\,(\mathrm{r}) = \mu(\mathrm{r})\, \mathrm{H}(\mathrm{r}) \qquad \text{2-10}$$

Here, ε and μ are the permittivity and permeability respectively [89]. The refractive index n can then be expressed as $\sqrt{\varepsilon\mu}$, however for most dielectric media where μ ≈ 1 we can write n = $\sqrt{\varepsilon}$. Let us assume unit magnetic permeability, so that **B**≡**H** and ε(r) is the spatially dependent dielectric constant [10, 90].

In the limits of linear, homogeneous, non-magnetic materials with no free carriers or currents, $\vec{\mathbf{H}}$ and $\vec{\mathbf{E}}$ fields can be written as time and space dependent functions [89]**.** To understand the operation of photonic crystals it is necessary to solve equations 2-9 and 2-10 in the frequency domain. We can write **H** and **E** as expressed in equations 2-11 and 2-12 [89-91]

$$\vec{H}(\vec{r},t) = \mathrm{H}_0(r)\mathrm{e}^{\mathrm{i}\omega\mathrm{t}} \qquad 2\text{-}11$$

$$\vec{E}(\vec{r},t) = \mathrm{E}_0(r)\mathrm{e}^{\mathrm{i}\omega\mathrm{t}} \qquad 2\text{-}12$$

where $\mathbf{E_0}$ and $\mathbf{H_0}$ are vectors that define the amplitudes of the fields, and ω=2πf is the angular frequency of the propagating wave. Maxwell's equations can be arranged into an equation that is given entirely in terms of H:

$$\nabla \times \left[\frac{1}{\varepsilon(\vec{r})}\,\nabla \times \vec{\mathrm{H}}(\vec{\mathrm{r}})\right] = \left(\frac{\omega}{c}\right)^2 \vec{H}(\vec{r}) \qquad 2\text{-}13$$

This equation is called the master equation [92]. The magnetic field equation is usually considered as the starting point for photonic band structure computation and is helpful when calculating the dispersion diagrams of different photonic crystals [91] as it takes the form of an eigenvalue problem:

$$\Theta\mathrm{H}(\mathrm{r}) = \frac{\omega^2}{c^2}\,H(r) \qquad 2\text{-}14$$

where Θ is a Hermitian operator [90].

The total potential energy V(r) of a perfect solid crystal must reflect the periodicity of the crystal lattice. Therefore the Schrodinger equation solution

$$\left(\frac{\hbar^2}{2m}\right)\nabla^2\Psi + [E - V(r)]\Psi = 0 \qquad 2\text{-}15$$

is a Bloch function:

$$H(k,r) = \mathrm{u_k}(r)\mathrm{e}^{-\mathbf{ik.r}} \qquad 2\text{-}16$$

in which $\mathrm{u_k}(r)$ is a function having the periodicity of the lattice [83-93]**.** The easiest solution for equation 2-15 is to consider V(r) to be constant and equal to zero. This produces plane waves and free electron wave functions in which electron energy is given by

$$E = \frac{\hbar^2\mathrm{k}^2}{2m} \qquad 2\text{-}17$$

If we include the periodicity of the lattice, but define the perturbing potential to be arbitrarily weak, the energy of an electron can be expressed as

$$E = \frac{\hbar^2}{2m}\,|k + G|^2 \qquad 2\text{-}18$$

where G is a reciprocal lattice vector (V = 0, ε_i =1 in free space) and is given by [88, 93]

$$G = \mathrm{n}\,\frac{2\pi}{a} \qquad 2\text{-}19$$

where n is an arbitrary integer. The value (2π/a) has an important connotation, as it defines the Brillouin zone [94]. In a photonic crystal, $\varepsilon(\vec{\mathrm{r}})$ is periodic, and so Bloch's theorem can be used to expand the **H** field in plane waves as

$$H_{(r)} = \textstyle\sum_G \sum_{\lambda=1}^{2} h_{G,\lambda}\,\hat{e}_\lambda e^{i(k+G).r} \qquad 2\text{-}20$$

where **k** is a wave vector in the Brillouin zone of the lattice and $\hat{e}$ is a unit vector perpendicular to (k+G) [95]. Thus is in a periodic medium, the **H** field behaves as a Bloch wave [96]**.** Furthermore the **E** field in a periodic medium with a 2d periodicity where d is the thickness of the layers, can also be written as

$$\mathrm{E(z + 2d) = e^{ik_B 2d}\,E(z)} \qquad 2\text{-}21$$

where $\mathrm{k_B}$ is a Bloch wavevector. When solving equation (2-21) in term of sin and cosine where cos ($2k_Bd$) is usually in the range of [−1, 1], there are some solutions we cannot find. The absence of solutions leads to the concept of bandgaps. The Bloch wavevector at the band-edges is given by $k_Bd = n\pi/2$. For a given direction of propagation characterized by k, one finds frequency regions in which propagation through the crystal is possible and frequency regions for which propagation is inhibited. The dispersion relation $\omega(k)$ can be found from each Bloch wavevector k_B [88-97].

2.4 Photonic band structure and photonic crystal dimensionality

The dispersion relation of a photon in free space is given by $\omega = ck$ which relates the angular frequency $\omega = 2\pi\nu$ of the photon to its wave vector $k = 2\pi/\lambda$. The speed of light c is the slope of this linear dependence and in a periodic dielectric structure the dispersion relation can be modified due to the interaction between light and matter [84, 88]. From this, we can also determine the group velocity $v = \frac{\partial\omega}{\partial k}$ and the phase velocity $v_p = \frac{\omega}{k}$ [100- 101]. In a photonic crystal, the frequency intervals result from coherent scattering and interference of electromagnetic radiation from the structured dielectric medium with no photon modes being allowed. An emitter placed within the photonic crystal cavity undergoes a suppression of spontaneous emission, resulting from the absence of allowed optical modes inside the photonic gap [94].

Photonic crystals can be classified on the basis of the dimensionality of the refractive index modification. Depending on the wavelength of light, light reflected from the periodic dielectric interfaces can interfere constructively or destructively and thus the lattice leads to a band structure for photons and exhibits bands in which photons can propagate, as well as photonic band gaps in which they cannot [90]. Depending on structure design, there are three categories of PhCs, called one-dimensional (1D), two-dimensional (2D) and three-dimensional (3D) structures as shown in figure 2.2 [102, 103]:

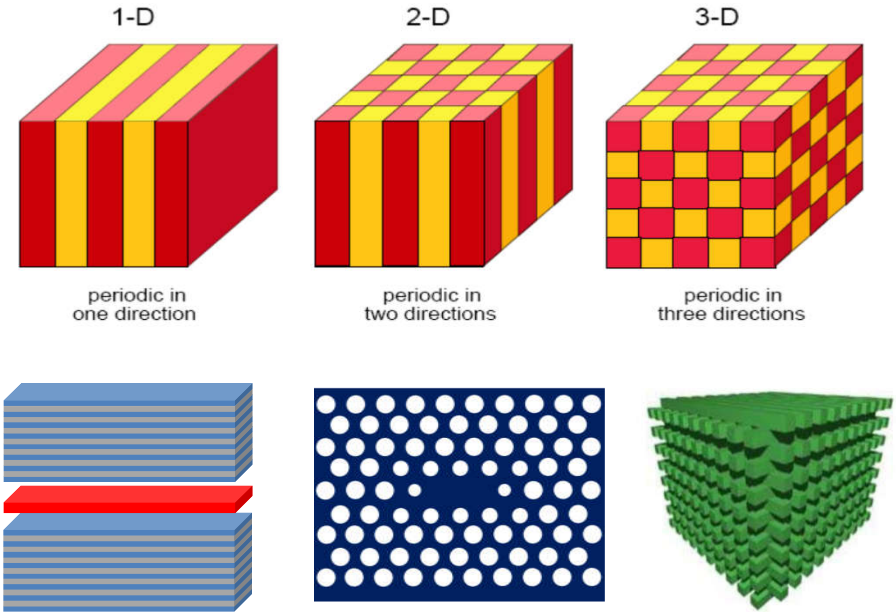

(a) (b) (c)

Figure 2.2: Schematic depiction of photonic crystals that are periodic in one, two, and three dimensions, where the periodicity is in the material (typically dielectric) structure of the crystal. This Figure was taken from Ref [104].

One-dimensional (1D) photonic crystals are known as Distributed Bragg reflectors (DBR). Two-dimensional (2D) photonic crystals have been used in photonic crystal fibres. The most challenging structures to fabricate are three-dimensional (3D) photonic crystals in which light propagation can be controlled completely in all directions by a photonic bandgap [105, 106]. PhCs can act as both waveguides and mirrors similar to a 1D Bragg mirror [107].

The propagation of photons in such periodic structures are defined by Bloch function as summarized by equations (2-16) and (2-19) where the wave vector k_r in Bloch theory can be referred to the Brillouin zone (BZ) of a periodic structure [84]. The dispersion relation for photon propagation in a two dimensional photonic crystal possessing a hexagonal array of holes, is shown in figure 2.2 (b). This is defined by three high symmetry points, which (known as Γ, K and M) define the irreducible Brillouin zone as shown in Figure 2.3:

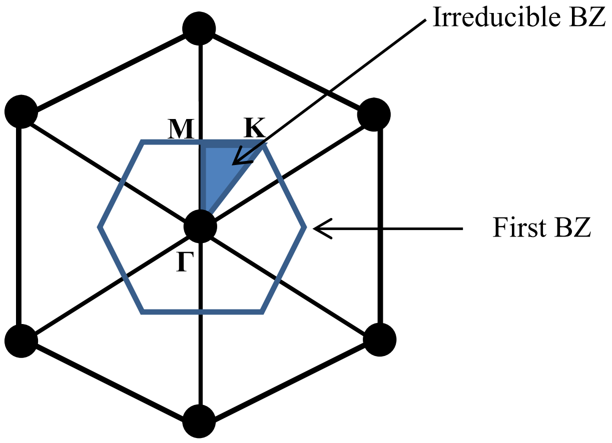

Figure 2.3 A hexagonal lattice and irreducible Brillouin zone [108].

By using the Bloch function, equation 2-16 and substituting it into the master equation 2-13 we obtain

$$(\nabla + ik) \times \left[\frac{1}{\varepsilon(\vec{r})} (\nabla + ik) \times \mathrm{u_k}(r)\right] = \left(\frac{\omega(k)}{c}\right)^2 \mathrm{u_k}(r) \qquad \text{2-22}$$

The eigenvalues $\left(\frac{\omega(k)}{c}\right)^2$ of equation 2-21 are continuous functions of the Bloch wavevector (***k***) inside the first Brillouin zone in both Γ-M and Γ-K directions and form a discrete set of eigenvalue (energies) when plotted in a band structure or dispersion diagram. This allows us to visualise the photonic band structure in a photonic crystal. The photonic band gap in a one dimensional photonic crystal consisting of dielectric layers with different dielectric constants (such as a Bragg multilayer stack or a Bragg mirror [84, 109]) is illustrated in Figure 2.4.

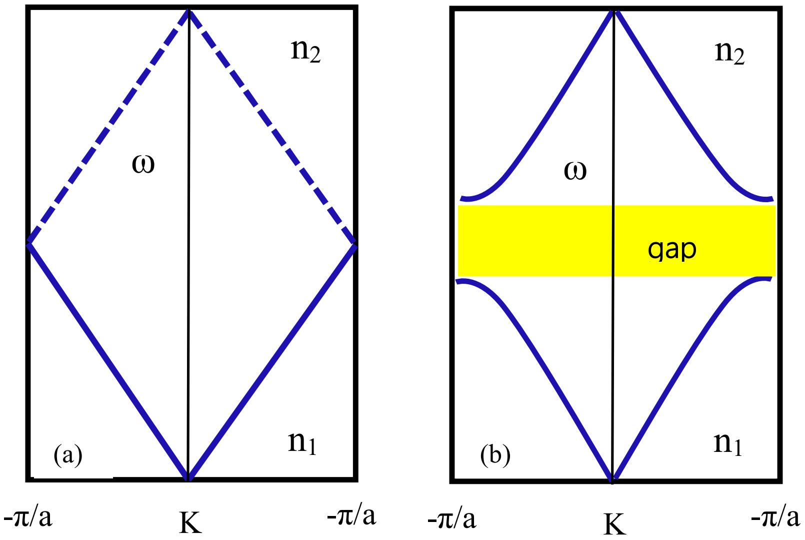

Figure 2.4 (a) A schematic photonic band diagram of a uniform one-dimensional medium in which the layers have the same dielectric constant (ε), with periodicity a. (b) A schematic of photonic band gap where there is a periodic dielectric variation, where the layers alternate between n_1 and n_2. Here, a gap has been opened by splitting the degeneracy at ±π/a, corresponding to the 1D Brillouin zone boundaries. This Figure was taken from Ref [110].

In a multilayer structure, the size of the photonic band gap depends on the contrast between the refractive index of the layers with the smaller the contrast, the smaller the band gap [110]. By increasing the photonic band gap, it is possible to create strong light confinement [111-113]. For a two dimensional photonic crystal consisting of a patterned layer, there are two main structures; a dielectric slab patterned with air holes in either a triangular or square array [114,116]. Villeneuve et al proved that the triangular lattice has a larger photonic band gap than a square lattice [116,117].This is as a result of having closer symmetry for the first Brillouin zone [118]. For this reason, the square lattice has been largely ignored as a result of its small bandgap with most effort focussed on a triangular lattice instead [119].

There are two different sets of optical modes in a 2D photonic crystal; transverse electric field modes (TE) which are even modes and transverse magnetic field modes (TM) that are odd modes [109]. Figure 2.5 illustrates the vector component directions where the transverse electric field – TE modes, the magnetic field vector components (H_x and H_y) are confined in the xy plane direction, and corresponding (E_z) field parallel to the Z- direction.

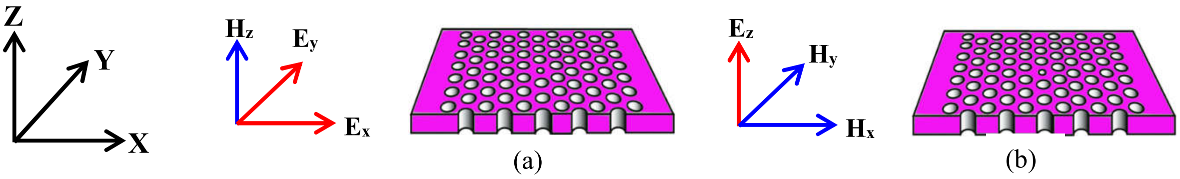

(a) (b)

Figure 2.5: illustrates the vector component directions for electromagnetic field that propagates in a 2D photonic crystal having a hexagonal lattice of air holes. (a) The transverse magnetic field – TM mode polarization. (b) The transverse electric field – TE mode polarization.

can be used to determine the photonic band gap using a plane wave basis method (MPB) [120] and a guided mode expansion method (GME) [121]. Figure 2.6 is the photonic band gap structure for a two dimensional photonic crystal having a hexagonal lattice of air columns r/a=0.48 with a high dielectric constant ε_r=13 for both TE and TM polarized light. A large photonic band gap is observed which is located within the normalized frequency band, *a/λ*, at 0.43 to 0.52 [84]

.

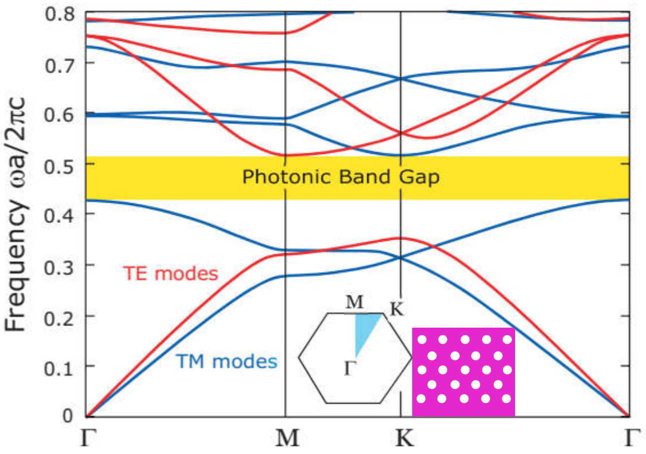

Figure 2.6 shows the photonic band gap for a hexagonal lattice of air columns (r/a=0.48) and (ε_r=13) for TE/TM polarized light in a high dielectric material, This Figure was taken from Ref [11].

The frequency intervals in a photonic crystal results from coherent scattering and interference of electromagnetic radiation in a structured dielectric medium in which no photon modes are allowed [122]. Usually, photonic band gaps can be distinguished depending on size and position of the band gap, where some modes are allowed to propagate and others are prohibited [123,124]. The band size is defined as the relative band gap width which is determined as the gap to the mid gap ratio ($\Delta\lambda/\lambda$, $\Delta\omega/\omega$ or $\Delta E/E$) [125-127].

2.5 Parameters that influence the photonic band gap and the optical properties of photonic crystals.

The main internal and external parameters that impact the size and position of a photonic band gap and the properties of a photonic crystal [128] are illustrated in figure 2.7.

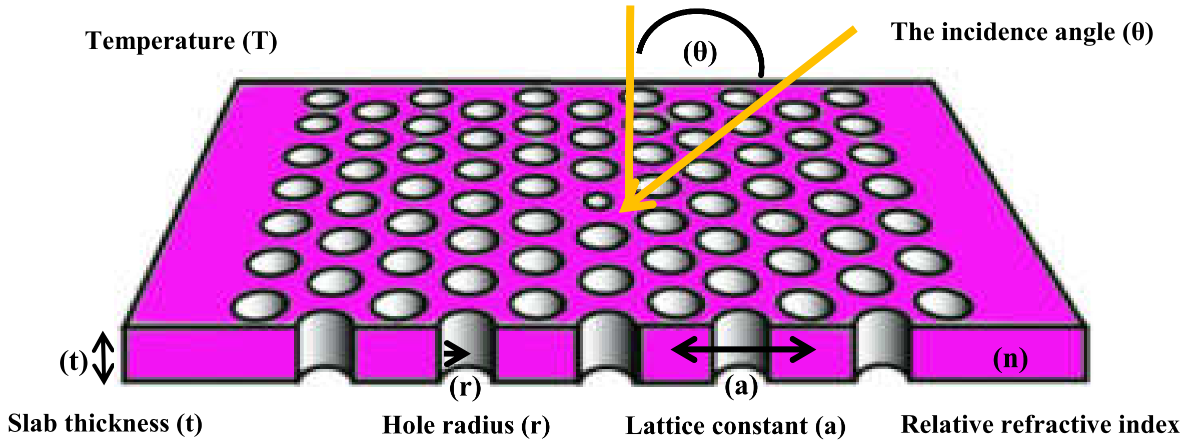

Figure 2.7 Two dimensional photonic crystals having a hexagonal lattice of air columns with the main parameters shown that affect the size of the photonic band gap and the properties of the photonic crystals

- Symmetry, or in other words the unit-cell arrangement of the PC structure. Square and hexagonal lattices are the main arrangements used in two dimensional photonic crystals [129-133].

- Slab thickness. If the slab thickness is very high (more than half wavelength), higher order modes can be supported with little energy cost by increasing number of horizontal nodal planes. As a result, such modes will act to prohibit the formation of the photonic band gap [134]**.**
- Filling fraction (FF). This is the relative volume occupied by each material (air or dielectric) in a photonic crystal [135]. The photonic bandgap increases with increasing fill factor [136].
- Refractive index contrast (n). The refractive index contrast (n_1/n_2) is defined as the ratio between the refractive index of the different materials in a periodic structure. When the dielectric constant increases, the resonant wavelength shifts to the higher wavelengths [137]. Moreover, increasing the refractive index of the slab leads to an increase in the width of the photonic band- gap [138].
- Lattice constant (a), is the length of the unit cell in a periodic structure [139,140]. This is the distance between air holes in a two dimensional photonic crystal. The position of a photonic band gap will undergo a red shift as a result of an increase in the lattice constant [141-143].
- Temperature (T). The photonic band gap of the photonic structure will shift to shorter wavelengths as a result of a decrease in temperature. This is due to the effect of temperature on the refractive index of a periodic structure [144].
- The incidence angle (θ). Decreasing the incidence angle leads to a decrease in the width of the photonic band gap and a shift to longer wavelengths. This results from a change in the cosine function in the phase equation [144].

$$\emptyset = \frac{2\pi d}{\lambda} \, n \, \cos\theta \qquad 2\text{-}23$$

Here, d and n are layer thickness and refractive index respectively.

2.6 Light confinement in a photonic nanostructure.

Light confinement without propagation is difficult, as photons do not like to be trapped for long times in a small volume. However, this is what Noda and his team achieved [145-146]. Confining photons in a mode volume smaller than $(\lambda/n)^3$ where λ is the wavelength of light results in an increase in interactions with matter, with effects controlled by the laws of quantum mechanics. This principle has been used in cavity quantum electrodynamics in which low-loss micro-resonators are used to confine light. The tight confinement of photons results in a strong coupling that can be used to build quantum gates between photonic qubits [147-148].

Light confinement in a small mode volume for a relatively long time can be achieved using a photonic nanostructure. The strong localization of photons has resulted in important new applications in quantum and nonlinear optics, such as low-power optical switches, zero-threshold lasers and memory elements [149].

Light can be confined by introducing a physical defect into a periodic photonic crystal. Such physical defects can act as a trap to confine light within the optical band gap of the photonic structure. We can determine the mode volume (*V*) over which light is confined by spatially integrating the total electric field energy and normalizing it, using the maximum electric field energy density as shown in equation 2-24 [150,151] :

$$V = \frac{\iiint \varepsilon\,(\mathrm{r})|\mathrm{E}(\mathrm{r})|^2\,\mathrm{dV}}{\max[\varepsilon(\mathrm{r})|\mathrm{E}(\mathrm{r})|^2]} \qquad 2\text{-}24$$

Here, V is the mode volume, ε(r) is the dielectric constant and E(r) is the electric field strength. The strength by which light is confined can be determined from the ratio between cavity quality factor (Q) and the mode volume (V). One of the most important parameters for optical micro or nano cavities is the quality factor, which is the ratio between the total energy stored in the cavity to the energy loss per cycle as shown in equation 2-25 below [152,153]:

$$Q = \omega\tau = \omega \frac{W}{\frac{-dW}{dt}} = 2\pi\nu \frac{W}{\frac{-dW}{dt}} \qquad \text{2-25}$$

Here $\boldsymbol{\omega}$ is angular frequency of the optical field, τ is photon storage lifetime, v is the optical frequency, W is the optical energy localized in the cavity and $-dW/dt$ is the loss or attenuation of the optical energy per unit time [154]. This can also be defined as the ratio between the central wavelength of the cavity (λ_o) to the full-width half-maximum (FWHM) ($\Delta\lambda$) of the cavity resonance:

$$Q = \frac{\lambda_o}{\Delta\lambda} \qquad \text{2-26}$$

Equation 2-26 can also be re expressed as:

$$Q = \frac{E}{\Delta E} = \frac{\omega_o}{\Delta\omega} \qquad \text{2-27}$$

Optical microresonators with long cavity lifetimes, high quality factors (Q) and a small mode volume can be used to control the spontaneous emission rate of an emitter and can be used as optical memories, delay lines, or highly selective filters for photonics applications and bio or chemical optical sensors [155,156].

Experimentally, confining light in one, two and three-dimensional photonic crystals depends on one or both of the main mechanisms as illustrated in figure 2.8. The first is in-plane confinement where the quality factor (Q_{in}) is determined via the total number of periodic layers in the dielectric structure around the nanocavity. The second mechanism is out-plane confinement, where the quality factor (Q_{out}) depends on the total internal reflection (TIR) of the light confined inside the nanocavity. To confine light by total internal reflection, the light waves should reflect at an angle beyond the critical angle of the dielectric material slab in the photonic crystal [157,158].

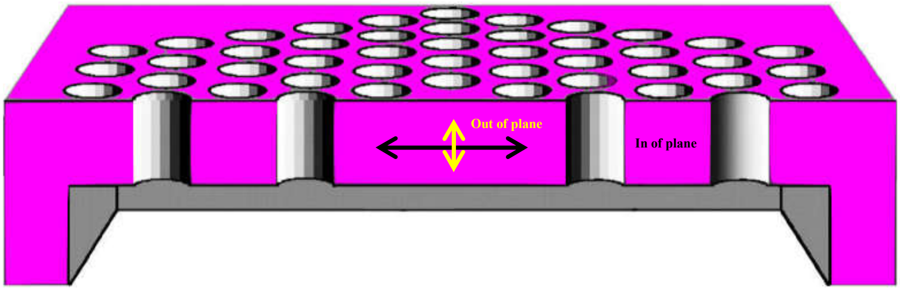

Figure 2.8 In-plane and out-plane mechanisms used to confine light in a two dimensional photonic crystal.

The total quality factor of a nanocavity can be expressed as:

$$\frac{1}{Q_t} = \frac{1}{Q_{in}} + \frac{1}{Q_{out}} \qquad 2\text{-}28$$

where Q_t is the total quality factor, Q_{in} is the quality factor resulting from in-plane light confinement and Q_{out} is the quality factor resulting from out of plane confinement. The efficiency of in-plane reflection can be improved by increasing the numbers of holes around the cavity region. This results in an increase in quality factor [159]. The out-plane confinement, (Q_{out}) can be improved by increasing the thickness of the photonic crystal slab [160-162]. In spite of the fact that two-dimensional photonic crystal slabs can strongly confine light within a volume of optical-wavelength dimensions [163], optical losses [164] can lead to an increase in the density of leaky modes in the photonic crystal [165-167]. Moreover, optical losses may occur as result of structural defects that arise through the fabrication process [168]. Such losses reduce the ideal value (theoretical value) of the quality factor in a two dimensional photonic crystal microcavity. The experimental total quality factor can thus be re-expressed as [169,170]:

$$\frac{1}{Q_{exp}} = \frac{1}{Q_{theo}} + \frac{1}{Q_{ab}} + \frac{1}{Q_{de}} \qquad 2\text{-}29$$

where Q_{theo} is the theoretical value of the quality factor expected using an ideal structure, while $1/Q_{ab}$ and $1/Q_{de}$ quantifies the additional loss in the quality factor resulting from the material absorption and structural defects respectively.

2.7 Distributed Bragg reflectors (DBRs).

The strength of light-matter interaction can be greatly enhanced by confining light in a small volume using planar semiconductor microcavities. A microcavity is a structure in which an active semiconductor layer is placed between two distributed Bragg reflectors (DBRs). A planar microcavity structure is illustrated in Figure 2.9. Here, the cavity layer has a thickness of around 200 nm and is placed between the DBRs. Such structures can be used to study either the weak and strong coupling regime [171-177]. The modification of the coupling between light and an atom placed in such a cavity was studied firstly by Kastler [178].

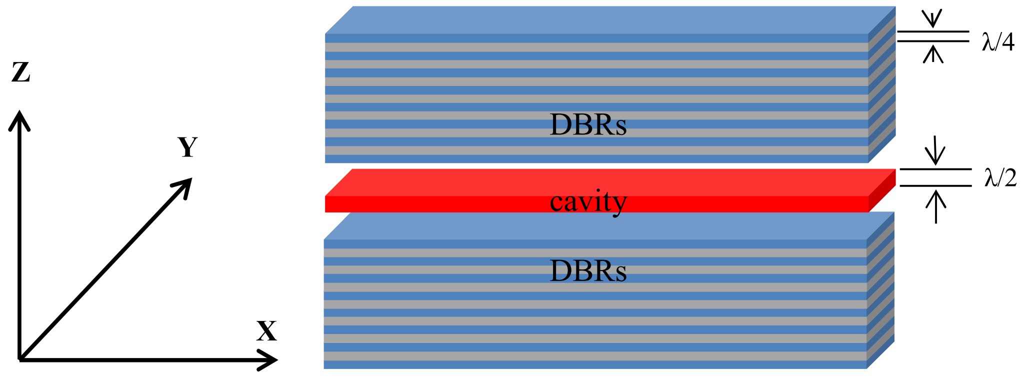

Figure 2.9: A schematic depiction of a photonic crystal structure that is periodic in one dimension, where the periodicity occurs in the (z) direction.

In this thesis, I describe the optical properties of micropillar microcavities. To create a micropillar, DBRs can be etched perpendicular to the substrate to create the structures shown schematically in Figure 2.10. If a single photon source is placed into a micropillar, such devices can find applications in quantum-cryptography and quantum-computation systems [179, 182].

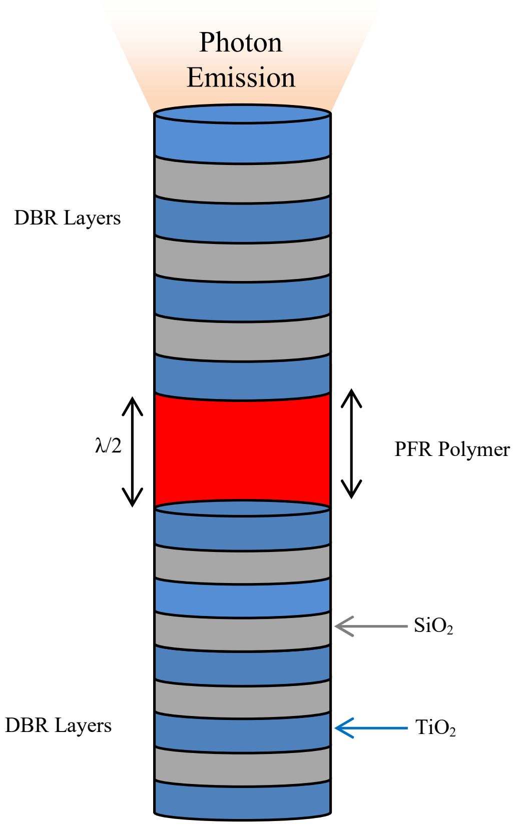

Fig 2.10: Schematic of a micropillar cavity containing an organic material embedded in its centre. Alternating quarter wavelength layers of TiO_2/ SiO_2 known as DBRs, causes constructive interference, which allows them to act as mirrors.

A Distributed Bragg reflector is a mirror, in which each optical layer thickness is set to one quarter of the wavelength for which the mirror is designed. Bragg mirrors can be made using a range of technologies and different geometries, with such structures having different applications:

- Electron beam evaporation or ion beam sputtering can be used to fabricate individual layers. This type of mirror is often used in solid-state lasers.

- DBRs can be fabricated into fibre-optic cables. Such fiber Bragg gratings, including long-period fiber gratings are often used in fiber lasers and other fiber devices.
- Semiconductor Bragg mirrors are often used in distributed feedback diodes laser and are produced using lithographic methods [183-184].

DBR mirrors are used to enhance transmission or reflection of light over a certain wavelength range. The characteristics of a DBR are dependent upon the number of layers in the quarter wave stack and on the thickness of the individual layers, and the refractive index difference between the layers [185-186]. DBRs are often used on precision optics such as Anti-Reflection (AR) coatings, High Reflective mirror (HR) coatings, beam splitter coatings and filter coatings [187]. Indeed, anti-reflection coatings are included on most refractive optics and are used to maximize optical throughput and reduce unwanted reflections. Highly reflective coatings are designed to maximize reflectance at either a single wavelength or across a broad range of wavelengths and are most often used to create mirrors. Beam splitter coatings are used to divide the incident light into transmitted and reflected light paths. In all cases, the index of refraction and thickness of the layers can be varied to optimize performance and to define the wavelength over which light reflectivity or transmission is required.

However, scattering and absorption are important loss processes in multilayer systems. Scattering happens as a result of defects in coatings which can be classified as either volume or surface defects (roughness). Absorption losses are connected with a material's extinction coefficient, however the advantage of a quarter-wave stack composed of weakly absorbing layers is that absorption losses are small but non-zero [186-188]. Micropillar cavities can suffer from increased losses from side-wall scatter as the cavity diameter is reduced [189].

2.8 Interference in Single Layer Films.

A single zinc sulphide dielectric layer having refractive index of ($n \approx 2.3$) and thickness of (d =134 nm) deposited on glass is able to reflect at most about 46% of the incident light at 45° [190]. As light propagates through a thin film system, reflections will happen at the two interfaces at which the refractive index changes corresponding to either side of the coating. For reflection each interface index layer, a phase shift of π radians can occur. If the optical thickness of the layer is set to $\lambda/4$ the reflected beams R_1 and R_2 have a path – length difference of $\lambda/2$. The total phase difference between the two optical paths is therefore π, and therefore corresponds to destructive interference. Figure 2.11 illustrates this concept. Note here that $n_f < n_s$ for a reflection at an interface where there is a reduction in refractive index, no phase change as reflection occurs.

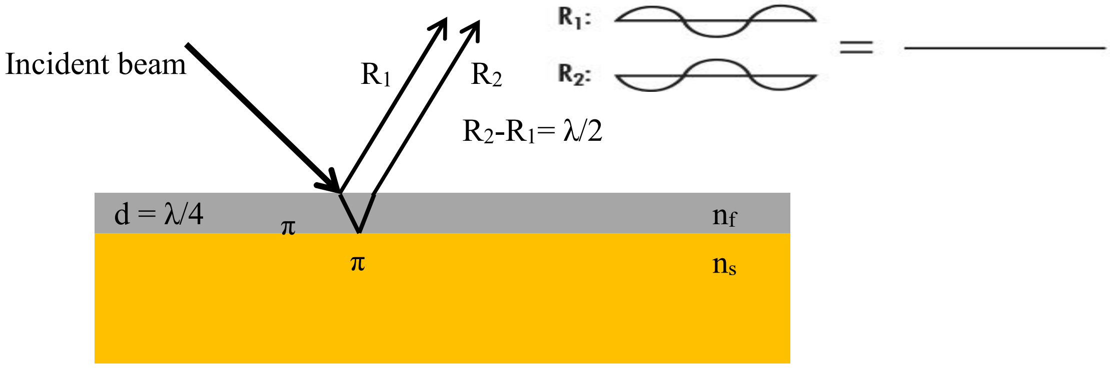

Figure 2.11: A 180° phase shift between two reflected beams results in destructive interference and as a result there is no reflected beam, where n_f is the thin film refractive index and n_s is the substrate refractive index [191].

The refraction index both influences optical path length and also the reflection characteristics at each interface. To understand the confinement of light between two parallel reflectors, Figure 2.12 demonstrates of the concept of a Fabry-Perot cavity with facet reflectivities of R1 and R2.

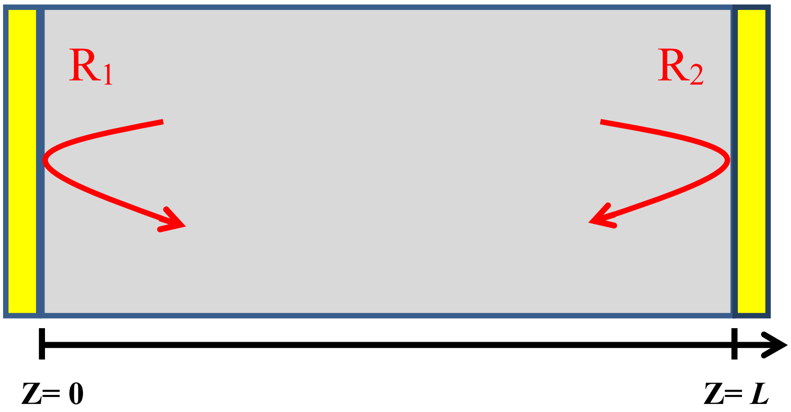

Figure 2.12: A Fabry-Perot cavity with facet reflectivities R1 and R2.

The condition for constructive interference which confines light in a planar cavity having a distance *L* between two parallel reflectors is:

$$L = \frac{\lambda}{2n} m \qquad 2\text{-}30$$

where m is an integer known as the cavity mode number. The reflectivity of the planar cavity is affected by a number of parameters as shown in equation 2-31:

$$R = 1 - \frac{[1 + R_\alpha^2 - R_1 - R_2 \, exp(-2\alpha L)]}{(1 - R_\alpha)^2} - \frac{1}{(1 + F \, sin^2 \emptyset)} \qquad 2\text{-}31$$

Where R_1 and R_2 are the intensity reflectivity for the first and second reflectors respectively, α is the linear absorption coefficient, *L* is cavity length, $2\emptyset$ is the cavity round trip phase change, $R_\alpha = (R_1 \, R_2)^{1/2} \exp(-\alpha L)$ and $F = 4R_\alpha/(1 - R_\alpha)^2$ represents the finesse of the planar cavity which measures the average number round trips that a resonant photon reflectedbetween the mirrors inside the cavity makes before leaving the cavity.

Finesse can be defined as:

$$F = \frac{\Delta v_{FSR}}{\delta v} \qquad 2\text{-}32$$

where δv is the resonance full width at half maximum and Δv_{FSR} is the free spectral range (FSR) that is defined as the frequency spacing between subsequent longitudinal modes.

$$FSR = \Delta\lambda = \frac{\lambda^2}{nL} \qquad 2\text{-}33$$

The net phase shift between two reflectors in a single round trip is given by

$$\emptyset = \frac{4\pi nL}{\lambda} \qquad 2\text{-}34$$

where n is the refractive index of the cavity medium and λ is wavelength of the light-source [192-202].

2.9 Distributed Bragg Reflectors (DBRs) and Interference in Multilayer Films.

The simplest example of a one dimensional photonic crystal structure is a Distributed Bragg Reflector. Such structures have frequency bands that are called stop bands [198, 200].

Light having a wavelength within the stop-band is unable to propagate within the stack and is completely reflected. Such optical bandgaps arise as a result of Bragg scattering from the periodic dielectric structure which is similar in nature to the bandgaps that arise in the energy spectrum of electrons in a semiconductor crystals, which arise due to Bragg scattering of the electrons from the periodic potential of the atoms.

The peak reflectivity of a DBR occurs when the wavelength of the incident light equals the Bragg wavelength λ_B of the DBR mirror. At this point, the reflected waves from every period of the structure add constructively in the backward direction, thereby enhancing the reflectivity [203-205].

Distributed Bragg reflectors can be created using a stack of multiple dielectric layers as shown in Figure 2.13 below:

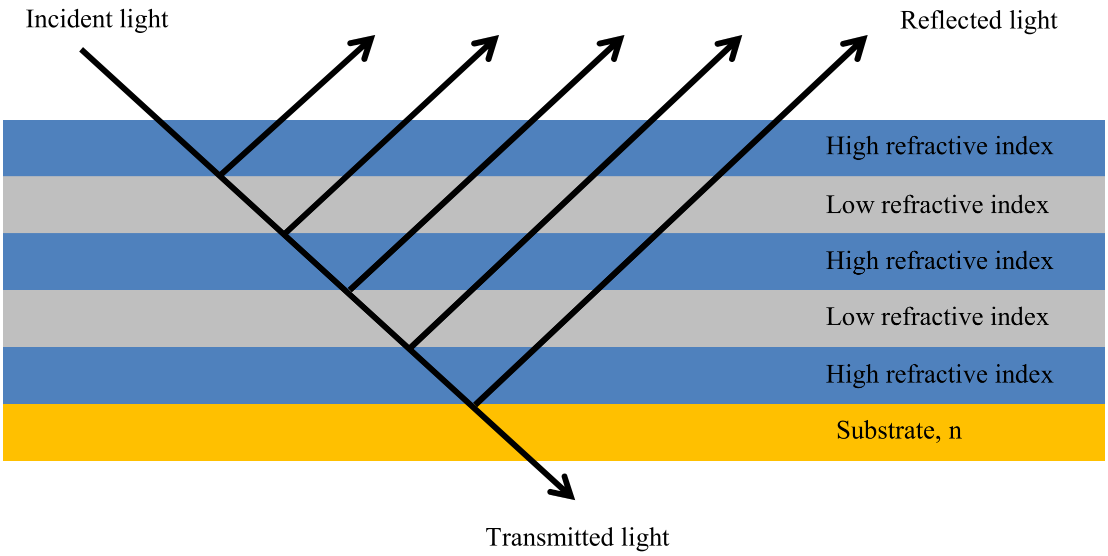

Figure 2.13: Shows the light reflected from a multilayer DBR structure using periodic refractive index thin films [206].

DBR mirrors consist of alternating dielectric layers of different refractive index, n_l and n_h, forming a periodic structure. In a DBR mirror with a peak reflectivity at the wavelength λ_B, the phase accumulated by a wave propagating through one complete period must be π [207-209]. The micropillar microcavities shown in figure 2.10 can control the radiative dynamics of light emission by confining photons vertically by the Bragg mirrors and horizontally by the refractive index contrast between air and the semiconductor. In general, it is necessary to confine light to precise resonance frequencies with little or no optical loss to obtain a high-quality microcavity [210-213]. Indeed, scattering by sidewall roughness can decrease the photon lifetime inside the cavity [214].

In a periodic multilayer dielectric mirror, constructive reflection occurs when ($\langle n_{eff}\rangle\Lambda/2=\lambda/4$), where n_{eff} is an effective refractive index. This means for a given pitch Λ, there is only one wavelength that satisfies the Bragg condition.

$$\lambda = \lambda_B = 2 < n_{eff} > \Lambda \qquad 2\text{-}35$$

where Λ is the pitch of the periodic thickness change and λ_B is Bragg wavelength [196]. The Bragg wavelength is also angle dependent as summarised by equation 2-36

$$\lambda_{DBR}\ (\Theta) = \lambda_{DBR}(0)cos\left(\frac{n_{air}}{n_{eff}}\ \Theta\right) \qquad 2\text{-}36$$

Here, Θ is the propagation angle of the cavity photon mode, and n_{eff} is equal to $\sqrt{n_l n_h}$.

The reflectivity (R) of a DBR can be calculated at the centre of the stopband using equation 2-37 [186]:

$$R = 1 - 4\frac{n_{air}}{n_{sub}}\left[\frac{n_l}{n_h}\right]^{2N} \qquad 2\text{-}37$$

where N is the number of dielectric pairs, n_{sub} is the refractive index of the substrate, n_{air} is the refractive index of air and (n_l,n_h) are the refractive index of low and high index materials respectively. Therefore, increasing N and increasing the refractive index contrast of the layers leads to a higher reflectivity and wider stopband. Furthermore, the stopband width $\Delta\lambda$ increases with increasing refractive index contrast. Figure 2.14 plots the simulated reflectance spectra of DBRs with specific numbers of layers from (N = 2, 3 and 4) for n_h and n_l equal to 3.6 and 1.405 respectively. The width of the stopband of a DBRs can be expressed as [215]

$$\Delta\lambda = \frac{2\Delta n\lambda_{DBR}}{\pi n_{eff}} \qquad 2\text{-}38$$

Here, Δn is the difference in refractive indices for materials used in the DBR, n_{eff} is the effective refractive index of the DBR and λ_{DBR} is the design wavelength which occurs at the centre of the stop band. The width of the stop-band for a high number of layers is given as:

$$\Delta\lambda = \frac{\lambda_{DBR}}{4\pi} sin^{-1}\left[\frac{n_h - n_l}{n_h + n_l}\right]^{2N} \qquad 2\text{-}39$$

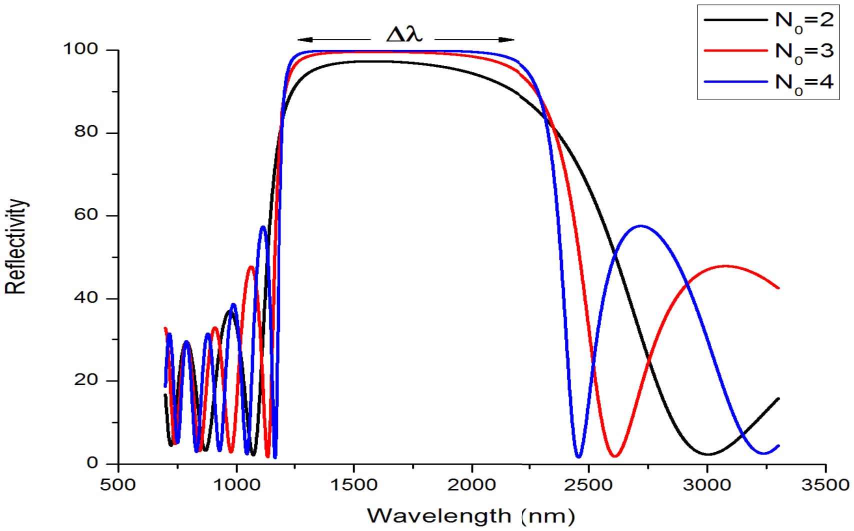

Fig 2.14: Shows Reflectivity simulation results of DBRs centred at λ_0 = 1584 nm (n_h-Si) = 3.6, (n_l-SiO2) = 1.405 on InP substrates with different N values. This Figure was taken from Ref [216].

The reflectivity can be calculated using Fresnel's Equations, which describes the reflectivity at each interface at normal incidence as a result of refractive index change [192-193].

$$R = \left(\frac{n_{h-}n_l}{n_{h+}n_l}\right)^2 \qquad 2\text{-}40$$

Here R is Fresnel reflection coefficient, n_h is the high refractive index and n_l the low refractive index of the layers [192].

From Fresnel's equation, the behaviour of the light at the interface between two thin films with different refractive indices can be determined [217-219]. For instance, in the case of DBRs used in a vertical-cavity surface-emitting laser (VCSELs), only light incident vertically to the surface is of interest. This simplifies the description of these structures, as the polarization no longer matters at normal incidence. The amplitude reflection coefficient, r, going from layer 1 having a high refractive index to layer 2 that has a low refractive index is then given by

$$r = \frac{E_r}{E_i} = \frac{n_{h-}n_l}{n_h+n_l} \qquad 2\text{-}41$$

Here, E_i and E_r are the amplitudes of the incident and reflected electric fields respectively. The reflectance (R) can be defined as the ratio of the reflected power to the incident power; therefore equation 2-41 can be re written as:

$$R = (r)^2 = (\frac{Er}{Ei})^2 = \left(\frac{n_{h-n_l}}{n_{h+n_l}}\right)^2 \qquad 2\text{-}42$$

again, it is appears that a larger contrast in refractive index results in a larger reflectance. For instance, a glass window with $n_{air} = 1$ and $n_{SiO2} = 1.452$ has a reflectance of 6 %. However, for thin film with a higher refractive index contrast with $n_{TiO2} = 2.135$ has a reflectance of 14 %. Equation 2-41 also gives some information the phase shifts at the interface layers. For $n_h > n_l$, the value of the reflectance will be positive. This means that the electric field of the reflected and the incident waves have the same phase. As a result, a π-phase shift has to occur at this dielectric-air boundary. For constructive interference all reflections from a DBR have to be in phase with each other. Figure 2.15 is a schematic figure of a DBR that highlights the phase-shift from each layer in the stack.

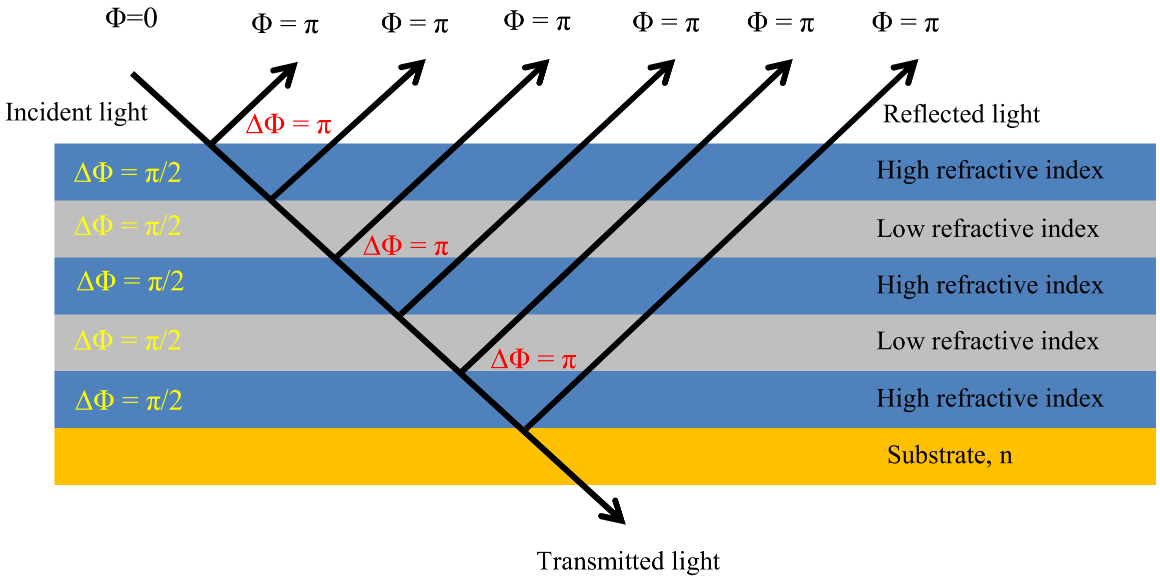

Figure 2.15: A schematic cross-section of DBR with light incident from air. In yellow are phase changes of light propagating through the layer, in red are phase changes due to reflections with black giving the overall phase of light leaving the surface.

It can be seen that the total phase shift is π when the light propagates through an odd number of multilayers before reflection, but there is no change in phase using an even number of multilayers. Furthermore, if the first thin film has a high refractive index, the reflection will occur at an interface between high and low refractive index materials, therefore no phase shift occurs. This means that an overall π-phase shift occurs for an odd number of multilayers. In the case of an even number of multilayers a reflection happens from low-to-high refractive index interface, so a π-phase change will happen resulting in a reflection at the surface with a π-phase shift. By this way all reflections will leave the surface with the same phase.

The simplest microcavity can be described by considering the cavity thickness to be a half wavelength layer. Such structures correspond to a DBR that includes one layer in its centre having twice the optical thickness of the DBR layers [220-234]. This layer can be considered as a defect which creates a characteristic defect state. The phase shift of a wave travelling through a λ/2 layer equals π, instead of π/2 in all other single quarter wavelength layers of the

DBR. As result, the previous condition for constructive interference on reflection is removed and instead destructive interference at the design wavelength occurs [216].

To design a planar microcavity with an odd number of layers, the structure must start and end with a high refractive index layer; therefore there will be J layers in the structure. The reflectivity at $\lambda=\lambda_0$ turns out to be [197]

$$R = \left(\frac{n_H^{J+1} - n_L^{J-1}\, n_s}{n_H^{J+1} + n_L^{J-1}\, n_s}\right) \qquad 2\text{-}43$$

where n_s, is refractive index of the structure.

The Q factor of a planar microcavity can be calculated from the reflectivity of the lower (r_l) and higher (r_h) mirrors using [235]:

$$Q = \frac{2L_{eff}}{\lambda}\,\frac{\pi}{1-r_1 r_2} \qquad 2\text{-}44$$

where L_{eff} is the effective cavity length.

2.10 Application of multilayer films.

Distributed Bragg reflectors (DBR) having a high reflectivity are used in many applications [236-237], such as a high power distributed Bragg reflector lasers [238], bistable diode lasers [239-240], band-pass filters and sensors for some alcoholic compounds such as methanol, acetone, ethanol and chlorobenzene [241], high speed optical communication devices [242] and ultra-violet (UV) wavelength emitting light emitting diodes (LEDs) [243].

2.11 Light – matter interaction and enhancement of spontaneous emission.

A theoretical description of the interaction between light and the matter was discussed by Bohr and Einstein last century. There are three forms of light – matter interaction, namely photon-absorption, spontaneous emission and stimulated emission. Photon absorption occurs as a result of an upward transition between energy levels in an atom, while photon emission occurs following a downward transition between energy levels [244].

Controlling the dynamics and directivity of spontaneous emission allows the efficiency of light emitting diodes to be enhanced, and the lasing threshold of a laser to be reduced. The process of spontaneous emission of light is widely used in optoelectronic devices such as light emitting diodes [245-247]. If an atom having two electronic levels is inserted into a cavity, it can undergo one of two kinds of coupling, depending on the strength of interaction between the atomic system and the cavity mode. Firstly, the strong coupling regime occurs when the spontaneous emission involves a periodic exchange of energy between the atom and the cavity mode (Rabi oscillation). This leads to the formation a doublet (vacuum Rabi splitting). Secondly, the weak coupling regime occurs when the atom couples to the part of the continuum that is at the same frequency as the atomic transition and undergoes a radiative decay of its energy [248].

Figure 2.16 illustrates the interaction between light and an atom inside a cavity. Here the atom is placed inside a cavity and absorbs photons from the cavity modes and then re-emits photons again into the cavity mode.

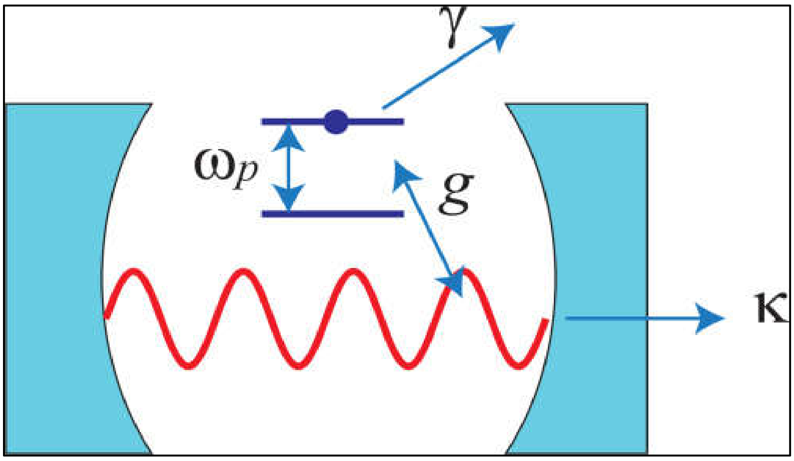

Figure 2.16: A two-level atom in a resonant cavity with modal volume that described by three parameters: g_0, κ, and γ. This Figure was taken from Ref [249].

An important case is when the transition frequency of the atom and one of the resonant cavity modes are similar. This leads to a strong interaction between the atom and the light field. The strength of the interaction between the atom and the cavity depends on three parameters: the photon decay rate of the cavity (κ) that is governed by the properties of the cavity, the non-resonant decay rate (γ) and the atom–photon coupling parameter (g_o) that are defined as [250]:

$$g_o = \left(\frac{\mu^2 \omega}{2\varepsilon_0 \hbar V}\right)^{1/2} \qquad \text{2-45}$$

$$\kappa = \frac{1}{\tau_{cavity}} = \frac{w}{Q} \qquad \text{2-46}$$

Here τ_{cavity} is photon lifetime, μ is the emitter dipole moment, ε_o the vacuum permittivity, V is the mode volume and w is the cavity mode resonant frequency. The cavity photon decay rate κ is related to the quality factor using equation 2-46. As a result, a high quality factor value means relatively small photon loss rates**.**

2-11-1 Strong coupling of the cavity:

Strong coupling happens in quantum electrodynamics when the coherent energy exchange between the quantum emitters and the light mode is faster than the decay and decoherence of either constituent, which means that the atom–photon interaction is faster than irreversible processes due to loss of photons out of the cavity mode [251-252]. The interaction between light and matter is said to be in the strong coupling limit when $g_o >> (\kappa, \gamma)$, where (κ, γ) represents the larger of κ and γ. This makes the emission of the photon a reversible process in which the photon is re-absorbed by the atom before it is lost from the cavity.

As a result, the spontaneous emission rate can be modified by the interaction between the emitter and local optical environment. This leads to a modification of the energy spectrum of the system, with modes obtained whose frequencies are different from the original oscillator modes [253]. Strong coupling in light-matter interactions is a fundamental phenomenon in physics that depends on the ratio of the quality factor of the cavity to the mode volume Q/V [254]. The absorption spectrum exhibits a characteristic doublet structure that arises from vacuum-field Rabi oscillations [255-257]. Strong coupling is associated with important phenomena such as polariton condensation [258-266].

2-11-2 Weak coupling of the cavity:

In the weak coupling regime, the modification of the original energies due to the coupling is negligible. Here, the emission of a photon by an atom is an irreversible process, as in normal free-space spontaneous emission, however the emission rate is affected by the cavity. On other words, weak coupling occurs when $g_o << (\kappa, \gamma)$.

High-quality cavities can be used to enhance the interaction times and enhance coupling strengths. However, in larger cavities the longer round trip for photons to return to the same emitter decreases the coupling, which scales as $g \propto 1/\sqrt{V}$, where V is the effective cavity volume and g is the coupling energy [267-268]. In this thesis I have concentrated on the study of micropillars and photonic crystal cavity structures that operate in the weak coupling regime.

2-11-3 Purcell effect

The Purcell effect occurs when the radiation of an atom in a wavelength size cavity is much faster than in free space [269]. Spontaneous emission is modified by the environment around the emitter depending on a change in the local density of states, with the cavity being able to enhance spontaneous emission [270].

The integrated probability of transition for each single mode resulting from coupling between an emitter and the cavity modes now depends on Fermi's Golden Rule [271-272]. This states that the emitter spontaneous emission rate Γ at energy ($\hbar\omega$) is proportional to the local density of optical states ρ(ω) see equation 2-47.

$$\Gamma_{i\to f} = \frac{2\pi}{\hbar}\left\langle f\middle|\vec{E}\,.\vec{\mu}\middle|i\right\rangle^2 \rho(\omega) \qquad \text{2-47}$$

Here $|i\rangle$ and $|f\rangle$ refer to the initial and final states of the emitter, $\vec{\mu}$ is the vector dipole moment of transition, $\vec{\mathrm{E}}$ is the electric field at the location of the emitter and ρ(ω) is the photon density of states which in free space is given by

$$\rho_{(\omega)} = \frac{\omega^2 V n^3}{\pi^2\, c^3} \qquad \text{2-48}$$

This emission rate can be enhanced in an optical cavity by comparing the emitter spontaneous emission rate $\Gamma_{\mathbf{cav}}$ to the free space spontaneous emission rate $\Gamma_{\mathbf{free}}$ using equation 2-49 [273]

$$\Gamma = \frac{\Gamma_{cav}}{\Gamma_{free}} = \frac{3}{4\pi^2}\left(\frac{\lambda}{2n}\right)^3 \; \frac{Q}{V_{mode}} \left(\frac{\vec{E}_r}{\left|\vec{E}_{max}\right| \cdot \left|\vec{\mu}\right|}\right)^2 \times \frac{\Delta\lambda_{cav}^2}{4(\lambda-\lambda_{cav})^2+\Delta\lambda_{cav}^2} \qquad 2\text{-}49$$

Here Γ [274] is the enhancement in the spontaneous emission rate, Q is the cavity quality factor, V mode is the mode volume, λ and λ_{cav} are the resonant wavelength of the emitter dipole and cavity mode respectively, n is the refractive index of the medium [273-275], $\overrightarrow{E_r}$ is the amplitude of the electric field at the position of the emitter dipole, E_{max} is the maximum amplitude of the electric field and Δλ is the linewidth of the optical mode [276-277].

Equation 2-49 is considered a key description of the Purcell effect and describes the modifications on the lifetime of an emitter inside a cavity. The first term in equation 2-49 depends on the parameters of the cavity, such as the cavity refractive index n, effective volume V, wavelength of the cavity mode and quality factor Q. The second term describes the spatial mismatch between the cavity mode and the emitter. The third term refers to the density of states of a single cavity mode in Fermi's Golden Rule formula, or in other words, it defines the spectral mismatch between the cavity mode and the emitter.

From equation 2-49, it can be seen that if the atomic transition frequency of an emitter is equal to the resonance of the cavity mode (i.e. λ equal to λ_{cav}) and possess a dipole moment located at the maximum of the electric field, the enhancement of the spontaneous emission takes a maximum value that is expressed by the Purcell factor F_P which is defined as [278] :

$$F = \frac{\Gamma}{\Gamma_0} = \frac{3}{4\pi^2}\left(\frac{Q}{V_{mode}}\right)\left(\frac{\lambda}{2n}\right)^3 \qquad 2\text{-}50$$

Note that the Purcell factor depends on the Q/V ratio of the cavity [279-280].

The enhancement of the spontaneous emission rate is important in many applications such as efficient single-photon sources [281], low threshold and ultra-low threshold photonic crystal nanocavity lasers [282-283].

In the 1980's, Drexhage and Kleppner [274] were the first to demonstrate an enhancement of spontaneous emission by 20 times. Brash et al [284] observed an increase in the spontaneous emission rate by up to 35 times using an InGaAs quantum dot as a single quantum emitter in a H1 photonic crystal where the quality factor was 764. In 2013 Gan et al, demonstrated an enhancement of the spontaneous emission rate by 70 times using a two dimensional photonic crystal containing a three-missing hole (L3) defect of a quality factor 880 with an enhancement in the photoluminescence intensity by up to 5.4 times [285]. A high enhancement in the spontaneous emission rate by up to 90 times was achieved by Pisanello et al using H1 silicon nitride photonic crystal resonator with a quality factor of 750 [286].

2-12 Finite Difference Time Domain (FDTD) modelling

Finite difference time domain (FDTD) is a computational method used to compute the resonant modes or eigenmodes in a cavity by solving Maxwell's curl equations in the time domain by dividing space and time into a regular grid [287]. The algorithms of FDTD have been widely used and applied in microwave circuit problems and in optics for many years [288]. The first formulation of FDTD was introduced in 1966 by Yee [289-290]. The first step in a FDTD calculation is to divide the structure into a discrete grid which is smaller than smallest feature in the structure. The solutions of the Maxwell's curl equations are then solved sequentially. The electric field E is solved first at a given instant of time, and at the next instant the solution of the magnetic field is then solved. This process is then repeated until the desired number of time steps is reached. In this thesis a 3D FDTD code (Crystal Wave) produced by Photonic Design Ltd [291] was used to study and calculate the optical properties of micro-nanocavity structures, such as quality factor and cavity mode structure etc.

2-13 Organic Semiconductors

Over the last twenty years, organic semiconductor materials have attracted a significant attention as a result of their optoelectronic properties and for their wide range of possible applications in optoelectronics and photonics [292-293]. In spite of the fact that inorganic semiconductor materials have been widely used in different applications, they frequently need to have very high purity and require very accurate processing under demanding conditions. Organic semiconductors however, combine ease of processing, tuning of optical and electric properties by changing their chemical structure; features that make such materials very attractive for optoelectronic applications [294-295].

Organic semiconductors are materials whose electrical properties lay between those of conductors and insulators [296]. They are composed of carbon and hydrogen atoms together with heteroatoms such as sulfur, oxygen, and nitrogen [297]. Carbon is the fundamental constituent of an organic molecule and can form long chains of alternating sigle and double bonds which give rise to their semiconducting properties [298-299]. There are two kinds of organic semiconductors; polymers and small molecules or oligomers [300]. Organic molecular crystals are formed through van-der-Waals bonds which result in significantly weaker intermolecular bonding as compared to covalently bonded semiconductors.

Sublimation or evaporation is used to deposit low-molecular weight materials from the gas phase however conjugated polymers can only be deposited from solution [301-303].

Organic semiconductors also combine other advantages such as the ability to effectively absorb light in a thin film only 100 nm thick [304], and to conduct electricity. Chemical synthesis [297], can also be used to modify optoelectronic properties [304-305]. Organic field-effect transistors can also be used in low-cost applications in organic integrated circuits [306]. The photoluminescence (PL) efficiency of many organic semiconductors is high. They can also have low toxicity and good biocompatibility [307] and high charge-carrier mobility at room temperature [308].

Organic light-emitting diodes have been used in different applications such as smartphones and large-screen televisions [309], DNA chips and single-photon sources [310]. They can also be deposited over both small and large areas, and are easy to integrate with conventional technologies [311-312]. Moreover, emission and absorption spectra of numerous organic materials can be modified by local electric fields produced by surrounding polar solvent molecules [313].

The formation of a molecular (Frenkel) exciton results from absorption of a photon by a molecule [302-303]. In the ground-state, electrons and holes are located in the highest occupied molecular orbital (HOMO) in a conjugated molecule. Excitons can be created following electronic transfer of an electron from the HOMO to LUMO levels following the absorption of light [314-315]. The exciton binding energy in an organic material is higher than the exciton binding energy for inorganic semiconductor materials by several orders of magnitude [316].

Due to their enhanced oscillator strength, light – matter interactions can be significantly enhanced. By placing an organic emitter possessing a narrow linewidth in microcavity having a high quality factor, it may be possible to enhance the radiative processes of the emitter and perhaps enhance quantum efficiency by controlling non-radiative rates. This could be an interesting approach to create new types of low threshold laser devices [317]. However, chemical oxidation, low mobility and degradation under environmental effects are known disadvantages of conjugated polymers and organic semiconductor materials.

2-13-1 The Electronic Structure of Organic Molecules

The properties of a molecular material depend on its chemical structure. For example, the backbone of a conjugated polymer is usually composed of a series of carbon atoms connected by alternating single and double bonds. The ground state of the single carbon atom contains six electrons which are distributed in the following electron configuration: 1s2 2s2 2p2. The carbon atoms are connected each other by two kind of bond; the first is a sigma bond (σ) sp3 hybridized which is the strongest kind of covalent bond. This is formed by the overlap of orbitals in an end-to-end style of the atomic orbitals where the density of the electrons is concentrated between the nuclei of the bonding atoms. The second type of bond is a (π) bond that is formed by the overlap of p_z orbitals in a side-by-side style where the density of the electrons is concentrated above and below the plane connecting the two carbon atoms [293-297]. The π bond is responsible for the different optical and electronic properties that result from delocalized electrons along the backbone of the molecule.

The distance between the individual bands of energy levels is called band gap which determines the optical properties of an organic semiconductor. The highest occupied molecular orbital (HOMO) i.e (highest filled molecular orbital) in a molecule approximately corresponds to the valence band while the lowest unoccupied molecular orbital (LUMO) i.e (lowest unfilled energy level) corresponds to the conduction band in a conventional in organic semiconductor [318-326].

2-13-2 Emission of Light in Organic Molecules

The processes of absorption and emission of light in a conjugated organic semiconductor are usually summarised by a Jablonski diagram as shown in Figure 2.17.

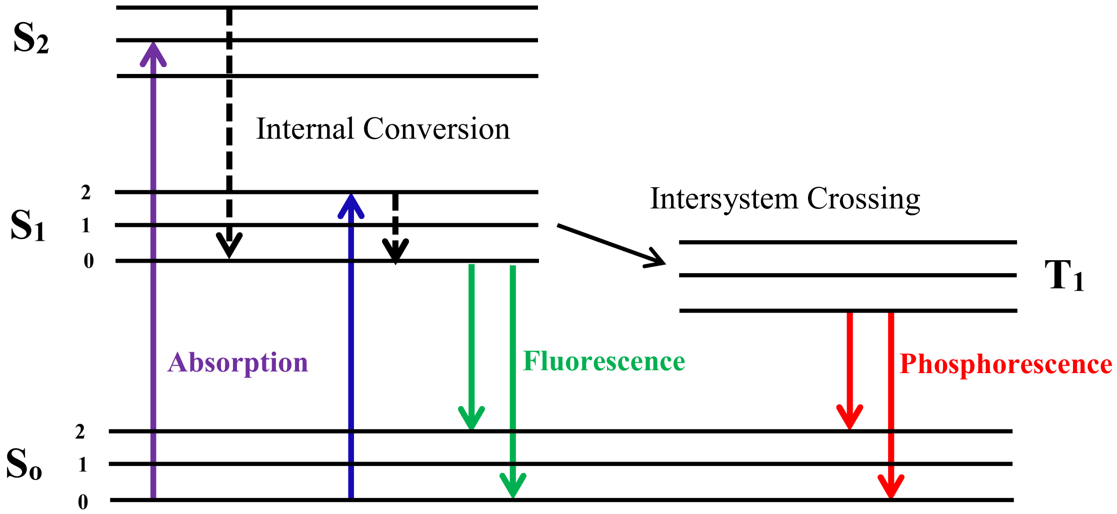

Figure 2.17: Shows a Jablonski diagram, illustrating the processes of absorption, fluorescence and phosphorescence of light from a conjugated organic semiconductor.

The electronic states in a conjugated molecule are arranged vertically depending on the energy levels that start from the ground state (S_o), then first and second exited singlet states (S_1 and S_2). T_1 is the first excited triplet state. Usually, several processes can occur after light absorption. When a molecule is excited to a higher vibrational level of either S_1 or S_2, relaxation occurs by internal conversion to the lowest vibrational level of S_1 within 10^{-12} s or less. Emission of a photon can then occur, with fluorescence lifetimes being around 10^{-9} s. Therefore, internal conversion is usually complete before light emission. Generally, fluorescence emission results from the lowest vibrational energy level of S_1. Phosphorescence can also occur after light absorption. Due to spin conversion, singlet excitons in S_1 can undergo intersystem crossing to the first triplet state T_1, however relaxation to the ground state is spin-forbidden. Figure 2.18 illustrates the processes of the absorption and fluorescence. In the process of light absorption, the different distinct peaks in the absorption spectra occur as a consequence of electronic transitions from the 0-vibrational level of the ground state to various higher vibrational levels of the S_1 state. In the emission process, the electron returns from the 0-vibrational level of the S_1 to various vibrational levels in the ground state. Frequently, the fluorescence spectrum tends to be red shifted as emitted photons have less energy than absorbed photons. This phenomenon is quantified by a Stokes shift where the energy is lost during internal nonradiative relaxation processes [327-335]:

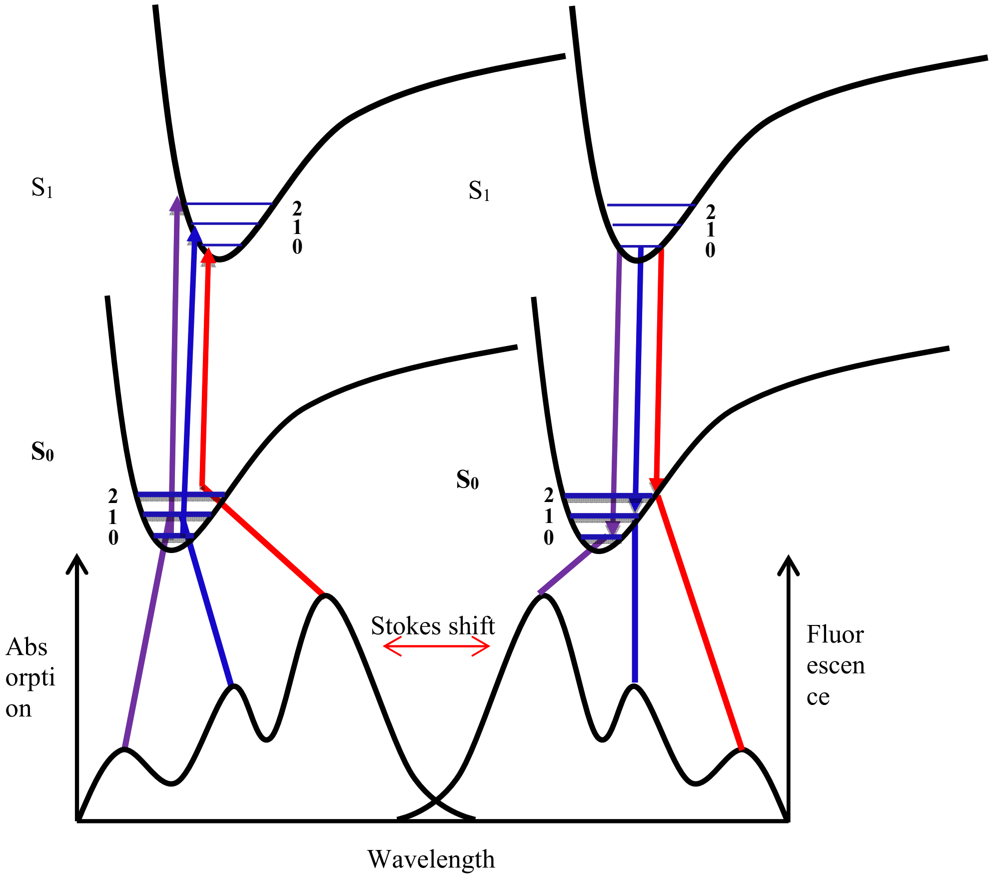

Figure 2.18: Shows the electronic absorption and emission bands in an organic molecule.

2-14 Summary and Conclusion

In this chapter, I have reviewed theoretically the principle of the photonic crystal. The propagation of light in such structures was studied using Maxwell's equations and physics of solid state. Here, Bloch theorem was applied to solve the eigen value problem over the unit cell of the structure of the photonic crystal as a result of the periodic function of photonic crystals. However, there are some solutions we cannot find. The absence of solutions leads to the concept of bandgaps. In a periodic dielectric material, light at a range of frequencies cannot propagate, thus creating a photonic band gap (PBG). When the structure of a photonic crystal prohibits the propagation of light in all directions, this means that the crystal possesses a complete photonic band gap.

To create optical nanocavities and micropillar microcavities that can confine light inside a volume smaller than a cubic wavelength $(\lambda/n)^3$, defects were placed into the structure of such a photonic crystal. High quality factor cavities were obtained from such structures, which lead to a strong localization of the optical field. This can be used in different applications that depend on the control of the spontaneous emission from a quantum emitter.

The main internal and external parameters such as filling factor, slab thickness, lattice constant, refractive index contrast, symmetry and temperature that influence the size and the position of the photonic band gap and the properties of the photonic crystal were discussed. Moreover, the theoretical description of the three forms of light – matter interaction between light and the matter was discussed. Finite difference time domain (FDTD) as a computational method was used to compute the resonant modes or eigenmodes in a cavity by solving Maxwell's curl equations in the time domain. Finally, the optoelectronic properties of an organic semiconductor materials and conjugated polymers were studied because of placing such materials in the photonic crystal cavities.

References:-

[1] Wu, J., Shen, Y.L., Reinhardt, K., Szu, H. and Dong, B., ‘‘A nanotechnology enhancement to Moore's Law’’. Applied Computational Intelligence and Soft Computing, 2013, 2, (2013).

[2] Bhattacharya, P., Fornari, R. and Kamimura, H., ‘‘Comprehensive Semiconductor Science and Technology’’. 6, Elsevier, USA, (2011).

[3] Thompson, S.E. and Parthasarathy, S., ‘‘Moore's law: the future of Si microelectronics’’. Materials today, 9, 20-25, (2006).

[4] Islam, S.K. and Haider, M.R., ‘‘Sensors and low power signal processing’’. Springer Science & Business Media, USA, (2009)

[5] De Mello Donegá, C. ed., ‘‘Nanoparticles: workhorses of nanoscience’’. Springer, USA, (2014).

[6] Notomi M. and Sogawa T. ‘‘Nanophotonic Technologies for On-chip Photonic Integration’’. NTT Technical Review, 16, 7, (2018).

[7] Chen, R., Ng, K.W., Ko, W.S., Parekh, D., Lu, F., Tran, T.T.D., Li, K. and Chang-Hasnain, C., ‘‘Nanophotonic integrated circuits from nanoresonators grown on silicon’’ Nature Communications, 5, 4325, (2004).

[8] Ishihara, T., Shinya, A., Inoue, K., Nozaki, K. and Notomi, M., ‘‘An Integrated Nanophotonic Parallel Adder’’. ACM Journal on Emerging Technologies in Computing Systems (JETC), 14, 26, (2018).

[9] Datta, A.K. and Munshi, S., ‘‘Information photonics: fundamentals, technologies, and applications’’. CRC Press, New York, (2016),

[10] Comoretto, D. ed., ‘‘Organic and hybrid photonic crystals’’ Springer International Publishing, Switzerland, (2015).

[11] Joannopoulos, J.D., Meade, R.D., Winn, J.N. and Russell, P.S.J., ‘‘Photonic Crystals: Molding the Flow of Light’’ Princeton Univ. Press, NJ, (2008).

[12] Johnson, S.G. and Joannopoulos, J.D., ‘‘Photonic crystals: the road from theory to practice’’. Springer Science & Business Media, (2001).

[13] Lath, S. and Goyal, R., ‘‘Photonic Crystal Structure’’. International Journal of Computer Applications, 975, 8887, (2016).

[14] Yablonovitch, E., ‘‘Inhibited spontaneous emission in solid-state physics and electronics’’. Physical Review Letters, 58, 2059, (1987).

[15] John, S., ‘‘Strong localization of photons in certain disordered dielectric superlattices’’. Physical Review Letters, 58, 2486, (1987).

[16] Habib, M.A., Khan, M.S., Al-Amin, C.G.S., Azad, I., Ullah, S.M. and Rafique, S., ‘‘Complete bandgap in two dimensional photonic crystals with square bravais lattice’’. In International Conference On Photonics, IEEE, 1-5, (2010).

[17] Park, S.Y., Kim, H. and Song, B.S., ‘‘Design of thin-film photonic crystals with complete photonic bandgap’’. Optics Express, 26, 29521-29526, (2018).

[18] Cerjan, A. and Fan, S., ‘‘Complete photonic band gaps in supercell photonic crystals’’. Physical Review A, 96, 051802, (2017).

[19] Moroz, A., ‘‘Three-dimensional complete photonic-band-gap structures in the visible’’. Physical Review Letters, 83(25), p.5274, (1999).

[20] Ota, Y., Kakuda, M., Watanabe, K., Iwamoto, S. and Arakawa, Y., ‘‘Thresholdless quantum dot nanolaser’’. Optics Express, 25, 19981-19994, (2017).

[21] Zhang, S., Turnbull, G.A. and Samuel, I.D., ‘‘Enhancing the emission directionality of organic light-emitting diodes by using photonic microstructures’’. Applied Physics Letters, 103, 213302, (2013).

[22] Hassan, S., Lowell, D. and Lin, Y., ‘‘Enhanced light out-coupling in organic light-emitting diodes (OLED) by patterning the cathode in graded photonic super-crystals’’. In Organic Photonic Materials and Devices XXI, Proc. of SPIE, 10915, 1091514, (2019).

[23] Kumar, V., Singh, K.S. and Ojha, S.P., ‘‘Band structure, reflection properties and abnormal behaviour of one-dimensional plasma photonic crystals’’. Progress In Electromagnetics Research, 9, 227-241, (2009).

[24] Srivastava, R., Srivastava, S. and Ojha, S.P., ‘‘Negative refraction by photonic crystal’’. Progress In Electromagnetics Research, 2, 15-26, (2008).

[25] Pandey, J.P. and Pandey, G.N., ‘‘Omni Directional Reflection Behaviour of Negative Index Materials’’. International Journal of Pure and Applied Physics, 13, 353-361, (2017).

[26] Soukoulis, C.M., Kafesaki, M. and Economou, E.N., ‘‘Negative-Index Materials: New Frontiers in Optics’’. Advanced Materials, 18, 1941-1952, (2006).

[27] Armstrong, E. and O'Dwyer, C., ‘‘Artificial opal photonic crystals and inverse opal structures–fundamentals and applications from optics to energy storage’’. Journal of Materials Chemistry C, 3, 6109-6143, (2015).

[28] Yoshioka, S. and Kinoshita, S., ‘‘Wavelength–selective and anisotropic light–diffusing scale on the wing of the morpho butterfly’’. Proceedings of the Royal Society of London. Series B: Biological Sciences, 271, 581-587, (2004).

[29] Tippets, C.A., Fu, Y., Jackson, A.M., Donev, E.U. and Lopez, R., ‘‘Reproduction and optical analysis of Morpho-inspired polymeric nanostructures’’. Journal of Optics, 18, 065105, (2016).

[30] Benson, T.M., Boriskina, S.V., Sewell, P., Vukovic, A., Greedy, S.C. and Nosich, A.I. ‘‘Micro-optical resonators for microlasers and integrated optoelectronics’’. In Frontiers in planar lightwave circuit technology, Springer, 39-70, (2006).

[31] Agranovich, V.M., Gartstein, Y.N. and Litinskaya, M., ‘‘Hybrid resonant organic–inorganic nanostructures for optoelectronic applications’’. Chemical Reviews, 111, 5179-5214, (2011).

[32] Podemski, P., Sęk, G., Misiewicz, J., Reitzenstein, S., Reithmaier, J.P. and Forchel, A., ‘‘Optically pumped lasing from single pillar microcavities with interface roughness InGaAs/GaAs quantum dots as active material’’. Quantum Dot Optoelectronics Symposium, (2007).

[33] Maximov, M.V., Kryzhanovskaya, N.V., Nadtochiy, A.M., Moiseev, E.I., Shostak, I.I., Bogdanov, A.A., Sadrieva, Z.F., Zhukov, A.E., Lipovskii, A.A., Karpov, D.V. and Laukkanen, J., ‘‘Ultrasmall microdisk and microring lasers based on InAs/InGaAs/GaAs quantum dots’’. Nanoscale Research Letters, 9, 657, (2014).

[34] Strzelecka, E.M., Robinson, G.D., Coldren, L.A. and Hu, E.L., ‘‘Fabrication of refractive microlenses in semiconductors by mask shape transfer in reactive ion etching‘’. Microelectronic Engineering, 35, 385-388, (1997).

[35] Reynolds, T., Riesen, N., Meldrum, A., Fan, X., Hall, J.M., Monro, T.M. and François, A., ‘‘Fluorescent and lasing whispering gallery mode microresonators for sensing applications’’. Laser & Photonics Reviews, 11, 1600265, (2017).

[36] Li, F. and Mi, Z., ‘‘Optically pumped rolled-up InGaAs/GaAs quantum dot microtube lasers’’. Optics Express, 17, 19933-19939, (2009).

[37] Portalupi, S.L., Hornecker, G., Giesz, V., Grange, T., Lemaître, A., Demory, J., Sagnes, I., Lanzillotti-Kimura, N.D., Lanco, L., Auffèves, A. and Senellart, P., ‘‘Bright phonon-tuned single-photon source’’. Nano Letters, 15, 6290-6294, (2015).

[38] Von Freymann, G., Kitaev, V., Lotsch, B.V. and Ozin, G.A., ‘‘Bottom-up assembly of photonic crystals’’. Chemical Society Reviews, 42, 2528-2554, (2013).

[39] Yablonovitch, E., Gmitter, T.J. and Leung, K.M., ‘‘Photonic band structure: The face-centered-cubic case employing nonspherical atoms’’. Physical Review Letters, 67, 2295, (1991).

[40] Russell, P., ‘’Photonic crystal fibers’’. Science, 299, 358-362, (2003).

[41] Jewell, J.L., Harbison, J.P., Scherer, A., Lee, Y.H. and Florez, L.T., ‘‘Vertical-cavity surface-emitting lasers: design, growth, fabrication, characterization’’. IEEE Journal of Quantum Electronics, 27, 1332-1346, (1991).

[42] Iga, K., Koyama, F. and Kinoshita, S., ‘‘Surface emitting semiconductor lasers’’. IEEE Journal of Quantum Electronics, 24, 1845-1855, (1988).

[43] Yablonovitch, E., Gmitter, T.J., Meade, R.D., Rappe, A.M., Brommer, K. and Joannopoulos, J.D., ‘‘Donor and acceptor modes in photonic band structure’’. Physical Review Letters, 67, 3380, (1991).

[44] Weisbuch, C., Nishioka, M., Ishikawa, A. and Arakawa, Y., ‘‘Observation of the coupled exciton-photon mode splitting in a semiconductor quantum microcavity’’. Physical Review Letters, 69, 3314, (1992).

[45] Christopoulos, S., Von Högersthal, G.B.H., Grundy, A.J.D., Lagoudakis, P.G., Kavokin, A.V., Baumberg, J.J., Christmann, G., Butté, R., Feltin, E., Carlin, J.F. and Grandjean, N., ‘‘Room-temperature polariton lasing in semiconductor microcavities’’. Physical Review Letters, 98, 126405, (2007).

[46] Wang, S. and Sheem, S.K., ‘‘Two dimensional distributed feedback devices and lasers’’. U.S. Patent 3,970,959, (1976).

[47] Wendt, J.R., Vawter, G.A., Gourley, P.L., Brennan, T.M. and Hammons, B.E., ‘‘Nanofabrication of photonic lattice structures in GaAs/AlGaAs’’. Journal of Vacuum Science & Technology B: 11, 2637-2640, (1993).

[48] Grüning, U., Lehmann, V. and Engelhardt, C.M., ‘‘Two-dimensional infrared photonic band gap structure based on porous silicon’’. Applied Physics Letters, 66, 3254-3256, (1995).

[49] Painter, O., Lee, R.K., Scherer, A., Yariv, A., O'brien, J.D., Dapkus, P.D. and Kim, I. ‘‘Two-dimensional photonic band-gap defect mode laser’’. Science, 284, 1819-1821, (1999).

[50] Ohtaka, K., ‘‘Energy band of photons and low-energy photon diffraction’’. Physical Review B, 19, 5057, (1979).

[51] Reithmaier, J.P., Sęk, G., Löffler, A., Hofmann, C., Kuhn, S., Reitzenstein, S., Keldysh, L.V., Kulakovskii, V.D., Reinecke, T.L. and Forchel, A., ‘‘Strong coupling in a single quantum dot–semiconductor microcavity system’’. Nature, 432, 197, (2004).

[52] Sanvitto, D., Daraei, A., Tahraoui, A., Hopkinson, M., Fry, P.W., Whittaker, D.M. and Skolnick, M.S., ‘‘Observation of ultrahigh quality factor in a semiconductor microcavity’’. Applied Physics Letters, 86, 191109, (2005).

[53] Stoltz, N.G., Rakher, M., Strauf, S., Badolato, A., Lofgreen, D.D., Petroff, P.M., Coldren, L.A. and Bouwmeester, D., ‘‘High-quality factor optical microcavities using oxide apertured micropillars’’. Applied Physics Letters, 87, 031105, (2005).

[54] Peter, E., Senellart, P., Martrou, D., Lemaître, A., Hours, J., Gérard, J.M. and Bloch, J., ‘‘Exciton-photon strong-coupling regime for a single quantum dot embedded in a microcavity’’. Physical Review Letters, 95, 067401, (2005).

[55] Ho, Y.L.D., Cao, T., Ivanov, P.S., Cryan, M.J., Craddock, I.J., Railton, C.J. and Rarity, J.G., ‘‘Three-dimensional FDTD simulation of micro-pillar microcavity geometries suitable for efficient single-photon sources’’. IEEE Journal of Quantum Electronics, 43, 462-472, (2007).

[56] Lecamp, G., Hugonin, J.P., Lalanne, P., Braive, R., Varoutsis, S., Laurent, S., Lemaître, A., Sagnes, I., Patriarche, G., Robert-Philip, I. and Abram, I., ‘‘Submicron-diameter semiconductor pillar microcavities with very high quality factors’’. Applied Physics Letters, 90, 091120, (2007).

[57] Reitzenstein, S., Bazhenov, A., Gorbunov, A., Hofmann, C., Münch, S., Löffler, A., Kamp, M., Reithmaier, J.P., Kulakovskii, V.D. and Forchel, A., ‘‘Lasing in high-Q quantum-dot micropillar cavities’’ Applied physics letters, 89, 051107, (2006).

[58] Reitzenstein, S., Hofmann, C., Gorbunov, A., Strauß, M., Kwon, S.H., Schneider, C., Löffler, A., Höfling, S., Kamp, M. and Forchel, A., ‘‘Al As⁄ Ga As micropillar cavities with quality factors exceeding 150.000’’. Applied Physics Letters, 90, 251109, (2007).

[59] Boulier, T., Bamba, M., Amo, A., Adrados, C., Lemaitre, A., Galopin, E., Sagnes, I., Bloch, J., Ciuti, C., Giacobino, E. and Bramati, A., ‘‘Polariton-generated intensity squeezing in semiconductor micropillars’’. Nature Communications, 5, 3260, (2014).

[60] Winkler, K., Gregersen, N., Häyrynen, T., Bradel, B., Schade, A., Emmerling, M., Kamp, M., Höfling, S. and Schneider, C., ‘‘High quality factor GaAs microcavity with buried bullseye defects’’. Physical Review Materials, 2, 052201, (2018).

[61] Stock E, Albert F, Hopfmann C, Lermer M, Schneider C, Höfling S, Forchel A, Kamp M, Reitzenstein S. ‘‘On-Chip Quantum Optics with Quantum Dot Microcavities’’. Advanced Materials, 25, 707-710, (2013).

[62] Bonato, C., Haupt, F., Oemrawsingh, S.S., Gudat, J., Ding, D., van Exter, M.P. and Bouwmeester, D., ‘‘CNOT and Bell-state analysis in the weak-coupling cavity QED regime’’. Physical review letters, 104, 160503, (2010).

[63] Höfner, M., Sadofev, S., Kobin, B., Hecht, S. and Henneberger, F. ‘‘Hybrid polaritons in a resonant inorganic/organic semiconductor microcavity’’. Applied Physics Letters, 107, 181109, (2015).

[64] Agranovich, V., Benisty, H. and Weisbuch, C., ‘‘Organic and inorganic quantum wells in a microcavity: Frenkel-Wannier-Mott excitons hybridization and energy transformation’’. Solid State Communications, 102, 631-636, (1997).

[65] Bykov, V.P., ‘‘Spontaneous emission from a medium with a band spectrum’’. Soviet Journal of Quantum Electronics, 4, 861, (1975).

[66] Dodabalapur, A., Rothberg, L.J., Miller, T.M. and Kwock, E.W., ‘‘Microcavity effects in organic semiconductors’’. Applied Physics Letters, 64, 2486-2488, (1994).

[67] Tessler, N., Denton, G.J. and Friend, R.H., ‘‘Lasing from conjugated-polymer microcavities’’. Nature, 382, 695, (1996).

[68] Dirr, S., Wiese, S., Johannes, H.H., Ammermann, D., Böhler, A., Grahn, W. and Kowalsky, W., ‘‘Luminescence enhancement in microcavity organic multilayer structures’’. Synthetic Metals, 91, 53-56, (1997).

[69] Mitschke, U. and Bäuerle, P., ‘‘The electroluminescence of organic materials’’. Journal of Materials Chemistry, 10, 1471-1507, (2000).

[70] Lidzey, D.G., Bradley, D.D.C., Skolnick, M.S., Virgili, T., Walker, S. and Whittaker, D.M., ’’Strong exciton–photon coupling in an organic semiconductor microcavity’’. Nature, 395, 53, (1998).

[71] Tokito, S., Tsutsui, T. and Taga, Y., ‘‘Microcavity organic light-emitting diodes for strongly directed pure red, green, and blue emissions’’. Journal of Applied Physics, 86, 2407-2411, (1999).

[72] Kozlov, V.G. and Forrest, S.R., ‘‘Lasing action in organic semiconductor thin films’’. Current Opinion in Solid State and Materials Science, 4, 203-208, (1999).

[73] Lin, C.L., Lin, H.W. and Wu, C.C., ‘‘Examining microcavity organic light-emitting devices having two metal mirrors’’. Applied Physics Letters, 87, 021101, (2005).

[74] Pisanello, F., Martiradonna, L., Qualtieri, A., Stomeo, T., Grande, M., Pompa, P.P., Cingolani, R., Bramati, A. and De Vittorio, M., ‘‘Silicon nitride PhC nanocavities as versatile platform for visible spectral range devices’’. Photonics and Nanostructures-Fundamentals and Applications, 10, 319-324, (2012).

[75] Kitamura, M., Iwamoto, S. and Arakawa, Y., ‘‘Organic Semiconductor Based Two-Dimensional Photonic Crystals with a Single Defect’’. In Conference on Lasers and Electro-Optics, Optical Society of America, (2005).

[76] Kitamura, M., Iwamoto, S. and Arakawa, Y., ‘‘Enhanced light emission of an organic semiconductor based two-dimensional photonic crystal with a nanocavity’’. In 2005 Pacific Rim Conference on Lasers & Electro-Optics, IEEE, 1132-1133. (2005).

[77] Adawi, A.M., Kullock, R., Turner, J.L., Vasilev, C., Lidzey, D.G., Tahraoui, A., Fry, P.W., Gibson, D., Smith, E., Foden, C. and Roberts, M., ‘‘Improving the light extraction efficiency of polymeric light emitting diodes using two-dimensional photonic crystals’’. Organic Electronics, 7, 222-228, (2006).

[78] Gourdon, F., Chakaroun, M., Fabre, N., Solard, J., Giacometti, A., Bouchoule, S., Fischer, A., Boudrioua, A. and Barbillon, G., ‘‘Lasing action from organic two-dimensional planar photonic crystal microcavity’’. In CLEO: Science and Innovations, Optical Society of America, CF1M-6, (2012).

[79] Dusel, M., Betzold, S., Brodbeck, S., Herbst, S., Würthner, F., Friedrich, D., Hecht, B., Höfling, S. and Dietrich, C.P., ‘‘Three-dimensional photonic confinement in imprinted liquid crystalline pillar microcavities’’. Applied Physics Letters, 110, 201113, (2017).

[80] Liu, J., Yao, M. and Shen, L., ‘‘Third generation photovoltaic cells based on photonic crystals’’. Journal of Materials Chemistry C, 7, 3121-3145, (2019).

[81] Chutinan, A., Kherani, N.P. and Zukotynski, S., ‘‘High-efficiency photonic crystal solar cell architecture’’. Optics Express, 17, 8871-8878, (2009).

[82] Park, Y., Drouard, E., El Daif, O., Letartre, X., Viktorovitch, P., Fave, A., Kaminski, A., Lemiti, M. and Seassal, C., ‘‘Absorption enhancement using photonic crystals for silicon thin film solar cells’’. Optics Express, 17, 14312-14321, (2009).

[83] Wooten, F., ‘‘Optical properties of solids’’. Academic Press. New York and London, (2013).

[84] Cho, K., ‘‘Reconstruction of Macroscopic Maxwell Equations’’. 2, Springer-Verlag Berlin An, (2013).

[85] Staelin, D.H., ‘‘Electromagnetics and applications’’. Massachusetts Institute of Technology, Cambridge, 1-442, (2011).

[86] Sukhoivanov, I.A. and Guryev, I.V., ‘‘Photonic crystals: physics and practical modeling’’. 152, Springer, (2009).

[87] Abramov, A. and Luan, L., ‘‘Propagation of electromagnetic wave through anisotropic graded refractive index profile’’. Journal of Applied Mathematics and Physics, 2, 47, (2014).

[88] Novotny, L. and Hecht, B., ‘‘Principles of nano-optics’’. Cambridge University Press, (2012).

[89] Tanner, D.B., ‘‘Optical effects in solids’’. Cambridge University Press, (2019).

[90] Joannopoulos, J.D., Villeneuve, P.R. and Fan, S., ‘‘Photonic crystals. Solid State Communications’’. 102, 165-173, (1997).

[91] LAZĂR, B. and STERIAN, P., ‘‘Band gaps in 2d photonic crystals with hexagonal symmetry’’. Academy of Romanian Scientists, 81, (2008).

[92] Ochiai, T. and Sakoda, K., ‘‘Dispersion relation and optical transmittance of a hexagonal photonic crystal slab’’. Physical Review B, 63, 125107, (2001).

[93] Ferry, D.K., ‘‘Semiconductors: Bonds and bands’’. IOP Publishing Ltd. UK, (2013).

[94] Robertson, W.M., Arjavalingam, G., Meade, R.D., Brommer, K.D., Rappe, A.M. and Joannopoulos, J.D., ‘‘Measurement of the photon dispersion relation in two-dimensional ordered dielectric arrays’’. Josab, 10, 322-327, (1993).

[95] Ho, K.M., Chan, C.T. and Soukoulis, C.M., ‘‘Existence of a photonic gap in periodic dielectric structures’’. Physical Review Letters, 65, 3152, (1990).

[96] Liu, L. and Liu, J.T., ‘‘Photonic band structure in the nearly plane wave approximation’’. The European Physical Journal B-Condensed Matter and Complex Systems, 9, 381-388, (1999).

[97] Joannopoulos, J.D., Villeneuve, P.R. and Fan, S., ‘‘Photonic crystals’’. Solid State Communications, 102, 165-173. (1997).

[98] Kim, K. and Stroud, D., ‘‘Photonic band structures of periodic arrays of pores in a metallic host: tight-binding beyond the quasistatic approximation’’. Optics Express, 21, 19834-19849, (2013).

[99] Jain, P.K., ‘‘Dispersion analysis of two dimensional metallic photonic band gap structures’’. International Conference on Emerging Trends in Electronic and Photonic Devices & Systems, IEEE, 413-417, (2009).

[100] Russell, P.S.J., Birks, T.A. and Lloyd-Lucas, F.D., ‘‘Photonic Bloch waves and photonic band gaps’’. In Confined electrons and photons, Springer, 585-633, (1995).

[101] Schilling, J., Müller, F., Wehrspohn, R.B., Gösele, U. and Busch, K., ‘‘Dispersion relation of 3D photonic crystals based on macroporous silicon’’. Materials Research Society, 722, (2002).

[102] Andreani, L.C., Panzarini, G. and Gérard, J.M., ‘‘ Strong-coupling regime for quantum boxes in pillar microcavities: Theory’’. Physical Review B, 60, 13276, (1999).

[103 Guha, S., Rice, J.D., Yau, Y.T., Martin, C.M., Chandrasekhar, M., Chandrasekhar, H.R., Guentner, R., De Freitas, P.S. and Scherf, U., ‘‘Temperature-dependent photoluminescence of organic semiconductors with varying backbone conformation’’. Physical Review B, 67, 125204, (2003).

[104] Lipson, R.H. and Lu, C., ‘‘Photonic crystals: a unique partnership between light and matter’’. European Journal of Physics, 30, S33, (2009).

[105] Arpin, K.A., Losego, M.D., Cloud, A.N., Ning, H., Mallek, J., Sergeant, N.P., Zhu, L., Yu, Z., Kalanyan, B., Parsons, G.N. and Girolami, G.S., ‘‘Three-dimensional self-assembled photonic crystals with high temperature stability for thermal emission modification’’. Nature communications, 4, 2630, (2013).

[106] Lu, L., Cheong, L.L., Smith, H.I., Johnson, S.G., Joannopoulos, J.D. and Soljačić, M., ‘‘Three-dimensional photonic crystals by large-area membrane stacking’’. Optics Letters, 37, 4726-4728, (2012).

[107] Kassa-Baghdouche, L., Boumaza, T. and Bouchemat, M., ‘‘Optimization of q-factor in nonlinear planar photonic crystal nanocavity incorporating hybrid silicon/polymer material’’. Physica Scripta, 90, 065504, (2015).

[108] Jamois, C., Wehrspohn, R.B., Andreani, L.C., Hermann, C., Hess, O. and Gösele, U., ‘‘Silicon-based two-dimensional photonic crystal waveguides’’. Photonics and Nanostructures-Fundamentals and Applications, 1, 1-13, (2003).

[109] Jean-Michel, L., Henri, B. and Vincent, B., ‘‘Photonic Crystals: Towards Nanoscale Photonic Devices’’. Springer, (2008).

[110] Ruda, H.E. and Matsuura, N., ‘‘Nano-Engineered Tunable Photonic Crystals’’. In Springer Handbook of Electronic and Photonic Materials, Springer, Cham, (2017).

[111] Wen, F., David, S., Checoury, X., El Kurdi, M. and Boucaud, P., ‘‘Two-dimensional photonic crystals with large complete photonic band gaps in both TE and TM polarizations’’. Optics Express, 16, 12278-12289, (2008).

[112] John, S., Toader, O. and Busch, K., ‘‘ Photonic band gap materials: a semiconductor for light’’. Encyclopedia of physical science and technology, 12, (2001).

[113] Meade, R.D., Rappe, A.M., Brommer, K.D. and Joannopoulos, J.D., ‘‘Nature of the photonic band gap: some insights from a field analysis’’. JOSA B, 10, 328-332, (1993).

[114] Zha, J., Zhong, Z.Y., Zhang, H.W., Wen, Q.Y. and Li, Y.X., ‘‘Differences of band gap characteristics of square and triangular lattice photonic crystals in terahertz range’’. Journal of Electronic Science and Technology, 7, 268-271, (2009).

[115] Yu, S.P., Muniz, J.A., Hung, C.L. and Kimble, H.J., ‘‘Two-dimensional photonic crystals for engineering atom–light interactions’’. Proceedings of the National Academy of Sciences, 116, 12743-12751, (2019).

[116] Villeneuve, P.R. and Piche, M., ‘‘Photonic band gaps in two-dimensional square and hexagonal lattices’’. Physical Review B, 46, 4969, (1992).

[117] Krishna, H., Pavan, V.D.R. and Roy, S., ‘‘Comparative photonic bandgap analysis on square and triangular lattice photonic crystal slabs’’. In International Conference on Optics and Photonics, International Society for Optics and Photonics, 9654, 96541E, (2015).

[118] Liu, D., Gao, Y., Gao, D. and Han, X., ‘‘Photonic band gaps in two-dimensional photonic crystals of core-shell-type dielectric nanorod heterostructures’’. Optics Communications, 285, 1988-1992, (2012).

[119] Ryu, H., Park, H., & Lee, Y. ‘‘Two-Dimensional Photonic Crystal Semiconductor Lasers : Computational Design, Fabrication, and Characterization’’. IEEE, 8, 891–908, (2002).

[120] Johnson, S.G. and Joannopoulos, J.D., ‘‘Block-iterative frequency-domain methods for Maxwell’s equations in a planewave basis’’. Optics Express, 8, 173-190, (2001).

[121] Andreani, L.C. and Gerace, D., ‘‘Photonic-crystal slabs with a triangular lattice of triangular holes investigated using a guided-mode expansion method’’. Physical Review B, 73, 235114, (2006).

[122] Robertson, W.M., Arjavalingam, G., Meade, R.D., Brommer, K.D., Rappe, A.M. and Joannopoulos, J.D., ‘‘Measurement of the photon dispersion relation in two-dimensional ordered dielectric arrays’’. JOSA B, 10, 322-327, (1993).

[123] Chun-Zhen, F., Jun-Qiao, W., Jin-Na, H., Pei, D. and Er-Jun, L., ‘‘Theoretical study on the photonic band gap in one-dimensional photonic crystals with graded multilayer structure’’. Chinese Physics B, 22, 074211, (2013).

[124] Zarbakhsh, J., Mohtashami, A. and Hingerl, K., ‘‘Geometrical freedom for constructing variable size photonic bandgap structures’’. Optical and Quantum Electronics, 39, 395-405, (2007).

[125] Moroz, A., ‘‘Three-dimensional complete photonic-band-gap structures in the visible’’. Physical Review Letters, 83, 5274, (1999).

[126] Broeng, J., Barkou, S.E., Bjarklev, A., Knight, J.C., Birks, T.A. and Russell, P.S.J., ‘‘Highly increased photonic band gaps in silica/air structures’’. Optics Communications, 156, 240-244, (1998).

[127] Ryu, H.Y., Hwang, J.K. and Lee, Y.H., ‘‘Effect of size nonuniformities on the band gap of two-dimensional photonic crystals’’. Physical Review B, 59, 5463, (1999).

[128] Bostan, C.G. and De Ridder, R.M., ‘‘Hexagon-type photonic crystal slabs based on SOI. In Proceedings’’ Seventh Annual Symposium of the IEEE/LEOS, 87-90, Vrije University, Amsterdam, (2002).

[129] Duque, C.A. and Mora-Ramos, M.E., ‘‘The two-dimensional square and triangular photonic lattice under the effects of magnetic field, hydrostatic pressure, and temperature’’. Optical and Quantum Electronics, 44, 375-392, (2012).

[130] Hillebrand, R., Hergert, W. and Harms, W., ‘‘Theoretical Band Gap Studies of Two-Dimensional Photonic Crystals with Varying Column Roundness’’. physica status solidi (b), 217, 981-989, (2000).

[131] Plihal, M., Shambrook, A., Maradudin, A.A. and Sheng, P., ‘‘Two-dimensional photonic band structures’’. Optics communications, 80, 199-204, (1991).

[132] Yang, X.L., Cai, L.Z. and Liu, Q., ‘‘Theoretical bandgap modeling of two-dimensional triangular photonic crystals formed by interference technique of three noncoplanar beams’’. Optics Express, 11, 1050-1055, (2003).

[133] Ryu, H.Y., Hwang, J.K. and Lee, Y.H., ‘‘Effect of size nonuniformities on the band gap of two-dimensional photonic crystals’’. Physical Review B, 59, 5463, (1999).

[134] Kowalsky, W., Becker, E., Benstem, T., Johannes, H.H., Metzdorf, D., Neuner, H. and Schöbel, J., ‘‘Organic semiconductors: fundamentals and applications’’. In Advances in Solid State Physics, Springer, 40, 795-808, (2000).

[135] Hou, J., Citrin, D.S., Wu, H., Gao, D., Zhou, Z. and Chen, S., ‘‘Slab-thickness dependence of photonic bandgap in photonic-crystal slabs’’. IEEE Journal of Selected Topics in Quantum Electronics, 18, 1636-1642, (2011).

[136] Kalra, Y. and Sinha, R.K., ''Photonic band gap engineering in 2D photonic crystals''. Pramana, 67, 1155-1164, (2006).

[137] Robinson, S. and Nakkeeran, R., ''Investigation on parameters affecting the performance of two dimensional photonic crystal based bandpass filter''. Optical and Quantum Electronics, 43, 69-82, (2012).

[138] Adawi, A.M., Chalcraft, A.R.A., Whittaker, D.M. and Lidzey, D.G., ''Refractive index dependence of L3 photonic crystal nano-cavities''. Optics Express, 15, 14299-14305, (2007).

[139] Guo, Z. and Tan, L., ''Fundamentals and applications of nanomaterials''. Artech House, London, (2009).

[140] Michaelides, A. and Scheffler, M., ''An introduction to the theory of crystalline elemental solids and their surfaces''. Surface and Interface Science, 1, (2012).

[141] Huang, Y., Liang, G., Lu, X., Bie, X. and Li, W., ''The Optical Transmission Characteristic of Hollow Carbon-Coated Fe_3O_4 Colloidal Photonic Crystal''. IEEE Photonics Journal, 7, 1-12, (2015).

[142] Kitamura, M., Iwamoto, S. and Arakawa, Y., ''Enhanced light emission from an organic photonic crystal with a nanocavity''. Applied Physics Letters, 87, 151119, (2005).

[143] Fu, X., Zhang, B., Kang, X., Xu, J., Xiong, C. and Zhang, G., ''Lattice constant effects of photonic crystals on the extraction of guided mode of GaN based light emitting diodes''. Science China Technological Sciences, 54, 1-5, (2011).

[144] Malik, J.V., Jindal, K.D., Kumar, V., Kumar, V., Kumar, A., Singh, K.S. and Singh, T.P., ''Effect of temperature on photonic band gaps in semiconductor-based one-dimensional photonic crystal''. Advances in Optical Technologies, 2013, 8, (2013).

[145] Notomi, M., ''Manipulating light with strongly modulated photonic crystals''. Reports on Progress in Physics, 73, 096501, (2010).

[146] Krauss, T.F., ''Photonic crystals: Cavities without leaks''. Nature Materials, 2, 777, (2003).

[147] Otterbach, J., Unanyan, R.G. and Fleischhauer, M., ''Confining stationary light: Dirac dynamics and Klein tunneling''. Physical Review Letters, 102, 063602, (2009).

[148] Santhosh, K., Bitton, O., Chuntonov, L. and Haran, G., ''Vacuum Rabi splitting in a plasmonic cavity at the single quantum emitter limit''. Nature communications, 7, 11823, (2016).

[149] Dvoynenko, M.M., ''About possibility of strong coupling between single molecule and surface plasmons''. arXiv preprint arXiv:1202.2535, (2012).

[150] Robinson, J.T., Manolatou, C., Chen, L. and Lipson, M., ''Ultrasmall mode volumes in dielectric optical microcavities''. Physical Review Letters, 95, 143901, (2005).

[151] Coccioli, R., Boroditsky, M., Kim, K.W., Rahmat-Samii, Y. and Yablonovitch, E., ''Smallest possible electromagnetic mode volume in a dielectric cavity''. IEE Proceedings-Optoelectronics, 145, 391-397, (1998).

[152] Capek, M., Jelinek, L. and Vandenbosch, G.A., ‘‘Stored electromagnetic energy and quality factor of radiating structures. Proceedings of the Royal Society’’ A: Mathematical, Physical and Engineering Sciences, 472, 20150870, (2016).

[153] Nawi, N., Majlis, B.Y., Mahdi, M.A., De La Rue, R.M., Lonĉar, M. and Zain, A.M., ‘‘Enhancement and reproducibility of high quality factor, one-dimensional photonic crystal/photonic wire (1D PhC/PhW) microcavities’’. Journal of the European Optical Society, 14, 6, (2018).

[154] Yan, S., Yan, Y., Ji, Z., Wang, B., Wang, S., Jiang, G., Xiong, J., Ye, X., Zhou, Z. and Zhang, W., ‘‘A precise measurement of quality factor for Planar Microtoroid Resonators’’. 4th IEEE International Conference on Nano/Micro Engineered and Molecular Systems IEEE, 13-16, (2009).

[155] Huet, V., Rasoloniaina, A., Guillemé, P., Rochard, P., Féron, P., Mortier, M., Levenson, A., Bencheikh, K., Yacomotti, A. and Dumeige, Y., ‘‘Millisecond photon lifetime in a slow-light microcavity’’. Physical Review Letters, 116, 133902, (2016).

[156] Burstein, E. and Weisbuch, C. eds., ,‘Confined electrons and photons: New physics and applications’’. Springer Science & Business Media, 340, (2012).

[157] Tang, L. and Yoshie, T., ‘‘High-Q hybrid 3D-2D slab-3D photonic crystal microcavity’’. Optics Letters, 35, 3144-3146, (2010).

[158] Lončar, M., Doll, T., Vučković, J. and Scherer, A., ‘‘Design and fabrication of silicon photonic crystal optical waveguides’’. Journal of Lightwave Technology, 18, 1402, (2000).

[159] Bayn, I. and Salzman, J., ‘‘Ultra high-Q photonic crystal nanocavity design: The effect of a low-ε slab material’’. Optics Express, 16, 4972-4980, (2008).

[160] Akahane, Y., Asano, T., Song, B.S. and Noda, S., ‘‘High-Q photonic nanocavity in a two-dimensional photonic crystal’’. Nature, 425, 944, (2003).

[161] Pugh, J.R., Ho, Y.D., Engin, E., Railton, C., Rarity, J.G. and Cryan, M.J., ‘‘Novel high-Q modes in thick 2D photonic crystal slabs’’. Journal of Optics, 15, 035004, (2013).

[162] Chen, G., Liu, J.F., Jiang, H., Zhuo, X.L., Yu, Y.C., Jin, C. and Wang, X.H., ‘‘Slab thickness tuning approach for solid-state strong coupling between photonic crystal slab nanocavity and a quantum dot’’. Nanoscale Research Letters, 8, 187, (2013).

[163] Xu, T., Wheeler, M.S., Nair, S.V., Ruda, H.E., Mojahedi, M. and Aitchison, J.S., ‘‘Highly confined mode above the light line in a two-dimensional photonic crystal slab’’. Applied Physics Letters, 93, 241105, (2008).

[164] Akahane, Y., Asano, T., Song, B.S. and Noda, S., ‘‘Fine-tuned high-Q photonic-crystal nanocavity’’. Optics Express, 13, 1202-1214, (2005).

[165] Nakamura, T., Takahashi, Y., Tanaka, Y., Asano, T. and Noda, S., ‘‘Improvement in the quality factors for photonic crystal nanocavities via visualization of the leaky components’’. Optics Express, 24, 9541-9549, (2016).

[166] Tanaka, Y., Upham, J., Nagashima, T., Sugiya, T., Asano, T. and Noda, S., ‘‘Dynamic control of the Q factor in a photonic crystal nanocavity’’. Nature Materials, 6, 862, (2007).

[167] Painter, O., Vučković, J. and Scherer, A., ''Defect modes of a two-dimensional photonic crystal in an optically thin dielectric slab''. JOSA B, 16, 275-285, (1999).

[168] Gumus, M.A., Tutgun, M., Yilmaz, D. and Kurt, H., ''Reduced Symmetric 2D Photonic Crystal Cavity with Wavelength Tunability''. arXiv preprint arXiv,1902.02590, (2019).

[169] Asano, T., Song, B.S. and Noda, S., ''Analysis of the experimental Q factors (~ 1 million) of photonic crystal nanocavities''. Optics Express, 14, 1996-2002, (2006).

[170] Minkov, M. and Savona, V., ''Automated optimization of photonic crystal slab cavities''. Scientific Reports, 4, 5124, (2014).

[171] Adawi, A.M., Cadby, A., Connolly, L.G., Hung, W.C., Dean, R., Tahraoui, A., Fox, A.M., Cullis, A.G., Sanvitto, D., Skolnick, M.S. and Lidzey, D.G., ''Spontaneous emission control in micropillar cavities containing a fluorescent molecular dye''. Advanced materials, 18, 742-747, (2006).

[172] Daraei, A., Sanvitto, D., Timpson, J.A., Fox, A.M., Whittaker, D.M., Skolnick, M.S., Guimarães, P.S.S., Vinck, H., Tahraoui, A., Fry, P.W. and Liew, S.L., ''Control of polarization and mode mapping of small volume high Q micropillars'' Journal of Applied Physics, 102, 043105, (2007).

[173] Albert, F., Sivalertporn, K., Kasprzak, J., Strauß, M., Schneider, C., Höfling, S., Kamp, M., Forchel, A., Reitzenstein, S., Muljarov, E.A. and Langbein, W., ''Microcavity controlled coupling of excitonic qubits'' Nature communications, 4, 1747, (2013).

[174] Kasprzak, J., Reitzenstein, S., Muljarov, E.A., Kistner, C., Schneider, C., Strauss, M., Höfling, S., Forchel, A. and Langbein, W., ''Up on the Jaynes-Cummings ladder of a quantum-dot/microcavity system'' Nature materials, 9, 304-308, (2010).

[175] Klein, T., Klembt, S., Durupt, E., Kruse, C., Hommel, D. and Richard, M., ''Polariton lasing in high-quality selenide-based micropillars in the strong coupling regime'' Applied Physics Letters, 107, 071101, (2015).

[176] Reithmaier, J.P., Sęk, G., Löffler, A., Hofmann, C., Kuhn, S., Reitzenstein, S., Keldysh, L.V., Kulakovskii, V.D., Reinecke, T.L. and Forchel, A., ''Strong coupling in a single quantum dot–semiconductor microcavity system. Nature, 432, 197, (2004).

[177] Reitzenstein, S., Bazhenov, A., Gorbunov, A., Hofmann, C., Münch, S., Löffler, A., Kamp, M., Reithmaier, J.P., Kulakovskii, V.D. and Forchel, A., ''Lasing in high-Q quantum-dot micropillar cavities'' Applied physics letters, 89, 051107, (2006).

[178] Kastler, A., ''Atomes à I'intérieur d'un interféromètre Perot-Fabry''. Applied Optics, 1, 17-24, (1962).

[179] Schouwink, P., Berlepsch, H.V., Dähne, L. and Mahrt, R.F., ''Observation of strong exciton–photon coupling in an organic microcavity''. Chemical physics letters, 344, 352-356, (2001).

[180] Madsen, K.H., Ates, S., Lund-Hansen, T., Löffler, A., Reitzenstein, S., Forchel, A. and Lodahl, P., ''Observation of non-Markovian dynamics of a single quantum dot in a micropillar cavity''. Physical review letters, 106, 233601, (2011).

[181] Gutbrod, T., Bayer, M., Forchel, A., Reithmaier, J.P., Reinecke, T.L., Rudin, S. and Knipp, P.A., ''Weak and strong coupling of photons and excitons in photonic dots'' Physical Review B, 57, 9950, (1998).

[182] El-Ella, H.A., Collins, D.P., Kappers, M.J., Taylor, R.A. and Oliver, R.A., ‘‘Optical cavity efficacy and lasing of focused ion beam milled GaN/InGaN micropillars’’ Journal of Applied Physics, 112, 113516, (2012).

[183] Adawi, A.M. and Lidzey, D.G., ‘‘Enhancing the radiative decay rate of fluorescent organic molecules using micropillar microcavities and optical nanocavities’’ Materials Science and Engineering: B, 149, 266-269, (2008).

[184] Al-Hillou A. M. A. and Mohammad E. J. ‘‘Design of Dielectric Bragg Mirror Consisting uarter-Wave Stacks Using Transfer-Matrix Method’’ Al-Mustansiriyah J. Sci, Vol. 22, No. 5, (2011).

[185] Ujager, F.S., Zaidi, S.M.H. and Younis, U., 2010, December. ‘‘A review of semiconductor lasers for optical communications’’ In High-Capacity Optical Networks and Enabling Technologies, IEEE, 107-111, (2010).

[186] Macleod, H.A., ‘’Thin-film optical filters’’ third edition, CRC press, (2001).

[187] Ghadimi-Mahani, A., Farsad, E., Goodarzi, A., Tahamtan, S., Abbasi, S.P. and Zabihi, M.S., ‘‘Improvement and characterization of high-reflective and anti-reflective nanostructured mirrors by ion beam assisted deposition for 944 nm high power diode laser’’. Optics Communications, 355, 94-102, (2015).

[188] Kats, M.A., Byrnes, S.J., Blanchard, R., Kolle, M., Genevet, P., Aizenberg, J. and Capasso, F., ‘‘Enhancement of absorption and color contrast in ultra-thin highly absorbing optical coatings’’ Applied Physics Letters, 103,101104, (2013).

[189] Dufferwiel, S., Fras, F., Trichet, A., Walker, P.M., Li, F., Giriunas, L., Makhonin, M.N., Wilson, L.R., Smith, J.M., Clarke, E. and Skolnick, M.S., ‘‘Strong exciton-photon coupling in open semiconductor microcavities’’ Applied Physics Letters, 104, 192107, (2014).

[190] Peatross, J. and Ware, M., ‘‘Physics of light and optics’’ Brigham Young University, Department of Physics, (2008).

[191] Pedrotti, L.S., ‘‘Basic physical optics’’ Fundamentals of Photonics, 1, 137, (2008).

[192] Dobrowolski, J.A., ‘‘Optical properties of films and coatings’’. Handbook of optics, 1, 42-3, (1995).

[193] Abed, S.M. and Al-Rashid, S.N.T., ‘‘Designing High Reflectivity Omnidirectional Coating of Mirrors for Near Infrared Spectrum (700-2500 nm)’’. Applied Physics Research, 5, 102, (2013).

[194] Petermann, K., ‘‘Laser diode modulation and noise’’, Vol. 3. Springer Science & Business Media, (2012).

[195] Bouchene, M.M. and Hamdi, R., ‘‘The effect of facets reflectivity on the static characteristics of (DFB) semiconductor laser’’ In 2018 International Conference on Electrical Sciences and Technologies in Maghreb, 1-4, IEEE, (2018).

[196] Avadhanulu, M.N., ‘‘An Introduction To Lasers Theory And Applications’’. S. Chand Publishing, (2001).

[197] Svelto, O. and Hanna, D.C., ‘‘Principles of lasers’’ Vol. 5. New York: Plenum press, (2010).

[198] Wherrett, B., ‘‘Fabry-Perot bistable cavity optimization on reflection’’ IEEE journal of quantum electronics, 20, 646-651, (1984).

[199] Smith, C.J.M., Krauss, T.F., De La Rue, R.M., Labilloy, D., Benisty, H., Weisbuch, C., Oesterle, U. and Houdré, R., ‘‘In-plane microcavity resonators with two-dimensional photonic bandgap mirrors’’. IEE Proceedings-optoelectronics, 145, 373-378, (1998).

[200] Bitarafan, M. and DeCorby, R., ‘‘On-chip high-finesse fabry-perot microcavities for optical sensing and quantum information’’. Sensors, 17, 1748, (2017).

[201] Greuter, L., Starosielec, S., Najer, D., Ludwig, A., Duempelmann, L., Rohner, D. and Warburton, R.J., ‘‘A small mode volume tunable microcavity: Development and characterization’’. Applied physics letters, 105, 121105, (2014).

[202] Pérennès, F., Beard, P.C. and Mills, T.N., ‘‘Analysis of a low-finesse Fabry–Perot sensing interferometer illuminated by a multimode optical fiber’’. Applied optics, 38, 7026-7034, (1999).

[203] Frezza, L., Patrini, M., Liscidini, M. and Comoretto, D., ‘‘Directional enhancement of spontaneous emission in polymer flexible microcavities’’ The Journal of Physical Chemistry C, 115, 19939-19946, (2011).

[204] Panzarini, G., Andreani, L.C., Armitage, A., Baxter, D., Skolnick, M.S., Astratov, V.N., Roberts, J.S., Kavokin, A.V., Vladimirova, M.R. and Kaliteevski, M.A., ‘‘Cavity-polariton dispersion and polarization splitting in single and coupled semiconductor microcavities’’ Physics of the Solid State, 41, 1223-1238, (1999).

[205] Orfanidis, S.J., ‘‘Electromagnetic waves and antennas’’ New Brunswick, NJ: Rutgers University, 227-250, (2002).

[206] Rabady, R.I. and Ababneh, A., ‘‘Global optimal design of optical multilayer thin-film filters using particle swarm optimization’’. Optik-International Journal for Light and Electron Optics, 125, 548-553, (2014).

[207] Ismail, F.D., Aziz, M.S., Teeka, C., Ali, J. and Yupapin, P.P., ‘‘Filter design using multi-bragg reflectors’’. World Journal of Modelling and Simulation, 8, 205-210, (2012).

[208] Persano, L., Camposeo, A., Del Carro, P., Mele, E., Cingolani, R. and Pisignano, D., ‘‘Very high-quality distributed Bragg reflectors for organic lasing applications by reactive electron-beam deposition’’. Optics Express, 14, 1951-1956, (2006).

[209] Babic, D.I. and Corzine, S.W., ‘‘Analytic expressions for the reflection delay, penetration depth, and absorptance of quarter-wave dielectric mirrors’’. IEEE Journal of Quantum Electronics, 28, 514-524, (1992).

[210] Bennett, A.J., Ellis, D.J.P., Shields, A.J., Atkinson, P., Farrer, I. and Ritchie, D.A., ‘‘Observation of the Purcell effect in high-index-contrast micropillars’’. Applied physics letters, 90, 191911, (2007).

[211] Schulz, W.M., Thomay, T., Eichfelder, M., Bommer, M., Wiesner, M., Roßbach, R., Jetter, M., Bratschitsch, R., Leitenstorfer, A. and Michler, P., ‘‘Optical properties of red emitting self-assembled InP/(Al 0.20 Ga 0.80) 0.51 In 0.49 P quantum dot based micropillars’’. Optics Express, 18, 12543-12551, (2010).

[212] Bajoni, D., Wertz, E., Senellart, P., Miard, A., Semenova, E., Lemaitre, A., Sagnes, I., Bouchoule, S. and Bloch, J., ‘‘Excitonic polaritons in semiconductor micropillars''. Acta Physica Polonica A, 114, 933-943, (2008).

[213] Stoltz, N.G., Rakher, M., Strauf, S., Badolato, A., Lofgreen, D.D., Petroff, P.M., Coldren, L.A. and Bouwmeester, D., ‘‘High-quality factor optical microcavities using oxide apertured micropillars’’. Applied Physics Letters, 87, 031105, (2005).

[214] Gérard, J.M., Sermage, B., Gayral, B., Legrand, B., Costard, E. and Thierry-Mieg, V., ‘‘Enhanced spontaneous emission by quantum boxes in a monolithic optical microcavity’’. Physical Review Letters, 81, 1110, (1998).

[215] Comoretto, D. ed., ‘‘Organic and hybrid photonic crystals ’’ .Springer International Publishing, (2015).

[216] Yuan, J., Chen, Y., Holmes, A.L. and Campbell, J.C., ‘‘Design, Fabrication, and Characterizations of Novel Multispectral Photodetectors Using Postgrowth Fabry–Perot Optical Filters for Simultaneous Near Infrared/Short-Wave Infrared Detection’’. IEEE Journal of Quantum Electronics, 50, 1-7, (2014).

[217] Lvovsky, A.I., ‘‘Fresnel equations’’ Encyclopedia of Optical Engineering, 27, 1-6, (2013).

[218] Hung, K.Y., Wu, P.H., Tsai, T.W., Shye, D.C. and Wu, H.C., ‘‘Application of Fresnel equations to improve interface reflection of inclined exposure and develop micro-mirrors for blu-ray DVDs’’ In 2009 IEEE International Conference on Industrial Technology,1-6, IEEE, (2009).

[219] Schubert, E.F., Kim, J.K. and Xi, J.Q., ‘‘Low-refractive-index materials: A new class of optical thin-film materials’’. physica status solidi (b), 244, 3002-3008, (2007).

[220] Takeuchi, T., Kamiyama, S., Iwaya, M. and Akasaki, I., ‘‘GaN-based vertical-cavity surface-emitting lasers with AlInN/GaN distributed Bragg reflectors’’. Reports on Progress in Physics, 82, 012502, (2018).

[221] Ghasemi, V.K.H., Orvatinia, M. and Ebrahimi, A., ‘‘Design of Tunable Multiple-Cavity Filter for Optical Fiber Communication’’. Advances in Computer Science: an International Journal, 2, 48-53, (2013).

[222] Weber, J.P. and Wang, S., ‘‘Effect of layer thickness variations in a distributed-Bragg-reflector mirror on the phase of the reflected light’’. Optics letters, 15, 526-528, (1990).

[223] Grieco, A. and Fainman, Y., ‘‘Characterization of distributed Bragg reflectors’’. IEEE Journal of Quantum Electronics, 50, 453-457, (2014).

[224] Kim, H.Y., Kim, K.B., Cho, S.H. and Kim, Y.I., ‘‘Analysis of resonance characteristics of Bragg reflector type film bulk acoustic resonator’’. Surface and Coatings Technology, 211, 143-147, (2012).

[225] Raut, H.K., Ganesh, V.A., Nair, A.S. and Ramakrishna, S., ‘‘Anti-reflective coatings: A critical, in-depth review’’. Energy & Environmental Science, 4, 3779-3804, (2011).

[226] Apfel, J.H., ‘‘Phase retardance of periodic multilayer mirrors’’. Applied Optics, 21, 733-738, (1982).

[227] Garmire, Elsa. "Theory of quarter-wave-stack dielectric mirrors used in a thin Fabry-Perot filter." Applied Optics 42, no. 27, 5442-5449, (2003).

[228] Babic, D.I. and Corzine, S.W., ‘‘Analytic expressions for the reflection delay, penetration depth, and absorptance of quarter-wave dielectric mirrors’’. IEEE Journal of Quantum Electronics, 28, 514-524, (1992).

[229] Zhang, C., ElAfandy, R. and Han, J., ‘‘Distributed Bragg Reflectors for GaN-Based Vertical-Cavity Surface-Emitting Lasers’’. Applied Sciences, 9, 1593, (2019).

[230] Ghulinyan, M., ‘‘One-dimensional photonic quasicrystals’’.arXiv preprint arXiv: 1505.02400, (2015).

[231] Bhattacharyya, A.K., ‘‘Electromagnetic Fields in Multilayered Structures: Theory and Applications’’ 179. Norwood, MA: Artech House, (1994).

[232] Eugene Hecht. ‘‘Optics’’, fourth edition. Addison-Wesley, (2001).

[233] H Angus Macleod. ‘‘Thin-film optical filters’’. CRC press, (2001).

[234] Rousset, J.G., Kobak, J., Janik, E., Jakubczyk, T., Rudniewski, R., Piotrowski, P., Ściesiek, M., Borysiuk, J., Slupinski, T., Golnik, A. and Kossacki, P., ‘‘MBE grown microcavities based on selenium and tellurium compounds’’. Journal of Crystal Growth, 401, 499-503, (2014).

[235] Reitzenstein, S. and Forchel, A., ‘‘Quantum dot micropillars’’. Journal of Physics D: Applied Physics, 43, 033001, (2010).

[236] Sychev, F.Y., Razdolski, I.E., Murzina, T.V., Aktsipetrov, O.A., Trifonov, T. and Cheylan, S., ‘‘Vertical hybrid microcavity based on a polymer layer sandwiched between porous silicon photonic crystals’’. Applied physics letters, 95, 276, (2009).

[237] Brovelli, L.R. and Keller, U., ‘‘Simple analytical expressions for the reflectivity and the penetration depth of a Bragg mirror between arbitrary media’’. Optics Communications, 116, 343-350, (1995).

[238] Achtenhagen, M., Amarasinghe, N.V., Jiang, L., Threadgill, J. and Young, P., ‘‘Spectral properties of high-power distributed bragg reflector lasers’’. Journal of Lightwave Technology, 27, 3433-3437, (2009).

[239] Rivera, T., Debray, J.P., Gérard, J.M., Legrand, B., Manin-Ferlazzo, L. and Oudar, J.L., ‘‘Optical losses in plasma-etched AlGaAs microresonators using reflection spectroscopy’’. Applied Physics Letters, 74, 911-913, (1999).

[240] Margalit, M., Nagar, R., Tessler, N., Eisenstein, G., Orenstein, M., Koren, U. and Burrus, C.A., ‘‘Bistability and optical control of a distributed-Bragg-reflector laser’’ Optics Letters, 18, 610-612, (1993).

[241] Chi Do T., Bui H., Nguyen T.1, Nguyen T., Nguyen T. and Pham V. ‘‘A microcavity based on a porous silicon multilayer’’ Nat. Sci.: Nanosci. Nanotechnol. 2, 5 (2011).

[242] Emsley, M.K., Dosunmu, O. and Unlu, M.S., ‘‘Silicon substrates with buried distributed Bragg reflectors for resonant cavity-enhanced optoelectronics’’. IEEE Journal of Selected Topics in Quantum Electronics, 8, 948-955, (2002).

[243] Xie, Z.L., Zhang, R., Liu, B., Ji, X.L., Li, L., Liu, C.X., Jiang, R.L., Gong, H.M., Zhao, H., Han, P. and Shi, Y., ''High reflectivity AlGaN/AlN DBR mirrors grown by MOCVD'', Journal of crystal growth, 298, 691-694, (2007).

[244] Saleh, B.E. and Teich, M.C., '' Fundamentals of photonics''. John Wiley & Sons, (1991).

[245] Shaw, A.J., Bradley, A.L., Donegan, J.F. and Lunney, J.G., ''GaN resonant cavity light-emitting diodes for plastic optical fiber applications''. IEEE Photonics Technology Letters, 16, 2006-2008, (2004).

[246] Francardi, M., Balet, L., Gerardino, A., Chauvin, N., Bitauld, D., Li, L.H., Alloing, B. and Fiore, A., ''Enhanced spontaneous emission in a photonic-crystal light-emitting diode''. Applied Physics Letters, 93, 143102, (2008).

[247] Braive, R., Beveratos, A., Sagnes, I., Lecamp, G., Guilet, S., Le Gratiet, L., Lemaître, A., Miard, A., Patriarche, G., Sauvan, C. and Lalanne, P., ''April. Photonic crystal nanolasers with controlled spontaneous emission''. In Nanophotonics II, International Society for Optics and Photonics, 6988, 698813, (2008).

[248] Bourdon, G., Robert, I., Adams, R., Nelep, K., Sagnes, I., Moison, J.M. and Abram, I., ''Enhancement and inhibition of spontaneous emission in room-temperature semiconductor microcavities with metallic mirrors''. In Conference Digest. 2000 International Quantum Electronics Conference, IEEE, 00TH8504, 1, (200).

[249] Taniyama, H., Sumikura, H. and Notomi, M., ''Finite-difference time-domain analysis of photonic crystal slab cavities with two-level systems''. Optics Express, 19, 23067-23077, (2011).

[250] Fox, M., '' Quantum optics: an introduction'', 15, OUP Oxford, (2006).

[251] Galego, J., Garcia-Vidal, F.J. and Feist, J., ''Cavity-induced modifications of molecular structure in the strong-coupling regime''. Physical Review X, 5, 041022, (2015).

[252] Gambino, S., Mazzeo, M., Genco, A., Di Stefano, O., Savasta, S., Patanè, S., Ballarini, D., Mangione, F., Lerario, G., Sanvitto, D. and Gigli, G., ''Exploring light–matter interaction phenomena under ultrastrong coupling regime''. ACS Photonics, 1, 1042-1048, (2014).

[253] Törmä, P. and Barnes, W.L., ''Strong coupling between surface plasmon polaritons and emitters: a review''. Reports on Progress in Physics, 78, 013901, (2014).

[254] Santhosh, K., Bitton, O., Chuntonov, L. and Haran, G., ''Vacuum Rabi splitting in a plasmonic cavity at the single quantum emitter limit''. Nature Communications, 7, 11823, (2016).

[255] Agarwal, G.S., ''Vacuum-field Rabi splittings in microwave absorption by Rydberg atoms in a cavity''. Physical Review Letters, 53, 1732, (1984).

[256] Huang, J.F., Liao, J.Q., Tian, L. and Kuang, L.M., ''Manipulating counter-rotating interactions in the quantum Rabi model via qubit frequency modulation''. arXiv preprint arXiv:1603.08641, (2016).

[257] Dvoynenko, M.M., ''About possibility of strong coupling between single molecule and surface plasmons''. arXiv preprint arXiv:1202.2535, (2012).

[258] Knupfer, M., ‘‘Exciton binding energies in organic semiconductors’’. Applied Physics A, 77, 623-626., (2003).

[259] Fox, M., ‘‘Optical properties of solids’’, Oxford University press, (2002).

[260] Vahala, K.J., ‘‘Optical microcavities’’. Nature, 424, 839, (2003).

[261] Pirotta, S., Patrini, M., Liscidini, M., Galli, M., Dacarro, G., Canazza, G., Guizzetti, G., Comoretto, D. and Bajoni, D., ‘‘Strong coupling between excitons in organic semiconductors and Bloch surface waves’’. Applied Physics Letters, 104, 051111.(2014).

[262] Li, R.Q., Hernángomez-Pérez, D., García-Vidal, F.J. and Fernández-Domínguez, A.I., ‘‘Transformation optics approach to plasmon-exciton strong coupling in nanocavities’’. Physical Review Letters, 117, 107401, (2016).

[263] Andreani, L.C., ‘‘Exciton-polaritons in superlattices’’. Physics Letters A, 192, 99-109, (1994).

[264] Gerace, D. and Andreani, L.C., ‘‘Strong exciton-light coupling in photonic crystal nanocavities’’. Physica Status Solidi (c), 2, 801-804, (2005).

[265] Novotny, L., ‘‘Strong coupling, energy splitting, and level crossings: A classical perspective’’. American Journal of Physics, 78, 1199-1202, (2010).

[266] Peter, E., Senellart, P., Martrou, D., Lemaître, A., Hours, J., Gérard, J.M. and Bloch, J., ‘‘Exciton-photon strong-coupling regime for a single quantum dot embedded in a microcavity’’. Physical Review Letters, 95, 067401, (2005).

[267] Chikkaraddy, R., De Nijs, B., Benz, F., Barrow, S.J., Scherman, O.A., Rosta, E., Demetriadou, A., Fox, P., Hess, O. and Baumberg, J.J., ‘‘Single-molecule strong coupling at room temperature in plasmonic nanocavities’’. Nature, 535, 127, (2016).

[268] Rodriguez, S.R.K., ‘‘Classical and quantum distinctions between weak and strong coupling’’. European Journal of Physics, 37, 025802, (2016).

[269] Hou, C.H., Bernal, M.P., Chen, C.C., Salut, R., Sada, C., Argiolas, N., Bazzan, M. and Ciampolillo, M.V., ‘‘Purcell effect observation in erbium doped lithium niobate photonic crystal structures’’. Optics Communications, 281, 4151-4154, (2008).

[270] Shakoor, A., Savio, R.L., Portalupi, S.L., Gerace, D., Andreani, L.C., Galli, M., Krauss, T.F. and O'Faolain, L., ‘‘Enhancement of room temperature sub-bandgap light emission from silicon photonic crystal nanocavity by Purcell effect’’. Physica B: Condensed Matter, 407, 4027-4031, (2012).

[271] Zhang, J.M. and Liu, Y., ‘‘Fermi’s golden rule: its derivation and breakdown by an ideal model’’. European Journal of Physics, 37, 065406, (2016).

[272] Debierre, V., Durt, T., Nicolet, A. and Zolla, F., ‘‘Spontaneous light emission by atomic hydrogen: Fermi's golden rule without cheating’’. Physics Letters A, 379, 2577-2585, (2015).

[273] Zhou, W., Dridi, M., Suh, J.Y., Kim, C.H., Co, D.T., Wasielewski, M.R., Schatz, G.C. and Odom, T.W., ‘‘Lasing action in strongly coupled plasmonic nanocavity arrays’’. Nature Nanotechnology, 8, 506, (2013).

[274] Boroditsky, M., Vrijen, R., Coccioli, R., Bhat, R. and Yablonovitch, E., ‘‘Spontaneous emission extraction and Purcell enhancement from thin-film 2-D photonic crystals’’. Journal of Lightwave Technology, 17, 2096, (1999).

[275] Todorov, Y., Sagnes, I., Abram, I. and Minot, C., ‘‘Purcell enhancement of spontaneous emission from quantum cascades inside mirror-grating metal cavities at THz frequencies’’. Physical Review Letters, 99, 223603, (2007).

[276] Englund, D., Fattal, D., Waks, E., Solomon, G., Zhang, B., Nakaoka, T., Arakawa, Y., Yamamoto, Y. and Vučković, J., ‘‘Controlling the spontaneous emission rate of single quantum dots in a two-dimensional photonic crystal’’. Physical Review Letters, 95, 013904, (2005).

[277] Kavokin, A. and Laussy, F.P., ‘‘Microcavities’’. Oxford University Press, (2007).

[278] Ryu, H.Y. and Notomi, M., ‘‘Enhancement of spontaneous emission from the resonant modes of a photonic crystal slab single-defect cavity’’. Optics Letters, 28, 2390-2392, (2003).

[279] Canet-Ferrer, J., Prieto, I., Muñoz-Matutano, G., Martínez, L.J., Muñoz-Camuniez, L.E., Llorens, J.M., Fuster, D., Alén, B., González, Y., González, L. and Postigo, P.A., ‘‘Excitation power dependence of the Purcell effect in photonic crystal microcavity lasers with quantum wires’’. Applied Physics Letters, 102, 201105, (2013).

[280] Inam, F.A., Gaebel, T., Bradac, C., Stewart, L., Withford, M.J., Dawes, J.M., Rabeau, J.R. and Steel, M.J., ‘‘Modification of spontaneous emission from nanodiamond colour centres on a structured surface’’. New Journal of Physics, 13, 073012, (2011).

[281] Claudon, J., Bleuse, J., Malik, N.S., Bazin, M., Jaffrennou, P., Gregersen, N., Sauvan, C., Lalanne, P. and Gérard, J.M., ‘‘A highly efficient single-photon source based on a quantum dot in a photonic nanowire’’. Nature Photonics, 4, 174, (2010).

[282] Nomura, M., Iwamoto, S., Kumagai, N. and Arakawa, Y., ‘‘Ultra-low threshold photonic crystal nanocavity laser’’. Physica E: Low-Dimensional Systems and Nanostructures, 40, 1800-1803, (2008).

[283] Lončar, M., Yoshie, T., Scherer, A., Gogna, P. and Qiu, Y., ‘‘Low-threshold photonic crystal laser’’. Applied Physics Letters, 81, 2680-2682, (2002).

[284] Brash, A., Liu, F., O'Hara, J., Martins, L.M.P.P., Coles, R.J., Phillips, C.L., Royall, B., Bentham, C., Itskevich, I., Wilson, L.R. and Skolnick, M.S., ‘‘Bright and coherent on-chip single photons from a very high Purcell factor photonic crystal cavity’’. In 2017 Conference on Lasers and Electro-Optics (CLEO), IEEE, 1-1, (2017).

[285] Gan, X., Gao, Y., Fai Mak, K., Yao, X., Shiue, R.J., Van Der Zande, A., Trusheim, M.E., Hatami, F., Heinz, T.F., Hone, J. and Englund, D., ‘‘Controlling the spontaneous emission rate of monolayer MoS2 in a photonic crystal nanocavity’’. Applied Physics Letters, 103, 181119, (2013).

[286] Pisanello, F., Qualtieri, A., Stomeo, T., Martiradonna, L., Cingolani, R., Bramati, A. and De Vittorio, M., ‘‘High-Purcell-factor dipolelike modes at visible wavelengths in H1 photonic crystal cavity’’. Optics Letters, 35, 1509-1511, (2010).

[287] Nickisch, L.J. and Franke, P.M., ‘‘Finite-difference time-domain solution of Maxwell's equations for the dispersive ionosphere’’. IEEE Antennas and Propagation Magazine, 34, 33-39, (1992).

[288] Choi, D.H. and Hoefer, W.J., ‘‘The finite-difference-time-domain method and its application to eigenvalue problems’’. IEEE Transactions on Microwave Theory and Techniques, 34, 1464-1470, (1986).

[289] Yee, K., ‘‘Numerical solution of initial boundary value problems involving Maxwell's equations in isotropic media’’. IEEE Transactions on antennas and propagation, 14, 302-307, (1966).

[290] Taflove, A. and Hagness, S.C., ‘‘Computational electrodynamics: the finite-difference time-domain method’’. Artech house, (2005).

[291] Photon design Ltd - https://www.photond.com

[292] Bulović, V., Kozlov, V.G., Khalfin, V.B. and Forrest, S.R., ‘‘Transform-limited, narrow-linewidth lasing action in organic semiconductor microcavities’’. Science, 279, 553-555, (1998).

[293] Ostroverkhova, O. ed., ‘‘Handbook of organic materials for optical and (opto) electronic devices’’: Properties and Applications. Elsevier, (2013).

[294] Liu, C., Li, Y., Minari, T., Takimiya, K. and Tsukagoshi, K., ‘‘Forming semiconductor/dielectric double layers by one-step spin-coating for enhancing the performance of organic field-effect transistors’’. Organic Electronics, 13, 1146-1151, (2012).

[295] Tsutsumi, N. and Ishibashi, T., ‘‘Organic dye lasers with distributed Bragg reflector grating and distributed feedback resonator’’. Optics Express, 17, 21698-21703, (2009).

[296] Yacobi, B.G., ‘‘Semiconductor materials: an introduction to basic principles’’. Springer Science & Business Media, (2003).

[297] Köhler, A. and Bässler, H., ‘‘Electronic processes in organic semiconductors: An introduction’’. John Wiley & Sons, (2015).

[298] Wang, Y., ‘‘Low Threshold Organic Semiconductor Lasers: Hybrid Optoelectronics and Applications as Explosive Sensors’’. Springer Science & Business Media, (2013).

[299] Kassa-Baghdouche, L., Boumaza, T. and Bouchemat, M., ‘‘Optimization of q-factor in nonlinear planar photonic crystal nanocavity incorporating hybrid silicon/polymer material’’. Physica Scripta, 90, 065504, (2015).

[300] Coropceanu, V., Cornil, J., da Silva Filho, D.A., Olivier, Y., Silbey, R. and Brédas, J.L., ‘‘Charge transport in organic semiconductors’’. Chemical reviews, 107, 926-952, (2007).

[301] Brütting, W. and Adachi, C. eds., ‘‘Physics of organic semiconductors’’. 1, Weinheim: Wiley-Vch, (2005).

[302] Muntwiler, M., Yang, Q. and Zhu, X.Y., ‘‘Exciton dynamics at interfaces of organic semiconductors’’. Journal of Electron Spectroscopy and Related Phenomena, 174, 116-124, (2009).

[303] Forrest, S.R., ‘‘Excitons and the lifetime of organic semiconductor devices’’. Philosophical Transactions of the Royal Society A: Mathematical, Physical and Engineering Sciences, 373, 20140320. (2015).

[304] Samuel, I.D.W. and Turnbull, G.A., ‘‘Organic semiconductor lasers’’. Chemical reviews, 107, 1272-1295, (2007).

[305] Huang, Y., Paloczi, G.T., Scheuer, J. and Yariv, A., ‘‘Soft lithography replication of polymeric microring optical resonators’’. Optics Express, 11, 2452-2458, (2003).

[306] Kramer, B. ed., ‘‘Advances in solid state physics’’ 42, Springer, (2007).

[307] Xu, X. and Li, L., ‘‘Organic Semiconductor Nanoparticle Film: Preparation and Application’’. In Smart Nanoparticles Technology. Intech Open, (2012).

[308] Hu, Y., Wang, C.W., Zhu, C., Gu, F. and Lin, S.H., , ‘‘Franck–Condon simulation for unraveling vibronic origin in solvent enhanced absorption and fluorescence spectra of rubrene’’. RSC Advances, 7, 12407-12418, (2017).

[309] Fujimoto, H., Yahiro, M., Kawashima, T., Konno, K., Chen, Q., Sawaya, K., Kawakami, S. and Adachi, C., ‘‘Improvement in the light outcoupling efficiency of organic light-emitting diodes using a hemispherical lens and a multipatterned one-dimensional photonic crystal fabricated by autocloning’’. Applied Physics Express, 8, 082102, (2015).

[310] Kitamura, M., Iwamoto, S. and Arakawa, Y., ‘‘Enhanced light emission from an organic photonic crystal with a nanocavity’’. Applied Physics Letters, 87, 151119, (2005).

[311] Boroumand, F.A., Hammiche, A., Hill, G. and Lidzey, D.G., ‘‘Characterizing Joule Heating in Polymer Light-Emitting Diodes Using a Scanning Thermal Microscope’’. Advanced Materials, 16, 252-256, (2004).

[312] Kitamura, M., Iwamoto, S. and Arakawa, Y., ‘‘Enhanced light emission of an organic semiconductor based two-dimensional photonic crystal with a nanocavity’’. In 2005 Pacific Rim Conference on Lasers & Electro-Optics, IEEE, 1132-1133, (2005).

[313] Reichardt, C., ‘‘Solvents and Solvent Effects in Organic Chemistry’’.4, Christian Reichardt and Thomas Welton, (2011).

[314] O’Neill, M. and Kelly, S.M., ‘‘Ordered materials for organic electronics and photonics’’. Advanced Materials, 23, 566-584, (2011).

[315] Sun, S.S. and Dalton, L.R., ‘‘Introduction to organic electronic and optoelectronic materials and devices’’. CRC Press, (2016).

[316] Ong, P.L. and Levitsky, I., ‘‘Organic/IV, III-V semiconductor hybrid solar cells’’ Energies, 3, 313-334, (2010).

[317] Zhang, W., Yao, J. and Zhao, Y.S., ‘‘Organic micro/nanoscale lasers’’. Accounts of Chemical Research, 49, 1691-1700, (2016).

[318] Barford, W., ‘‘Electronic and optical properties of conjugated polymers’’. 159, Oxford University Press, (2013).

[319] Moliton, A. and Hiorns, R.C., ‘‘Review of electronic and optical properties of semiconducting π-conjugated polymers: applications in optoelectronics’’. Polymer International, 53, 1397-1412, (2004).

[320] Molapo, K.M., Ndangili, P.M., Ajayi, R.F., Mbambisa, G., Mailu, S.M., Njomo, N., Masikini, M., Baker, P. and Iwuoha, E.I., ‘‘Electronics of conjugated polymers (I): polyaniline’’. International Journal of Electrochemical Science, 7, 11859-11875, (2012).

[321] Inagaki, M., Kaneko, K., Endo, M., Oya, A. and Tanabe, Y., ‘’ Carbon alloys: novel concepts to develop carbon science and technology’’. Elsevier, (2003).

[322] Alabugin, I.V., Bresch, S. and Manoharan, M., ‘‘Hybridization trends for main group elements and expanding the Bent’s rule beyond carbon: More than electronegativity’’ The Journal of Physical Chemistry A, 118, 3663-3677, (2014).

[323] Schlögl, R., ‘’Carbon. In Handbook of Heterogeneous Catalysis’’. 2, Wiley-VCH Verlag GmbH & Co. KGaA, 357-427, (2008).

[324] Moore, J.W., Stanitski, C.L. and Jurs, P.C., ‘‘Principles of chemistry: the molecular science’’. Hampshire: Brooks/Cole Cengage Learning, USA, (2010).

[325] Bruice, P.Y., ‘‘Electronic structure and bonding acids and bases’’. Organic Chemistry, 6, 25-33, (2011).

[326] Mulliken, R.S., ‘‘Structure and ultraviolet spectra of ethylene, butadiene, and their alkyl derivatives’’. Reviews of Modern Physics, 14, 265, (1942).

[327] Zhu, X., Su, Q., Feng, W. and Li, F., ‘‘Anti-Stokes shift luminescent materials for bio-applications’’. Chemical Society Reviews, 46, 1025-1039, (2017).

[328] Lakowicz, J.R. ed., ‘‘Principles of fluorescence spectroscopy’’.3, Springer Science & Business Media, USA, (2013).

[329] Albani, J.R., ‘‘Principles and applications of fluorescence spectroscopy’’. 8, 255 Oxford: Blackwell Science, (2007).

[330] Lakowicz, J.R. ed., ‘‘Principles of fluorescence spectroscopy’’. Springer Science & Business Media, (2013).

[331] Mukamel, S., ‘‘Principles of nonlinear optical spectroscopy’’. 29, New York: Oxford university press, (1995).

[332] Pope, M. and Swenberg, C.E., ‘‘Electronic processes in organic crystals and polymers’’. Oxford University Press on Demand, (1999).

[333] Stopel, M.H., Blum, C. and Subramaniam, V., ‘‘Excitation spectra and stokes shift measurements of single organic dyes at room temperature’’. The Journal of Physical Chemistry Letters, 5, 3259-3264, (2014).

[334] Ehrenreich, H. and Spaepen, F. ‘‘Solid State Physics: Advances in Research and Applications’’ 49. Academic Press, INC, 22-66, (1995)

[335] Lettow, R., Rezus, Y.L.A., Renn, A., Zumofen, G., Ikonen, E., Götzinger, S. and Sandoghdar, V., ‘‘Quantum interference of tunably indistinguishable photons from remote organic molecules’’. Physical Review Letters, 104, 123605, (2010).

Chapter 3
Experimental Methods

3.1 Introduction

The fabrication and characterization of two-dimensional photonic crystals and micropillar microcavities is discussed in this chapter. The fabrication of two-dimensional photonic crystals involves four steps: a hard mask deposition, Electron Beam Lithography (EBL), resist development and finally dry etching using Reactive Ion Etching (RIE) and Inductively Coupled Plasma (ICP). Such fabrication steps will be described in detail. The deposition of a thin film of an organic material on the surface of a nanocavity structure and inside micropillar microcavities is also discussed. The fabrication of micropillar microcavities similarly involves two steps: Electron Beam Evaporation and Focused Ion Beam (FIB) lithography. Finally, the photoluminescence (PL) and optical properties of the samples were measured and investigated using a number of spectroscopy techniques.

3.2 Description of nanocavity substrate

In this work, freestanding silicon nitride (Si_3N_4) membranes having a refractive index n = 2.1 were used. Such SiN substrates were purchased from Silson Ltd [1]. Silicon nitride is a dielectric material having a high refractive index. SiN is widely utilized in silicon-on-insulator (SOI) semiconductor platforms because the large refractive index difference between the SiO_2 cladding ($\Delta n \approx 0.5$) and the refractive index of the SiN core allows light to be effectively confined. Si_3N_4 also has high transparency over the infrared and visible regions. It can also be integrated into photonic applications, has low optical losses and low-cost. Silicon nitride has been used in bio-sensing applications at visible and near-infrared wavelengths due to its low thermal loss and weak sensitivity to thermal changes [2-14].

The SiN membranes used were fabricated from a 200 nm SiN layer deposited on a 381 µm thick silicon wafer having a maximum surface roughness of about 4 nm. Here, the Si frame size was 5×5 mm^2 with a SiN window opened by chemical etching having a lateral size of 0.5 × 0.5 mm^2. Such samples are fragile, and care needs to be taken during subsequent fabrication processes. Figure 3.1 shows a schematic diagram of (a) the top the SiN membrane, (b) a cross-section through the membrane and (c) an image of a real sample. Here, my thumb is visible to give a sense of scale.

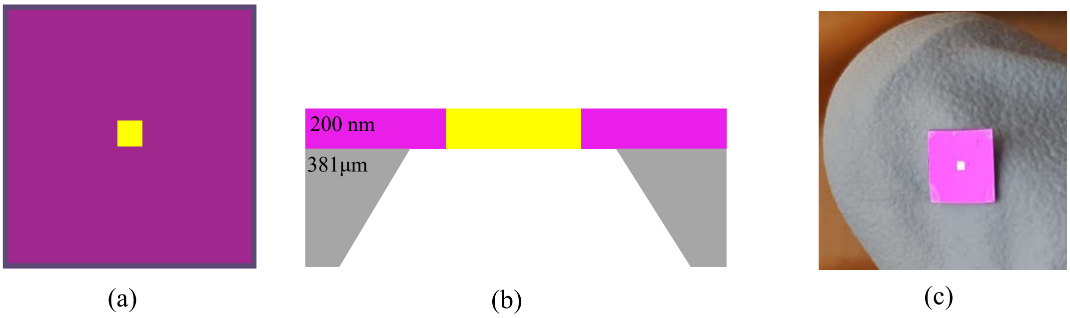

Figure 3.1: Shows (a) a schematic diagram from the bottom of the SiN membrane, (b) a cross-section and (c) an image of a real sample.

Before starting deposition, the SiN membranes have to be cleaned to remove any contamination or dust particles from their surface by rinsing in isopropyl alcohol (IPA) for 30 sec. They are then dried using a nitrogen (N_2) gas jet. Finally, the membranes are placed on a hot plate at 100° C for 60 sec to evaporate any remaining solvent.

3.3 Sample Fabrication

3.3.1 Hard mask deposition

The pattering of a Si_3N_4 membrane starts with the deposition of a hard mask such as poly-methyl-methacrylate (PMMA) [15-16] or chemical semi amplified resist CSAR [17-21].

Here, films have a typical thickness of 200 nm and a maximum surface roughness of ≈ 1.8 nm. The deposition of this resist is by spin coating at a speed of 4000 rpm. After that, the solvent of the hard mask layer is allowed to evaporate by baking the samples at a temperature of 180° for 10 minutes. This baking reduced the thickness of the mask layer to 180 nm. Figure 3.2 shows the thickness of the PMMA e-beam resist before and after baking at a temperature of 180°c.

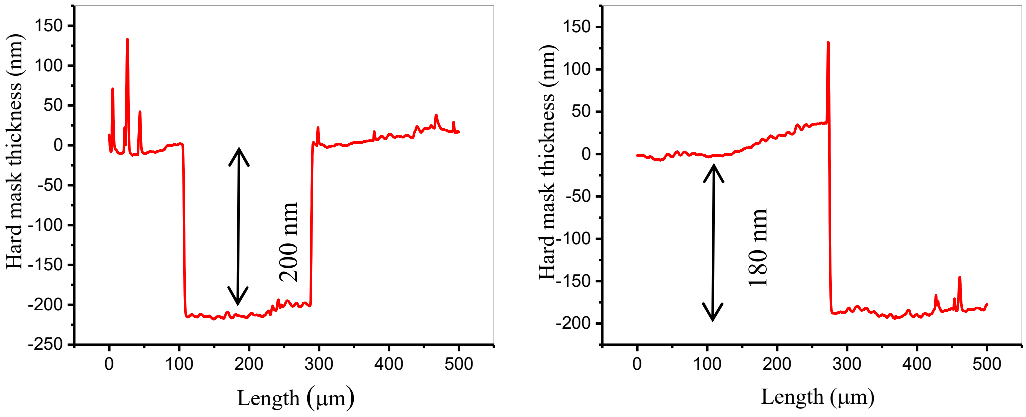

(a) (b)

Figure 3.2: Shows (a) the thickness of the e-beam resist hard mask before baking and (b) after baking.

3.3.2 Electron Beam Lithography (EBL)

Lithography is a process used to transfer a desired pattern or design into a sensitive thin film of a resist material. Thermal, x-ray, optical, ion beam and electron beam radiation sources are some different techniques that have been used to define a desired pattern into a hard mask. The feature size of a design of interest determines the appropriate radiation source. For example, optical lithography can also be used to print micron size features because of the optical diffraction limit. For this reason, electron beam sources are used to create patterns having a feature size of sub-ten nanometers, with very high resolution of a 50 Ȧ precision possible [22-28].

Electron beam lithography (EBL) is a popular advanced lithography technique in which a high-energy beam of focussed electrons is used to expose a pattern having sub-nanometer features into an e-beam resist. The advantages of using EBL are that a CAD (Computer-aided design) tool can be rapidly changed and used to improve the structure of the samples. This flexibility is useful and allows a user to reduce the time and cost of the work.

In the work described here, a high performance electron beam lithography system (Raith 150- Voyager) was used to create two dimensional photonic crystal nanocavities. The EBL system is located in the Centre for Nanoscience and Technology at the University of Sheffield as shown in figure 3.3 (a). The Raith 150 – Voyager software has its own built-in design tools based on the GDSII format. GDSII is a binary format that supports a hierarchical library of structures. Here, polygons, circles, open paths, filled rectangles and single dots are the basic structures that can be drawn using the GDSII as shown in figure 3.3(b).

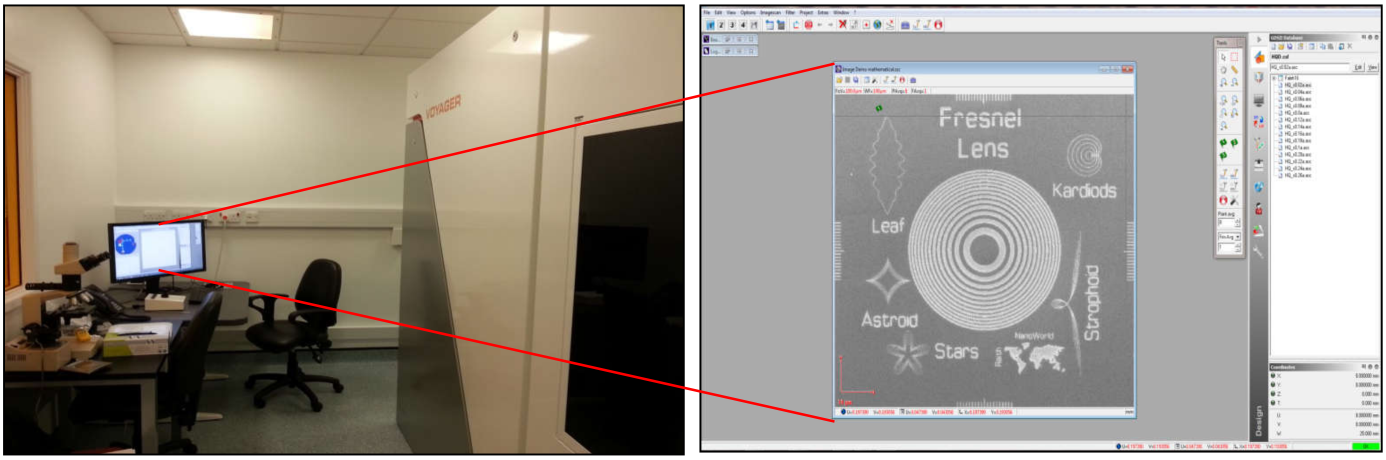

(a) (b)

Figure 3.3: (a) The EBL system located in the Centre for Nanoscience and Technology at the University of Sheffield, (b) an image of GDSII format software having a library of different structures.

Moreover, the system enables dose rate to be controlled for each element in the design, with any part of the structure to be removed, shifted or rotated [29-32].

Three layers were utilized to design two dimensional photonic crystal nanocavities. The first layer (layer 0) is used to label the properties of the nanocavities and is called the text layer. The second layer (layer 1) defines the structure of 14 photonic crystal nanocavities that are located close to the edge of the membrane. Finally, a manual mark layer (layer 2) is used to determine the membrane and nanocavity border. Figures 3.4 (a) and (b) illustrate the software used to design the structures and an image of the resultant photonic crystal nanocavities fabricated. Table 3.1 shows the EBL parameters used in thiswork.

3.3.3 Electron beam resists

Electron beam resists are sensitive materials that are based on organic materials / polymers that can be developed using specific developers after exposure. There are two type of e-beam resist; positive and negative [33]. When the EBL resist is exposed using an electron beam, it undergoes a fundamental change in its physical or chemical properties. For a positive e-beam resist, the bonds of the polymer chains in the exposed area are broken, creating an increase in its solubility in the developer solvent. As a result, a positive image is created in the exposed pattern. Negative resists however become insoluble in the developer after exposure and can be utilized to produce a negative image of the exposed pattern as illustrated in Figure 3.5 [34, 35]. The position and the intensity of the e-beam can be controlled using the Raith -150 to obtain the desired structure.

Table 3.1 EBL parameter used to fabricate two dimensional photonic crystal nanocavities.

E- beam energy (KV)	E- beam current (nA)	Dose (μC/cm^2)	Dose factor
50	0.46	350	1.8

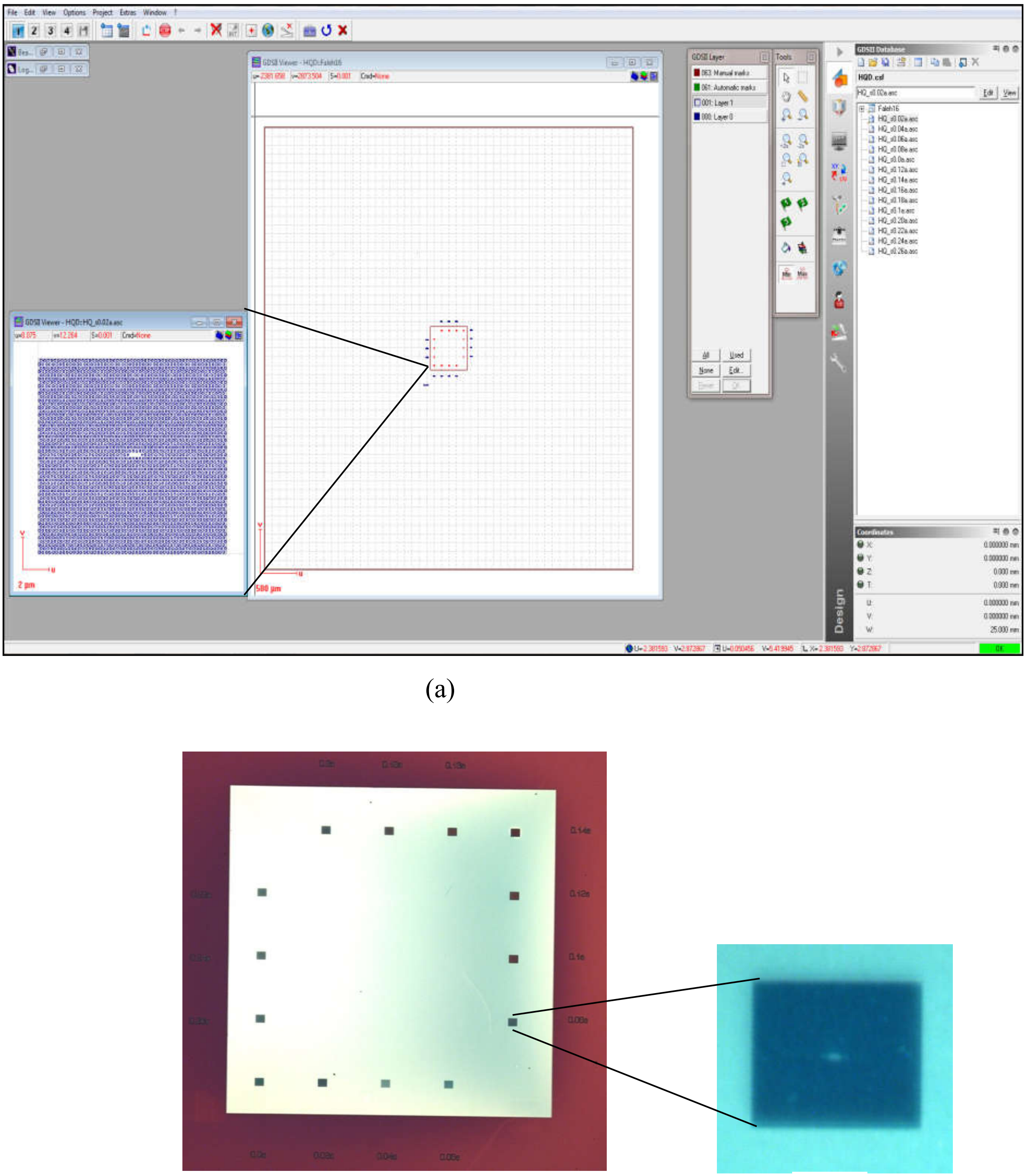

(a)

(b)

(c)

Figure 3.4: (a) An editing window for photonic crystal nanocavities designed using Raith-150 software. (b) a SiN membrane window containing 14 PC nanocavities and (c) an image of a PC nanocavity.

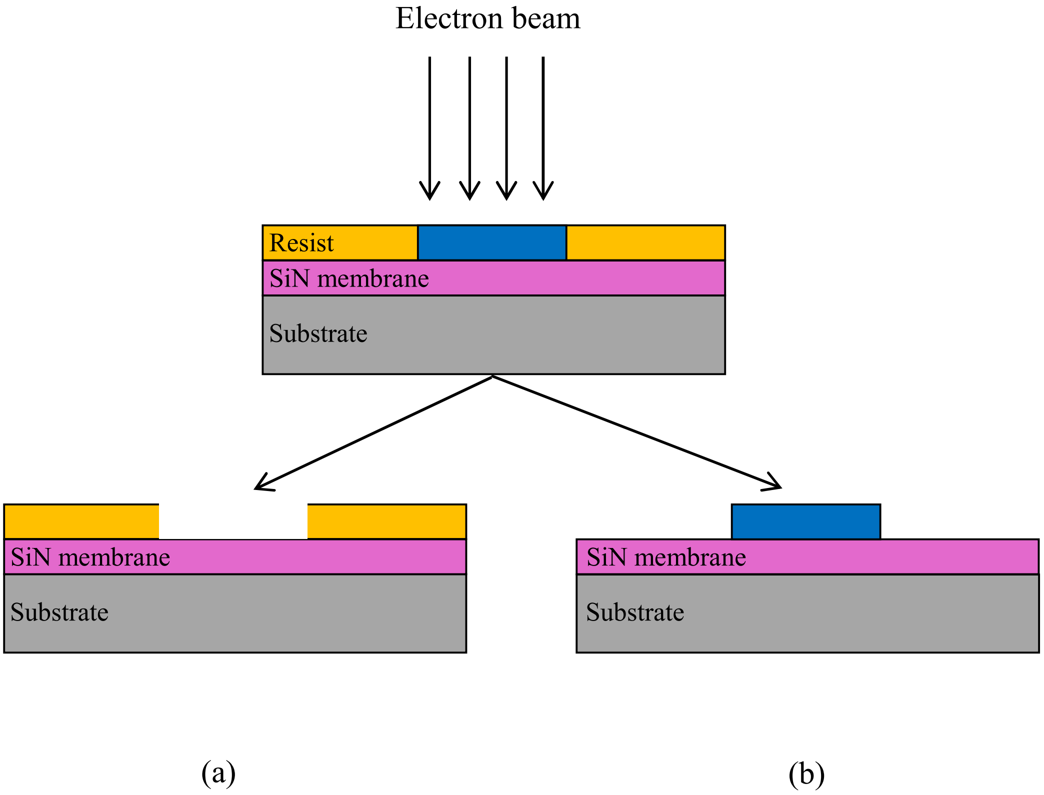

Figure 3.5: Shows (a) a positive e-beam resist and (b) a negative e-beam resist.

3.3.4 Proximity effect correction

The most important problem in E- beam lithography is the proximity effect that impacts on the pattern resolution. Here, during the exposure process, a beam of electrons collides with atoms of the resist or the substrate. As a result, the trajectories of the electrons change in the resist or the substrate. This leads to an exposure of an undesired area, causing a deviation and distortion in the pattern. Forward and back scattering are two type of scattering in the samples. Forward scattering results from electrons being scattered by the resist. Here, electrons deflected through small angles lead to an increase the incident beam diameter that affects the size and shape of the pattern. The second process is back scattering that results from the electron beam striking atoms in the substrate. This leads to an increase of the background dose over lateral distances of several micrometres. This phenomenon is often known as a proximity effect [36-43].

To overcome or reduce the problem of the proximity effect, higher electron beam voltages are often used to expose resists. As a result, the spread of the electrons reduces as the electron beam passes through the resist. Back scattering is also reduced due as the high energy electrons can penetrate the substrate [44]. Figure 3.6 shows a Monte Carlo simulation of forward and back scattering leading to proximity effect. The absorption of energy as a function of the beam voltage in the resist (such as PMMA) can be modelled to adjust the appropriate exposure for the electron beam [45- 47].

3.3.5 Resist Development

To transfer a pattern to a substrate (such as a SiN membrane), the exposed pattern in the resist is developed in a solution called a developer. It is important that the developed resist sidewalls are perpendicular. Non-perpendicular resist side walls result from problems with either electron beam dose or the development time. In experiments reported here, the exposed positive resist was developed for 30 seconds using a 1:3 MIBK: IPA (1:3 methyl- iso-butyl-ketone: Isopropyl alcohol) solution that is a commonly used developer for PMMA resists. The sample was then rinsed for 15 seconds to remove the remaining solution from the samples. In other experiments, a Xylene developer (Dimethylbenzene) was used for CSAR resists. Here, the exposed resist was developed for 60 seconds with the sample then rinsed for 30 seconds. Finally, the sample was dried gently using a N_2 gas jet for 30 seconds to be ready for the etching process [48, 49].

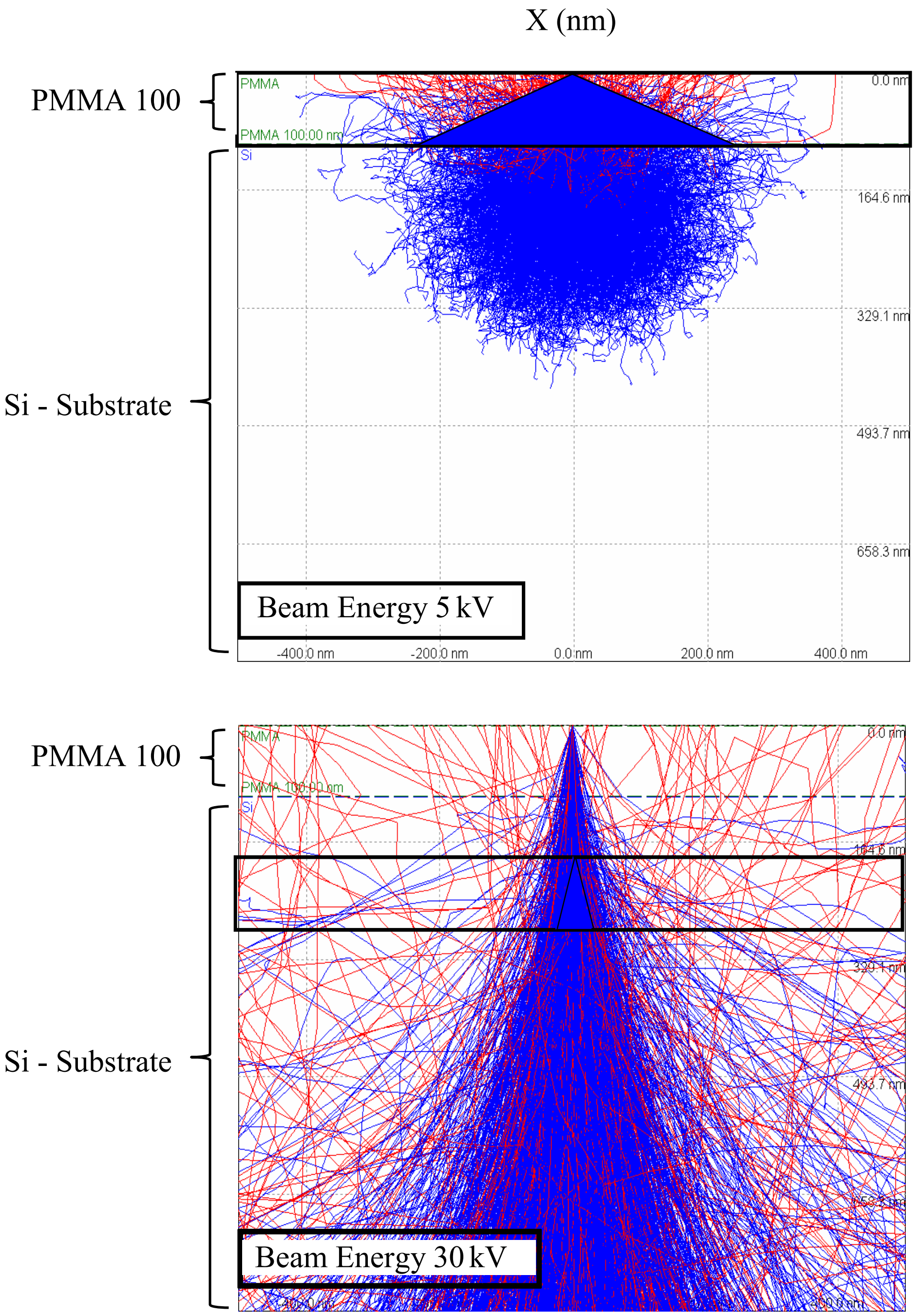

(b)

Figure 3.6: A Monte Carlo simulation of forward and back scattering causing proximity effect phenomena in a PMMA resist on a silicon substrate at (a) 5 kV and (b) 30 kV (image taken from technical notes produced by Raith Ltd).

3.3.6 Dry Etching

After resist development, a patterned structure is defined into the resist. An etching process is then used to transfer the patterned structure from the resist to the substrate using either a reactive ion beam etching (RIE) or an inductively coupled plasma (ICP) technique [50-56]. Dry etching techniques can be classified into three categories; physical, chemical and physical - chemical dry etching. A chemical reaction that uses gases or plasmas is used in chemical dry etching to remove substrate materials. Physical dry etching uses a high kinetic energy ion beam to knock out the atoms from a substrate's surface. Reactive ion etching (RIE) is a physical - chemical dry etching technique. A dry etching technique is distinguished by the use of low temperature plasma that generates free radicals or ions to remove material, and does not use any liquid chemicals. This main advantage of this technique is the ability to control sidewall through anisotropic etching [52], [57-62].

3.3.7. Plasma dry etching systems (RIE and ICP)

In this thesis, two dry etching systems have been used; reactive ion beam etching (RIE) and inductively coupled plasma etching (ICP) to transfer EBL structures patterned in a resist to a SiN membrane. These systems have many advantages such as high etching rates, low active-layer damage, smooth sidewall morphology, vertical anisotropic etching (producing a pattern of narrow lines), and high selectivity to the masking material [63-66].

High selectivity is one of the most important issues in the selection of etching gas. Fluorocarbon based gasses (halocarbons and hydrogen-rich fluorocarbon) such as CF_4 and CHF_3 can be used to etch a SiN membrane. It is known that adding gases such as Ar or O_2 to the plasma allows the angle of the hole sidewalls in the structure to be controlled [67-71]. The mechanism of the etching process can be described as follows; first during etching of

SiN_3 in a pure CHF_3 plasma, a layer of fluorocarbon gradually forms on the membrane surfaces. Ions and radicals are created as a result of this process which reacts with the Si in the SiN. The etching then starts as chemical species pass through this layer and then are converted to volatile products that come out of the system in the gas exhaust. Finally, Oxygen is used to control the angle of the sidewalls and remove any remaining resist from the surface of the membrane.

Figure 3.7 illustrates a schematic of the RIE system chamber. Here, upper and lower electrodes are positioned between a base where the samples are placed. An electromagnetic field is created inside the chamber by connecting electrodes to a radio frequency (RF) power source.

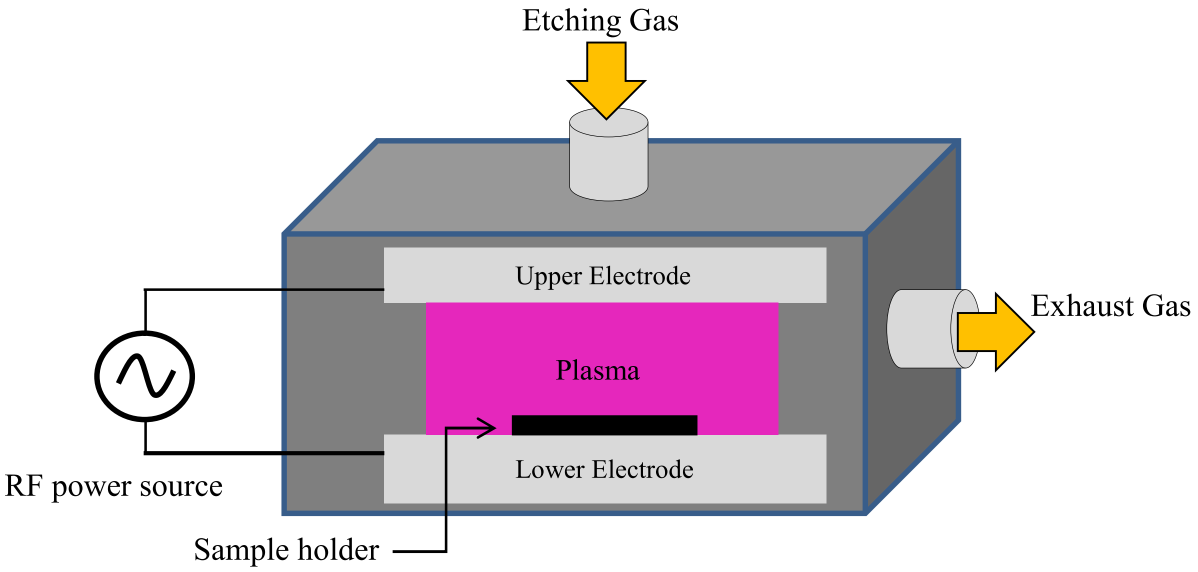

Figure 3.7: A schematic of RIE system [72].

By maintaining a gas flow inside the chamber at low pressure, the upper and lower electrodes produce plasma (radicals, ions and electrons) and direct the plasma towards the surface of the sample thereby enhancing the etching rate [66-67]. Various gas recipes, flow rates, pressures, RF power levels and etching times can be used to control the rate of the etching process. The value of the etching parameters used in this work is summarised in Table 3.2.

Table 3.2 RIE and ICP parameters used to etch a SiN membrane.

Etching system	Gas	Gas Rate (sccm)	Pressure (mTorr)	RF power (W)	Etching Time (min)
RIE	CHF3	40	35-25	75	16
ICP	CHF3	30	16	200	10

The final step in the fabrication process is the removal of residual resist from the surface of the SiN membrane. This is done using an oxygen asher tool for 10 minutes. Figure 3.8 summarizes the whole fabrication process used to pattern the SiN membranes. Figure 3.9 shows four images of SiN photonic crystal L3 nanocavity structures that were fabricated and then imaged using a scanning electron microscope (SEM). Figure 3.9 (b) shows an image of a SiN photonic crystal L3 nanocavity using PMMA as a resist. Here, unwanted material can be seen on the surface of the cavity, whereas Figure 3.9 (c-f) shows images of SiN photonic crystal L3 nanocavity patterned using CSAR as a resist. It is clear that the holes in all structures are circular in shape having straight side-walls, indicating the cavity is likely to have a high quality factor using RIE as a coarse etching system and ICP as a fine etching system respectively. The high quality of the nanocavities results from a number of factors, including using a high energy E- beam lithography system (50 kV), using different type of resists (PMMA and CSAR), dry etching systems (RIE and ICP) and the use of the asher tool.

The taper angle of the air holes in the structures can be measured from the underside of the SiN membrane using SEM [73] as illustrated in Figure 3.10.

(a) A 200 nm SiN membrane supported in a Si wafer.

(b) A 180 nm resist layer spin coated on the top surface of the SiN and then baked at 180° C for 10 min.

(c) An L3 nanocavity structure defined into the resist using EBL. The sample then is developed using Xylene or MIBK: IPA (1:3) solvent.

(d) The structure in the resist is then transferred into the SiN membrane using a plasma etching system

(e) The residual resist is removed using an oxygen plasma asher.

Figure 3.8: A schematic showing the fabrication process used to pattern the SiN membranes.

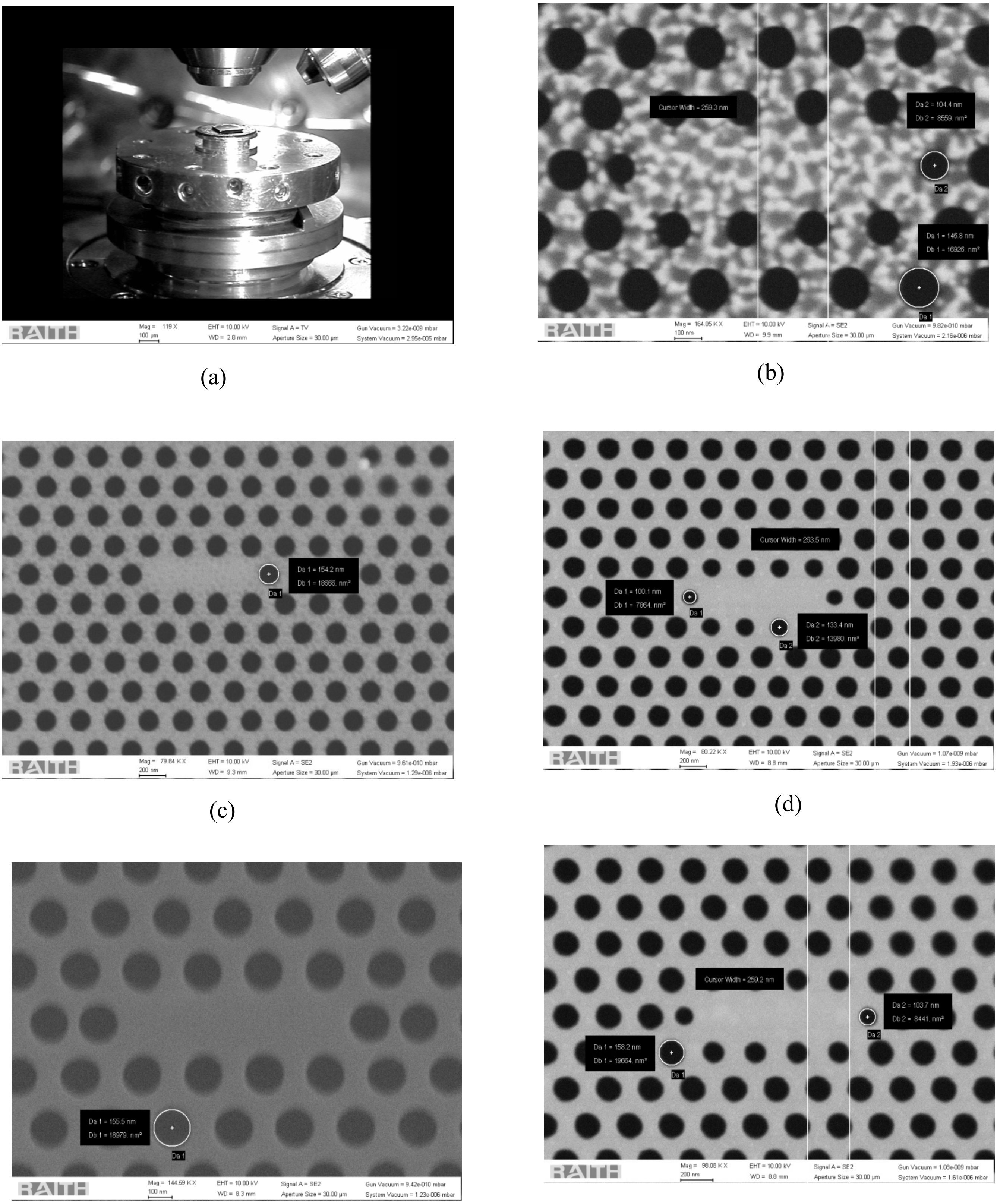

(a) (b)

(c) (d)

(e) (f)

Figure 3.9: shows (a) The SEM system, (b) shows an image of SiN photonic crystal L3 nanocavity using PMMA as an e beam resist. (c, d, e and f) a number of different L3 nanocavities structure designed in this work that were patterned using CSAR as a resist.

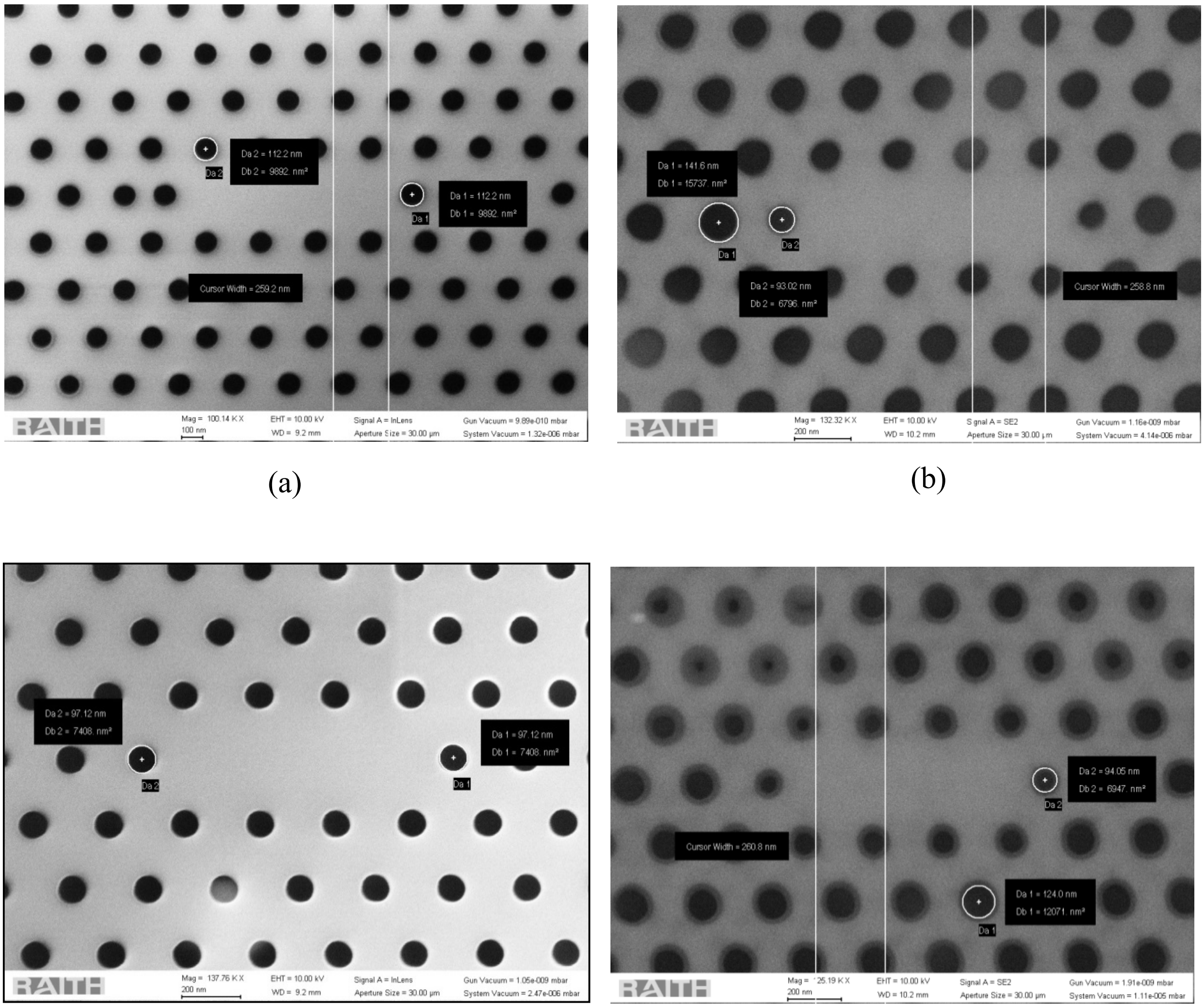

(a) (b)

(c) (d)

Figure 3.10: Shows (a-d) SEM images of four different undersides of the SiN membranes based photonic crystal nanocavities using a SCAR e-beam resist.

From Figure 3.9 and Figure 3.10, it can be seen that the smallest air hole size is reduced from 103 nm to 94 nm, which indicates a side-wall taper angle of around 4°. Taper angles in previous work on SiN based photonic crystal nanocavities ranged from 4° to 8° [74].

3.4 Electron Beam Evaporation

Planar multilayers composed of quarter-wave thin films of periodic low and high refractive indices were deposited onto a S151 synthetic quatrz coated substrates in the form of a stack using an electron beam evaporation technique. This allowed highly reflecting structures called aDistributed Bragg Reflectors (DBR) to be created as shown schematically in Figure 3.11.

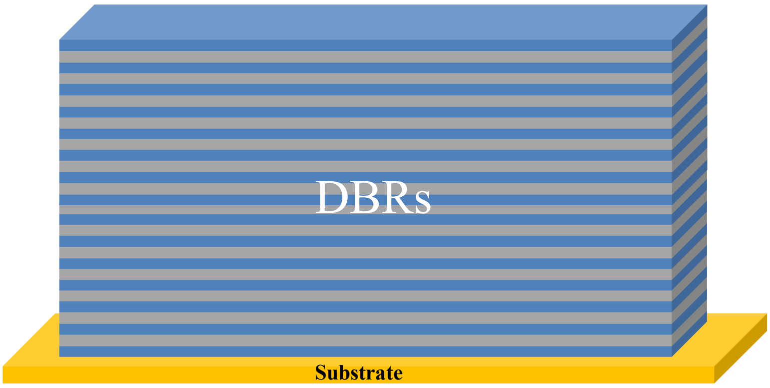

Figure 3.11: A schematic depiction of a one dimensional photonic structure called a Distributed Bragg Reflector (DBR).

The S151 synthetic quatrz coated substrates used had a thickness of 1.1mm and were purchased from Ossila. The substrates were first cleaned in an ultrasonic cleaner bath (Sonic 3MX) using a dilute 2 % Hellmanex solution for 10 min and then rinsed in dionized water. After that, they were cleaned again in an ultrasonic cleaner bath using isopropyl alcohol (IPA) for 10 min. Finally, substrates were dried using a N_2 gas jet and UV ozone cleaned for 10 min to remove any remaining IPA. They were then ready for the evaporation process using a low temperature reactive electron-beam evaporation system.

The electron-beam evaporation system is shown schematically in Figure 3.12(a). This is a physical evaporating deposition device that uses thermal evaporation created by an electron beam to deposit a wide range of materials. The electron-beam evaporation equipment used in this work is provided by Angstrom Engineering as shown in Figure 3.12(b). The deposition occurs when a target material is placed in a crucible in a high vacuum chamber (around 8×10^{-8} mbar). A crucible containing the material to be deposited is then irradiated using a high voltage unified electron beam from a charged tungsten filament. This can be used to evaporate metal and dielectric materials having very high melting temperatures. These materials are then converted to a gaseous state and are then deposited as a thin film coating on the substrate of interest [75-82].

During the evaporation process, a partial pressure of a reactive gas such as oxygen is added to oxidise the evaporating metals, producing a metal oxide thin film on the substrate. Here, dielectric mirrors consisting of a number of quarter- wave pairs of TiO_2 and SiO_2 were used. The thickness and the rate of each metal oxide deposition (2Ȧ /s) were controlled using a quartz-crystal microbalance. A uniform deposition was obtained by rotating the substrates around a fixed axis inside the chamber. The reactive electron beam evaporation system has many advantages such as high purity material can be deposited, with any contamination from other materials being reduced. A single source can be used to deposit different materials using pocket indexing system that moves in a circular motion to provide higher deposition rates. Using this technique, DBR mirrors with thickness $\lambda/4n$ were deposited. A thin film of a Red-F polymer having a thickness of 195 nm was then spin-cast on top of a DBR to create a $\lambda/2n$ layer.

A second DBR was then deposited onto the top of the organic material at room temperature using electron beam evaporation. Micropillar microcavities were then fabricated from such structures using a focused ion beam lithography technique.

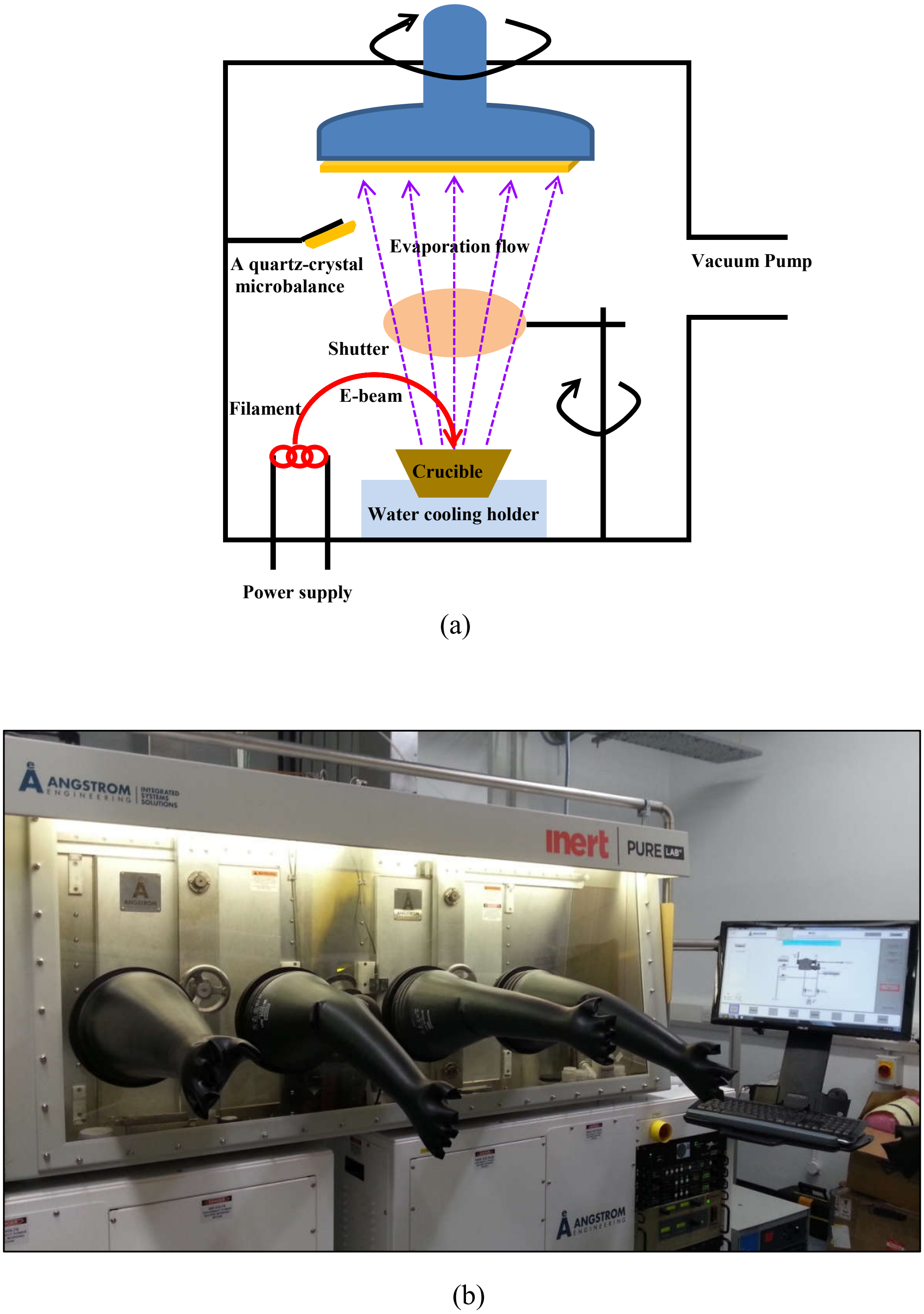

Figure 3.12: (a) A schematic of the electron-beam evaporation system. (b) The electron-beam evaporation system located inside a glove-box at Sheffield University.

3.5 Focused Ion Beam Lithography (FIB)

A focused ion beam (FIB) technique was used to fabricate three dimensional photonic structures such as micropillar microcavities. Here, a focused beam of Gallium ions was used to etch a specific area from a planar microcavity. In this thesis, a FEI Quanta 200 3D SEM/FIB was used as shown in Figure 3.13 (a). A FIB system consists of eight parts; a chamber, vacuum system, ion source, electron source, sample stage, detector, camera and computer to control the melting process. The melting process is shown schematically in Figure 3.13 (b). A gallium liquid metal ion source (LMIS) is used in the melting (etching) process, with the Ga ions having a much greater momentum than electrons used in EBL [83-89].

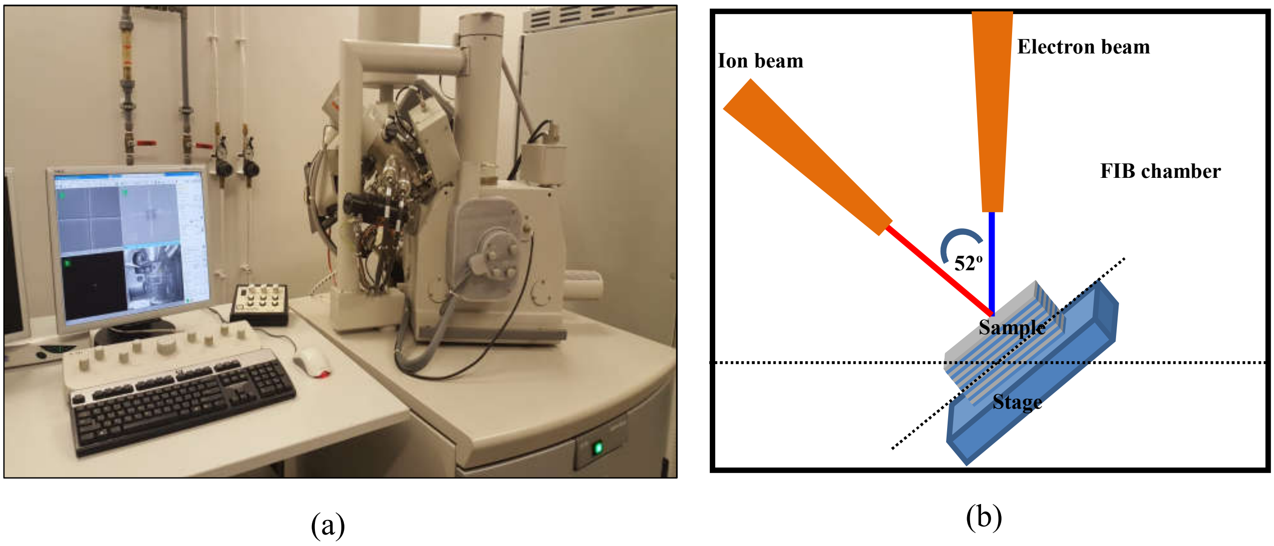

(a) (b)

Figure 3.13: (a) Focused ion beam system (Quanta 200 3D SEM/FIB) in the Sorby centre at Sheffield University, (b) A schematic showing the melting process inside the FIB system.

The melting process occurs under vacuum of 8×10^{-5} mbar. During lithography, Gallium metal is placed in contact with a tungsten needle and heated. Once the emitted ions are extracted from the source, they enter an ion column that contains an electrostatic condenser and objective lens which accelerates and focuses the 30kV ion beam onto the sample surface, with the beam current being in the range from 10 pA to 5nA depending on the desired milling rate. Here, the sample is placed on a slanted holder at 52° with respect to the ion column. A SEM inside the chamber is used to focus the ion beam on the surface of the sample to ensure high resolutions etch. A large quantity of DBR material can be removed by the lithography process, allowing the sample to be patterened at a nanometer scale.

Using this technique, three dimensional micropillar microcavities were created as shown in Figure 3.14. The optical properties of the micropillars microcavities were explored using far field optical spectroscopy as described in Chapter 4.

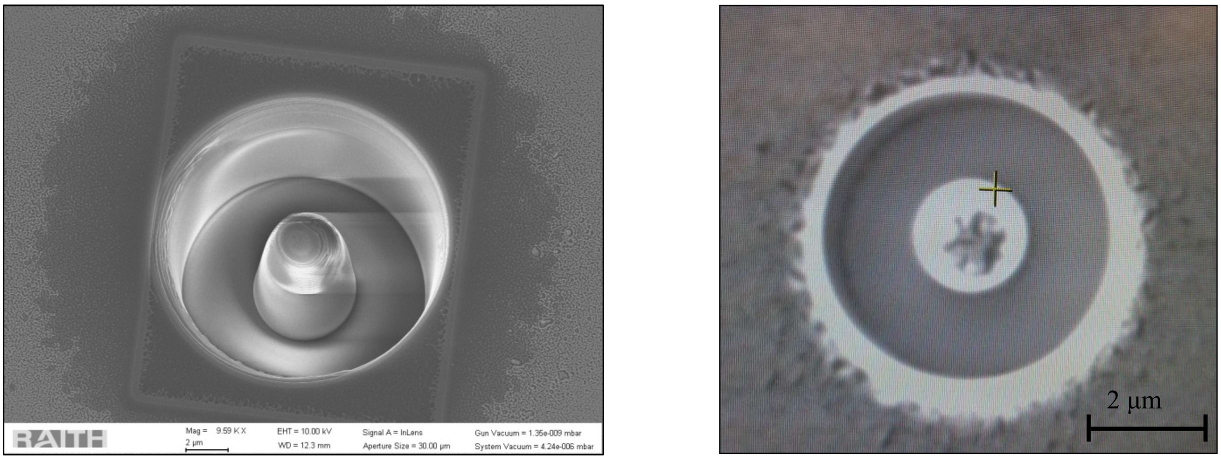

(a) (b)

Figure 3.14: Shows three dimensional micropillar microcavities that were created using the FIB (a) A micropillar microcavity having a diameter of 4 µm (b) A vertical image of a micropillar microcavity having a diameter of 2 µm.

3.6 Atomic force microscope (AFM)

An atomic force microscope (AFM) is an instrument that uses a sharp probe to record an image from a surface of a specimen. It cab be used to study surfaces at near atomic scale on conducting and non-conducting materials and create an image in both vertical and lateral directions. During this work, a Veeco-Dimension 3100 (AFM) operating in tapping mode as shown in Figure 3.15 was used to measure the maximum high and surface roughness of SiN membranes and polymers that were spin coated onto their surface.

An AFM works by allowing a sharp probe at the end of a cantilever to make contact with the surface of the sample. When the tip of the sharp probe approaches a surface, the forces between the tip and the atoms of the sample deflect the cantilever. By measuring the motion of a laser signal reflected from the cantilever using photodiode detector, a three-dimensional image can be recorded. Here, a silicon cantilever (model TESPA- having a force constant 20-80 N/m and resonant frequency 290-357 kHz) was used. Tapping mode was used to avoid sample damage because of lateral forces. The motion of the cantilever is achieved using a piezoelectric scanner. Using such techniques, an image of structure topography of a specimen surface can be obtained [90-98].

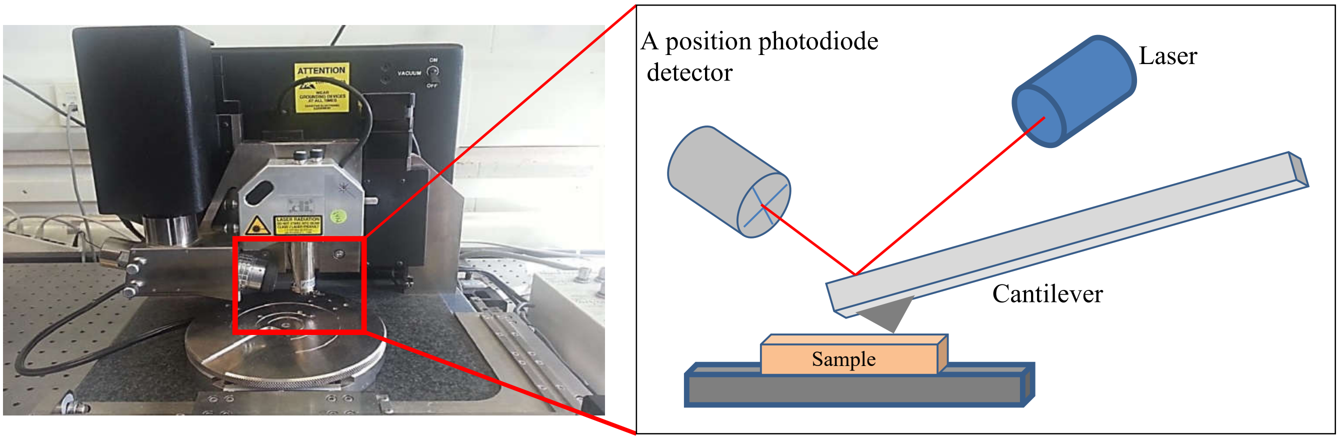

(a) (b)

Figure 3.15: shows (a) Veeco- Dimension 3100 atomic force microscopy device. (b) Schematic of an atomic force microscope [99].

3.7 Organic thin film deposition.

In this work, spin casting [100] was used to coat polymer films onto the surface of photonic crystal nanocavities and other substrates. Here, solutions were prepared by dissolving a Red-F polymer in 1, 2-Dichlorobenzene at a concentration of 2.5 mg/ml. A spin speed of 4000 rpm was then used to produce a thin film of 10 nm thickness having a maximum surface roughness of 1.9 nm. A thicker film of 195 nm could be deposited by dissolving Red-F polymer in 1, 2-Dichlorobenzene at a concentration of 50 mg/ml using a spin speed of 3500 rpm.

3.8 Photoluminescence (PL) Spectroscopy

The optical properties of the photonic crystal nanocavities and micropillar microcavities were explored using far field optical spectroscopy as illustrated schematically in Figure 3.16. Here, a diode laser at 405 nm was used in a dark field configuration to excite the sample at a room temperature. The laser beam was focused on the samples using a 100X objective lens having a numerical aperture (NA) of 0.77, with a working distance of 6mm and spot size diameter of 10 μm. Equation 3-1 shows the relation between the numerical aperture and the spatial resolution of the objective lens [101-104].

$$\mathrm{R} = \frac{1.22\lambda}{2(\mathrm{NA})} = \frac{1.22\lambda}{2(\mathrm{n}\sin\theta)} \qquad 3\text{-}1$$

Here, n is the refractive index of the medium between the sample and the objective lens and θ is the half angle of the collection cone of the light. The intensity of the laser beam incident on the sample surface was controlled using a neutral density filter. The objective lens was placed on a 3D piezo motor stage that moved the lens close to the sample. The emission from the cavities was then collected using the objective lens at normal incident from the nanocavity surface.

A polarizer and a long pass filter having a cut-off wavelength of 488 nm was placed after the beam splitter to prevent any scattered or reflected laser beam from entering the spectrometer. Light emitted from the samples was collected using a convex lens having a focal length of 20 cm and then directed through a 0.08 mm width entrance slit to a spectrometer (Jobin Yvon Triax 320). The advantage of reducing the entrance slit width is to control the spectral resolution. The emitted light from the nanocavities was dispersed inside the spectrometer using one of two different gratings having either 1200 lines/mm with a spectral resolution of 0.07 nm or 300 lines/mm having a spectral resolution of 0.3 nm.

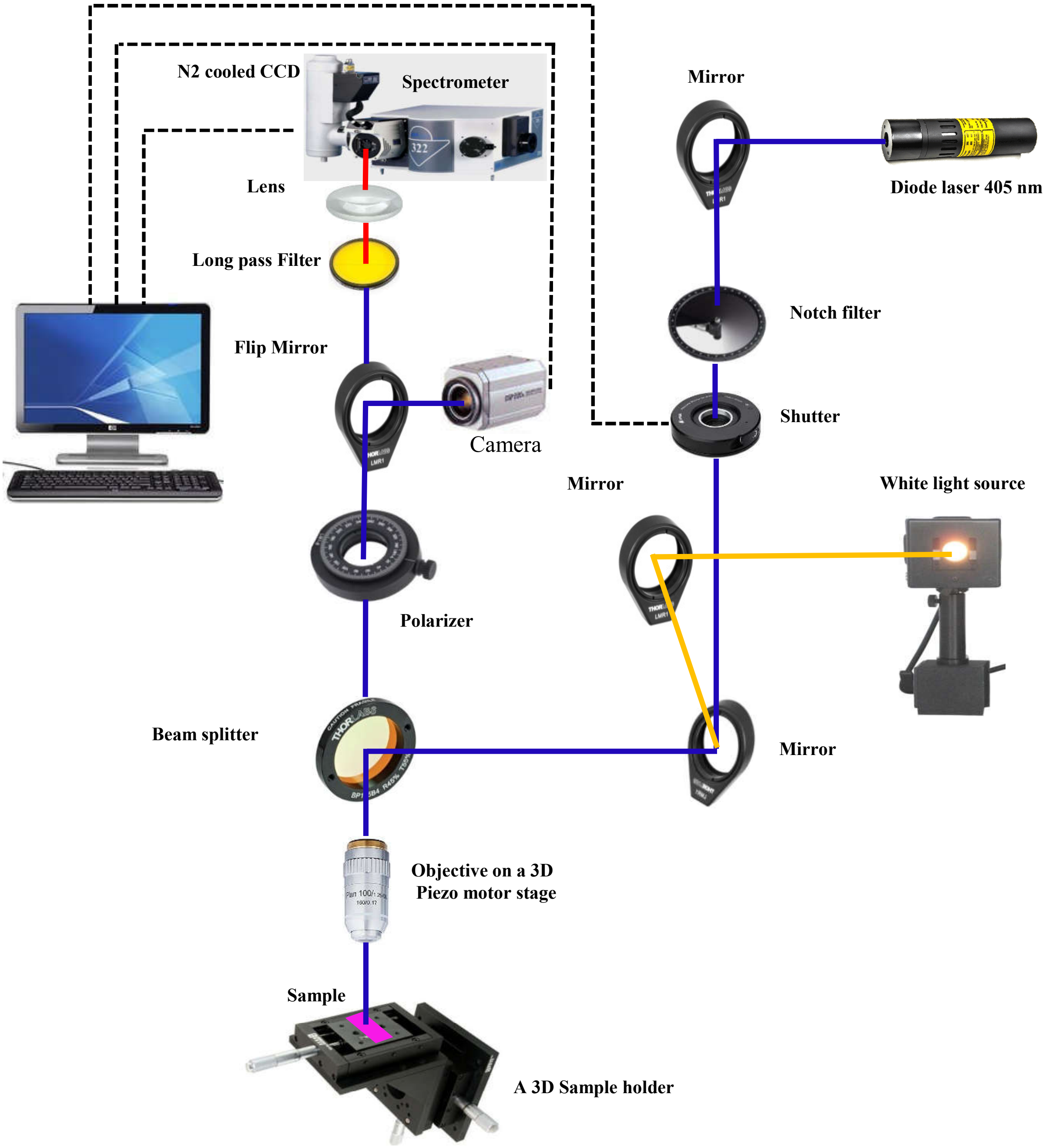

3.16: A schematic of the photoluminescence system used to study the optical properties of the photonic structures explored in this thesis.

Finally, the emission from the samples was imaged onto a nitrogen cooled charge coupled device (CCD) which is a highly sensitive photon detector [105-106]. The system in Figure 3.12 was aligned using a white light source and a camera to direct the laser spot on the PC nanocavity.

3.9 Spectral tomography techniques and K-Space imaging

Spectral tomography can be used to obtain information from the micropillar microcavity samples. Here, an image from a sample is divided into a number of slices on the entrance slit of the monochrometer depending on the size of the slits and the size of the luminescence image on the slits as illustrated in Figure 3.17(a). This technique allows the energy dispersion of emission to be characterized in a single measurement by projecting the Fourier-image into the spectrometer. Fourier space imaging can be used to study the energy of photons emitted from a micropillar microcavity along a given azimuth angle [107-111].

Here, by horizontally shifting the imaging lens that is placed at a distance from the monochrometer slit, the image that is formed on the slits is displaced. As a result, different lines of the initial image are permitted to enter the monochrometer to perform spectral tomography on a variety of images. Finally, each slice represents a two dimensional image with real or momentum space on one axis and energy on the other. This tomographic technique can be used to determine real space and k-space images.

In this thesis, the angular distribution of light by quantum emitters coupled to micropillar microcavity was investigated. To study the allowed modes and the dispersion relation in our samples, K-space imaging was used. In This technique, a Fourier plane imaging lens was placed between the objective and the final collection lens with the K-space image being the Fourier transform of the real space image [112-116].

To do this, a Ti: Sapphire laser having a wavelength of 445 nm was focused on the micropillar microcavity at normal incidence using an aspherical lens with a NA = 0.63

(Edmund Optics 20X), with the PL signal collected through the same optical path using a beam splitter. The emitted light was then focused into the spectrometer using a final collection lens. For k space imaging, an additional Fourier-plane imaging lens was placed before the final lens allowing the Fourier plane to be imaged by the spectrometer. Here, the unwanted real space signal was rejected by using a pinhole that was positioned before the final collection lens that leads the emission to be spatially filtered as shown schematically in Figure 3.17 (b).

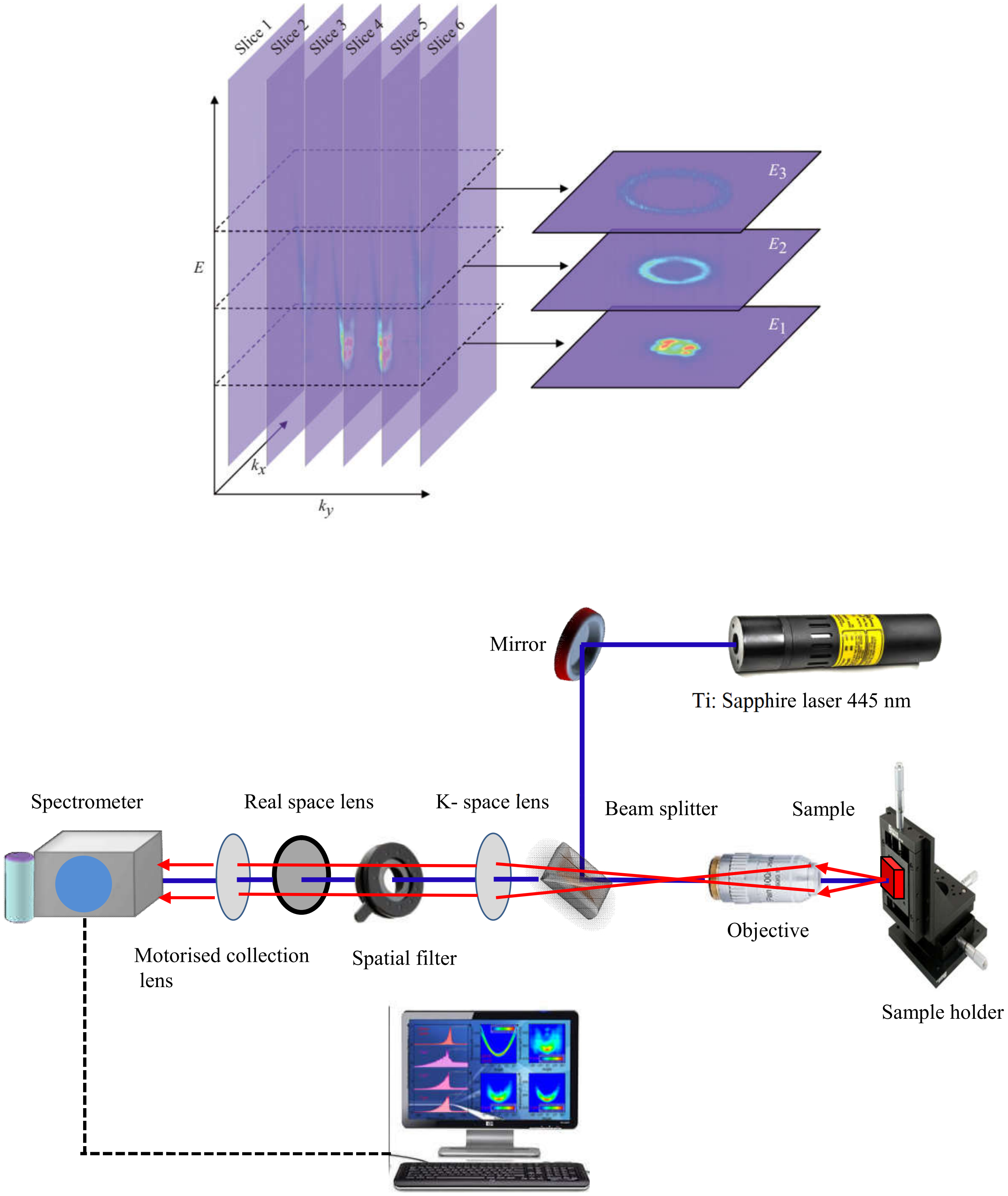

Figure 3.17 (a) shows the spectral tomographic imaging technique performed in K-space. Here, each of the slices on the left side corresponds to a specifc k_y and has energy versus k_x information[106]. (a) A schematic of K-space imaging system used to study the allowed modes and this dispersion relation in the micropillar samples studied in this thesis.

3.10 Summary and Conclusion

This chapter discussed the fabrication and characterization of two-dimensional photonic crystals nanocavities and three-dimensional micropillar microcavities. Here, all of the four fabrication steps for the two-dimensional photonic crystals were performed in the clean room of Nanoscience and Technology building laboratories at the University of Sheffield. The fabrication of two-dimensional photonic crystals involves four steps: a hard mask deposition, Electron Beam Lithography (EBL), resist development and finally dry etching using Reactive Ion Etching (RIE) and Inductively Coupled Plasma (ICP). The fabrication of micropillar microcavities was also discussed. Electron Beam Evaporation and Focused Ion Beam (FIB) lithography were the main two steps to fabricate micropillar microcavities. Here, the micropillar microcavities were performed using the Focused Ion Beam (FIB) in the Sorby centre laboratories at the University of Sheffield. The deposition of a thin film of an organic material on the surface of a nanocavity structure and inside micropillar microcavities was also described. Finally, the photoluminescence (PL) and optical properties of the samples were measured and investigated using a number of spectroscopy techniques such as far field optical spectroscopy, spectral tomography techniques and K-space imaging.

References:-

[1] http://www.silson.com/

[2] Yashima, M., Ando, Y. and Tabira, Y., ‘‘Crystal structure and electron density of α-silicon nitride: experimental and theoretical evidence for the covalent bonding and charge transfer’’. The Journal of Physical Chemistry B, 111, 3609-3613, (2007).

[3] Hammadi, O.A., Khalaf, M.K. and Kadhim, F.J., ‘‘Fabrication and characterization of ultraviolet photodetectors based on silicon nitride nanostructures prepared by magnetron sputtering’’. Journal of Nanomaterials, Nanoengineering and Nanosystems, 230, 32-36, (2016).

[4] Li, Y.X., French, P.J. and Wolffenbuttel, R.F., ‘‘Selective reactive ion etching of silicon nitride over silicon using CHF3 with N2 addition’’ Journal of Vacuum Science & Technology B, 13, 2008-2012, (1995).

[5] Deshpande, S.V., Gulari, E., Brown, S.W. and Rand, S.C., Optical properties of silicon nitride films deposited by hot filament chemical vapor deposition’’ Journal of Applied Physics, 77, 6534-6541, (1995).

[6] Zwickl, B.M., Shanks, W.E., Jayich, A.M., Yang, C., Bleszynski Jayich, A.C., Thompson, J.D. and Harris, J.G.E., ‘‘High quality mechanical and optical properties of commercial silicon nitride membranes’’, Applied Physics Letters, 92, 103-125. (2015).

[7] Lipiñski, M., ‘‘Silicon nitride for photovoltaic application’’, Archives of Materials Science and Engineering, 46, 69-87, (2010).

[8] Grande, M., Calo, G., Petruzzelli, V. and D'Orazio, A., ‘‘High-Q photonic crystal nanobeam cavity based on a silicon nitride membrane incorporating fabrication imperfections and a low-index material layer’’. Progress In Electromagnetics Research, 37, 191-204, (2015).

[9] Pernice, W.H.P., Li, M., Gallagher, D.F.G. and Tang, H.X., ‘‘Silicon nitride membrane photonics’’. Journal of Optics A: Pure and Applied Optics, 11, 114017, (2009).

[10] Pernice, W.H.P., Li, M., Gallagher, D.F.G. and Tang, H.X., ‘‘Silicon nitride membrane photonics. Journal of Optics A: Pure and Applied Optics, 11(11), 114017, (2009).

[11] Kassa-Baghdouche, L., Boumaza, T., Cassan, E. and Bouchemat, M., ‘‘Enhancement of Q-factor in SiN-based planar photonic crystal L3 nanocavity for integrated photonics in the visible-wavelength range’’, Optik, 126(22), 3467-3471, (2015).

[12] Bernard, S., Reinhardt, C., Dumont, V., Peter, Y.A. and Sankey, J.C., ‘‘Precision resonance tuning and design of SiN photonic crystal reflectors’’. Optics Letters, 41, 5624-5627, (2016).

[13] Barbillon, G., Gourdon, F., Cambril, E., Fabre, N., Yacomotti, A.M. and Bouchoule, S., ‘‘SiNx/organic photonic crystal microcavity optimization for the fabrication of thin-film micro-laser’’. Optics Communications, 325, 15-22. (2014).

[14] Dong, Y., Zhao, H., Song, J., Gao, F., Cheng, C., Chang, Y., Du, G., Yu, M.B. and Lo, G.Q., ‘‘Low threshold two-dimensional organic photonic crystal distributed feedback laser with hexagonal symmetry based on SiN’’. Applied Physics Letters, 92, 202, (2008).

[15] Granström, M. and Inganäs, O., ‘‘White light emission from a polymer blend light emitting diode’’ Applied physics Letters, 68, pp.147-149, (1996).

[16] Semaltianos, N.G., ‘‘Spin-coated PMMA films’’, Microelectronics Journal, 38, 754-761, (2007).

[17] Andok, R., Bencurova, A., Vutova, K., Koleva, E., Nemec, P., Hrkut, P., Kostic, I. and Mladenov, G., ‘‘Study of the new CSAR62 positive tone electron-beam resist at 40 keV electron energy’’. In Journal of Physics: Conference Series, 700, 012030, (2016).

[18] Greibe, T., Anhøj, T.A., Johansen, L.S. and Han, A., ‘‘Quality control of JEOL JBX-9500FSZ e-beam lithography system in a multi-user laboratory’’. Microelectronic Engineering, Elsevier, 155, 25-28, (2016).

[19] Schirmer, M., Büttner, B., Syrowatka, F., Schmidt, G., Köpnick, T. and Kaiser, C., ‘‘Chemical Semi-Amplified positive E-beam Resist (CSAR 62) for highest resolution’’, 29th European Mask and Lithography Conference, International Society for Optics and Photonics, 8886, 88860D, (2013).

[20] Meng, X., Gomard, G., El Daif, O., Drouard, E., Orobtchouk, R., Kaminski, A., Fave, A., Lemiti, M., Abramov, A., i Cabarrocas, P.R. and Seassal, C., ‘‘Absorbing photonic crystals for silicon thin-film solar cells: Design, fabrication and experimental investigation’’, Solar Energy Materials and Solar Cells, 95, S32-S38. (2011).

[21] Thoms, S. and Macintyre, D.S., ‘‘Investigation of CSAR 62, a new resist for electron beam lithography’’. Journal of Vacuum Science & Technology B, 32(6), 06FJ01, (2014).

[22] Kuwahara, M., Mihalcea, C., Atoda, N., Tominaga, J., Fuji, H. and Kikukawa, T., ‘‘Thermal lithography for 0.1 µm pattern fabrication. Microelectronic engineering, Elsevier, 61, 415-421, (2002).

[23] Brewer, G. ‘‘Electron-beam technology in microelectronic fabrication’’. Elsevier. (2012).

[24] Tseng, A.A., Chen, K., Chen, C.D. and Ma, K.J., ‘‘Electron beam lithography in nanoscale fabrication: recent development’’, IEEE, 26, 141-149, (2003).

[25] Manfrinato, V.R., Wen, J., Zhang, L., Yang, Y., Hobbs, R.G., Baker, B., Su, D., Zakharov, D., Zaluzec, N.J., Miller, D.J. and Stach, E.A., ‘‘Determining the resolution limits of electron-beam lithography: direct measurement of the point-spread function’’ Nano Letters, 14, 4406-4412, (2014).

[26] Vieu, C., Carcenac, F., Pepin, A., Chen, Y., Mejias, M., Lebib, A., Manin-Ferlazzo, L., Couraud, L. and Launois, H., ‘‘Electron beam lithography: resolution limits and applications’’ Applied Surface Science, 164, 111-117, (2000).

[27] Zhou, Z.J., 2005. Electron beam lithography. In Handbook of microscopy for nanotechnology, Springer, 287-321, (2005).

[28] Hasan, R.M.M. and Luo, X., ‘‘Promising Lithography Techniques for Next-Generation Logic Devices’’. Nanomanufacturing and Metrology, 1, 67-81, (2018).

[29] Wehrspohn, R.B., Rau, U. and Gombert, A. ‘‘Photon management in solar cells’’ John Wiley & Sons, (2015).

[30] Rai-Choudhury, P., ’’Handbook of microlithography, micromachining, and microfabrication’’, Iet, 1, (1997).

[31] Gangnaik, A.S., Georgiev, Y.M. and Holmes, J.D., ‘‘New generation electron beam resists: a review’’, Chemistry of Materials, 29, 1898-1917, (2017).

[32] Altissimo, M., ‘‘E-beam lithography for micro- /nanofabrication, Biomicrofluidics, 4, 026503, (2010).

[33] Nabity, J., Compbell, L.A., Zhu, M. and Zhou, W., ‘‘E-beam nanolithography integrated with scanning electron microscope’’. Scanning Microscopy for Nanotechnology, 120-151, Springer, (2006)

[34] Grigorescu, A.E. and Hagen, C.W., ‘‘Resists for sub-20-nm electron beam lithography with a focus on HSQ: state of the art’’. Nanotechnology, 20, 292001, (2009).

[35] Zheng, N., Min, H., Jiang, Y. and Cheng, X., ‘‘Polycarbonate as a negative-tone resist for electron-beam lithography’’. Journal of Vacuum Science & Technology B, 36, 021603, (2018).

[36] Nien, C., Chang, L.C., Ye, J.H., Su, V.C., Wu, C.H. and Kuan, C.H., ‘‘Proximity effect correction in electron-beam lithography based on computation of critical-development time with swarm intelligence’’. Journal of Vacuum Science & Technology B, 35, 051603, (2017).

[37] Kamikubo, T., Abe, T., Oogi, S., Anze, H., Shimizu, M., Itoh, M., Nakasugi, T., Takigawa, T., Iijima, T., Hattori, Y. and Tojo, T., ‘‘Proximity effect correction for electron beam lithography: highly accurate correction method’’, Japanese Journal of Applied Physics, 36, 7546. (1997).

[38] Geraint Owen ‘’ Proximity effect correction in electron-beam lithography’’ Optical Engineering, 32, 2446—2451 (1993).

[39] Frye, R.C., Cummings, K.D. and Rietman, E.A., ‘‘Proximity effect corrections in electron beam lithography using a neural network’’. In Advances in Neural Information Processing Systems, 443-449, (1991).

[40] Li, P., ‘‘A review of proximity effect correction in electron-beam lithography’’, arXiv preprint arXiv: 1509.05169, (2015).

[41] Ren, L. and Chen, B., ‘‘Proximity effect in electron beam lithography’’ 7th International Conference on Solid-State and Integrated Circuits Technology, IEEE, 1, 579-582, (2004).

[42] Seo, E., Choi, B.K. and Kim, O., 2000. Determination of proximity effect parameters and the shape bias parameter in electron beam lithography. Microelectronic Engineering, Elsevier , 53, 305-308, (2000).

[43] Manfrinato, V.R., Cheong, L.L., Duan, H., Winston, D., Smith, H.I. and Berggren, K.K.,‘‘Sub-5 keV electron-beam lithography in hydrogen silsesquioxane resist’’, Microelectronic Engineering, Elsevier, 88, 3070-3074. (2011).

[44] Christenson, K.K., Viswanathan, R.G. and Hohn, F.J., ‘‘X-ray mask fogging by electrons backscattered beneath the membrane’’. Journal of Vacuum Science & Technology B, 8, 1618-1623, (1990).

[45] Wang M. ‘‘Lithography’’, InTech, 571, (2010).

[46] Urbánek, M., Kolařík, V., Krátký, S., Matějka, M., Horáček, M. and Chlumská, J., ‘‘Monte carlo simulation of proximity effect in e-beam lithography’’, the 5th International Conference Nanocon, 723-726, (2013).

[47] Samardak, A., Anisimova, M., Samardak, A. and Ognev, A., ‘‘Fabrication of high-resolution nanostructures of complex geometry by the single-spot nanolithography method’’. Beilstein Journal of Nanotechnology, 6, 976-986, (2015).

[48] Cui, B. and Veres, T., ‘‘High resolution electron beam lithography of PMGI using solvent developers’’, Microelectronic Engineering, 85, 810-813, (2008).

[49] Spurny, M., O’Faolain, L., Bulla, D.A., Luther-Davies, B. and Krauss, T.F., ‘‘Fabrication of low loss dispersion engineered chalcogenide photonic crystals’’, Optics Express, 19, 1991-1996, (2011).

[50] Arafin, S., McFadden, A.P., Paul, B., Hasan, S.M., Gupta, J.A., Palmstrøm, C.J. and Coldren, L.A., ‘‘Study of wet and dry etching processes for antimonide-based photonic ICs’’, Optical Materials Express, 9, 1786-1794, (2019).

[51] Pommereau, F., Legouezigou, L., Hubert, S., Sainson, S., Chandouineau, J.P., Fabre, S., Duan, G.H., Lombardet, B., Ferrini, R. and Houdre, R., ‘‘Fabrication of low loss two-dimensional InP photonic crystals by inductively coupled plasma etching’’. Journal of Applied Physics, 95, 2242-2245, (2004).

[52] Souk, J., Morozumi, S., Luo, F.C. and Bita, I. eds., ‘‘Flat Panel Display Manufacturing’’, John Wiley & Sons, (2018).

[53] Shul, R.J. and Pearton, S.J. ‘‘Handbook of advanced plasma processing techniques’’ Springer Science & Business Media, (2011).

[54] Zhou, L., Li, Z., Zhang, J., Li, D., Liu, D., Li, Y. and Wang, X., ‘‘Thin layer broadband porous chromium black absorber fabricated through wet-etching process’’, RSC Advances, 9, 14649-14656, (2019).

[55] Yoo, J., Oh, G., Kim, M.W., Song, S.H., Yoo, S.D., Shim, T.H. and Kim, E.K., ‘‘Performance of thyristor memory device formed by a wet etching process’’, Nanotechnology, 30, 035205, (2018).

[56] Clawson, A.R., ‘‘Guide to references on III–V semiconductor chemical etching’’, Materials Science and Engineering: R: Reports, 31, 1-438, (2001).

[57] Nguyen, N.T., " Micromixers: fundamentals, design and fabrication". William Andrew, second edition, (2011)

[58] Park, T.G., Min, J., Han, D.C., Oh, Y. and Seo, W., ‘‘The characteristics of glass deep dry etching process with a single PR mask’’, In IEEE International Conference on Nano/Micro Engineered and Molecular Systems, 885-888, (2011)

[59] Nojiri, K., ‘‘Dry etching technology for semiconductors’’, Springer International Publishing, (2015).

[60] Ashraf, M., Sundararajan, S.V. and Grenci, G., ‘‘Low-power, low-pressure reactive-ion etching process for silicon etching with vertical and smooth walls for mechanobiology application’’, Journal of Micro/Nanolithography, MEMS, and MOEMS, 16, 034501, (2017).

[61] Zhang, J.X. and Hoshino, K., Molecular ‘‘Sensors and Nanodevices: Principles, Designs and Applications in Biomedical Engineering’’ Academic Press, (2018).

[62] Grover, R., Hryniewicz, J.V., King, O.S. and Van, V., ‘‘Process development of methane–hydrogen–argon-based deep dry etching of InP for high aspect-ratio structures with vertical facet-quality sidewalls’’. Journal of Vacuum Science & Technology B: 19, 1694-1698, (2001)

[63] Vrtacnik, D., Resnik, D., Aljancic, U., Mozek, M. and Amon, S., ‘‘Silicon dry etching profile control by RIE at room temperature for MEMS applications’’. Proc. of SPIE, 6037, 603720, (2006).

[64] Williams, K.R. and Muller, R.S., ‘‘Etch rates for micromachining processing’’, Journal of Microelectromechanical Systems, 5, 256-269, (1996).

[65] Zhu, Y.C., Karouta, F., Geluk, E.J., de Vries, T., van der Tol, J.J.G.M. and Smit, M.K., ‘‘ICP etching of InP and its applications in photonic circuits’’. Proc. IEEE/LEOS Benelux, 81-84, (2003).

[66] Park, S., Kim, S.S., Wang, L. and Ho, S.T., ‘‘InGaAsP-InP nanoscale waveguide-coupled microring lasers with submilliampere threshold current using Cl/sub 2/--N/sub 2/-based high-density plasma etching’’, IEEE Journal of Quantum Electronics, 41, 351-356, (2005).

[67] Okumura, T., 2011. ‘‘Inductively coupled plasma sources and applications’’. Physics Research International, (2010).

[68] Kaspar, P., Jeyaram, Y., Jäckel, H., Foelske, A., Kötz, R. and Bellini, S., ‘‘Silicon nitride hardmask fabrication using a cyclic CHF 3-based reactive ion etching process for vertical profile nanostructures’’. Journal of Vacuum Science & Technology B, 28, 1179-1186, (2010).

[69] Li, Y.X., French, P.J. and Wolffenbuttel, R.F., ‘‘Selective reactive ion etching of silicon nitride over silicon using CHF3 with N2 addition’’. Journal of Vacuum Science & Technology B, 13, 2008-2012, (1995).

[70] Gatzert, C., Blakers, A.W., Deenapanray, P.N., Macdonald, D. and Auret, F.D., ‘‘Investigation of reactive ion etching of dielectrics and Si in CHF 3⁄ O 2 or CHF 3⁄ Ar for photovoltaic applications’’ Journal of Vacuum Science & Technology A: Vacuum, Surfaces, and Films, 24, 1857-1865, (2006).

[71] Pant, B.D. and Tandon, U.S., ‘‘Etching of silicon nitride in CCl 2 F 2, CHF 3, SiF 4, and SF 6 reactive plasma: a comparative study’’ Plasma Chemistry and Plasma Processing, 19, 545-563, (1999).

[72] Jung, P.G., Jung, I.D., Lee, S.M. and Ko, J.S., ‘‘Fabrication of self-encapsulated nickel microchannels and nickel nanowalls by reactive ion etching’’. Journal of Materials Processing Technology, 208, 111-116, (2008).

[73] Beggs, D.M., O’Faolain, L. and Krauss, T.F., ‘‘Accurate determination of the functional hole size in photonic crystal slabs using optical methods’’ Photonics and Nanostructures-Fundamentals and Applications, 6, 213-218, (2008).

[74] Barth, M., Kouba, J., Stingl, J., Löchel, B. and Benson, O., 2007. Modification of visible spontaneous emission with silicon nitride photonic crystal nanocavities. Optics express, 15(25), pp.17231-17240.

[75] Persano, L., Camposeo, A., Del Carro, P., Mele, E., Cingolani, R. and Pisignano, D., ‘‘Very high-quality distributed Bragg reflectors for organic lasing applications by reactive electron-beam deposition’’ Optics Express, 14, 1951-1956, (2006).

[76] Feng, I.W., Jin, S., Li, J., Lin, J. and Jiang, H., ‘‘SiO_2/TiO_2 distributed Bragg reflector near 1.5 μ m fabricated by e-beam evaporation’’. Journal of Vacuum Science & Technology A, 31, 061514, (2013).

[77] Hong, K., Yu, H.K., Lee, I., Kim, S., Kim, Y., Kim, K. and Lee, J.L., ‘‘Flexible top-emitting organic light emitting diodes with a functional dielectric reflector on a metal foil substrate’’ RSC Advances, 8, 26156-26160, (2018).

[78] Persano, L., Mele, E., Pisignano, D., Frascerra, V. and Cingolani, R., ‘‘Polymer microcavities by room temperature electron-beam evaporation of TiOx and SiOx’’. Synthetic metals, Elsevier, 153, 329-332, (2005).

[79] Liu, X., Li, H., Song, C., Liao, Y. and Tian, M., ‘‘Microcavity organic laser device under electrical pumping’’. Optics Letters, 34, 503-505, (2009).

[80] Lin, Y. ed., ‘‘Advanced nano deposition methods’’. John Wiley & Sons, (2016).

[81] Ang, P.C., Ibrahim, K. and Pakhuruddin, M.Z., ‘‘Electrical properties and surface morphology of electron beam evaporated p-type silicon thin films on polyethylene terephthalate for solar cells applications’’ In AIP Conference proceedings, AIP Publishing, 1657, 040003. (2015)

[82] Routledge, T.J., Wong-Stringer, M., Game, O.S., Smith, J.A., Bishop, J.E., Vaenas, N., Freestone, B.G., Coles, D.M., McArdle, T., Buckley, A.R. and Lidzey, D.G., ‘‘Low-temperature, high-speed reactive deposition of metal oxides for perovskite solar cells’’. Journal of Materials Chemistry A, 7, 2283-2290, (2019).

[83] Ho, Y.L., Gibson, R., Hu, C.Y., Cryan, M.J., Rarity, J.G., Heard, P.J., Timpson, J.A., Fox, A.M., Skolnick, M.S., Hopkinson, M. and Tahraoui, A., ‘‘Focused ion beam etching for the fabrication of micropillar microcavities made of III-V semiconductor materials’’ Journal of Vacuum Science & Technology B, 25, 1197-1202, (2007).

[84] Chelnokov, A., Wang, K., Rowson, S., Garoche, P. and Lourtioz, J.M., ‘‘Near-infrared Yablonovite-like photonic crystals by focused-ion-beam etching of macroporous silicon’’ Applied Physics Letters, 77, 2943-2945, (2000).

[85] Ay, F., Wörhoff, K., De Ridder, R.M. and Pollnau, M., ‘‘Focused-ion-beam nanostructuring of Al_2O_3 dielectric layers for photonic applications’’. Journal of Micromechanics and Microengineering, 22, 105008, (2012).

[86] De Luca, E., Sanatinia, R., Anand, S. and Swillo, M., ‘‘Focused ion beam milling of gallium phosphide nanostructures for photonic applications’’. Optical Materials Express, 6, 587-596, (2016).

[87] El-Awady, J.A., Woodward, C., Dimiduk, D.M. and Ghoniem, N.M., ‘‘Effects of focused ion beam induced damage on the plasticity of micropillars’’ Physical Review B, 80, 104104, (2009).

[88] Giannuzzi, L.A. Stevie. F.A., ‘‘Introduction to focused ion beams: instrumentation, theory, techniques and practice’’ Springer Science & Business Media (2005).

[89] Yao, N. ed., ‘‘Focused ion beam systems: basics and applications’’ Cambridge University Press, (2007).

[90] Binnig, G., Quate, C.F. and Gerber, C., ‘‘Atomic force microscope’’, Physical Review Letters, 56, 930, (1986).

[91] Hutter, J.L. and Bechhoefer, J., ‘‘Calibration of atomic-force microscope tips’’. Review of Scientific Instruments, 64, 1868-1873, (1993).

[92] Binnig, G., Gerber, C., Stoll, E., Albrecht, T.R. and Quate, C.F., ‘‘Atomic resolution with atomic force microscope’’, EPL, Europhysics Letters, 3, 1281, (1987).

[93] Meyer, G. and Amer, N.M., ‘‘Novel optical approach to atomic force microscopy’’. Applied physics Letters, 53, 1045-1047, (1988).

[94] Zhong, Q., Inniss, D., Kjoller, K. and Elings, V.B., ‘‘Fractured polymer/silica fiber surface studied by tapping mode atomic force microscopy’’. Surface Science Letters, 290, 688-692, (1993).

[95] Tortonese, M., Barrett, R.C. and Quate, C.F., ‘‘Atomic resolution with an atomic force microscope using piezoresistive detection’’. Applied Physics Letters, 62, 834-836, (1993).

[96] Zhong, Q., Inniss, D., Kjoller, K. and Elings, V.B., ‘‘Fractured polymer/silica fiber surface studied by tapping mode atomic force microscopy’’. Surface Science Letters, 290(1-2), L688-L692, (1993).

[97] Yong, Y.K., Moheimani, S.R., Kenton, B.J. and Leang, K.K., ‘‘Invited review article: High-speed flexure-guided nanopositioning: Mechanical design and control issues’’ Review of Scientific Instruments, 83, 121101, (2012).

[98] Yong, Y.K. and Mohemani, S.R., ‘‘A z-scanner design for high-speed scanning probe microscopy’’, IEEE International Conference, 4780-4785, (2012).

[99] Alexander, S.L.O.J.V.P.K.M., Hellemans, L., Marti, O., Schneir, J., Elings, V., Hansma, P.K., Longmire, M. and Gurley, J., ‘‘An atomic-resolution atomic-force microscope implemented using an optical lever’’. Journal of Applied Physics, 65, 164-167, (1989).

[100] Song, T.B., Chen, Q., Zhou, H., Jiang, C., Wang, H.H., Yang, Y.M., Liu, Y., You, J. and Yang, Y., ‘‘Perovskite solar cells: film formation and properties’’. Journal of Materials Chemistry A, 3, 9032-9050, (2015).

[101] Meinhart, C.D. and Wereley, S.T., ‘‘The theory of diffraction-limited resolution in microparticle image velocimetry’’. Measurement Science and Technology, 14, 1047, (2003).

[102] Santiago, J.G., Wereley, S.T., Meinhart, C.D., Beebe, D.J. and Adrian, R.J., ‘‘A particle image velocimetry system for microfluidics’’. Experiments in Fluids, Springer, 25, 316-319, (1998).

[103] Ippolito, S.B., Goldberg, B.B. and Ünlü, M.S., ‘‘High spatial resolution subsurface microscopy’’. Applied Physics Letters, 78, 4071-4073, (2001).

[104] Ippolito, S.B., Goldberg, B.B. and Ünlü, M.S., ‘‘Theoretical analysis of numerical aperture increasing lens microscopy’’. Journal of Applied Physics, 97, 053105, (2005).

[105] Seitz, P. and Theuwissen, A.J. eds., ‘‘’Single-photon imaging’’, Springer Science & Business Media, 160, (2011).

[106] Magnan, P., ‘‘Detection of visible photons in CCD and CMOS: A comparative view’’ Elsevier Science B.V, 504, 199-212. (2003).

[107] Lagoudakis, K., ‘‘The physics of exciton-polariton condensates’’. EPFL Press, (2013).

[108] Collings, N., ‘‘Fourier Optics in Image Processing’’. CRC Press, (2018).

[109] Mignuzzi, S., Mota, M., Coenen, T., Li, Y., Mihai, A.P., Petrov, P.K., Oulton, R.F., Maier, S.A. and Sapienza, R., ‘‘Energy–Momentum Cathodoluminescence Spectroscopy of Dielectric Nanostructures’’. ACS Photonics, 5, 1381-1387, (2018).

[110] Gan, X., Clevenson, H., Tsai, C.C., Li, L. and Englund, D., ‘‘Nanophotonic filters and integrated networks in flexible 2D polymer photonic crystals’’. Scientific Reports, 3, 2145, (2013).

[111] Richard, M., Kasprzak, J., Romestain, R., André, R. and Dang, L.S., ‘‘Spontaneous coherent phase transition of polaritons in CdTe microcavities’’. Physical Review Letters, 94, 187401, (2005).

[112] Jayaprakash, R., Kalaitzakis, F.G., Christmann, G., Tsagaraki, K., Hocevar, M., Gayral, B., Monroy, E. and Pelekanos, N.T., 2017. ‘‘Ultra-low threshold polariton lasing at room temperature in a GaN membrane microcavity with a zero-dimensional trap’’. Scientific Reports, 7, 5542, (2017).

[113] Hwang, C.C., ‘‘Angle-Resolved Photoemission Spectroscopy: Momentum-Space Microscope’’. Applied Microscopy, 45, 115-118, (2015).

[114] Moratal, D., Vallés-Luch, A., Martí-Bonmatí, L. and Brummer, M.E., ‘‘k-Space tutorial: an MRI educational tool for a better understanding of k-space’’. Biomedical Imaging and Intervention Journal, 4, (2008)

[115] Hwang, J.K., Ryu, H.Y. and Lee, Y.H., ‘‘Spontaneous emission rate of an electric dipole in a general microcavity’’. Physical Review B, 60, 4688, (1999).

[116] Suzuki, T. and Paul, K.L., ‘‘Emission power of an electric dipole in the photonic band structure of the fcc lattice’’. JOSA B, 12, 570-582, (1995).

Chapter 4

The optical structure of micropillar microcavities containing a fluorescent conjugated-Polymer

4.1 Introduction

Optical microcavity micropillars containing an organic emitter have attracted a significant interest as a result of their different applications in optoelectronic devices such as light sources for optical communication, quantum computing and quantum information technology. These structures allow a three dimensional confinement of light in small volumes of the order of few wavelengths of the confined light, providing a considerable opportunity to study light-matter interactions and increase the efficiency of controlling the radiative dynamics of single-photon sources [1-11].

In this chapter, light emission from a series of micropillar microcavities containing a thin fluorescent, red-emitting conjugated polymer film in one dimensional micropillar microcavities are investigated. We characterise the photoluminescence emission from the cavities using a Fourier imaging technique and find that emission is quantised into a mode-structure resulting from both vertical and lateral optical confinement within the pillar. We show that optical-confinement effects result in a blue-shift of the fundamental mode as the pillar-diameter is reduced, with a model applied to describe the energy and distribution of the confined optical modes. The results in this chapter have recently been published as Al-Jashaam et al, Advanced Quantum Technologies, 2019, 1900067. Here, the Fourier imaging results were obtained in collaboration with Dr. Rahul Jayaprakash, and the measurement of the quantum efficiency of the Red- F fluorescent conjugated-polymer were obtained by collaboration with Dr Kyriacos Georgiou.

4.2 Micropillar microcavities structure

By defining a pattern into a dielectric material at sub-micron length-scales, it is possible to create a structure that can confine photons within a localised volume and thus act as an optical cavity [12-16]. By depositing a light-emitting semiconductor within such a cavity, it is possible to engineer a range of effects - for example within the so-called 'weak-coupling regime' it is possible to modify the local density of optical states such that the spontaneous emission rate can be modified via the Fermi Golden Rule (Purcell Factor) [17-18]. Such an approach is widely used in a range of advanced photonic devices; for example, planar resonant cavity light emitting diodes are structures in which an active emissive region is placed between two dielectric mirrors forming a 2-dimensional optical cavity [19-23]. The resulting optical confinement can be used to enhance the intensity of emission from the semiconductor within the cavity and also control its emission-colour [24-25].

A higher level of photon confinement can be achieved in so-called micropillar structures. Such structures typically take the form of a 1 dimensional cylinder, in which an emissive material is positioned between two dielectric mirrors as shown in Figure 4.1. Such structures are usually fabricated from a 2D resonant cavity structure that is vertically etched following micro-patterning using electron-beam lithography. Micropillar structures achieve optical confinement both parallel to the pillar axis (by in-phase reflection from the dielectric mirrors) and normal to the pillar axis through total internal reflection due to the large different in refractive index [26]. The high level of sophistication achievable using inorganic semiconductor processing techniques has allowed micropillar structures to be realised having very high quality (Q) factors [27], with recent pillar-structures demonstrated having Q-factors in excess of 250,000 [28]. This strong confinement can be used to realise to engineer enhancements in spontaneous emission rates (the Purcell Factor) [29-31], and thus by placing a single quantum emitter in a micropillar, a device can be created that acts as a source of near indistinguishable single photons [32].

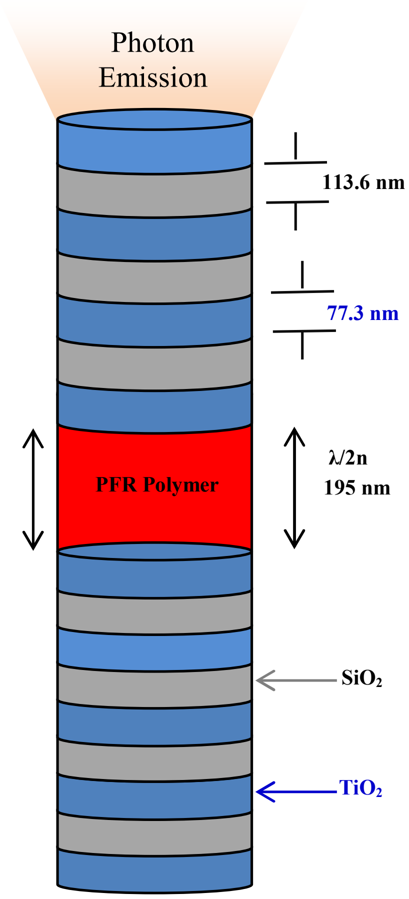

Figure 4.1: Schematic of micropillar cavity. The distributed Bragg reflectors (DBRs) consist of alternating λ/4n-thick layers of dielectric materials with contrasting index of refraction, where λ is the centre of the mirror stop-band. The active layer is a pure spin-cast film of the conjugate polymer PFR. The micropillar geometry shown is etched into the full planar structure after fabrication.

For this reason, micropillar structures and devices are now being explored as practical systems for quantum-cryptography technologies [33,34]. They also allow a range of phenomena to be explored, including strong coupling between single photons and a single quantum-dot [35, 36] and the realisation of low-threshold polariton lasing [37].

In contrast to inorganic semiconductors, organic-semiconductors combine the advantages of strongly-bound excitons having high oscillator strength which survive to room temperature [38], high fluorescence quantum efficiency [39] and ease of processing into thin-film light-emitting devices [40]. There is thus growing interest in the development of micro-pillar structures in which the active material is based on an organic semiconductor. Here, Adawi et al first reported the fabrication of a micropillar microcavity containing a fluorescent molecular dye using an ion-beam etching technique. Using near-field optical imaging techniques, it was shown that such structures were able to modify spontaneous emission rates [41]. Organic micropillars have also previously been fabricated using a thermal imprint technology to pattern a liquid-crystalline molecular dye into pillar shapes on the surface of a dielectric mirror. By coating such structures with a thin film of gold, the hemispherical pillar geometry-cavities created were shown to support several families of quantized optical modes [42]. Other work has used an optical writing technique to selectively change the refractive index of a thin film of a biologically produced fluorescent protein by photobleaching [43]. Such films were then used as the active layer of a micropillar, with lateral photonic confinement leading to a reduction in lasing thresholds compared to an un-patterned control. Further approaches to fabrication of laterally quantised states in organic photonic structures include the use of advanced shadow-masking techniques. [44] Conjugated-polymers operating in the strong-coupling regime have also been engineered into microcavities containing a zero-dimensional Gaussian-defect, fabricated by focussed ion-beam milling [45]. Such structures have been shown to undergo polariton-condensation at high excitation density, and are of interest as analogue quantum simulators.

Depending on the desired emission wavelength, micropillar microcavities designs with different material compositions can be fabricated. For example, single-mode stimulated emission at a wavelength of 510 nm using micropillar microcavity having a diameter of 3.5μm based on II-VI semiconductors was observed by Kruse et al [46]. Additionally, micropillar microcavities emitting in the blue wavelength was achieved by Nathan et al [47]. Moreover, an organic film placed in micropillar microcavities emitting in the red wavelength was achieved by Adawi et al [48]. Such structures have been shown to enhance spontaneous emission rate of organic dyes by a factor of 1.78 times [41].

Here, we have explored the optical structure of a micropillar containing a thin film of a highly fluorescent red-emitting conjugated polymer. Following our previous methodology [41] using a focussed ion beam to directly pattern a planar cavity, we have created a series of micropillar structures characterised by a number of optical modes. We image the luminescence from such structures using a Fourier-technique and use an optical model to provide a comprehensive description of the cavity mode structure. We note that the polymer used in our cavities is typical of many conjugated organic-semiconductors used to create high efficiency light emitting diodes, and thus our work represents a step towards the development of new types of electrically-driven light-sources. Importantly, we believe the techniques used here could be used to create lattices of micropillars in which there is a delocalised band-structure within the plane of the substrate. Such systems are currently receiving significant interest as structures in which there is a unidirectional flow of a polariton wave packet around the edge of the lattice, forming a topological insulator [49].

4.3 Experimental methods

4.3.1 Preparation of the samples

A schematic of the micropillars fabricated is shown in Figure 4.1. To create such structures, a dielectric mirror (Distributed Bragg Reflector [DBR]) consisting of a number of quarter-wave pairs of TiO_2 and SiO_2 (n = 2.135 and 1.452 respectively) was first deposited on a quartz substrate. Here, we used the TiO_2 as it has a high refractive index (> 2.1), lower optical absorption which is ten times less than silicon, small thermal expansion coefficient and a high degree of transparency over the visible spectrum. Such material is also a desirable candidate for photonic crystal engineering [50].

The DBR was designed to have a centre-wavelength of 660 nm to coincide with the peak of the fluorescence of the organic semiconductor. Here, all dielectric films were deposited using electron-beam evaporation from TiO_2 and SiO_2 sources that were placed in graphite crucibles. The growth of the individual layers in the DBR was monitored using a quartz-crystal microbalance (deposition rates maintained at 2 $Ås^{-1}$), with each TiO_2 and SiO_2 layer having a thickness of 77.3 and 113.6 nm respectively. The reflectivity of a DBR consisting of TiO_2 / SiO_2 mirror pairs is shown in Figure 4.2 along with its simulation obtained using a standard transfer matrix model. As is can be seen, the reflectivity stop-band extends from 546 nm to 734 nm, with the maximum mirror reflectivity being around 96% at 660 nm.

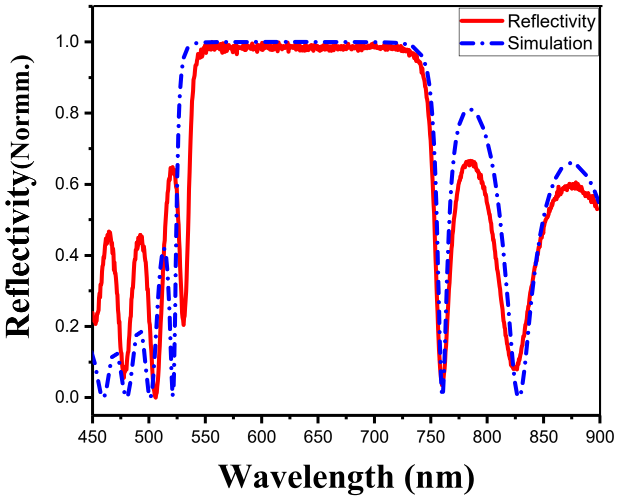

Figure 4.2: Shows the reflectivity spectrum of the bottom DBR with its simulation.

A 195 nm thick film of the polymer PFR was then spin-cast onto this DBR from a dichlorobenzene solvent. PFR was chosen as it has a high fluorescence quantum efficiency of 45%, and emits luminescence that peaks around 660 nm. Figures 4.3(a) and (b) show the chemical structure of PFR and its UV-V is absorbance and fluorescence emission respectively. As it can be seen, the peak of the PFR emission approximately coincides with the centre of the DBR stop-band. A second DBR (8.5 pairs TiO_2 / SiO_2) was then deposited onto the surface of the PFR film, forming a planar microcavity. Transfer matrix modelling indicates that this cavity supports a λ /2 modes around 650 nm, with the cavity having an EM field antinode positioned in the centre of the PFR active layer.

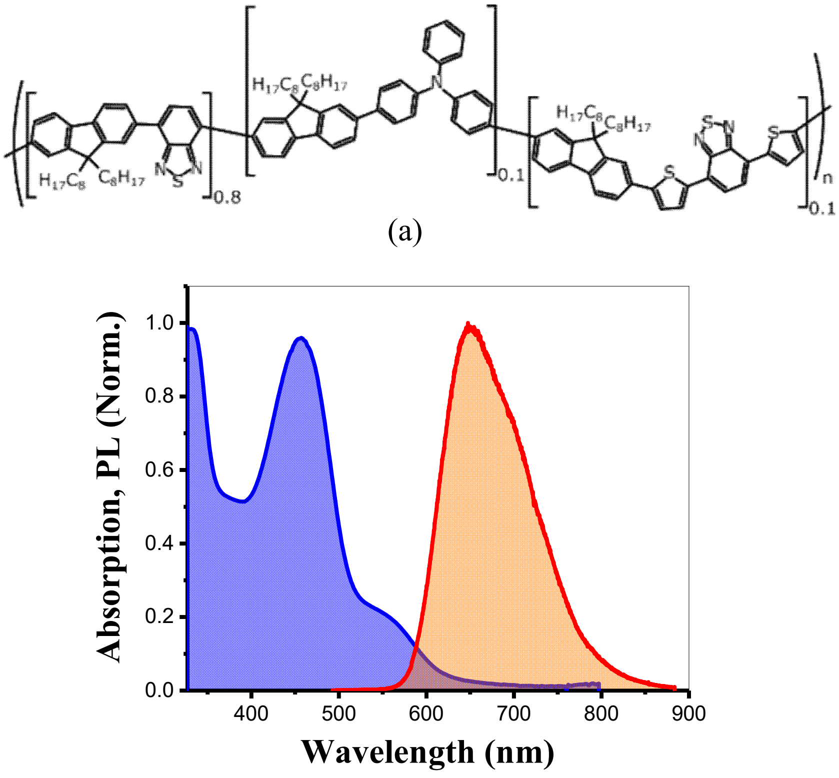

(a)

(b)

Figure 4.3: The conjugated polymer PFR. (a) Chemical structure of PFR and (b) its absorption (blue) and photoluminescence (red) spectra.

Before fabricating the planar cavity into micropillars, we have firstly characterised the optical properties of the un-patterned cavity. This is shown in Figures 4.4 (a) and (b) respectively, where we plot white-light reflectivity and photoluminescence emission (PL) recorded as a function of angle. Here, measurements were made using a goniometer system, which used a series of lenses to deliver or collect light from the cavity surface that were coupled to optical fibres. White light (for reflectivity measurements) was generated using a fibre coupled deuterium halogen lamp, with luminescence generated using light at 405 nm from a Thorlabs continuous wave laser. In all cases, spectral measurements were made using a fibre-coupled Andor Shamrock SR-303i-A triple-grating imaging spectrograph, with a focal length of 0.303m. The spectra were recorded using a 300 grooves / mm grating blazed at 500 nm, where the smallest angle at which white light reflectivity could be measured was 12°, although PL emission could be recorded at all angles including normal incidence.

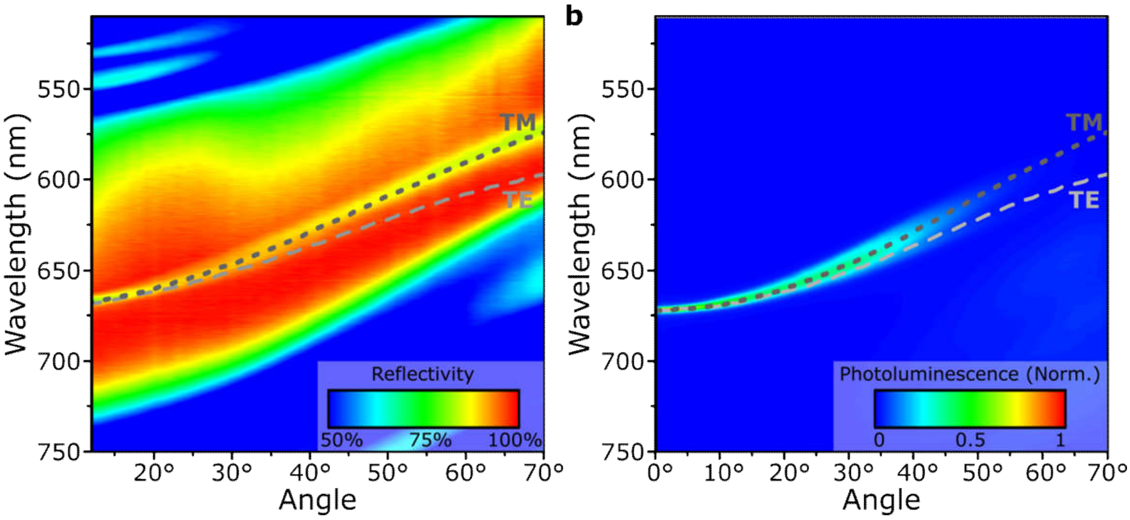

(a) (b)

Figure 4.4: Shows the planar cavity characteristics. (a) Angle-resolved reflectivity of the unpatterned full cavity (DBR-PFR-DBR). The confined cavity mode is evident as a dip in the reflectivity in the centre of the DBR stop-band. (b) Angle-resolved photoluminescence of the un-patterned full cavity. The emission is limited to the spectral range 600-675 nm, constrained by the overlap of the cavity mode with the PFR film emission spectrum. At high angles a slight TE/TM splitting can be observed in both reflectivity and photoluminescence.

It can be seen in Figure 4.4 (a) that the white-light reflectivity is characterised by a broad stop-band onto which a sharp dip is apparent; a feature that corresponds to the cavity mode. This mode has a strong angular dispersion which we can fit using a transfer-matrix model (see dashed line). We find that the PL emission as shown in Figure 4.4 (b) undergoes a similar angular-dependent dispersion, however emission is approximately concentrated over the angular / wavelength range 0 - 50° (675 – 600 nm). This angular / wavelength range is in fact defined by the emission properties of the PFR, which emits PL at wavelengths longer than approximately 575 nm. Interestingly, we observe some splitting of the cavity emission, with this effect observed both in reflectivity and in emission.

We have used such planar cavities to construct micropillar devices. Here, a FEI quanta 200 3D ion-beam lithography system was used to write a series of micropillar structures into the cavity surface as illustrated in Figure 4.5 (a). This was done using a 30 keV beam of Ga ions that was directed to the microcavity surface at normal incidence to write a series of circular trenches of depth 5 μm having diameters between 4 and 11 μm. To avoid charging the surface of the sample during ion-beam writing, the planar microcavity was coated with a 10 nm thin film of gold. This gold film remained on the micropillar surface, with a transfer-matrix model indicating that it slightly attenuated the PL emitted by the structure by around 16%. An SEM image of a typical micropillar (in this case having a diameter of 11 μm) is shown in Figure 4.5(b).

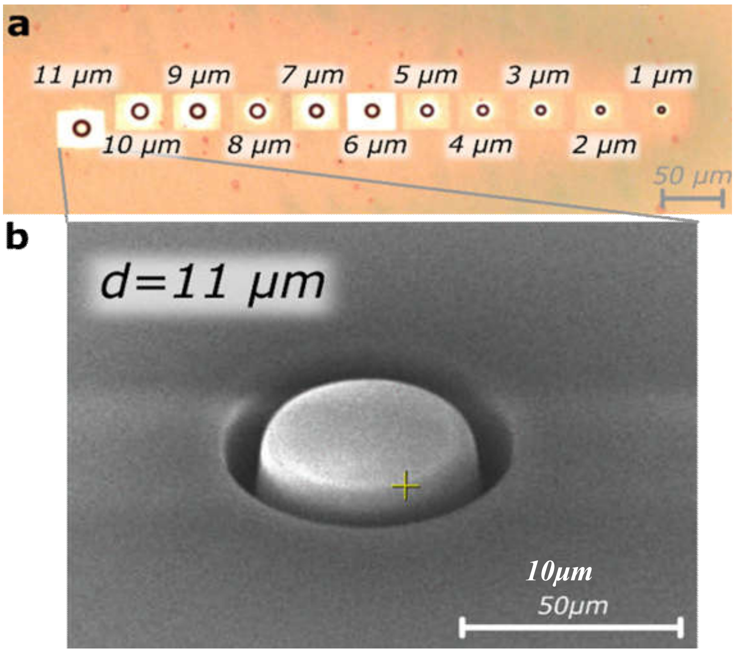

Figure 4.5: Micropillar array. (a) Optical microscope image of micropillars etched out of full planar cavity, with diameters indicated. (b) SEM image of a typical micropillar with 11 µm diameter.

4.3.2 Results and discussion

We have characterised the emission from our cavities using a 405 nm semiconductor laser that was focused onto the sample surface in a spot having diameter of 10 µm. The emitted PL from the micropillars and some of the surrounding un-patterned cavity was collected through a 0.7 NA lens and directed into a 0.25 m nitrogen-cooled charge-coupled device (CCD) spectrometer having a spectral resolution of 0.5 Å, with all measurements performed in air and at room temperature. Here, the use of high NA lens collects all light emitted in a forward cone of ± 44.4°. Photoluminescence emission from an un-patterned region of the cavity is shown in Figure 4.6 (a) together with emission from pillars having a diameter of 4, 6 and 7 µm. When this un-patterned cavity is etched into a micropillar, we find a significant evolution in emission pattern, with emission now characterised by a series of sharp peaks having a typical FWHM linewidth of 1.8 nm. In the figure, it can be seen that this mode undergoes a progressive blue-shift as pillar diameter is reduced as illustrated in Figure 4.7. Here, the planar cavity emission wavelength of 670.9 nm was recorded as shown in the blue straight line. The micropillar microcavity fundamental mode wavelength then decreased as the pillar diameter decrease as shown in the red curved line. We also find that as pillar diameter is reduced from 11 to 4 μm, the spacing between adjacent modes increases, with the fundamental cavity mode undergoing a blue shift of around 5.3 nm.

To gain further insight into the origin of the optical modes observed in the spectra shown in Figure 4.6, we have performed Fourier-space (k-space) imaging of the pillar emission. This technique permits the energy dispersion of emission to be characterised in a single measurement by projecting the Fourier-image of the pillar directly onto the slits of a spectrometer (Andor Shamrock SR-303i-A). This was achieved by placing a Fourier plane imaging lens between the objective (Edmund Optics, NA = 0.6) and the final collection lens. It should be noted that the real-space image has been spatially filtered to extract k-space emission from just the pillar and reject emission from the surrounding un-patterned cavity region. Typical energy-angle dependent photoluminescence dispersion data recorded from an un-patterned cavity region is shown in Figure 4.6 (b), with emission from 4, 6 and 7 μm diameter pillars shown in Figures 4.6 (c), (d) and (e) respectively. We can use the emission dispersion curve of the un-patterned cavity (Figure 4.6 (b)) to determine the cavity Q-factor. Here, we find that the PL emission linewidth at $k = 0$ is 1.3 nm, corresponding to a cavity Q-factor of 520.

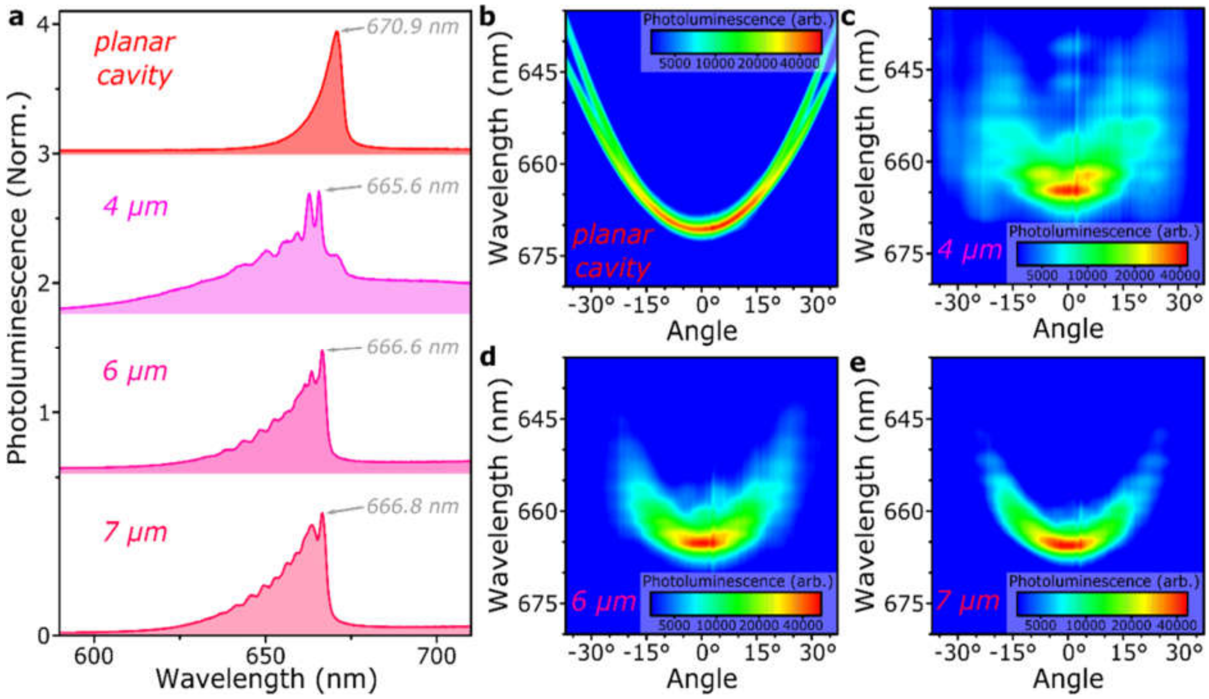

Figure 4.6: Confined micropillar optical modes. (a) Integrated emission from an un-patterned region of the cavity (planar cavity) and three micropillars, revealing significant additional structure due to 1-dimensional confinement. The gradual red-shift of the primary cavity mode with increasing diameter is highlighted. (b) Fourier-space imaging of un-patterned region photoluminescence reveals no structure aside from TE/TM splitting at high angles. Equivalent measurements on (c) 4 µm, (d) 6 µm and (e) 7 µm micropillars reveal finer mode structure. Emission through additional modes is particularly evident in 4 µm micropillars.

On etching the planar cavity into micropillars, it can be seen that the cavity mode dispersion is characterised by a series of optical modes having an approximately parabolic dispersion. As the diameter of the micropillars is reduced, we find that emission is dominated by two discreet modes that are evident between 662 and 665 nm (corresponding to angles 0 to ± 10°), together with a series of modes that are less well defined that exist at higher energy.

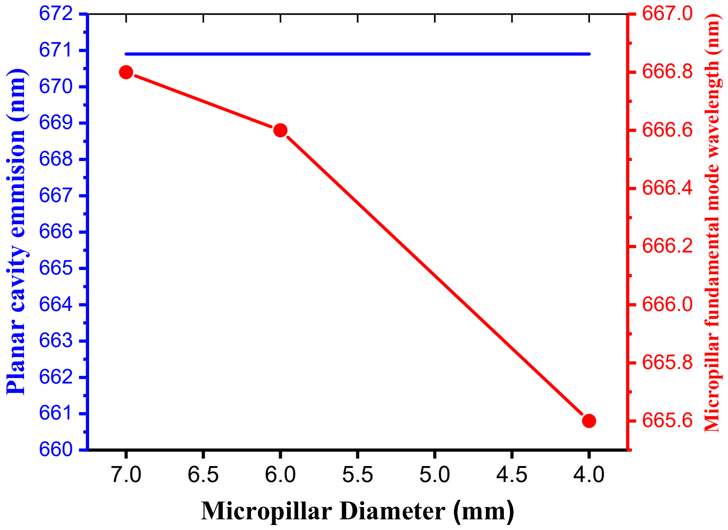

Figure 4.7: Shows the relationship between the cavity fundamental mode wavelengths with micropillar diameter. The blue straight line indicates to the fundamental mode of the planar cavity. The micropillar microcavity fundamental mode wavelength as a function of the pillar diameter is shown in the red curved line.

We have also performed real-space tomographic imaging of the pillar emission using a slight modification of the Fourier-space imaging setup described above. Here an additional lens was placed between the imaging and final collection lenses, forming two telescopes that result in an overall magnification of 113X. By scanning the piezo-controlled final collection lens across the spectrometer slits (x-axis), and by extracting intensity data from pixels along the CCD columns (y-axis) we can precisely map the real-space energy distribution of the emission and thus energetically map the optical mode-structure of the pillars.

A series of real-space tomographic images recorded from a 4 µm pillar at wavelengths corresponding to four distinct modes are shown in Fig. 4.8 (a). From a comparison to the k-space distribution and modelling (see below) we assign these modes as $E_{0,1}$, $E_{1,1}$, $E_{0,2/2,1}$, and $E_{3,1}$. The fundamental mode is centred on the middle of the micropillar, although it is found to be slightly asymmetric. This asymmetry is most likely attributed to a slight ellipticity arising from the FIB etching of the planar cavity; an effect that is also evident in the $E_{1,1}$

mode. By contrast, the higher order modes have larger mode volume and appear less affected by the slight ellipticity of the pillar. We note that the mode labelled $E_{0,2/2,1}$ is in fact a combination of two distinct modes (a four-lobed structure around the pillar perimeter and a single peak in the pillar centre) that are too close in energy to be separately resolved by our system. In the $E_{3,1}$ mode most emission occurs from the perimeter of the pillar and can thus be assigned to a whispering-gallery mode.

To understand the origin of such modes, we have modelled the cavities using Schrödinger's equation for a particle in an infinite circular well, which in the relevant polar coordinates is given by

$$-\frac{\hbar^2}{2\mu}\left(\frac{\delta^2}{\delta r^2}+\frac{1}{r}\frac{\delta}{\delta r}+\frac{1}{r^2}\frac{\delta^2}{\delta\theta^2}\right)\psi(\mathrm{r},\theta)=E\psi(\mathrm{r},\theta) \qquad \text{4-1}$$

Here, $\psi(\mathrm{r},\theta)$ corresponds to the real-space wavefunctions, E to their respective eigenenergies and μ the effective mass of a photon which is ~ $10^{-5}m_o$ (where m_o is the effective mass of an electron). Taking into account appropriate boundary conditions defined by the cavity geometry, equation 4-2 summarises the energy of the various confined optical states within the cavity.

$$E_{(m,n_r)}=\frac{\hbar^2}{2\mu R^2}\left(z_{(m,n_r)}\right)^2 \qquad \text{4-2}$$

Here m is the azimuthal quantum number, n_r is the radial quantum number, R is the radius of the circular well and $z_{(m,n_r)}$ is the n_r-th zero of the regular Bessel function $J_m(z)$. The wavefunction of the various azimuthal and radial modes is then given by

$$\psi_{(m,n_r)}(r,\theta) = N_{(m,n_r)} J_m\left(\frac{z_{(m,n_r)}}{R} r\right) e^{im\theta} \qquad 4\text{-}3$$

where $N_{(m,n_r)}$ is a normalisation factor calculated using

$$2\pi . N^2_{(m,n_r)} \int_0^R J_m^2\left(\frac{z_{(m,n_r)}}{R} r\right) rdr = 1 \qquad 4\text{-}4$$

The wavefunction in Fourier space is then obtained by integrating the wavefunctions in real-space using

$$\psi_{(m,n_r)}(k) = \int \psi_{(m,n_r)}(r,\theta) . \exp\left(i\left(k_x r cos(\theta)\right)\right) . rdrd\theta \qquad 4\text{-}5$$

where k is the wavevector. This yields the following solutions of the circular micropillar.

$$\psi_{(m,n_r)}(k_x) = N_{(m,n_r)} \frac{J_m(k_x R)}{z^2_{(m,n_r)} - k_x R^2} \qquad 4\text{-}6$$

The spatial distribution of the modes calculated using the model is plotted in Fig 4.8 (b). It can be seen that there is an excellent match to the real-space tomographic measurements, both in mode distribution and energetic position. We superimpose the calculated energies of the various modes onto the dispersion data shown in Fig 4.8 (c) and also plot their corresponding Fourier-space distributions in Fig 4.8 (d).

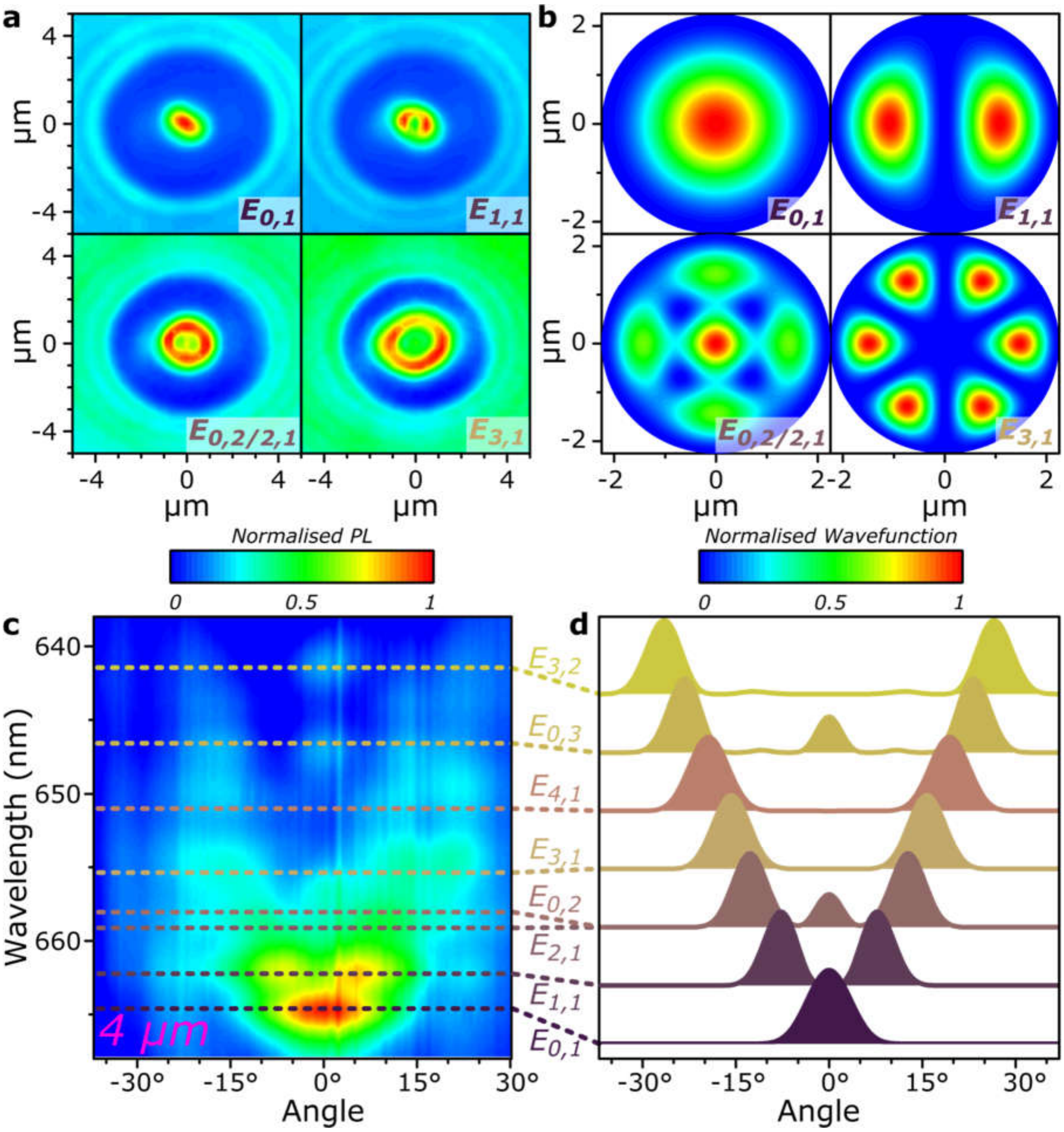

Figure 4.8: Real- and Fourier-space distributions of micropillar modes. (a) Real-space tomographic images of the 4 μm micropillar, measured at 664.8 ± 1 nm ($E_{0,1}$), 662.6 ± 1 nm ($E_{1,1}$), 658.3 ± 1 nm ($E_{0,2/2,1}$) and 654.4 ± 1 nm ($E_{3,1}$). The emission intensity corresponds directly to distribution of the confined optical modes within the pillar. (b) Corresponding calculated real-space distribution of the various confined modes. The micropillar centre is at the origin in parts (a and b. c) Fourier-space image of the 4 μm micropillar, reproduced from Figure 5c. Dashed lines indicate the calculated energy of the various optical modes in the structure (see text for details). It can be seen that emission is dominated by the $E_{0,1}$ and $E_{1,1}$ modes. (d) Calculated Fourier-space distribution of each mode.

It can be seen that the modes that dominate the micropillar emission correspond to modes $E_{0,1}$ and $E_{1,1}$. These modes are predominantly localised within the centre of the pillar, with the emission from modes having higher azimuthal and radial quantum number being relatively weaker in emission intensity. This observation most likely indicates that modes that are closer to the pillar walls are more likely to suffer from scattering-induced loss mechanisms as a result of roughness caused by the focussed-ion beam lithography process.

4.3.3 FDTD modelling

We have also used finite difference time domain (FDTD) simulation method to predict and analyse the emission spectra series of micropillar structures [51-54]. Here, the micropillar structure was explored using a Lumerical FDTD program with the design of the structure shown in Figure 4.9(a). A micropillar microcavity consisting of TiO_2 and SiO_2 stack having a diameter of 4 µm was designed for the simulation process. The thickness of the organic material used in the modelling was then calculated using transfer matrix software as illustrated in Figure 4.9 (b). This program allows the thickness of the organic material to be adjusted to determine the required cavity mode wavelength (660 nm).

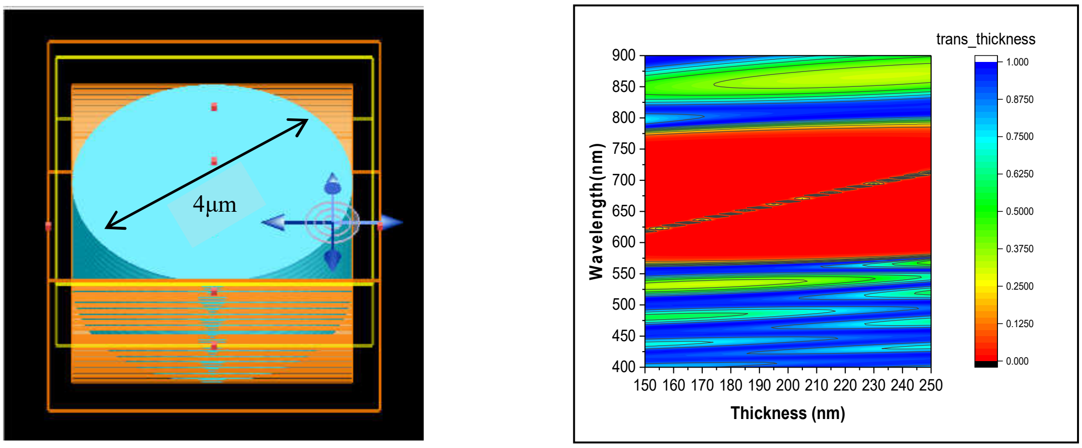

(a) (b)

Figure 4.9: (a) shows a schematic of a micropillar cavity and an organic material was embedded in the centre by using Lumerical FDTD program. (b) The thickness of the used organic material

A source was placed on the micropillar at a placed defined by the arrow place as shown in Figure 4.9 (a). The emission from the micropillar was then recorded using a sensor on the top of the micropillar. The emission was found to be consistent with the results from experiments as shown in Fig. 4.10. Here, in Figure 4.10 (a) the calculation indicates a series of sharp peaks having a fundamental mode of 665 nm, and another sharp peak of 660 nm. To compare these results with the experiments, Figure 4.10 (b) plots far-field emission from a micropillar microcavity designed having a diameter of 4 µm. Here, the structure has a fundamental mode of 665.5 nm, and another sharp peak of 662 nm.

It can be seen that there is a good agreement between the fundamental mode wavelength between the simulation and the experimental measurement. There is however a difference of 2 nm for the second peak between measurement and FDTD simulation. This could be due to errors in the fabrication process.

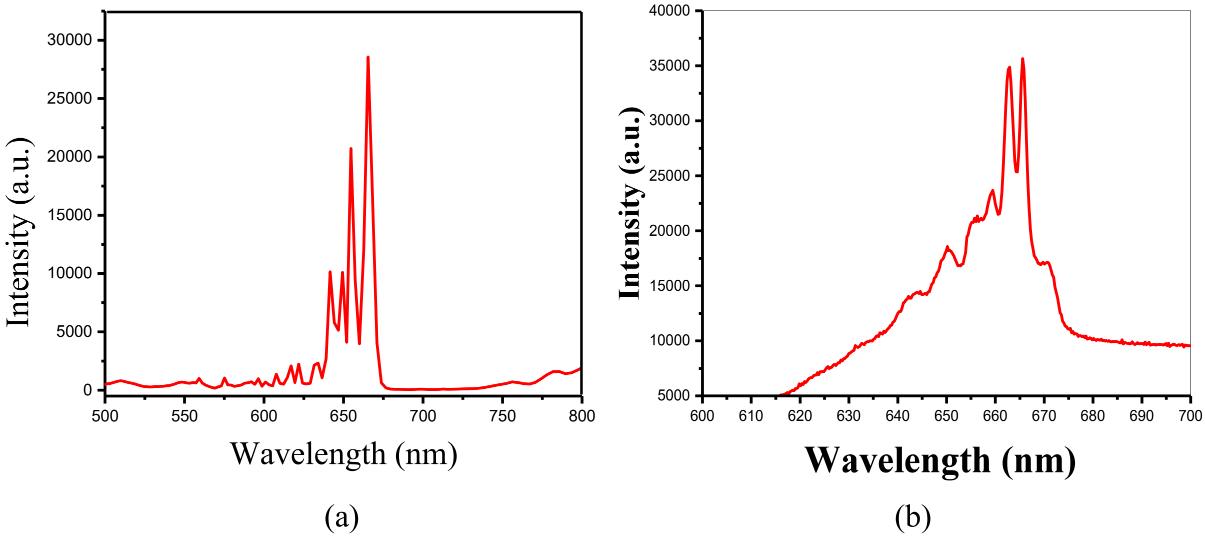

Figure 4.10: Shows the emission spectra from a micropillar with a diameter of 4 µm using (a) Lumerical FDTD program. (b) Experimental measurement.

The series of emission peaks are characteristic fingerprint of Whispering-gallery modes, resulting from closed circular waves trapped by total internal reflection (TIR) inside an axially symmetric dielectric body [55-65]. As a result of this three- dimensional confinement, the optical mode spectrum is split into a set of discrete states as given by [66]

$$E_{n_x,\ n_y} = \sqrt{E_0^2 + \frac{\hbar^2 c^2}{\varepsilon}\left(k^2{}_{x,\ n_x} + k^2{}_{y,\ n_y}\right)} \qquad 4\text{-}7$$

where $E_0 = \hbar\, c\, k_0/\sqrt{\varepsilon}$ is the energy of the un-patterned cavity and k_0 is the corresponding wave vector. In the case of a circular cavity with perfectly reflecting sidewalls, the energies of the optical modes in Figure 4.10 can be expressed

$$E_{n_x,\ n_y} = \sqrt{E_0^2 + \frac{\hbar^2 c^2}{n^2}\left(\frac{x^2{}_{n_{x\theta},\, n_r,}}{R^2}\right)} \qquad 4\text{-}8$$

where E_o here is the energy of the fundamental cavity mode, R is the radius of the pillar and $x_{n_{x\theta},\ n_r,}$ is the n_rth zero of the Bessel function, that describes the separation of the wave equation in cylindrical or polar coordinates as a result of using the function of zero order as a solution to the problem of an oscillating chain suspended at one end [67-72]. Here, Equation 4-8 was used to calculate the energy of the fundamental optical mode $E_{n_x,\ n_y}$ for the micropillar microcavity having a diameter of 4 μm as shown in the appendix A.

4.4 Summary and Conclusion

In summary, we have fabricated micropillar structures that contain a red-fluorescent conjugated polymer. We have characterised the optical mode structure of such pillars using combined white-light reflectance and photoluminescence emission (recorded using both far-field and Fourier-space imaging techniques). Structures having a Q-factor of 520 were deserved in a 4 μm diameter micropillar.

We characterised optical emission properties for such cavities and observed a gradual blue-shift of the energy of all cavity modes as the pillar diameter is reduced. A series of emission peaks deserved are characteristic of whispering gallery mode spectra from micropillars. Optical modelling of the pillar emission on the basis of the Schrödinger equation was also successfully used to describe the distribution of the cavity modes, with modes localised towards the centre of the pillar dominating the emission. A Lumerical FDTD program was used to simulate the experimental results and a good agreement was obtained.

The fabrication of such structures based on the use of focussed ion-beam now presents an exciting opportunity to explore polaritonic effects in micropillars. It has been shown that molecular dyes dispersed into a polymeric matrix undergo strong-coupling and lasing [73] when fabricated into a 2-dimensional (planar) microcavity. It will be interesting to utilise such material systems in a micropillar to explore whether polariton condensation and lasing thresholds can be reduced. Furthermore, organic semiconductors can also be diluted into an inert matrix at low concentration, allowing single chromophore emission to be identified from spatially-separated molecules [74,75]. If such single-chromophore emitting films were placed in a micropillar, it would potentially offer a route to creating high repetition-rate, single-photon light sources that operate at room-temperature. Finally, there are opportunities to study optical-band structure within two-dimensional lattices of such micropillar structures.

References

[1] Stoltz, N.G., Rakher, M., Strauf, S., Badolato, A., Lofgreen, D.D., Petroff, P.M., Coldren, L.A. and Bouwmeester, D., ‘‘High-quality factor optical microcavities using oxide apertured micropillars’’. Applied Physics Letters, 87,031105, (2005).

[2] Jakubczyk, T., Pacuski, W., Duch, P., Godlewski, P., Golnik, A., Kruse, C., Hommel, D. and Gaj, J.A., ‘‘Far field emission of micropillar and planar microcavities lattice-matched to ZnTe’’. Central European Journal of Physics, 9, 428-431, (2011).

[3] Schneider, C., Gold, P., Reitzenstein, S., Hoefling, S. and Kamp, M.,n ‘‘Quantum dot micropillar cavities with quality factors exceeding 250,000’’. Applied Physics B, 122, 19, (2016).

[4] Pyshkin, S. and Ballato, J. eds., ‘‘Optoelectronics: Advanced Device Structures’’. Intech, Croatia, (2017).

[5] Reitzenstein, S., Bazhenov, A., Gorbunov, A., Hofmann, C., Münch, S., Löffler, A., Kamp, M., Reithmaier, J.P., Kulakovskii, V.D. and Forchel, A., ‘‘Lasing in high-Q quantum-dot micropillar cavities’’. Applied Physics Letters, 89, 051107, (2006).

[6] Bennett, A.J., Ellis, D.J.P., Shields, A.J., Atkinson, P., Farrer, I. and Ritchie, D.A., ‘‘Observation of the Purcell effect in high-index-contrast micropillars’’. Applied Physics Letters, 90, 191911, (2007).

[7] Daraei, A., Sanvitto, D., Timpson, J.A., Fox, A.M., Whittaker, D.M., Skolnick, M.S., Guimarães, P.S.S., Vinck, H., Tahraoui, A., Fry, P.W. and Liew, S.L., ‘‘Control of polarization and mode mapping of small volume high Q micropillars’’. Journal of Applied Physics, 102, 043105, (2007).

[8] Stoltz, N.G., Rakher, M., Strauf, S., Badolato, A., Lofgreen, D.D., Petroff, P.M., Coldren, L.A. and Bouwmeester, D., ‘‘High-quality factor optical microcavities using oxide apertured micropillars’’. Applied Physics Letters, 87, 031105, (2005).

[9] Xiao, Y.F. and Gong, Q., ‘‘Optical microcavity: from fundamental physics to functional photonics devices’’. Science Bulletin, 61, 185-186, (2016).

[10] Takada, N., Kamata, T. and Bradley, D.D., ‘‘Polariton emission from polysilane-based organic microcavities’’. Applied Physics Letters, 82, 1812-1814, (2003).

[11] Holmes, R.J. and Forrest, S.R., ‘‘Exciton-photon coupling in organic materials with large intersystem crossing rates and strong excited-state molecular relaxation’’. Physical Review B, 71, 235203, (2005).

[12] Vahala, K.J., ‘‘Optical microcavities’’. Nature, 424, 839, (2003).

[13] Skolnick, M.S., Fisher, T.A. and Whittaker, D.M., ‘‘Strong coupling phenomena in quantum microcavity structures’’. Semiconductor Science and Technology, 13, 645, (1998).

[14] Lidzey, D.G., Bradley, D.D.C., Skolnick, M.S., Virgili, T., Walker, S. and Whittaker, D.M., ‘‘Strong exciton–photon coupling in an organic semiconductor microcavity’’. Nature, 395, 53, (1998).

[15] Dodabalapur, A., Rothberg, L.J., Jordan, R.H., Miller, T.M., Slusher, R.E. and Phillips, J.M., ‘‘Physics and applications of organic microcavity light emitting diodes’’. Journal of Applied Physics, 80, 6954-6964, (1996).

[16] Bajoni, D., ‘‘Polariton lasers. Hybrid light–matter lasers without inversion’’. Journal of Physics D: Applied Physics, 45, 313001, (2012).

[17] Weisbuch, C., Benisty, H. and Houdré, R., ‘‘Overview of fundamentals and applications of electrons, excitons and photons in confined structures’’. Journal of Luminescence, 85, 271-293, (2000).

[18] Barbour, R.J., Dalgarno, P.A., Curran, A., Nowak, K.M., Baker, H.J., Hall, D.R., Stoltz, N.G., Petroff, P.M. and Warburton, R.J., ‘‘A tunable microcavity’’. Journal of Applied Physics, 110, 053107, (2011).

[19] Schubert, E.F., Wang, Y.H., Cho, A.Y., Tu, L.W. and Zydzik, G.J., ‘‘Resonant cavity light-emitting diode’’. Applied Physics Letters, 60, 921-923, (1992).

[20] Shaw, A.J., Bradley, A.L., Donegan, J.F. and Lunney, J.G., ‘‘GaN resonant cavity light-emitting diodes for plastic optical fiber applications’’. IEEE Photonics Technology Letters, 16, 2006-2008, (2004).

[21] Dorsaz, J., Carlin, J.F., Zellweger, C.M., Gradecak, S. and Ilegems, M., ‘‘InGaN/GaN resonant-cavity LED including an AlInN/GaN Bragg mirror’’. Physica Status Solidi (A), 201(12), pp.2675-2678, (2004).

[22] Adawi, A.M., Connolly, L.G., Whittaker, D.M., Lidzey, D.G., Smith, E., Roberts, M., Qureshi, F., Foden, C. and Athanassopoulou, N., ‘‘Improving the light extraction efficiency of red-emitting conjugated polymer light emitting diodes’’. Journal of Applied Physics, 99, 054505, (2006).

[23] Bulović, V., Khalfin, V.B., Gu, G., Burrows, P.E., Garbuzov, D.Z. and Forrest, S.R., ‘‘Weak microcavity effects in organic light-emitting devices’’. Physical Review B, 58, 3730, (1998).

[24] Park, M.J., Kim, G.H., Son, Y.H., Bae, H.W., Kong, J.H. and Kwon, J.H., ‘‘High efficiency red top-emitting micro-cavity organic light emitting diodes’’. Optics Express, 22, 19919-19929, (2014).

[25] Xiang, C., Koo, W., So, F., Sasabe, H. and Kido, J., ‘‘A systematic study on efficiency enhancements in phosphorescent green, red and blue microcavity organic light emitting devices’’. Light: Science & Applications, 2, 74, (2013).

[26] Reitzenstein, S. and Forchel, A., ‘‘Quantum dot micropillars’’. Journal of Physics D: Applied Physics, 43, 033001, (2010).

[27] Reitzenstein, S., Hofmann, C., Gorbunov, A., Strauß, M., Kwon, S.H., Schneider, C., Löffler, A., Höfling, S., Kamp, M. and Forchel, A., ‘‘Al As⁄Ga As micropillar cavities with quality factors exceeding 150.000’’. Applied Physics Letters, 90, 251109, (2007).

[28] Schneider, C., Gold, P., Reitzenstein, S., Hoefling, S. and Kamp, M., ‘‘Quantum dot micropillar cavities with quality factors exceeding 250,000’’. Applied Physics B, 122, 19, (2016).

[29] Gérard, J.M., Sermage, B., Gayral, B., Legrand, B., Costard, E. and Thierry-Mieg, V., ‘‘Enhanced spontaneous emission by quantum boxes in a monolithic optical microcavity’’. Physical Review Letters, 81, 1110, (1998).

[30] Jakubczyk, T., Pacuski, W., Smoleński, T., Golnik, A., Florian, M., Jahnke, F., Kruse, C., Hommel, D. and Kossacki, P., ‘‘Pronounced Purcell enhancement of spontaneous emission in CdTe/ZnTe quantum dots embedded in micropillar cavities’’. Applied Physics Letters, 101, 132105, (2012).

[31] Bayer, M., Reinecke, T.L., Weidner, F., Larionov, A., McDonald, A. and Forchel, A., ‘‘Inhibition and enhancement of the spontaneous emission of quantum dots in structured microresonators’’. Physical review letters, 86(14), p.3168, (2001).

[32] Ding, X., He, Y., Duan, Z.C., Gregersen, N., Chen, M.C., Unsleber, S., Maier, S., Schneider, C., Kamp, M., Höfling, S. and Lu, C.Y., ‘‘On-demand single photons with high extraction efficiency and near-unity indistinguishability from a resonantly driven quantum dot in a micropillar’’. Physical Review Letters, 116, 020401, (2016).

[33] Nowak, A.K., Portalupi, S.L., Giesz, V., Gazzano, O., Dal Savio, C., Braun, P.F., Karrai, K., Arnold, C., Lanco, L., Sagnes, I. and Lemaître, A., ‘‘Deterministic and electrically tunable bright single-photon source’’. Nature Communications, 5, p.3240, (2014).

[34] Böckler, C., Reitzenstein, S., Kistner, C., Debusmann, R., Löffler, A., Kida, T., Höfling, S., Forchel, A., Grenouillet, L., Claudon, J. and Gérard, J.M., ‘‘Electrically driven high-Q quantum dot-micropillar cavities’’. Applied Physics Letters, 92, 091107, (2008).

[35] Reithmaier, J.P., Sęk, G., Löffler, A., Hofmann, C., Kuhn, S., Reitzenstein, S., Keldysh, L.V., Kulakovskii, V.D., Reinecke, T.L. and Forchel, A., ‘‘Strong coupling in a single quantum dot–semiconductor microcavity system’’. Nature, 432, 197, (2004).

[36] Hennessy, K., Badolato, A., Winger, M., Gerace, D., Atatüre, M., Gulde, S., Fält, S., Hu, E.L. and Imamoğlu, A., ‘‘Quantum nature of a strongly coupled single quantum dot–cavity system’’. Nature, 445, 896, (2007).

[37] Bajoni, D., Senellart, P., Wertz, E., Sagnes, I., Miard, A., Lemaître, A. and Bloch, J., ‘‘Polariton laser using single micropillar GaAs− GaAlAs semiconductor cavities’’. Physical Review Letters, 100, 047401, (2008).

[38] Scholes, G.D. and Rumbles, G., ‘‘Excitons in nanoscale systems’’. In Materials For Sustainable Energy: A Collection of Peer-Reviewed Research and Review Articles from Nature Publishing Group, 12-25, (2011).

[39] Kawamura, Y., Goushi, K., Brooks, J., Brown, J.J., Sasabe, H. and Adachi, C., ‘‘100% phosphorescence quantum efficiency of Ir (III) complexes in organic semiconductor films’’. Applied Physics Letters, 86, 071104, (2005).

[40] Khan Z. H. ‘’Nanomaterials and Their Applications’’ Springer, Singapore, (2018).

[41] Adawi, A.M., Cadby, A., Connolly, L.G., Hung, W.C., Dean, R., Tahraoui, A., Fox, A.M., Cullis, A.G., Sanvitto, D., Skolnick, M.S. and Lidzey, D.G., ‘‘Spontaneous emission control in micropillar cavities containing a fluorescent molecular dye’’. Advanced Materials, 18, 742-747, (2006).

[42] Dusel, M., Betzold, S., Brodbeck, S., Herbst, S., Würthner, F., Friedrich, D., Hecht, B., Höfling, S. and Dietrich, C.P., ‘‘Three-dimensional photonic confinement in imprinted liquid crystalline pillar microcavities’’. Applied Physics Letters, 110, 201113, (2017).

[43] Dietrich, C.P., Karl, M., Ohmer, J., Fischer, U., Gather, M.C. and Höfling, S., ‘‘Molding photonic boxes into fluorescent emitters by direct laser writing’’. Advanced Materials, 29, 1605236, (2017).

[44] Langner, M., Gehlhaar, R., Schriever, C., Fröb, H., Lyssenko, V.G. and Leo, K., ‘‘Strong optical confinement and multimode emission of organic photonic dots’’. Applied Physics Letters, 91, 181119, (2007).

[45] Scafirimuto, F., Urbonas, D., Scherf, U., Mahrt, R.F. and Stöferle, T., ‘‘Room-temperature exciton-polariton condensation in a tunable zero-dimensional microcavity’’. ACS Photonics, 5, 85-89, (2017).

[46] Kruse, C., Lohmeyer, H., Sebald, K., Gutowski, J., Hommel, D., Wiersig, J. and Jahnke, F., ‘‘Green laser emission from monolithic II-VI-based pillar microcavities near room temperature’’. Applied Physics Letters, 92, 031101, (2008).

[47] Rex, N.B., Chang, R.K. and Guido, L.J., ‘‘Threshold lowering in GaN micropillar lasers by means of spatially selective optical pumping’’. IEEE Photonics Technology Letters, 13, 1-3, (2001).

[48] Adawi, A.M. and Lidzey, D.G., ‘‘Enhancing the radiative decay rate of fluorescent organic molecules using micropillar microcavities and optical nanocavities. Materials Science and Engineering: B, 149, 266-269, (2008).

[49] Klembt, S., Harder, T.H., Egorov, O.A., Winkler, K., Ge, R., Bandres, M.A., Emmerling, M., Worschech, L., Liew, T.C.H., Segev, M. and Schneider, C., ‘‘Exciton-polariton topological insulator’’. Nature, 562, 552, (2018).

[50] Wang, X., Fujimaki, M. and Awazu, K., ‘‘Photonic crystal structures in titanium dioxide (TiO 2) and their optimal design’’. Optics Express, 13, 1486-1497, (2005).

[51] Cookson, T., Georgiou, K., Zasedatelev, A., Grant, R.T., Virgili, T., Cavazzini, M., Galeotti, F., Clark, C., Berloff, N.G., Lidzey, D.G. and Lagoudakis, P.G., ‘‘A yellow polariton condensate in a dye filled microcavity’’. Advanced Optical Materials, 5, 1700203, (2017).

[52] Lounis, B. and Orrit, M., ‘‘Single-photon sources’’. Reports on Progress in Physics, 68, 1129, (2005).

[53] Lupton, J.M., ‘‘Single-Molecule Spectroscopy for Plastic Electronics: Materials Analysis from the Bottom-Up’’. Advanced Materials, 22, 1689-1721, (2010).

[54] Ilchenko, V.S., Gorodetsky, M.L., Yao, X.S. and Maleki, L., ‘‘Microtorus: a high-finesse microcavity with whispering-gallery modes’’. Optics Letters, 26, 256-258, (2001).

[55] Song, Q., Zhang, N., Zhai, H., Liu, S., Gu, Z., Wang, K., Sun, S., Chen, Z., Li, M. and Xiao, S., ‘‘The combination of high Q factor and chirality in twin cavities and microcavity chain’’. Scientific Reports, 4, 6493, (2014).

[56] Astratov, V.N., Yang, S., Lam, S., Jones, B.D., Sanvitto, D., Whittaker, D.M., Fox, A.M., Skolnick, M.S., Tahraoui, A., Fry, P.W. and Hopkinson, M., ‘‘Whispering gallery resonances in semiconductor micropillars’’. Applied Physics Letters, 91, 071115, (2007).

[57] Nowicki-Bringuier, Y.R., Claudon, J., Böckler, C., Reitzenstein, S., Kamp, M., Morand, A., Forchel, A. and Gérard, J.M., ‘‘High Q whispering gallery modes in GaAs/AlAs pillar microcavities’’. Optics Express, 15, 17291-17304, (2007).

[58] Boriskina, S.V., Benson, T.M., Sewell, P. and Nosich, A.I., ‘‘Spectral shift and Q change of circular and square-shaped optical microcavity modes due to periodic sidewall surface roughness’’. JOSA B, 21, 792-1796, (2004).

[59] Teraoka, I. and Arnold, S., ‘‘Theory of resonance shifts in TE and TM whispering gallery modes by nonradial perturbations for sensing applications’’. JOSA B, 23, 1381-1389, (2006).

[60] Schunk, G., Fürst, J.U., Förtsch, M., Strekalov, D.V., Vogl, U., Sedlmeir, F., Schwefel, H.G., Leuchs, G. and Marquardt, C., ''Identifying modes of large whispering-gallery mode resonators from the spectrum and emission pattern''. Optics Express, 22, 30795-30806, (2014).

[61] Jones, B.D., Oxborrow, M., Astratov, V.N., Hopkinson, M., Tahraoui, A., Skolnick, M.S. and Fox, A.M., ''Splitting and lasing of whispering gallery modes in quantum dot micropillars''. Optics Express, 18, 22578-22592, (2010).

[62] Cao, H. and Wiersig, J., ''Dielectric microcavities: Model systems for wave chaos and non-Hermitian physics''. Reviews of Modern Physics, 87, 61, (2015).

[63] Foreman, M.R., Swaim, J.D. and Vollmer, F., ''Whispering gallery mode sensors''. Advances in Optics and Photonics, 7, 168-240, (2015).

[64] Song, Q., Zhang, N., Zhai, H., Liu, S., Gu, Z., Wang, K., Sun, S., Chen, Z., Li, M. and Xiao, S., ''The combination of high Q factor and chirality in twin cavities and microcavity chain''. Scientific Reports, 4, 6493, (2014).

[65] Gutbrod, T., Bayer, M., Forchel, A., Reithmaier, J.P., Reinecke, T.L., Rudin, S. and Knipp, P.A., ''Weak and strong coupling of photons and excitons in photonic dots''. Physical Review B, 57, 9950, (1998).

[66] Andrews L.C. ''Special Functions of Mathematics for Engineers'' Second edition, Oxford University Press, UK. The Aeronautical Journal, 102, 438-438, (1998).

[67] Liu, S., Wei, Y., Su, R., Su, R., Ma, B., Chen, Z., Ni, H., Niu, Z., Yu, Y., Wei, Y. and Wang, X. ''A deterministic quantum dot micropillar single photon source with> 65% extraction efficiency based on fluorescence imaging method''. Scientific Reports, 7, 13986, (2017).

[68] Idris A. F, Buhari L. A. and Adamu U. T ''Bessel Functions and Their Applications: Solution to Schrödinger equation in a cylindrical function of the second kind and Hankel Functions'' International Journal of Novel Research in Physics Chemistry & Mathematics, 3, 17-31, (2016).

[69] Kalevich, V.K., Afanasiev, M.M., Lukoshkin, V.A., Solnyshkov, D.D., Malpuech, G., Kavokin, K.V., Tsintzos, S.I., Hatzopoulos, Z., Savvidis, P.G. and Kavokin, A.V., ''Controllable structuring of exciton-polariton condensates in cylindrical pillar microcavities''. Physical Review B, 91, 045305, (2015).

[70] Niegemann, J., Pernice, W. and Busch, K., ''Simulation of optical resonators using DGTD and FDTD''. Journal of Optics A: Pure and Applied Optics, 11, 114015, (2009).

[71] Niedziela, J., ''Bessel Functions and Their Applications''. University of Tennessee-Knoxville, (2008).

[72] Cho, D.H., Shin, J.W., Joo, C.W., Lee, J., Park, S.K., Moon, J., Cho, N.S., Chu, H.Y. and Lee, J.I., ‘‘Light diffusing effects of nano and micro-structures on OLED with microcavity’’. Optics Express, 22, 1507-1518, (2014).

[73] Sebald, K., Seyfried, M., Klembt, S. and Kruse, C. ‘‘Optical properties of photonic molecules and elliptical pillars made of ZnSe-based microcavities’’. Optics Express, 19, 19422-19429, (2011).

[74] Hagness, S.C., Rafizadeh, D., Ho, S.T. and Taflove, A., ‘‘FDTD microcavity simulations: design and experimental realization of waveguide-coupled single-mode ring and whispering-gallery-mode disk resonators’’. Journal of Lightwave Technology, 15, 2154-2165, (1997).

[75] Liu, Y.C. and Byrnes, T., ‘‘FDTD and transfer matrix methods for evaluating the performance of photonic crystal based microcavities for exciton-polaritons’’. Semiconductor Science and Technology, 31, 115019, (2016).

Chapter 5
The optical properties of L3 Silicon Nitride photonic crystal nanocavities

5.1 Introduction

The Study of optical nanocavities based on photonic crystal slabs (PCSs) has received high attention as a result of possible optoelectronic device applications such as optical sensing, enhancement of spontaneous emission, low-threshold lasers and optical switching [1-5]. Two dimensional (2D) photonic crystals (PC) having dimensions of the order of the cubic wavelengths defined into thin periodic optical structures of dielectric semiconductors can also control light propagation at the nanoscale [6-16].

By deliberately introducing a physical defect into a 2D photonic crystal, an optical nanocavity can be formed where light can be effectively confined. Such structures can act as nanocavities with high quality factors (Q) and very small modal volumes (V) with the resultant high Q/V values resulting in an enhancement of the radiative rates of emissive emitters placed on the surface of the cavity by means of the Purcell effect [17-20].

The majority of ongoing work in this field has focused on PCs structures having high refractive index based on III-V semiconductors such as GaAs and silicon that emit in the near infrared (NIR) [21]. Organic materials such as PMMA, polystyrene are transparent at the visible wavelength and are of interest for material for nanocavity applications. However, they cannot strong confine of the light as a result of their low refractive index which leads to high optical losses and thus low quality factor nanocavities [22].

Consequently, to create a two dimensional nanocavity working at visible wavelengths requires the use of a high refractive index material that is transparent at the visible wavelengths.

Gallium nitride (GaN), AlN, InGaAlP, diamond and TiO_2 are materials that have been used to design photonic crystals that emit at violet-green and red wavelengths respectively. Such materials have some disadvantage as nanocavities require the fabrication of a high-quality periodic structure with a lattice constant between 100 and 200nm and these materials can have rough surfaces, poor structural properties and are difficulty to pattern. However, silicon nitride has been utilized for nanocavity application as a result of its emission at yellow to red wavelengths at room temperature [23].

To create a high quality factor nanocavity, Adawi et al were the first authors to use a hybrid structure that combined a semiconductor having a high refractive index that is transparent at visible region with an organic material having a high photoluminescence quantum efficiency that was deposited onto the nanocavity structure using either a spin casting or a thermal evaporation technique [24].

In this chapter, SiN membranes are used as a thin dielectric slab to create a PC nanocavity that emits light at visible wavelengths. Here, the optical properties of two dimensional photonic crystal nanocavities are explored with hole size, lattice constant and hole shift being varied to improve cavity quality factor. A cavity with quality factor up to 1100 was obtained as a result of modifying the size and location of the air holes around the nanocavity; a value that is 6 times higher in comparison with an unmodified structure. Finally, the optical properties of the nanocavities in SiN membranes coated with an organic emitter are explored using fluorescence spectroscopy.

5.2 Silicon Nitride photonic crystals

Silicon nitride (Si_3N_4) is a wide-band gap semiconductor that has been used to fabricate photonic crystals having band gaps in the wavelength range between 500 nm and 875 nm [25].

Si_3N_4 is a polymorphic dielectric material composed of silicon and nitrogen having refractive index of ($n \approx 2.1$). It is transparent at visible wavelengths with the bonds that bind silicon to nitrogen being about 70% covalent and 30% ionic [26-27]. Thin films of silicon nitride, silicon oxynitride SiO_xN_y and silicon-on-insulator (SOI) are widely used in integrated circuit technology and electronic device applications [28-29].

The wide use of Si_3N_4 comes from its useful properties including high refractive index and compatibility with standard technology of complementary metal oxide semiconductor (CMOS). Furthermore, scattering and two-photon absorption (TPA) close to infrared wavelengths is low. Si_3N_4 has also been explored for bio-sensing applications at visible and near-infrared wavelengths due to its low thermal loss and weak sensitivity to thermal changes [30-31].

Si_3N_4 also has favourable mechanical properties such as high strength, high hardness, chemical corrosion resistance and a high chemical stability [32-37]. This is useful properties as it allows established etching processes to be used with designs being easy to transfer from the e-resist to the SiN membrane [10-24-38]. However, it is weakly luminescent [39] with broad PL emission that peaks around 600 nm with a full width at half maximum (FWHM) of 200 nm as illustrated in Figure 5.1 (a). The broad emission has been attributed to quantum confined emission from silicon nanocrystals in the SiN structures or emission from defects and interface states. Figure 5.1(b) shows the basic building unit of Si_3N_4 which is a silicon-nitrogen tetrahedron, in which Si is bonded to four N atoms.

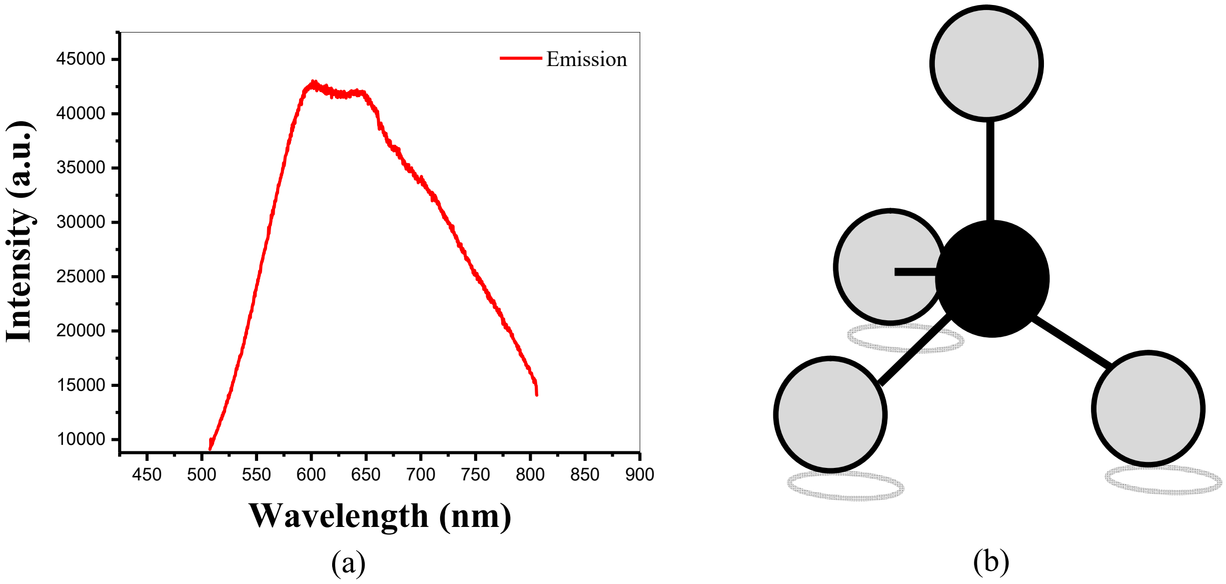

(a) (b)

Figure 5.1: Shows (a) the photoluminescence (PL) emission of SiN, (b) a basic tetrahedral unit in Si_3N_4 [27].

Confinement of light in a two dimensional photonic crystal nanocavity occurs through both total internal reflection (TIR) at the membrane – air interfaces and horizontally as a result of the photonic band gap created by differences in the refractive index of air holes and patterned dielectric [40-42].

The quality factor of such structure is determined through radiation losses from the nanocavity surface as illustrated by equations 5-1 and 5-2,

$$\frac{1}{Q_{\text{experimental}}} = \frac{1}{Q_{theoretical}} + \frac{1}{Q_{imperfections}} \tag{5-1}$$

$$\frac{1}{Q_{imperfections}} = \frac{1}{Q_{scattering\ loss}} + \frac{1}{Q_{absorption\ loss}} \tag{5-2}$$

Generally, differences between experimental and theoretical values of the Q factor result from imperfections in the fabrication of the nanocavities. There are two types of losses; the first is scattering loss resulting from structural imperfections in the air holes, which can be reduced by modifying the design of the air holes. The second process is absorption loss that can be reduced using materials having relatively a high refractive index [43]. Equation 5-3 shows the relation between absorption coefficient of the materials and the cavity Q factor.

$$Q = \frac{2\pi n_o}{\alpha\lambda} \qquad \text{5-3}$$

where n_o, α and λ are the refractive index, the absorption coefficient of the material, and the resonant wavelength of the cavity respectively [42-44].

Netti et al have experimentally shown the existence of a complete PBG in a SiN based photonic crystal waveguide using a broadband waveguide characterization [45]. A high quality factor up to 45,000 was obtained experimentally by Akahane et al using *L*3 (three missing air holes) defect that was the first type of photonic crystal nanocavity. A number of attempts have been reported on the fabrication and characterisation of S_3iN_4 photonic crystal nanocavities [46]. Makarova et al studied the emission properties of Si-rich S_3iN_4 photonic crystal membranes. They demonstrated optical modes between 600-800 nm in a *L*3 nanocavity structure, reporting Q-factors in the range of 200-300 that resulted in a seven times enhancement of the photoluminescence intensity [47]. Adawi et al in later used a guided mode expansion method to demonstrate that full band-gap exists in non-modified L3 nanocavities having a refractive index as low as 1.6. They predicted that the quality factor in such structures increases in a super-linear fashion with the refractive index of the photonic crystal membrane. However, by shifting the nanocavity side holes, the cavity quality factor should improve by a factor of three times for cavities based on a dielectric with n=2.45, and by a factor of 10 times for n = 3.4 as illustrated in Figure 5.2 [48].

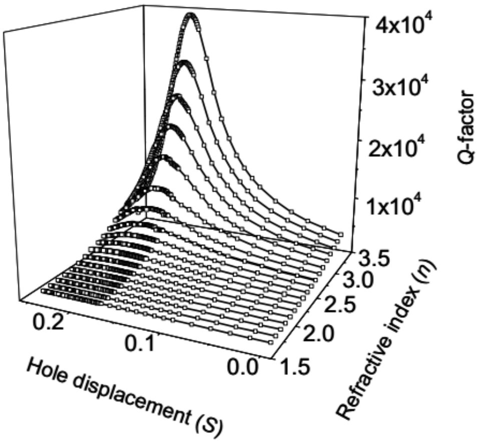

Figure 5.2: The Q-factor of a three missing air hole nanocavity as a function of the outside hole displacement S, and refractive index n. This Figure was taken from ref [48].

Adawi et al later reported an *L*3 nanocavity photonic crystal based on a free standing silicon nitride (SiN) membrane that was coated with a thin-film of a fluorescent molecular-dye having a quality factor of 2650 [49].

5.3 The thickness of a Silicon Nitride membrane

The dielectric slab thickness used to create a nanocavity has a high influence on the position and the size of the photonic band gap. If the slab thickness is too thick, higher order modes can be supported with little cost in energy. Therefore, such modes will take a position slightly overhead the lowest-order mode to prohibit the formation of an energy gap. If the thickness of the slab is around one wavelength or more, some energy cost is required to produce higher-order modes [50-52]. However, such modes cannot be supported by the slab if its thickness is less than half a wavelength [53].

The optimum slab thickness (*h*) has been estimated by Johnson et al is expressed using equation 5-4

$$slab\ thickness\ h \approx \frac{1}{2\omega_{gap-bottom}\sqrt{\varepsilon}} \qquad 5\text{-}4$$

Here, the slab thickness h is in units of a (the lattice constant) and $\omega_{\mathrm{gap-bottom}}$ is the angular frequency expressed in units of (a/c) where c is the speed of light and ε is the effective dielectric constant. The impact of slab thickness on the photonic band gap in a Si_3N_4 was investigated by Pisanello et al. They observed that a PBG existed for t = 0.7a which then vanished when the slab thickness was increased to 1.55a [54]. In a two dimensional photonic crystal, it is necessary to use a S_3iN_4 membrane thickness in which the reflectivity is high at a wavelength coinciding to the required photonic band gap wavelength. Here, the reflectivity of a 200 nm SiN membrane thickness was calculated using the complex matrix form that depending on Fresnel equations [55]. Figure 5.3 illustrates the membrane reflectivity as a function of wavelength; here it can be seen that reflectivity spectrum covers a broad range of the visible spectrum (425 nm to 775 nm) and peaks 540 nm.

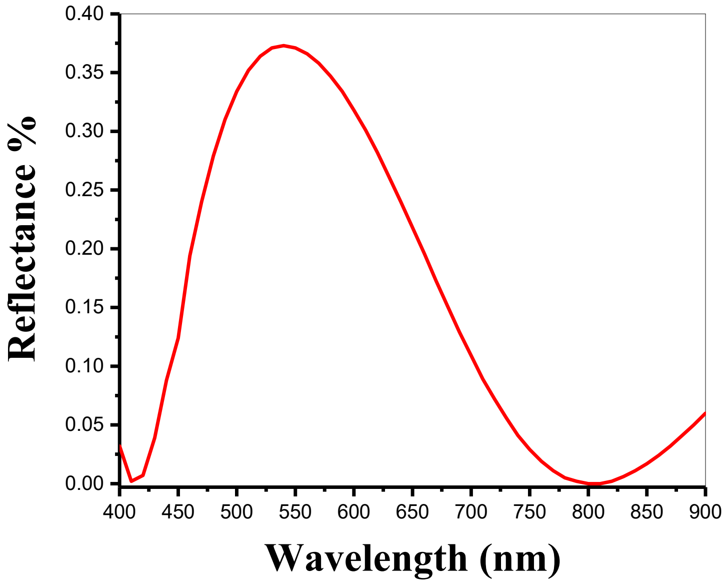

Figure 5.3: The reflectance of a 200 nm thick of SiN membrane.

5.4 Fabrication of an *L*3 Two Dimensional SiN based Photonic Crystal Nanocavity

Two dimensional photonic crystal nanocavities of the type *L*n, where n is the number of missing holes, have attracted high attention because of their applications in various fields such as low threshold nano-lasers and single-photon emitters for quantum communication [53-56].

The structure explored in this chapter is termed an *L*3 (three missing holes) nanocavity designed in a hexagonal 2D photonic crystal membrane. This form of cavity was first explored by Akahane et al [46]. The cavity was defined in a Si PC membrane, with the side holes on the long x- axis of the cavity being shifted out from the centre by an amount S, with S being some fraction of the lattice constant (a). Chalcraft et al illustrated that such structures can support a multitude of optical modes, with the longest wavelength mode being the fundamental mode, together with a number of additional modes having a shorter wavelengths [57-58].

L3 nanocavity structures have been extensively studied due to their small mode volume, high Q- factor and large spectral separation between the fundamental cavity mode and the other higher order modes. Indeed, a Q-factor up to one million was achieved by Pirotta et al using a L3 photonic crystal nanocavity based on a Si membrane having a thickness of 220 nm. Here, a group of five holes at both sides of the cavity were shifted to optimize cavity quality factor [59].

In this chapter, I investigate the effect of a shift in the position of the edge- side holes along the long x- axis of the cavity on the mode wavelength and cavity Q-factor which is effective used to reduce the leaky components, thereby maintaining the small V of a cavity. A schematic diagram of the structure explored is shown in Figure 5.4. Here, the nanocavity is located at the centre of a photonic crystal that was etched into a SiN membrane having a thickness (*d*) of 200 nm, a refractive index (n) of 2.1, lattice constant (a) of 260 nm, hole radius (*r*) of 78 nm, with the hole structure having a lateral size of (31×16√3)a . Here, it is necessary that the size of the PC should not be smaller than (28×14√3)a, as in-plane losses increase due to weaker lateral confinement [60]. However, in-plane losses could be reduced by increasing the number of the air holes around the nanocavity [61]. Furthermore, the energy losses by out plane losses due to a weakly total internal reflection are fundamentally determined as a result of the leaky modes (see Figure 2.8). The L3 nanocavity PC design need to be modified to obtain a Gaussian field distribution of nanocavity's resonant mode that result in increasing the vertical confinement of cavity mode to reduce the out-of-plane losses [62].

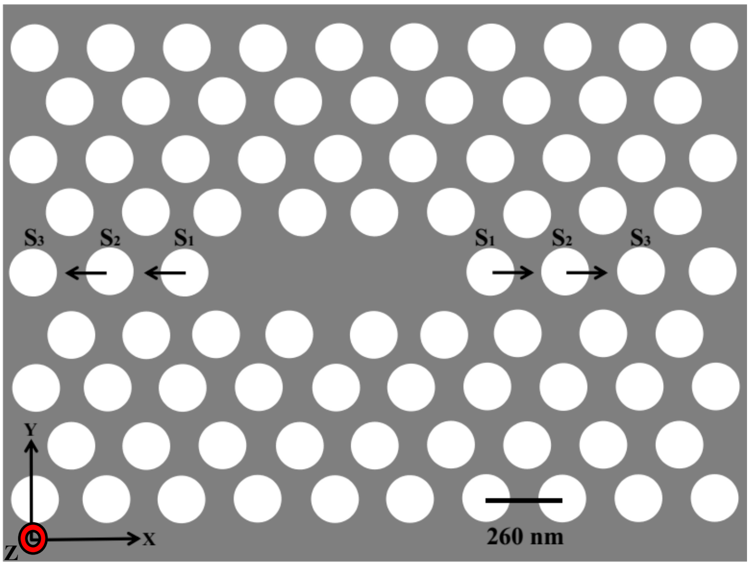

Figure 5.4: A schematic diagram of the L3 nanocavity PC having a hexagonal lattice of air holes of lattice constant a = 260 nm, radius r = 78 nm, slab thickness is *d* = 200nm and S is the cavity side hole shift.

5.5 *L*3 2D PC nanocavity modes using FDTD

To design photonic crystal nanocavities, a FDTD-program was used comprising of four essential parts: first, boundary conditions are defined. Secondly, the main algorithm calculates the electromagnetic field over time and points in space. Thirdly, a source term is included in the structure. Finally, the data is extracted.

Such FDTD calculations have been applied to the structure shown in Figure 5.4. The model indicate that an unmodified nanocavity (S=0) can support five confined modes that exist at visible wavelengths over the range 1.87eV to 2 eV which fall within the band gap as illustrated in Figure 5.5 (a). This result corresponds to the other calculations also obtained using FDTD [63], a plane wave expansion (PWE) [64] and a guided mode expansion method (GME) [65]. Here, the fundamental mode M1 is spectrally separated from higher order modes and possesses the highest Q-factor of 825 compared with the other modes M2, M3, M4, and M5 [66,67]. A similar calculation was applied to *L*4 nanocavity as shown in Figure 5.5(b). This structure can also support a number of confined modes existing at visible wavelengths over the spectral range between 1.8eV to 2.006 eV. However, in the *L*4 cavity, the fundamental mode appears to be more weakly confined and red shifted as a result of the increased cavity length.

Figure 5.6 shows a calculation of the field distribution (E^2) for the fundamental mode in an *L*3 cavity for the field components (E_x and E_y). This can be used to understand the polarization characteristics of the fundamental mode and the other modes in terms of the symmetric (even) and anti-symmetric (odd) electric field lobes around the x and y axes [68].

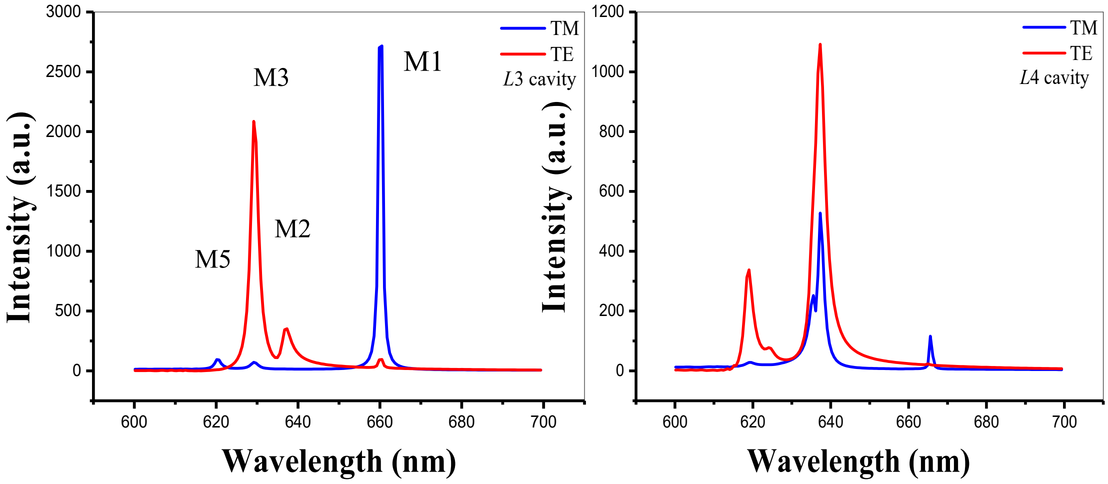

Figure 5.5: Demonstrates results of a FDTD calculation that indicate multimode emission from an unmodified (S=0) (a) L3 nanocavity and (b) L4 nanocavity having a lattice constant a = 260 nm and hole radius r = 78 nm. The slab thickness is t = 200 nm. Here M1 indicates the fundamental mode.

For instance, the E_x component of the fundamental mode undergoes destructive interference as a result of anti-symmetric lobes around the x and y axis, leading to a reduction in intensity in the far –field (i.e. z>>0). However, for the E_y component, M1 undergoes constructive interference as a result of the symmetric lobes around the x and y axis, thus has stronger amplitude for (z>>0) [69-70].

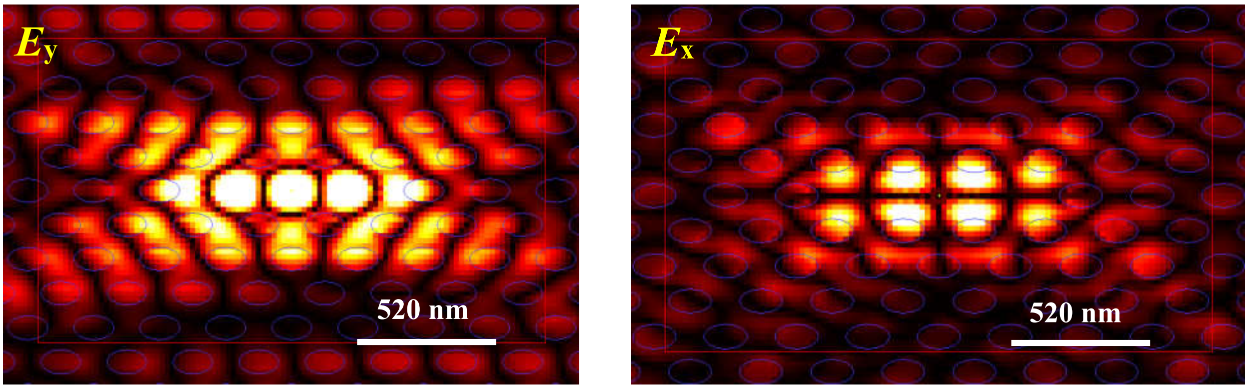

(a) (b)

Figure 5.6: Demonstrates a FDTD calculation of unmodified L3 nanocavity field distribution of the fundamental mode M1 (a) for the E_y component (b) for the Ex component respectively.

The fundamental mode and Q- factor of the nanocavities can be tuned by adjusting four parameters; lattice constant, hole size, edge-hole position and the number of shifted edge-holes. The quality factor of the photonic nanocavity can be affected by varying these parameters as shown in Figure 5.7 as revealed using FDTD modelling depending on the nanocavity design shown in Figure 5.4.

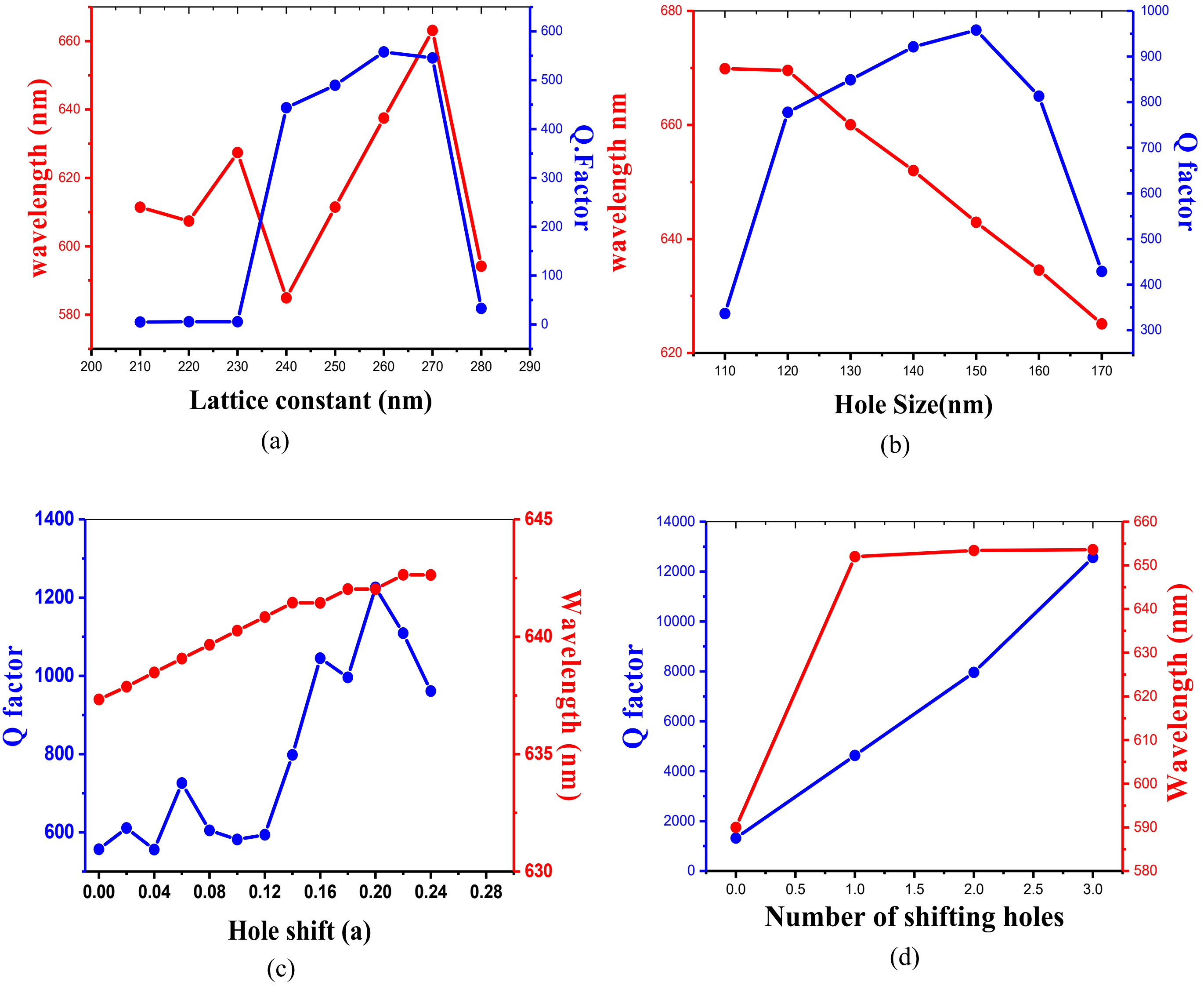

(a)

(b)

(c)

(d)

Figure 5.7: Shows the impact of (a) changing lattice constant (b) hole size (c) hole displacement and (d) the number of shifting holes on the Q. factor and the peak of the fundamental mode.

It was found that a maximum quality factor of 550 could be obtained for a lattice constant of a= 260 nm at a wavelength in the red end of the spectrum as shown in Figure 5.7(a). The influence of the hole size on the Q factor was explored as shown in Figure 5.7(b). Here the modelling shows that a best Q-factor of 927 could be obtained for a hole size of 150 nm. However, the model shows that the wavelength of the fundamental mode tends to a blue shift as a result of increasing hole size. The effect of edge hole shift on the value of the Q factor was studied as shown in Figure 5.7(c). Here, the model shows that the Q factor increased significantly when the cavity edge holes are shifted by S_1= 0.20a in the opposite direction, where a is the lattice constant. Finally, effect of number of shifting holes on of Q factor is shown in Figure 5.7 (d). Here, it can be seen that if three edge holes (S_1, S_2 and S_3) are shifted in opposite direction, a Q factor of 12,565 can be obtained.

According to these calculations, cavity quality factor can be increased by modifying the structure that surrounds the cavity, with Q factor increasing by a factor of 2 as a result of increasing one edge hole shift and by factor of 12 times as result of a three hole shift. Here, such increases in Q factor results from reduced vertical losses because of decreases the leaky regions, with shifted side holes resulting in a smooth decay of the electric field in the surrounding PC structure as shown schematically in Figure 5.8 [71].

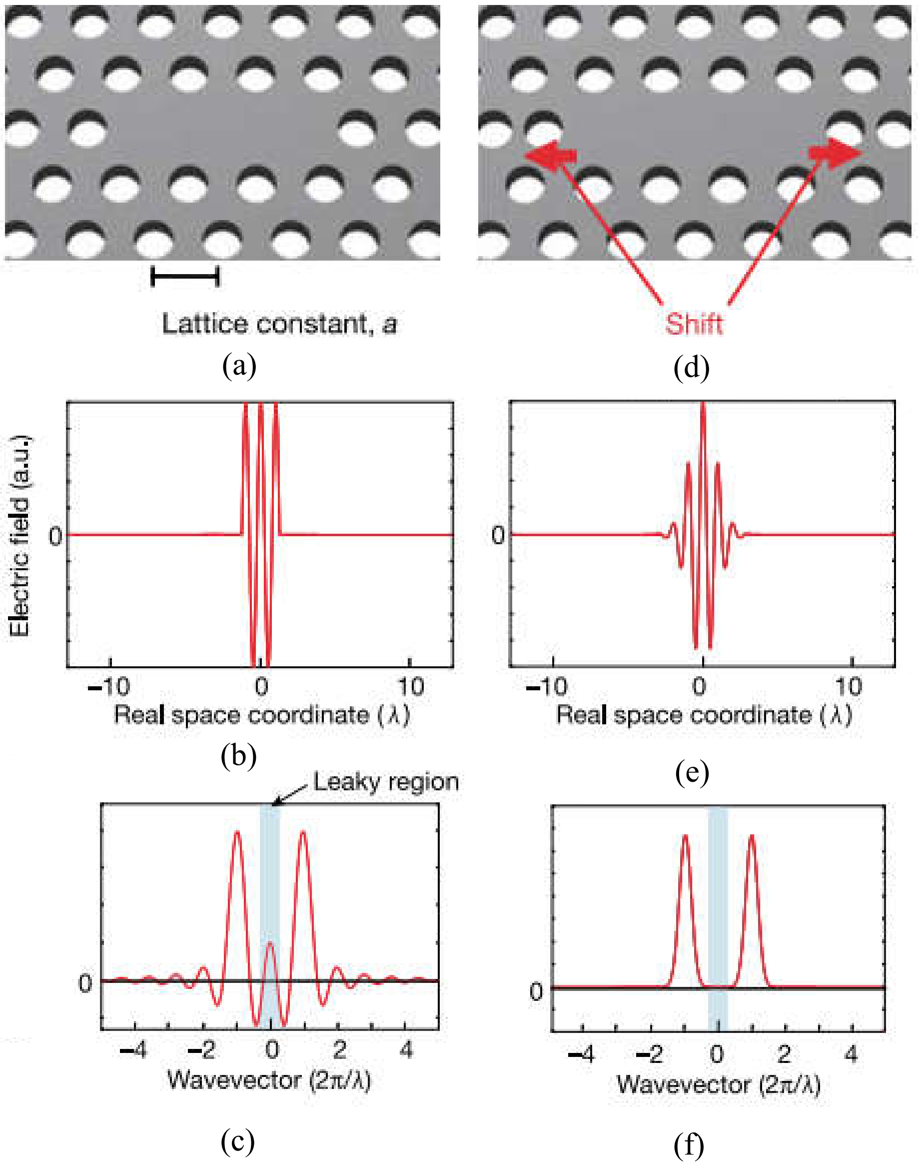

Figure 5.8: Shows (a) A non-modified *L*3 nanocavity structure. (b) and (c) An electric field profile of the fundamental mode inside the nanocavity and the spatial Fourier transform (FT) spectra respectively. It can be seen the leaky region is pointed as a blue area. (d) A modified *L*3 nanocavity structure with $S = 0.15a$. (e) and (f) An electric field profile of the fundamental mode inside the modified nanocavity and the spatial Fourier transform (FT) spectra respectively. This Figure was taken from ref [71].

5.6 Experimental results and discussion

5.6.1 Optical Properties of the SiN Based on L3 Nanocavity

The optical properties of an unmodified (S=0) *L*3 nanocavity structure are first studied before exploring the effect of modifying the holes surrounding the nanocavity using far field optical spectroscopy. Here, the photonic crystals had a lattice constant a=260 nm, hole radius = 77 nm and membrane thickness *d*=200 nm. Figure 5.9 shows scanning electron microscope (SEM) images of the structure. The cavity PL emission spectrum is shown in Figure 5.9 (c). This spectrum was recorded from an L3 nanocavity using a laser focussed onto the cavity region. The sharp peaks evident result from the different optical modes confined within the L3 nanocavity structure.

It can be seen that only four modes are evident instead of the five modes that were predicted using FDTD modelling. The reason for this is most likely attributed to fabrication errors that impact on the higher modes more than on the fundamental mode [72]. Previous work has shown that L3 nanocavities based on a SiN membrane often only display four optical modes [63-73]; a result in agreement with result shown in Figure 5.9(c). It can be seen that the emission intensity of modes M2 and M3 are relatively enhanced compared to the surrounding background PL by a factor of 2 to 3 times respectively. Such modes are predicted to lie in the band gap in such a structure.

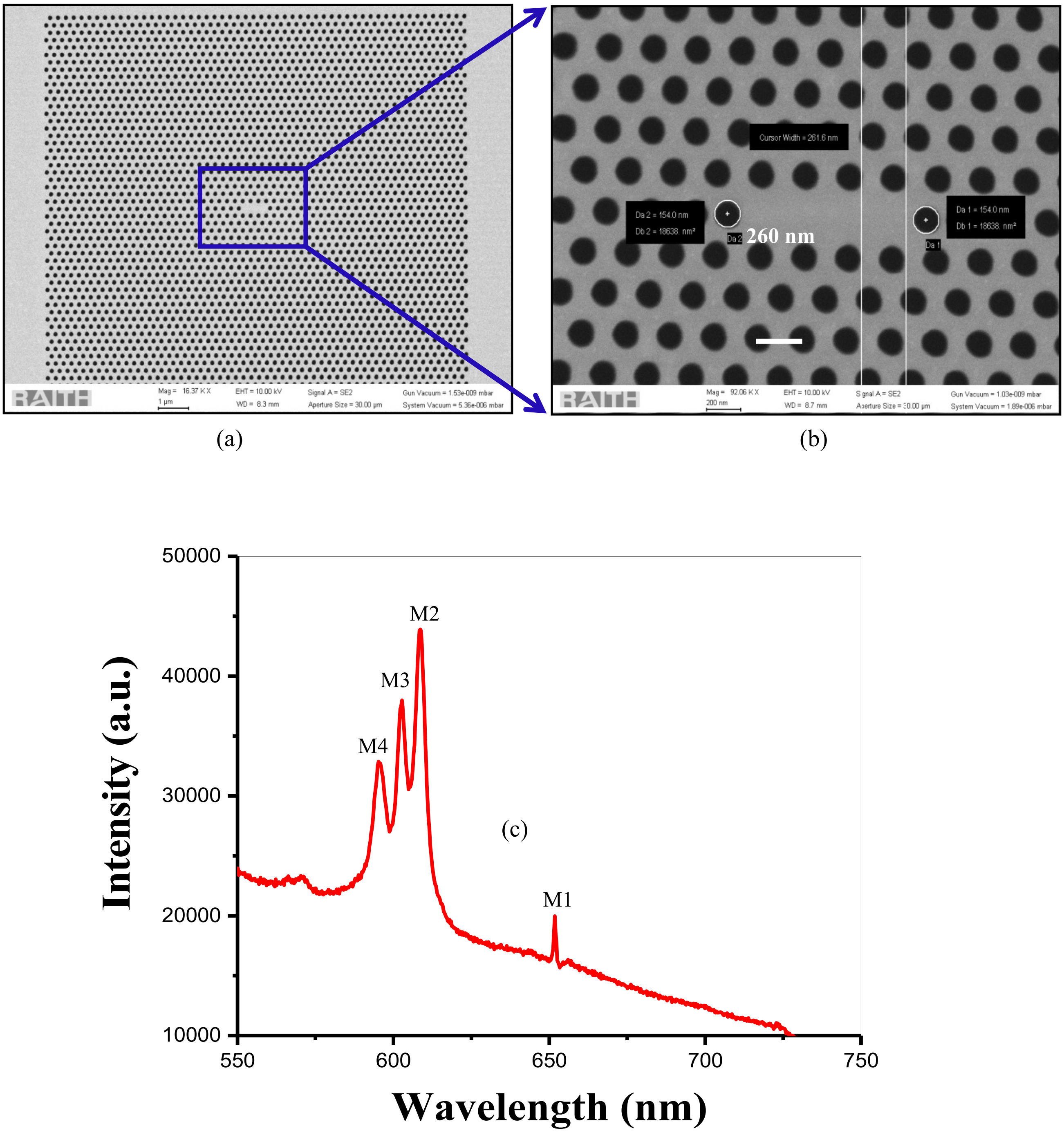

Figure 5.9: (a) and (b) show SEM images of the SiN based *L*3 nanocavity. Here *a* = 261 nm, *r* = 77 nm and d = 200 nm. (c) PL emission spectra recorded from the centre of the cavity.

5.6.2 PL Polarisation properties of the SiN membrane based L3 nanocavity.

The PL emission from L3 SiN nanocavity was measured as a function of polarisation angle as illustrated in Figure 5.10. This should be compared with the unpolarised emission from the same nanocavity as shown in Figure 5.9 (c). Figure 5.10 (a) shows the PL emission polarised perpendicularly to the nanocavity short axis (here called y- polarisation). The fundamental mode (M1) is the dominant peak and has a Q factor of 590. The polarisation parallel to the nanocavity long axis is shown in Figure 5.10 (b). Here, it can be seen that modes M2, M3 and M4 are polarised along the cavity long axis (termed x- polarisation).

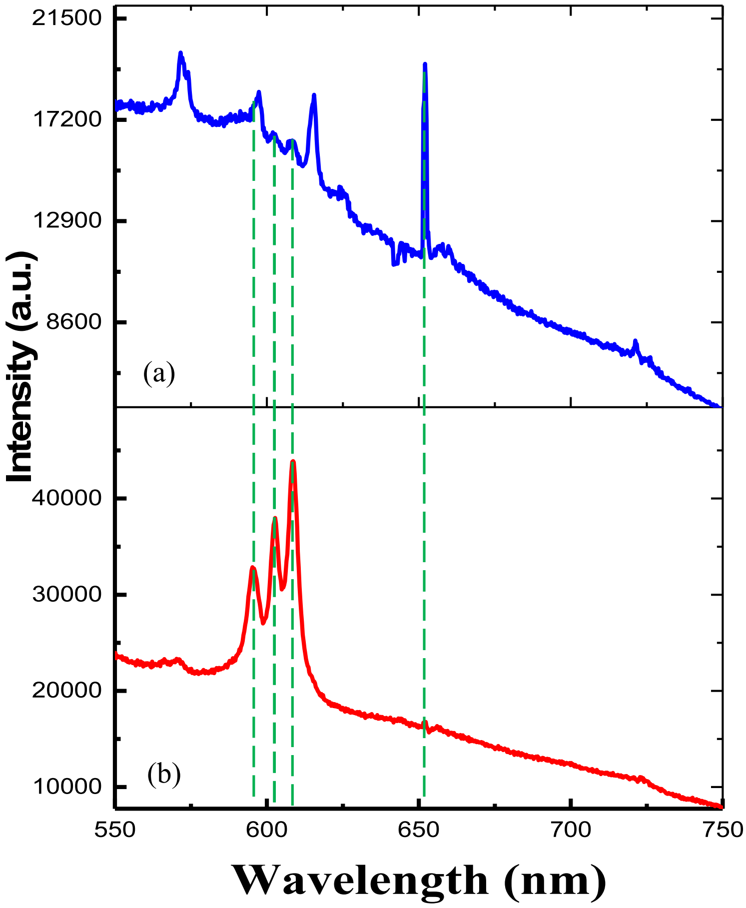

Figure 5.10: Shows the PL emission of a SiN L3 cavity with a polarisation (a) perpendicular to the nanocavity short axis and (b) parallel to the nanocavity long axis. Here, the green dashed line identifies the modes in both polarisations.

5.6.3 Q factor and position of the fundamental mode vs. side hole shift

The effect of shifting the side holes of two dimensional nanocavity is an important parameter that can be used to control both cavity Q factor and the fundamental mode wavelength. The Q factor of the fundamental cavity mode was calculated from PL emission through a Lorentzian fit where Q=λ/Δλ in which λ is the fundamental mode wavelength and Δλ is its FWHM.

Figure 5.11 illustrates the experimental values of Q factor of the fundamental mode M1 for different nanocavities with the holes radius of 78 nm as a function of the first nanocavity edge-hole shift (S_1). It can be seen the highest Q factor value recorded was 685 corresponding to a side hole shift of *S*= 0.20, without modifying around the cavity.

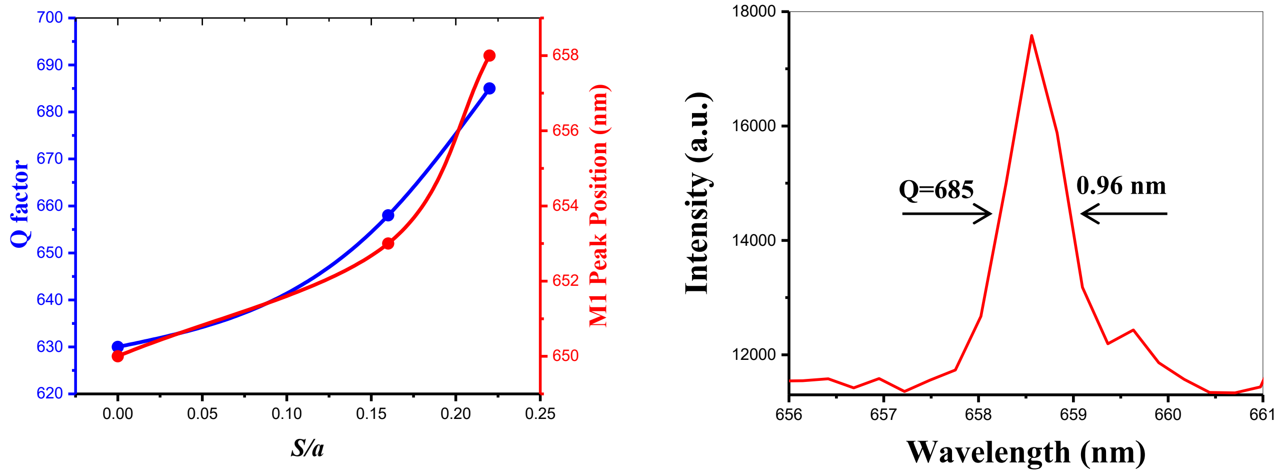

(a) (b)

Figure 5.11: (a) Q factor and the peak position of the fundamental as a function of the cavity edge- hole shift (S/a), (b) the PL emission from the nanocavity with a side-hole shift of *S*=0.22 with the cavity having a Q factor of 685.

5.6.4 Q factor and position of the fundamental mode vs. side hole shift for SiN L3 cavity having a large hole size

The air hole size of L3 nanocavity structure is an important parameter that can be used to control the value of Q factor and position of the fundamental cavity mode wavelength. The influence of hole size on the fundamental mode M1 of an *L*3 nano-cavity has been studied. A triangle lattice shape was used with a lattice constant of a=260 nm and a 200 nm thick membrane. The diameter of the hole size was systematically changed from 120 nm to 180nm. Figure 5.12 (a) to (d) shows the structures for four different L3 nanocavities having a hole size of 130, 140, 150 and 160 nm respectively.

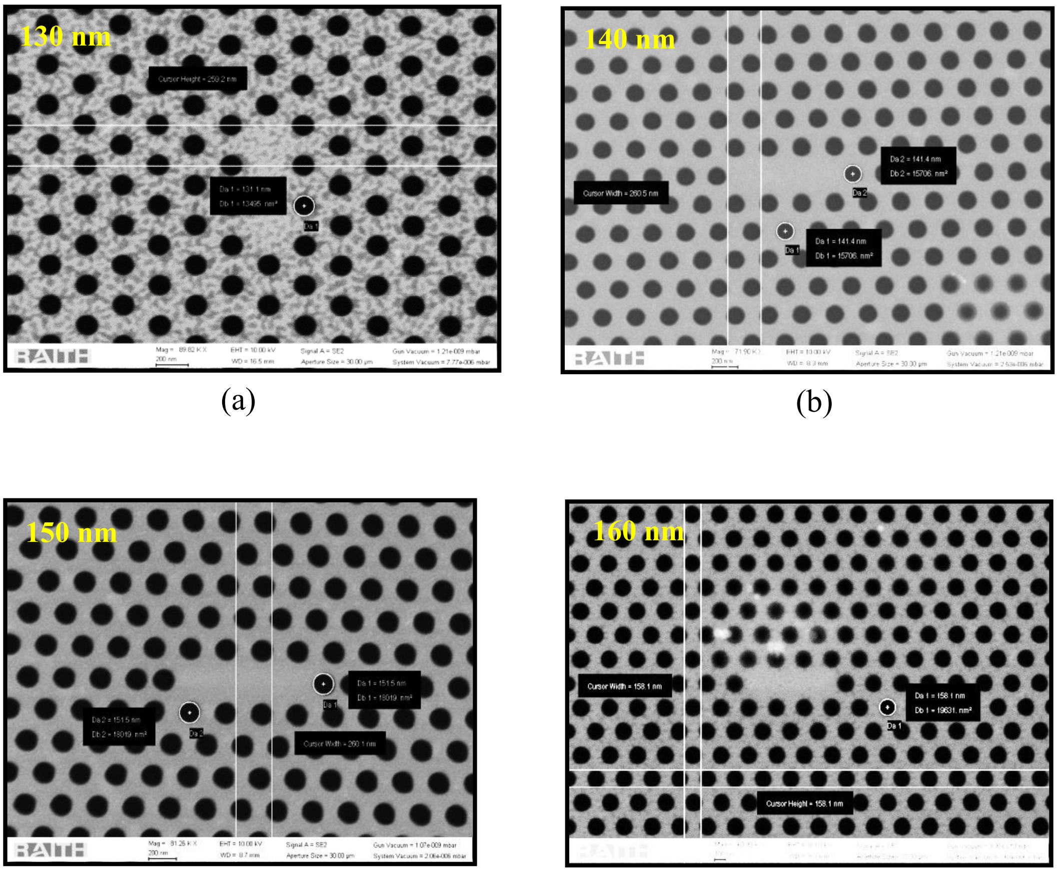

(a) (b)

(c) (d)

Figure 5.12: SEM images of four different nanocavities fabricated having a hole size of (a) 130 nm, (b) 140 nm, (c) 150 nm and (d) 160 nm.

The sensitivity of cavity mode wavelength to hole size is clear, with a shifts to higher frequencies observed as hole size increases as shown in Figure 5.13.

Here, we find that the peak position of the fundamental mode shifts from 720 nm to 612 nm as the hole size is increased from 120 nm to 180 nm. This result agrees with the results from FDTD modelling (see Figure 5.7(b)). It is also apparent that Q factor decreased from 560 to 395 as a result of increasing hole size [74]. Q factor cavity is sensitive to loss from in-plane scattering of the optical mode inside the cavity, and so increasing the hole size can lead to increase optical losses as observed here [75].

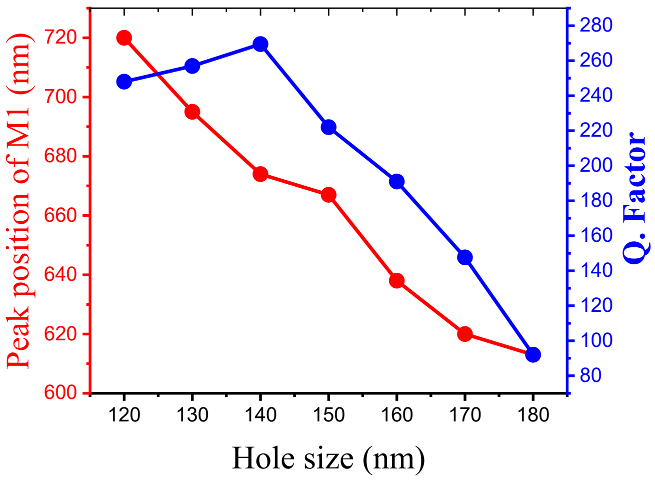

Figure 5.13: The peak position of the fundamental mode M1 and Q factor as a function of hole size for different nanocavities having a hole size of 120 to 180 nm.

The side holes around an L3 cavity having a hole size of 160 nm (see Figure 5.12 (d)) were shifted away from the centre of the cavity to study the effect on the Q factor and M1 peak position in a large hole size nanocavity. Here, Figure 5.14 illustrates the impact of side hole shift on Q factor and peak position of the fundamental mode M1.

It can be seen experimentally that, a red shift is observed of the fundamental mode, going from 637 nm in an unmodified nanocavity (S_1 = 0) to 643 nm after the side holes are shifted by S_1 = 0.24a. This is accompanied by an increase in Q factor from 455 to 630. It can also be seen that the fundamental mode is clear in TM polarization (y- polarised) in Figure 5.14(a), but disappears for TE polarization (x- polarised).

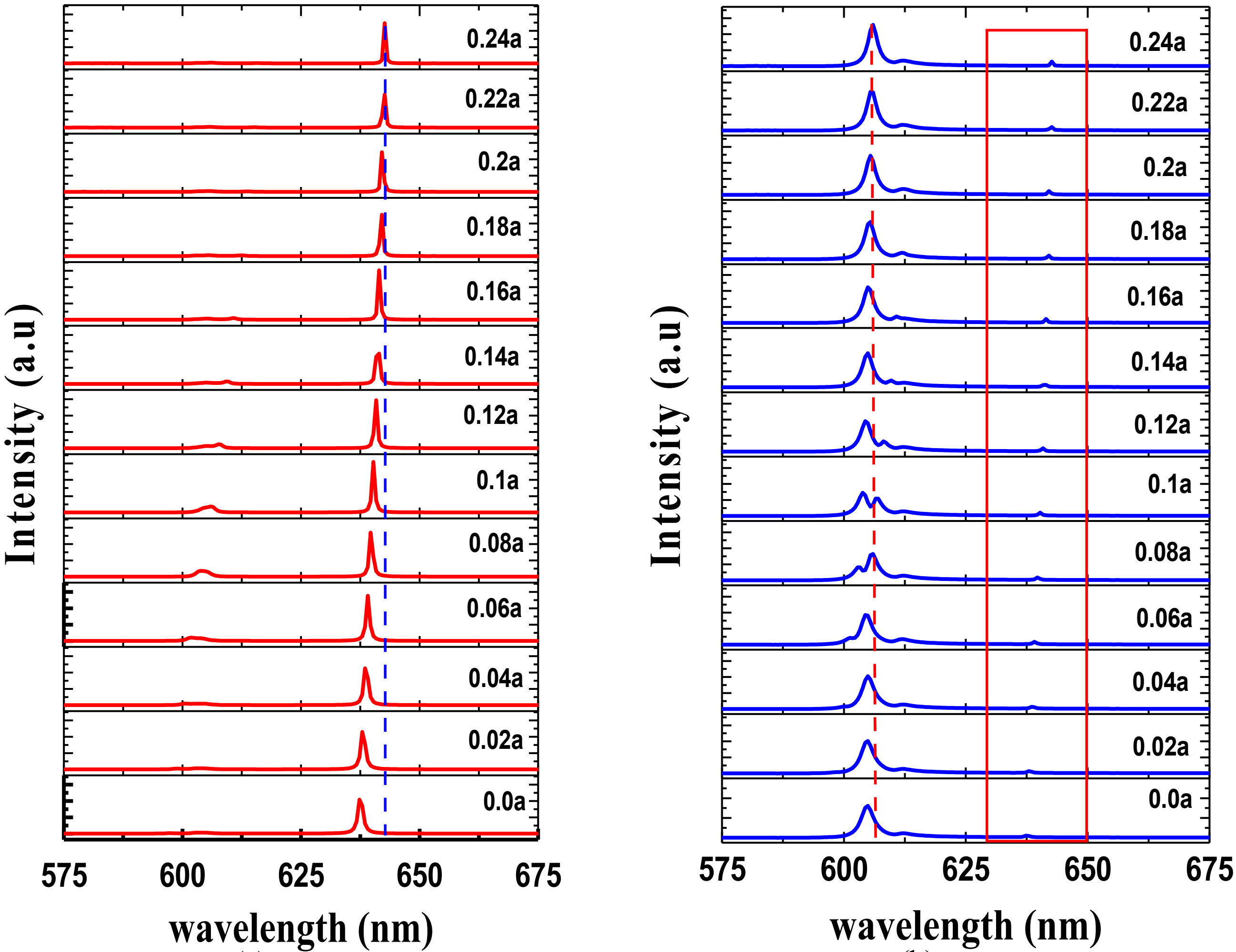

(a) (b)

Figure 5.14: (a) and (b) the peak position of the fundamental mode M1 as a function of the nanocavity first side hole (S_1) shift for both TM and TE respectively.

5.7 An L3 Nanocavity having a high Q factor.

Developing nanocavities having a high Q factor are of considerable interest for a range of different applications such as sensors, high resolution filters and low threshold nano-laser. Many varied designs have been introduced to increase Q factor based on tow dimensional photonic crystal nanocavity [48-76]. For example, a Q factor of 11,700 was achieved by Fu et al using a H1 nanocavity based on GaAs PhC membrane [77]. A higher Q factor of 320,000 was achieved by Tanabe et al using a 2D hexapole PhC nanocavity [78]. A much higher Q factor of 1.45×10^6 was achieved by Lai et al by optimizing a 2D *L*3 PC nanocavity designed into a Si slabs having a small effective mode volume of $0.96(\lambda/n)^3$ [79]. The highest Q factor of 9×10^6 reported was achieved by Sekoguchi et al using a Si based PhC. This cavity was fabricated using a line defect of 17 missing air holes in which the lattice constant was increased every two periods in the x-direction [80].

Here, I have used the FDTD to study the parameters by which Q-factor can be increased. Three mechanisms have been studied. First, the refractive index was varied between 1.5 and 2.5. Here, a significant increase in the Q factor in an unmodified structure from 500 to 37,000 is seen, which is accompanied by a red shift of the fundamental mode M1 from 512 nm to 781 nm as shown in Figure 5.15 (a). However, the Q factor then decreases once the value of the refractive index increase to 2.7. Secondly, the membrane thickness was increased from 100 nm to 450 nm as illustrated in Figure 5.15 (b). It can be seen that the Q factor increased from 500 to a maximum value of 13,557 at a membrane thickness of 300 nm. Beyond this thickness the Q factor then decreased. Again, it can be seen a red shift occurs in the fundamental mode as a function of increasing membrane thickness.

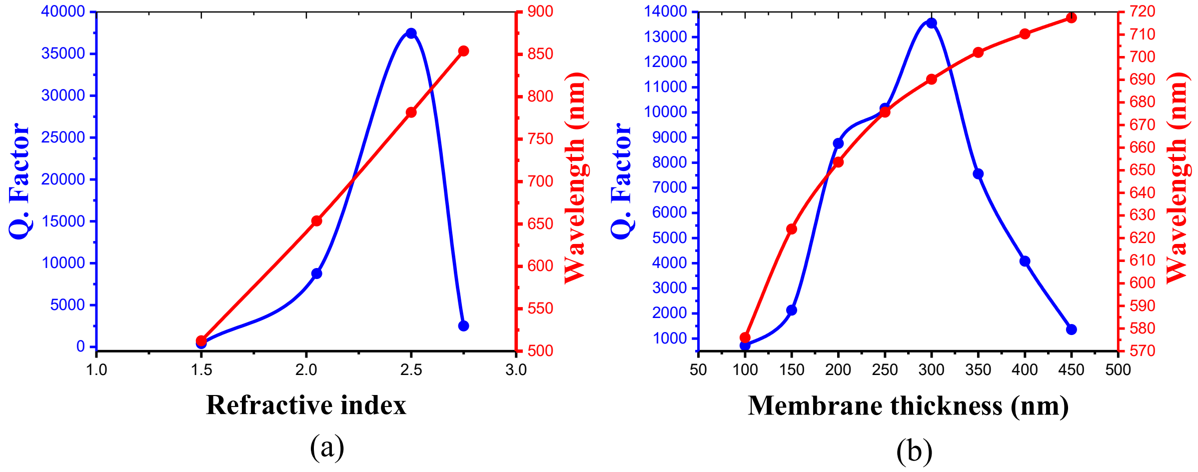

Figure 5.15: Shows a calculated value of Q factor and peak position of the nanocavity fundamental mode as a function of (a) refractive index, (b) membrane thickness using FDTD simulation.

Finally, more sophisticated modification of the L3 nanocavity structure explored increase the Q factor using the two different designs as shown in Figure 5.16. Here, the lattice constant was a= 260 nm, with the size of the first hole (shown as r_1 red color) at each side of the nanocavity was reduced to a radius of 52 nm and then shifted by a value of between $S/a = 0$ to 0.26. The size of the holes around the cavity (shown as r_2 purple color) was also reduced to a radius of 65 nm, with the other holes (shown as r_3 white color) having a radius of 78 nm have not been changed. A Q factor of 8657 for the fundamental mode M1 at 654 nm was predicted for this structure as shown in Figure 5.16 (a). The second design (see Figure 5.16 (b)) had reduced size of three edge holes with the first and the second hole at both sides of the cavity shifted by value of $S/a = 0$ to 0.26. A higher Q factor of 12,565 was predicted for this structure.

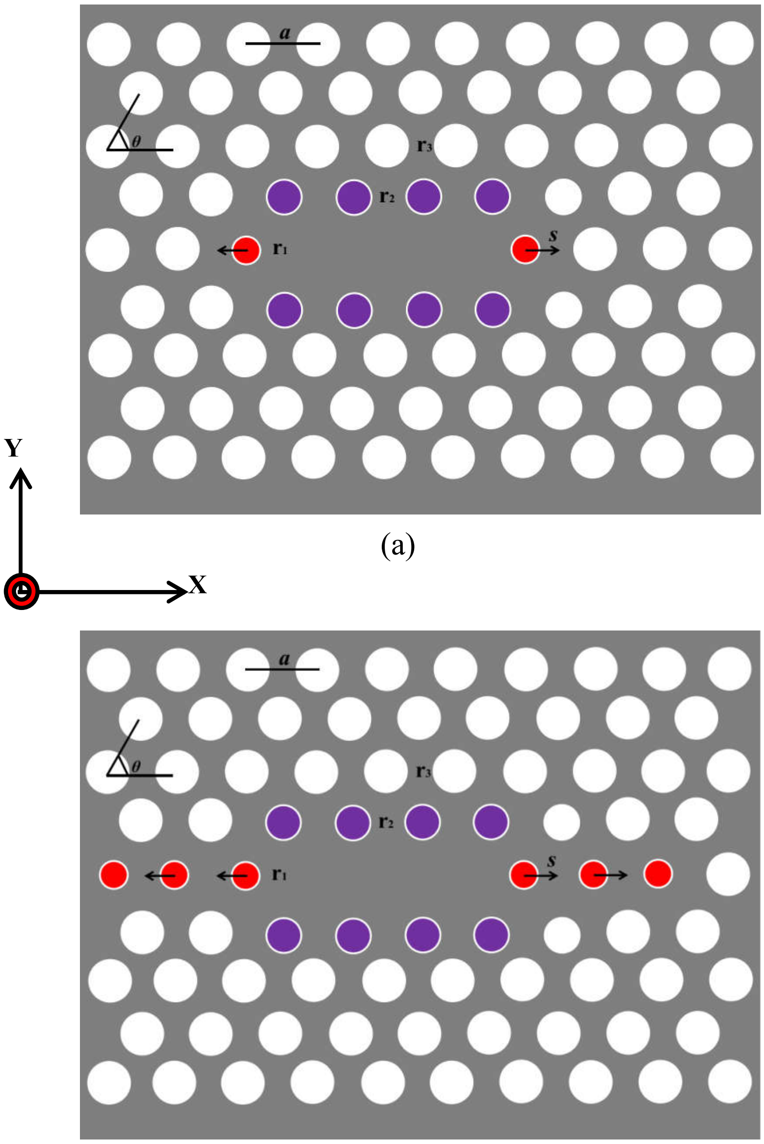

(a)

(b)

Figure 5.16: A schematic diagram of a modified 2D PhC L3 nanocavity illustrating the design of the air holes. In part (a) the size of one hole is decreased and shifted in an opposite direction from the centre of the cavity (red circles) with the four holes surrounding the cavity (purple circles) having reduced size. The structure in part (b) has three holes at the edge of the cavity that are shifted and having reduced size.

We have used FDTD to simulate the PL emission from these structures. Figure 5.17 (a) shows the relation between the number of shifted hole (shown as r_1 red color) on the Q factor and peak position of the fundamental mode M. Parts (b) and (c) show a simulation of the TM and TE modes for *L*3 cavity with a non-displaced air holes (*S*=0).

It can be seen that there are five modes, two modes appear on the short axis polarisation (y- polarised), with the M1 fundamental mode having a wavelength of 654 nm and mode M4 being at 604 nm. Three modes appear on the long axis polarisation (x-polarised) having a wavelength of 629, 626 and 595 nm for modes M2, M3 and M5 respectively.

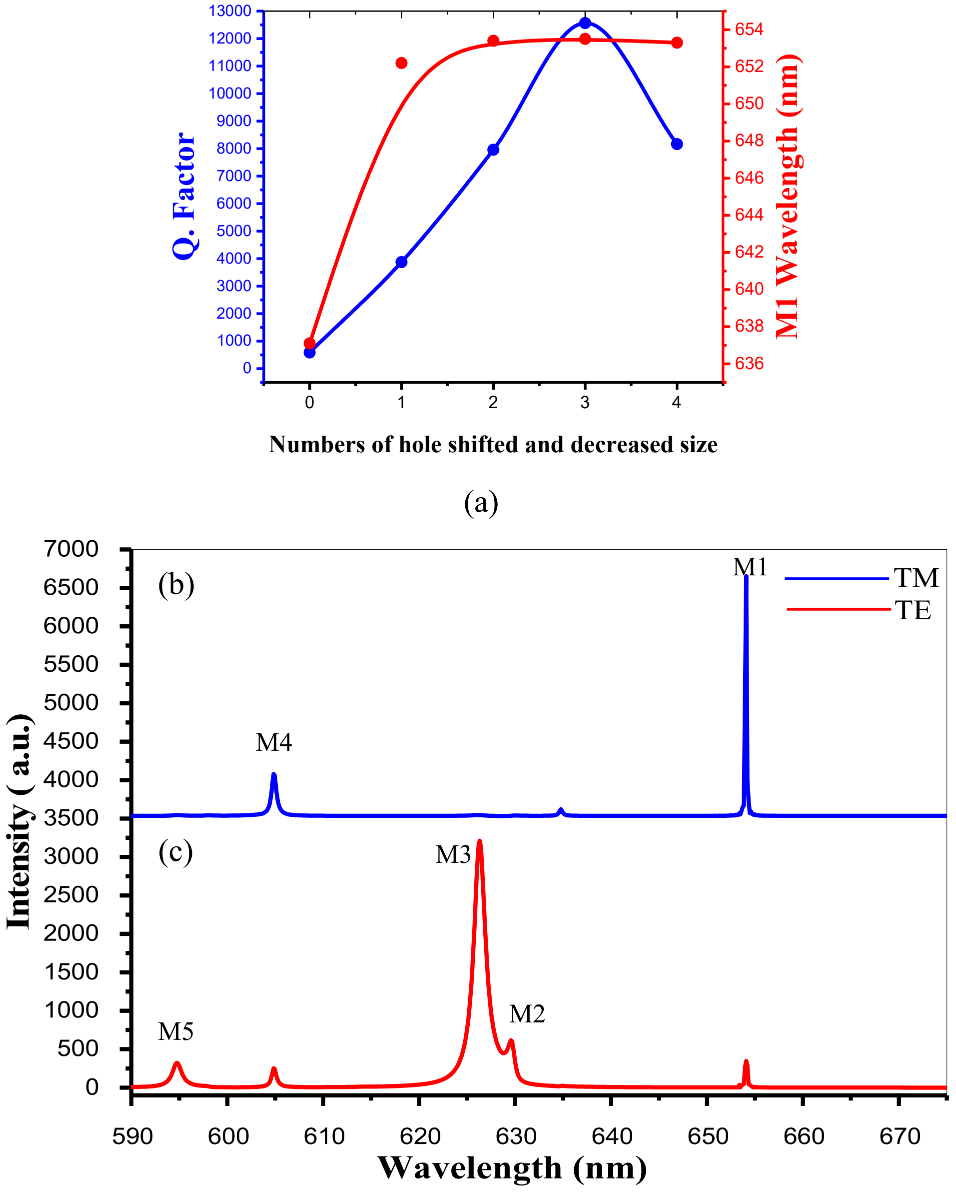

Figure 5.17: Shows the PL emission spectrum of a modified L3 nanocavity with shifted holes of *S*=0 using FDTD simulation for (a) TM modes and (b) TE modes

5.7.1 Towards a high Q factor *L*3 Nanocavity.

In this section, I describe attempts to experimentally fabricate modified *L*3 structures having a high Q-factor that operate at visible wavelengths. Here, reducing the radiation loss is a central goal to increase cavity Q factor, and therefore it will be necessary to reduce light scattering due to roughness at the hole side-walls and the top interface with the air. As I show below, this requires close control of the etching process. Initial experiments however only produced cavities with a low Q factor.

Here, Scanning Electron Microscopy (SEM) indicated that there was unwanted material (presumed to be remaining PMMA) stuck on the surface of the nanocavities that most likely resulted in unwanted scattering and thereby reduced the cavity Q factor as shown in figure 5.18. Therefore, a chemical solvent remover called 1165 was used to remove unwanted material from the cavity surface. This treatment caused an enhancement of luminescence for such cavities.

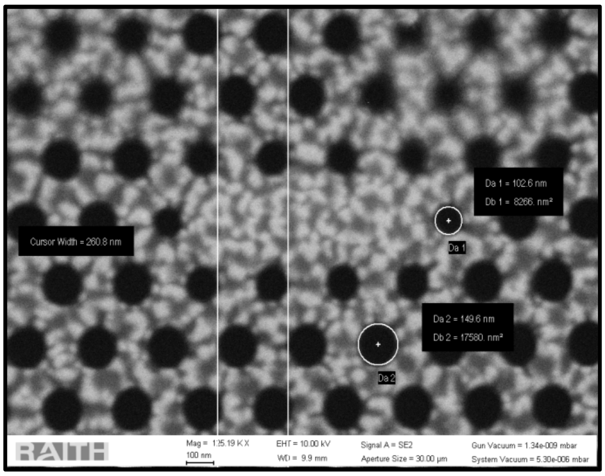

Figure 5.18: A SEM image showing indicated unwanted material (PMMA resist) stuck on the surface of the nanocavities.

It was also found that the small size hole at the edge of the nanocavity (r_1=52 nm) required increased etching time for 1.5 time compared with a large sized holes size (r_3=78 nm). This meant that the etching time needed to transfer the modified design from the resist to the SiN membrane was increased. Here however, another issue was encountered; it was found that the PMMA resist was damaged after etching for a long times. Figure 5.19 illustrates a nanocavity covered by a PMMA resist that had been etched for 18 minutes.

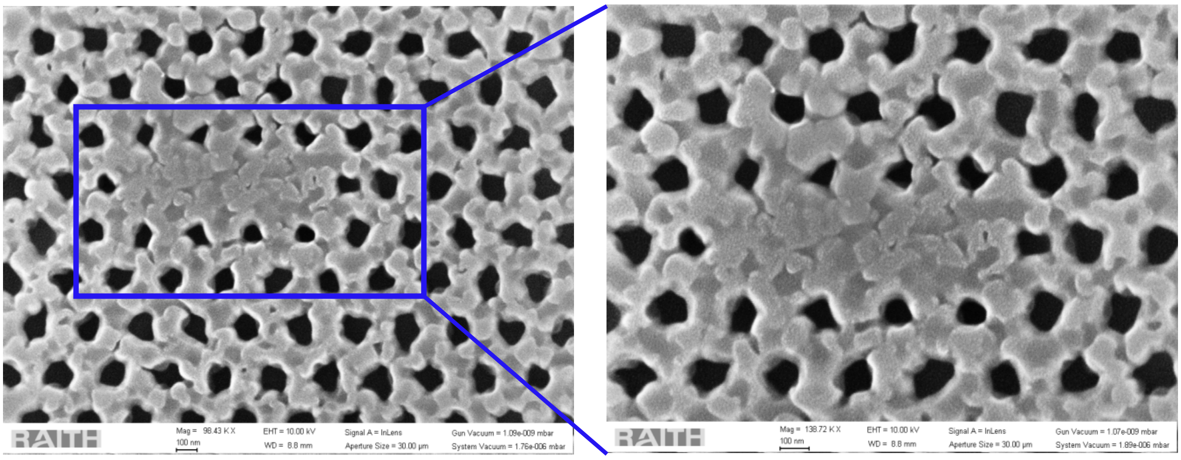

Figure 5.19: A SEM showing the modified nanocavity structure after extended etching time.

It was therefore necessary to identify a new e-beam resist that could allow an *L*3 nanocavity to be fabricated with one and three shifted side holes at both side of the cavity. Here, a SCAR-62 e-beam resist was then selected as an alternative to PMMA, due to its hardness and high resistance to etching.

The optical properties of a one hole modified L3 nanocavity structure was first studied before exploring the effect of modifying the three holes structure, with the cavity fabricated using the SCAR-62 e-beam resist.

The structure of the membranes fabricated had a thickness of d=200 nm, lattice constant of a=260 nm, hole radius (r_1, r_2 and r_3 = 52 nm, 65 nm and 78 nm respectively) as shown in Figure 5.16 (a). Figure 5.20 shows (a) scanning electron microscope (SEM) image and (b) an atomic force microscopy (AFM) image of the resultant structure. Here, it can be seen that the cavity surface appears much smother and more homogeneous.

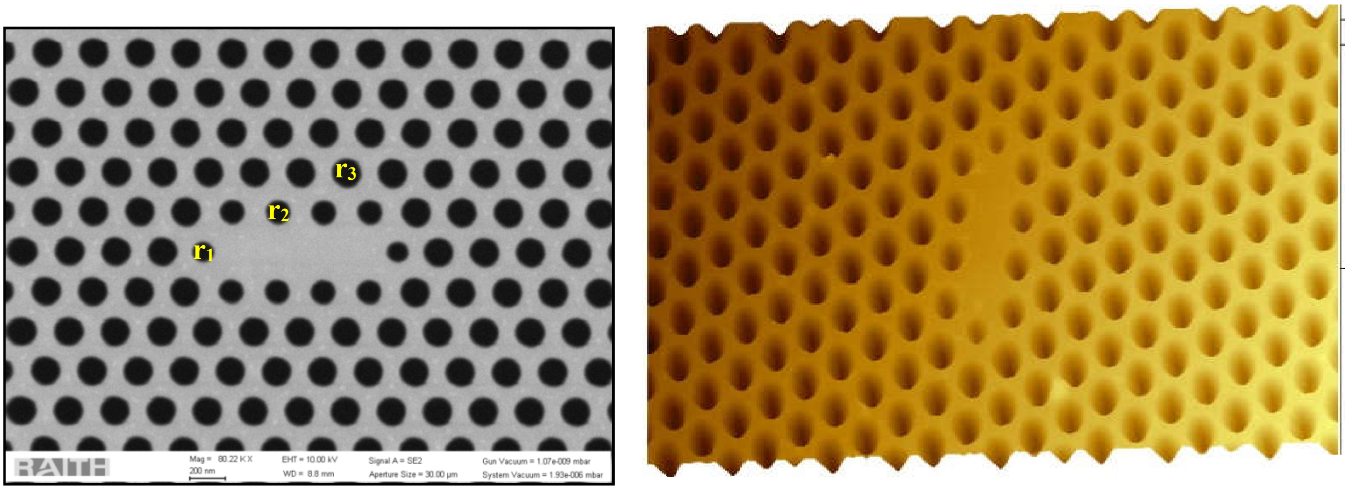

(a) (b)

Figure 5.20: Shows (a) a scanning electron microscope (SEM) image and (b) an Atomic force microscopy (AFM) image of the structure.

The PL emission spectrum recorded from such nanocavities fabricated using the SCAR-62 shown in Figure 5.21 (a). Here, it can be seen that a number of sharp peaks are visible due to the strength of the confined optical field inside the modified *L*3 nanocavities. Moreover, a red shift in the peak position of fundamental mode M1 is evident as the lateral edge hole is shifted away from the centre of the cavity as shown in Figure 5.21 (b).

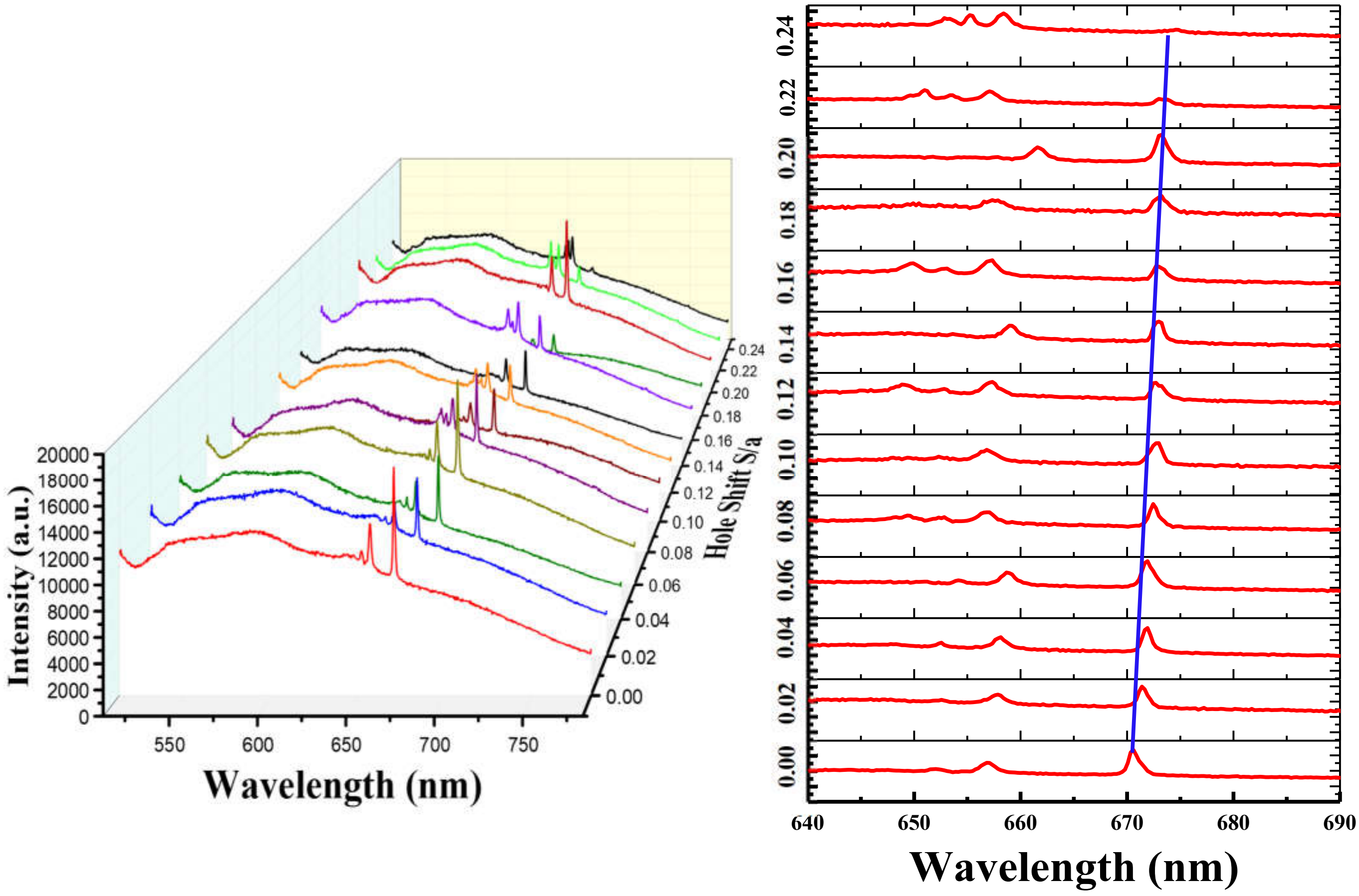

(a) (b)

Figure 5.21: (a) the PL emission spectrum recorded from a modified L3 nanocavities as a function of the hole shift and (b) the peak position of the fundamental mode M1 as a function of hole shift.

Here, a Q factor of 838 is obtained as a result of using a modified structure as shown in Figure 5.22. Here, the effect of shift in the edge holes of the cavity on the Q factor was explored. The Q factor was found to increase from 645 for (*S*=0) to 838 for (*S*=0.20). It can be seen that there are five modes, two modes appear on the short axis polarisation (y- polarised) having a wavelength of 671 nm for M1 (fundamental mode) together with three modes on the long axis polarisation (x-polarised).

Interestingly, we found that the peak position of the fundamental mode is shifted of 17 nm compared with the FDTD simulation results as predicted in Figures 5.17 (b) and (c). This is most likely due to small differences between modelled and fabricated structures.

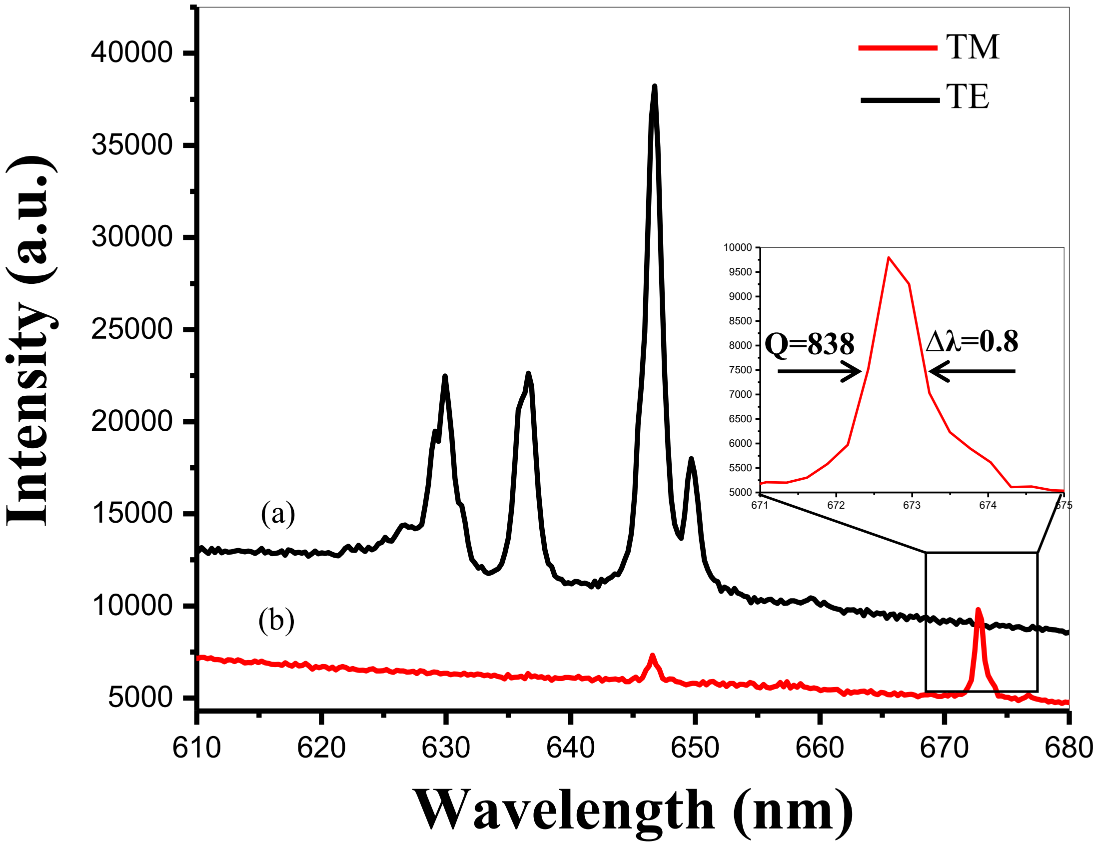

Figure 5.22: The measured PL emission spectrum of a modified L3 nanocavity with shifted holes of *S*=0.20a experimentally. Part (a) is TE modes and part (b) shows TM modes.

5.7.2 An L3 Nanocavity containing a Red-F Fluorescent Molecular Dye.

Organic semiconductor materials have attracted significant attention as result of their optoelectronic properties and for their wide range of possible applications in optoelectronics and photonics [81-82]. These include ease of manufacture and tuneable electronic properties by changing chemical structure and efficient operator in light emitting devices, features that make these materials very attractive [83-84]. The photoluminescence (PL) efficiency of many organic semiconductors is high with such materials also having high charge-carrier mobility at room temperature [85]. Organic semiconductors are also able to effectively absorb light in a thin film only 100 nm thick making these ideal materials for photovoltaic application [86-87].

We have therefore explored placing an organic material on the top surface of the an *L*3 nanocavity [88-91]. This leads to change the L3 nanocavity structure with such surface emitter structures being of potential interest in different optoelectronic applications. We also expect the cavity to modify optical transitions of the organic thin film as a result of the confined and enhanced electromagnetic field at the nanocavity surface [92].

We have again used the red-luminescent polymer Red-F and deposited it on the top surface of the nanocavities. The red- emission from these materials makes it ideal to be combined with the nanocavities explored here. Figure 5.23 shows in part (a) the PL emission of Red-F and (b) its chemical structure.

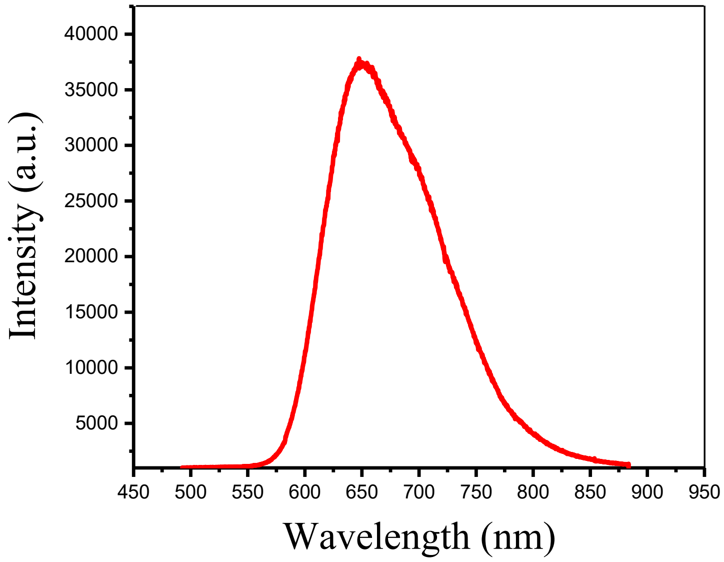

(a)

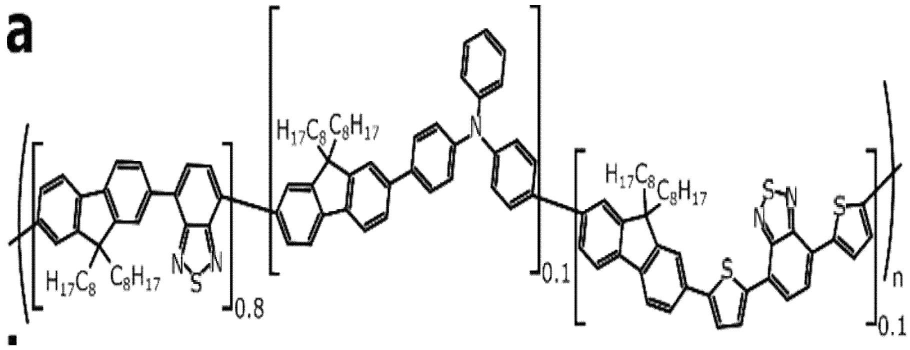

(b)

Figure 5.23: Shows (a) the PL emission of Red - F organic materials. (b) Its chemical structure.

The nanocavity surface was coated with a thin film of 10 nm of Red emitter fluorescent conjugated polymer having a surface roughness of 1.26 nm. The emission from the cavity now results from an overlap of the luminescence from the thin film with the cavity mode wavelength that results in an enhancement of the emission of the film. Here, the photoluminescence quantum yield of the Red-F is significantly higher compared to the SiN. The Red-F solution was prepared of a concentration 2.5g/L in 1,2-Dichlorobenzene solvent. Such material is considered typical of polymers that are used in light emitting diodes [93] and lasing [94]. Figure 5.24 (a) shows a schematic image of the cavity and (b) and (c) an AFM image taken for the cavity shown in Figure 5.20 after coating with 10 nm of Red- F polymer. Figure 5.24(c) confirms that the conjugated polymer covers the complete nanocavity suface without filling the holes of the photonic crystal.

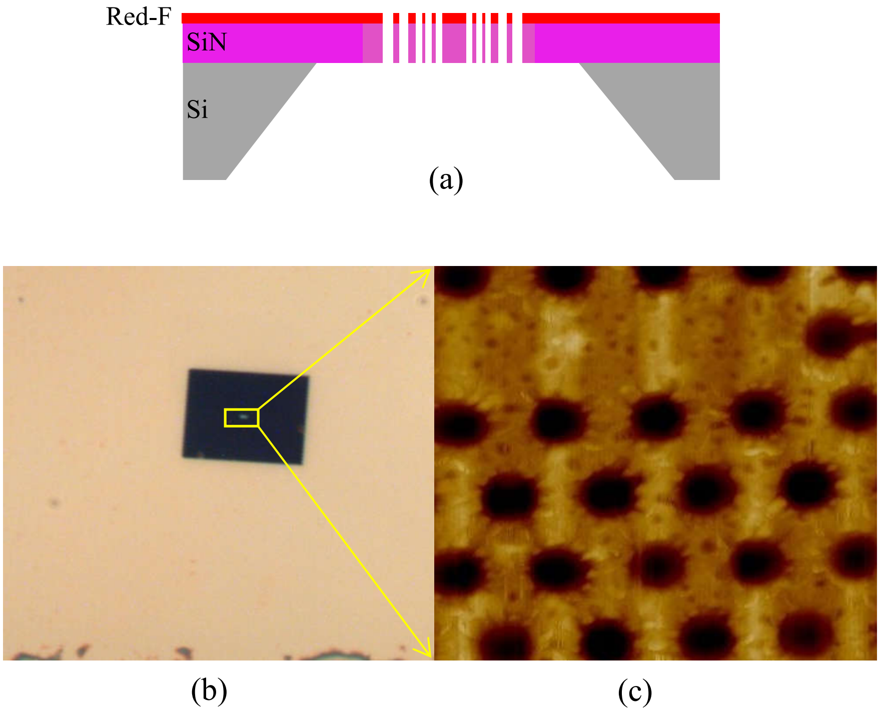

Figure 5.24: (a) A schematic diagram of a hybrid L3 nanocavity and (b) and (c) images after coating with a Red-F polymer film.

Far field spectroscopy was used to record the PL emission from the Red-F on the cavity as shown in Figure 5.25. It can be seen that the PL emission spectrum consist of a number of a sharp lines that are superimposed on the spontaneous emission spectrum of the Red-F that peaks at 660nm that leaks from the nanocavity surface.

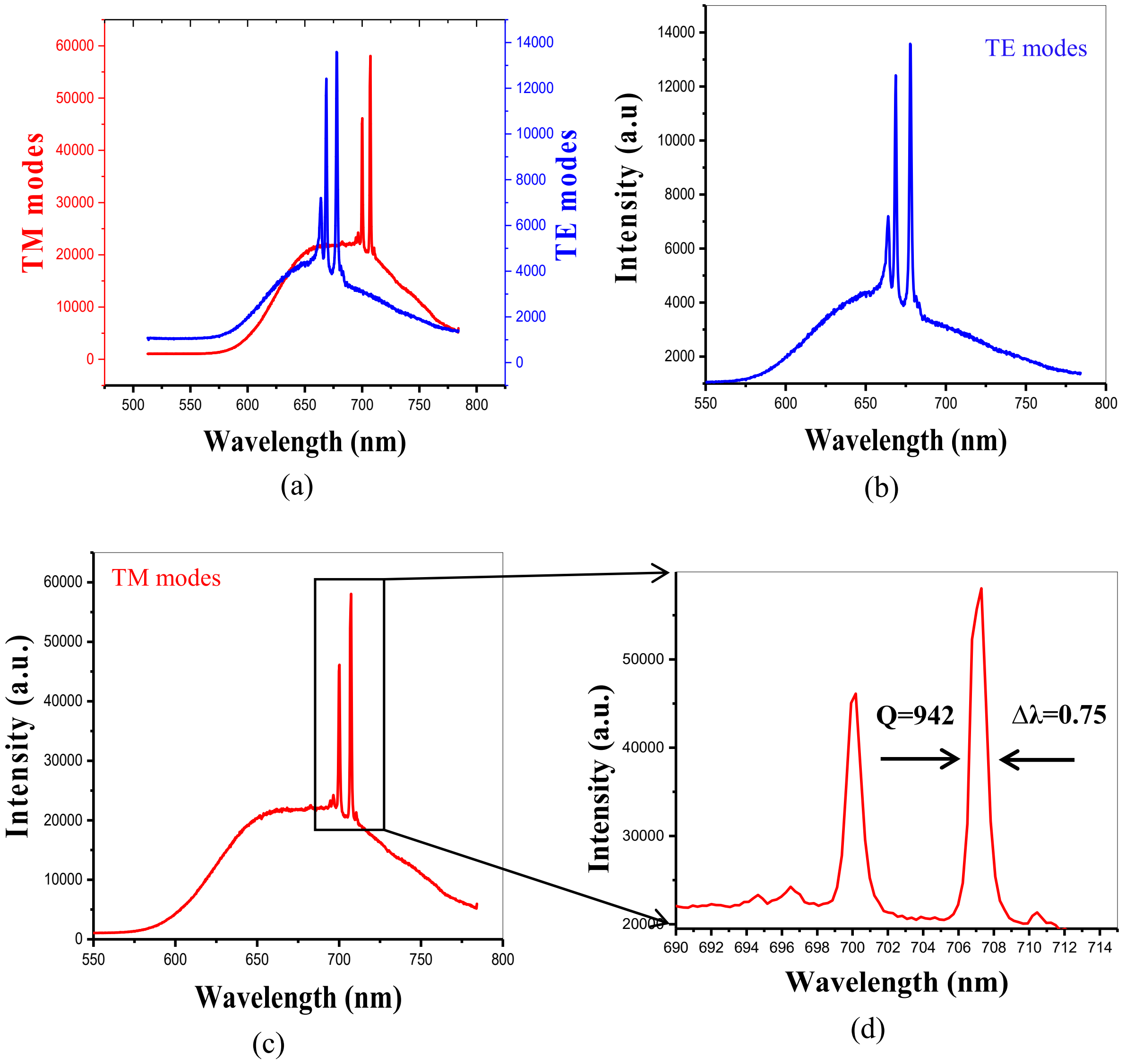

(a) (b)

(c) (d)

Figure 5.25: Illustrates (a) The PL emission of a Red-F / L3 SiN nanocavity, (b) and (c) TE and TM modes for a polarisation parallel and perpendicular to the nanocavity long axis respectively and (d) the close-up of the emission of the fundamental mode M1.

It can be seen that the PL emission from the L3 cavity coated with a thin film Red- F polymer is different from the same SiN L3 nanocavity that emits much weaker fluorescence, has a broad emission spectrum with mode peaks observed at shorter wavelength. Here, the sharp peaks result from an overlap between the Red-F emission and the optical modes of the cavity.

interestingly, it is clear from figure 5.25 (d) that the fundamental mode M1 has a Q factor of 942; a value that is higher than those recorded from the uncoated nanocavity, with the peak position of the M1 undergoing a red shift. This red shift can be explained as a result of changing the hole size together with changing the top surface refractive index and the effective thickness of the slab.

By comparing Figures 5.22 and 5.25 (c), it can be seen that the intensity of the fundamental mode M1 was inhanced by a factor of 6 times after coating with the Red-F polymer. This enhancement has a number of origins. Firstly, the quantum efficiency of the Red-F polymer is much higher than SiN. Secondly, the absorption of the laser exatation wavelength is enhanced, allowing more energy to be deposited into the cavity. Finally, we may also expect a degree of enhancement of emission intensity as a result of the Purcell effect. Indeed, the spontaneous emission of an emitter was spectrally located at the cavity mode of the nanocavity. However, it should be noted that the emitters are placed at the surfaces of the membrane, where the intensity of the confined electric field is around 20% of $\left|\overrightarrow{E_{(r)}}\right|^2_{max}$ value in the centre of the membrane, a result that would reduce the possible Purcell factor by around 20% [95].

5.7.3 An L3 Nanocavity containing a Red-F Fluorescent Molecular Dye having three shifted holes.

In this section, the optical properties of the second design shown in Figure 5.16 (b) were explored using a red-emitting polymer. A higher Q factor of 12,565 was predicted for this structure as a result of reducing the size of three neighbouring holes and shifting the first and the second holes at both cavity sides by value of *S*/*a* = 0 to 0.26. Here, the membranes on which cavities were fabricated had a thickness of d=200 nm, with the PC having a lattice constant of a=260 nm and hole radius of r_1, r_2 and r_3 = 52 nm, 65 nm and 78 nm respectively. Figure 5.26 shows (a) a SEM image and (b) an AFM image of the uncoated structure.

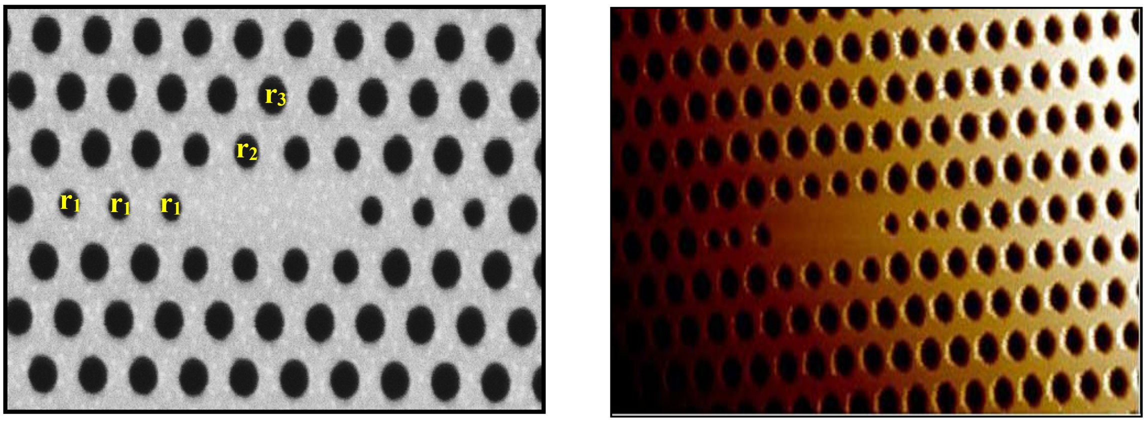

Figure 5.26: (a) A SEM image and (b) an AFM image of the uncoated structure.

The PL emission spectrum was recorded from the such structures as shown in Figure 5.27 (a). Again, it can be seen that emission is characterized by sharp peaks due to the strength of the optical field confined inside structure. Moreover, a red shift in the position of the fundamental mode M1 is clear as the lateral three edge holes are shifted away from the centre of the cavity as illustrated in Figure 5.27 (b).

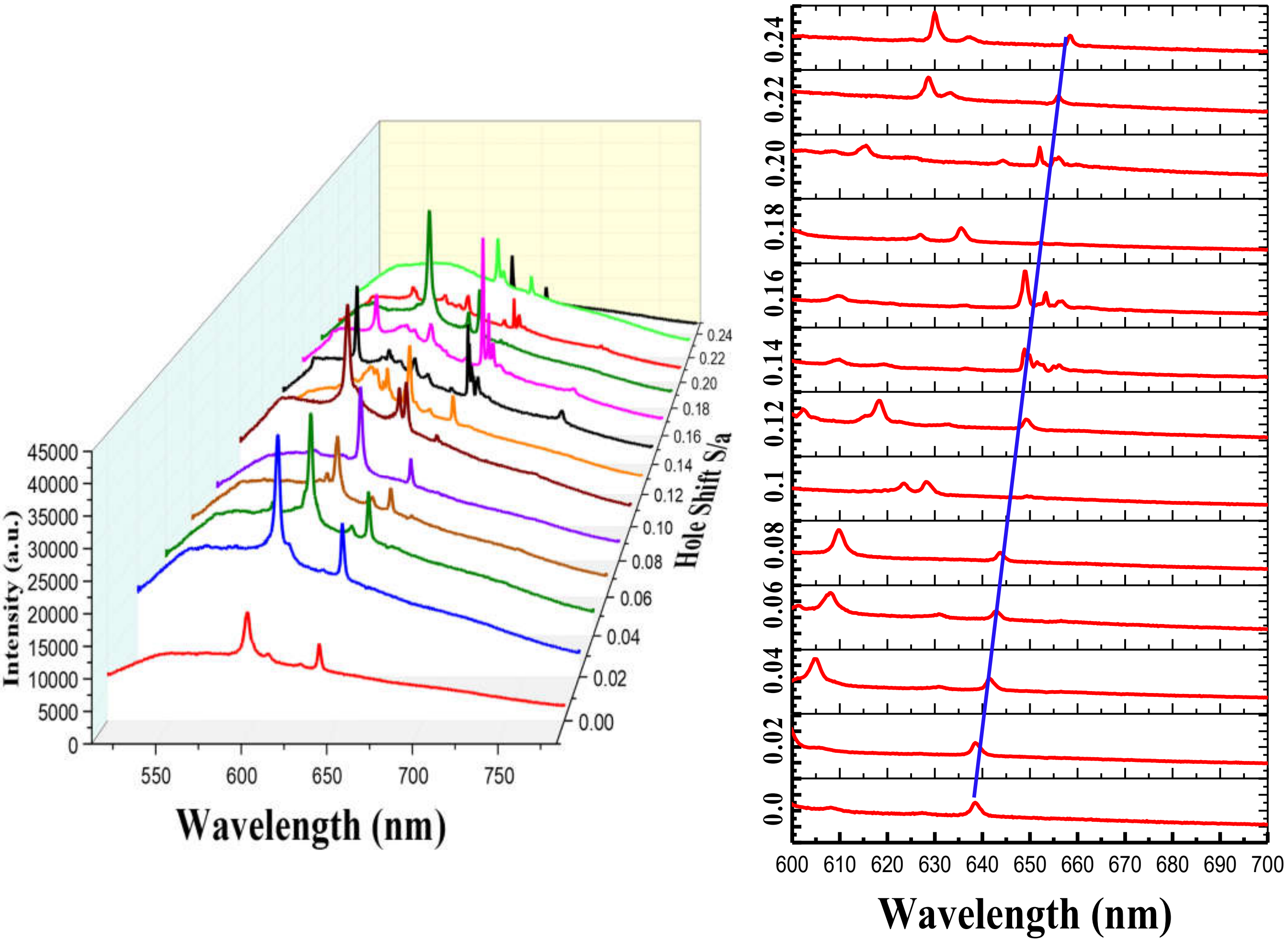

(a) (b)

Figure 5.27: (a) The PL emission spectrum recorded from modified L3 nanocavities as a function of the hole shift and (b) the peak position of the fundamental mode M1 as a function of hole shift.

Here, a Q factor of 931 was obtained as a result of using the modified structure as shown in Figure 5.28. The effect of shifting the edge holes on the cavity Q factor was explored. The Q factor increased from 710 for *S*=0 to 931 for *S*=0.20a where a is the lattice constant. Again it can be seen that there are five modes, two modes appear on the short axis polarisation (y-polarised) with a fundamental mode M1 wavelength of 652 nm. Three modes appear on the long axis polarisation (x-polarised). We find that the peak position of the fundamental mode is shifted by 2 nm compared with the FDTD simulation as illustrated in Figure 5.16 (b) and (c). This could be result from small errors in the structure fabrication.

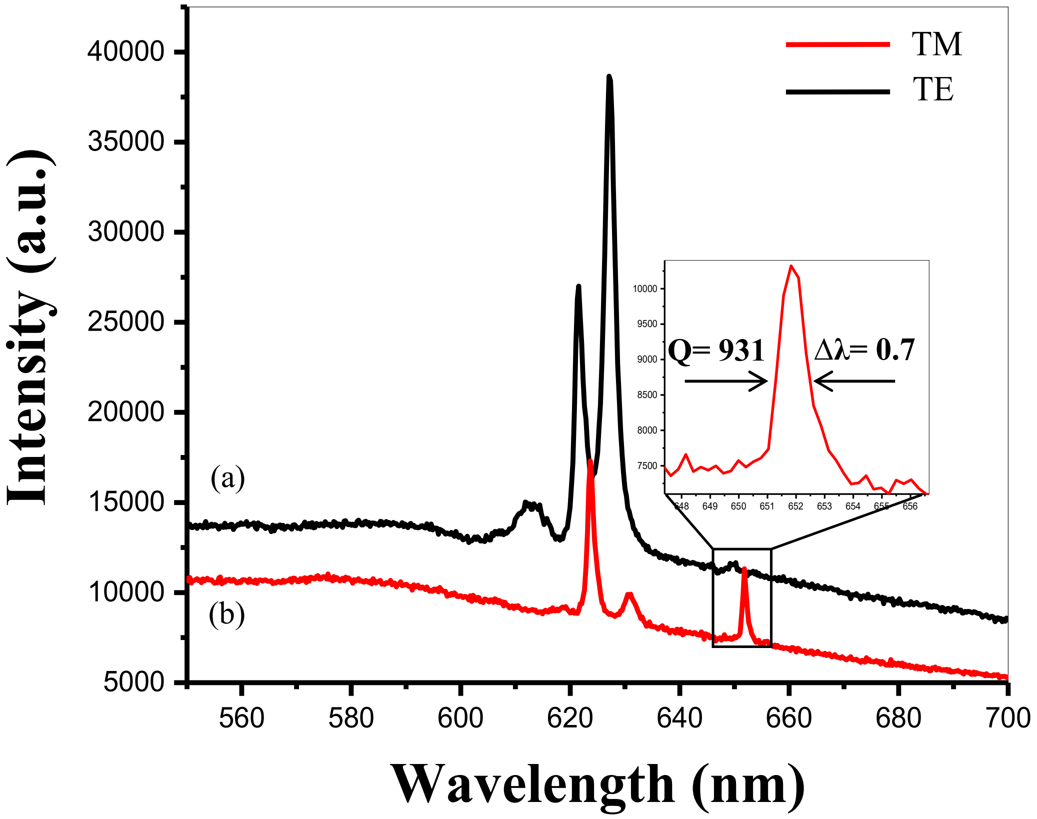

Figure 5.28: Shows the PL emission spectrum of modified L3 nanocavity with three shifted holes of S=0. 20a experimentally (a) TE modes and (b) TM modes.

Again, the Q factor of this structure is lower than predicted by FDTD simulation indicating optical losses, such as unwanted material causing roughness of the surface of the nanocavity. To create this structure, the etching dose factor was modified in order to improve the uniformity size and quality of the etching holes. Figure 5.23 shows an AFM image of some samples that were etched using a different dose factor.

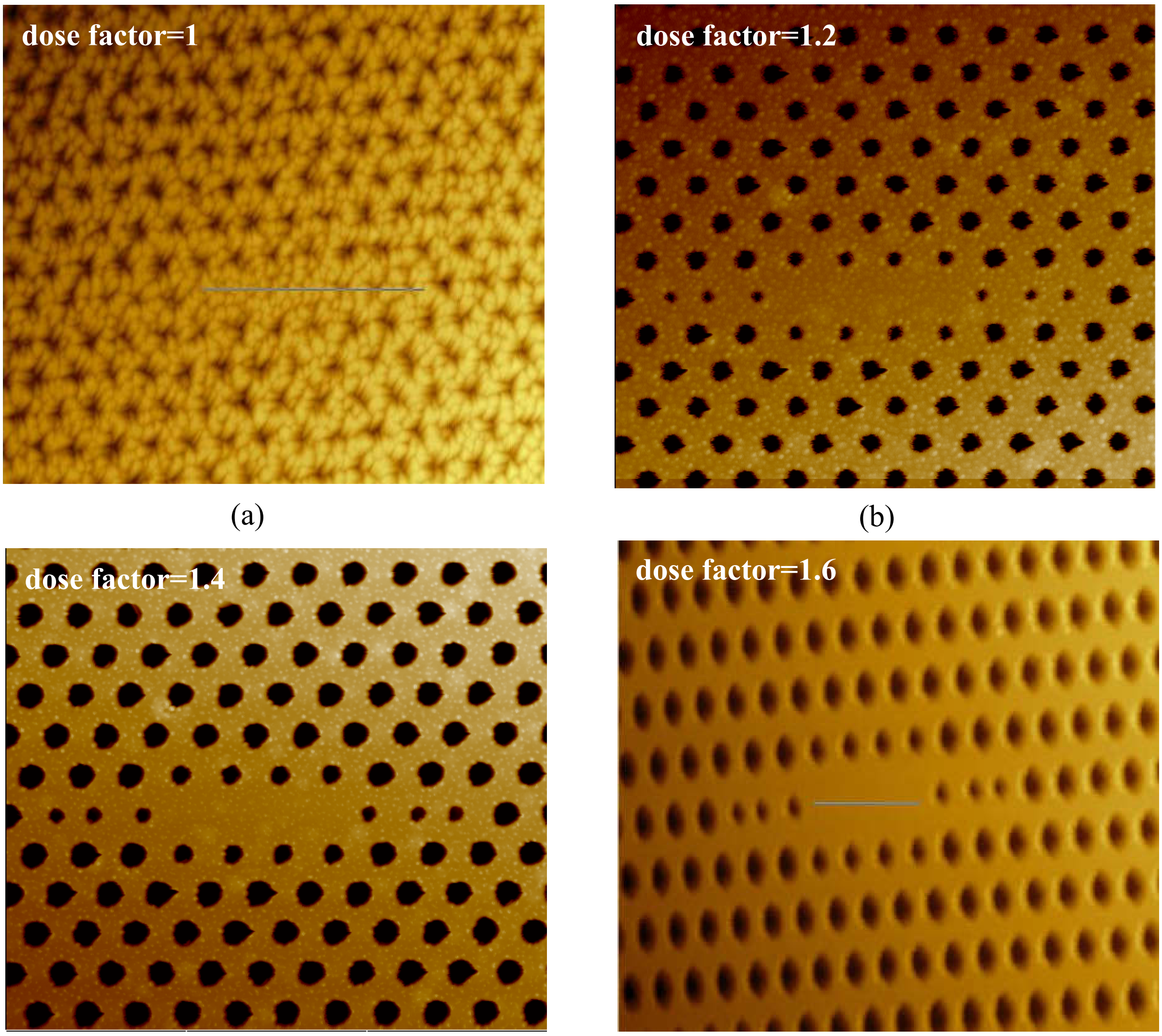

(a) (b)

(c) (d)

Figure 5.29: Shows an AFM images for different modified L3 nanocavities with three shifted holes that exposed with different dose factor in the EBL (a) dose factor = 1, (b) dose factor = 1.2, (c) dose factor = 1.4 and (d) dose factor = 1.6.

Here, the best dose factor that was used to etch the of *L*3 modified structure with three shifted holes in the SCAR e-beam resist was 1.8. Figure 5.26 illustrates the structure after using such dose factor. This high quality of the etch is likely due to the use of SCAR resist. This modified L3 nanocavity was then coated using 10 nm of film of the Red-F conjugated polymer. Here, as demonstrated in the previous structure, the emission from the cavity results from an overlap of the luminescence of the thin film with the cavity mode wavelength, leading to a high emission intensity from the cavity.

Figure 5.30 (a) shows the unpolarised PL emission spectra from the nanocavity. Figures 5.30 (b) and (c) illustrate the PL emission from the cavity having a polarisation parallel and perpendicular respectively to the long axis of the cavity. It can be seen that the PL emission spectrum consists of a number of sharp lines that are superimposed on the spontaneous emission spectrum of the Red-F. Moreover, it can be seen that the intensity of the fundamental mode M1 enhanced significantly by a factor of 3 times having a Q factor of 1100.

The improvement in the Q factor of such L3 modified nanocavity structure can be attributed to the small taper angle of the air holes that surround the cavities. A scanning electron microscope was used to measure the taper angle in our samples by measuring the air hole diameter at both sides of the membranes with a value of 3° deduced. Reducing this angle results in an improvement of the symmetry in the vertical direction, previous work has found that Q-factor can be reduced by 40% as a result of a 5° taper-angle [96].

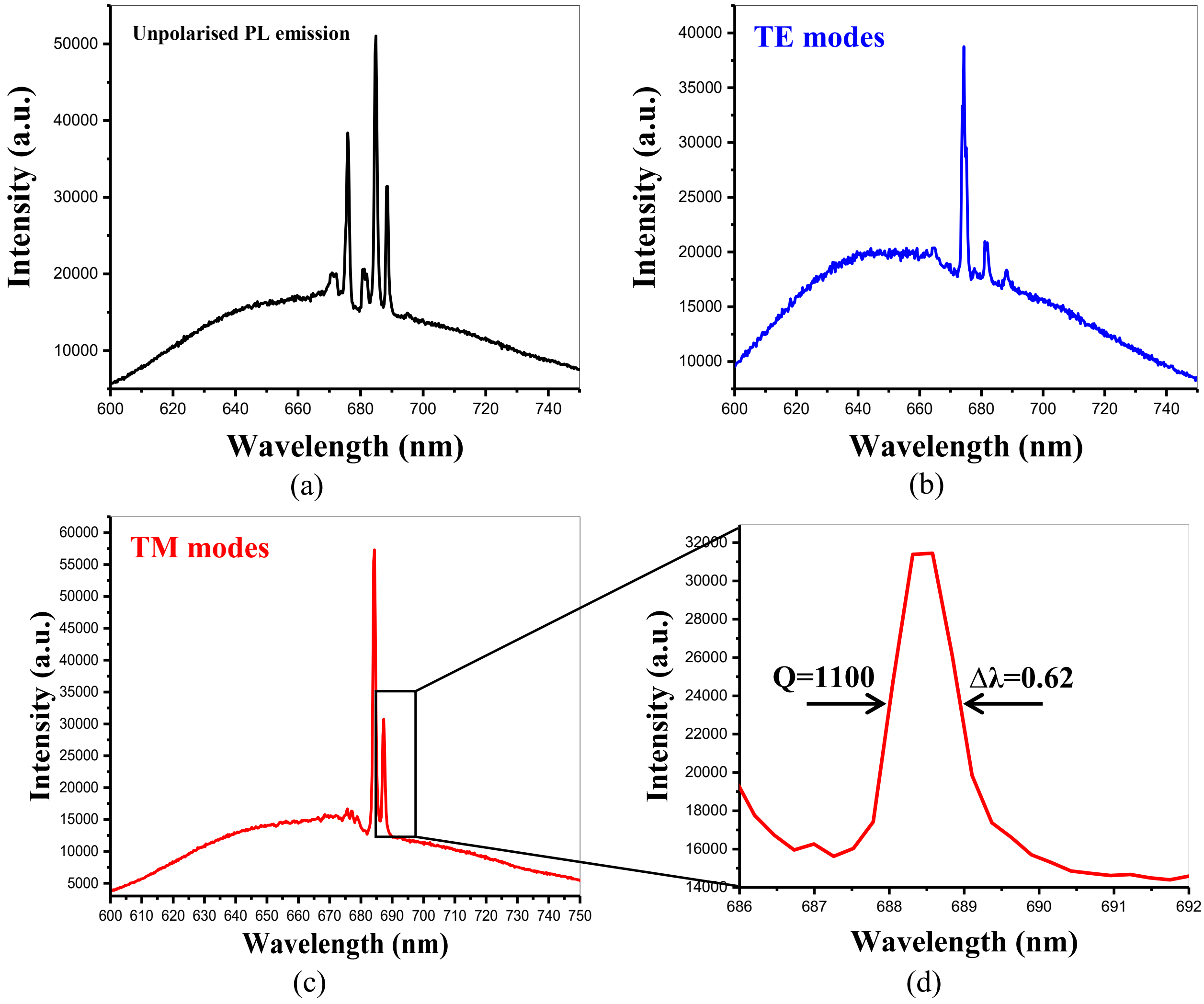

Figure 5.30: Illustrates (a) the unpolarised PL emission of a Red-F / L3 SiN nanocavity with three shifted holes. (b) and (c) show TE and TM modes for a polarisation parallel and perpendicular to the nanocavity long axis respectively. (d) illustrates the fundamental mode M1 having a Q factor of 1100.

5.8 Amplified spontaneous emission of the Red- F polymer.

I have explored whether laser action can be obtained using the high Q factor of a modified L3 nanocavity photonic crystal. Such structures are promising laser resonators due to present of photonic band gap (PBG) that is able to modify the optical density of optical modes and enhance the spontaneous emission rate of the emitter [97-99]. Optical gain is an essential demand for materials that are utilized as laser media. Amplified spontaneous emission (ASE) results after an optical excitation of the Red-F film and then spontaneous emission result in a stimulated emission of identical photons.

Experiment was achieved using a Picolo pulse laser having a wavelength of 532 nm, repetition rate of 5 KHz and pulse length of 500 ps. The PL emission measurements as a function of the excitation power were performed on samples prepared by the deposition of 200, 400 and 500 nm of Red-F polymer on the top surface of a SiN membrane nanocavity structure. Figure 5.32 shows the PL emission from the structure. It can be seen that by increasing the excitation power, a superlinear increase of intensity was obtained of the thin film of 200 nm as shown in Figure 5.31.

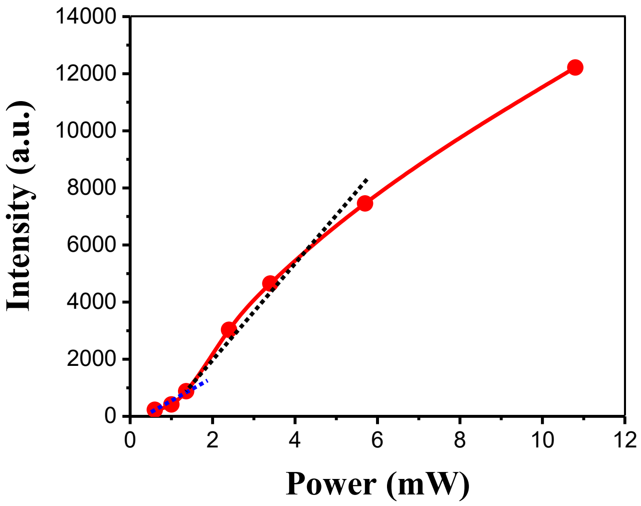

Figure 5.31: Shows the peak intensity of the PL emission as a function to the excitation power.

This is clear evidence of an amplified spontaneous emission process. It can be seen that the excitation power of 0.6, 1 and 1.36 mW is below ASE threshold (blue dots line), 2.4, 3.4 and 5.7 mW corresponds to the ASE threshold (black dots line) and excitation power by 10.8 is above threshold. Then, the PL emission from 200 nm, 400 and 500 nm film thickness was recorded as shown in Figure 5.32 (a), (b) and (c) respectively.

Here, it can be seen that the PL spectrum for several excitation power that adjusted to get a high output. Figure 5.32 (c) shows that a gain narrowing at red (678 nm) was obtained from 500 nm film thickness at excitation pulse of 300 µW. Such structure is a promising for application as laser or optical amplifiers. This result can be explained as, the gain threshold is reduced as a result of increasing the concentration of the film, indicating that the intermolecular distances of the polymer used are reduced result from using a larger number of molecules per unit volume. In addition to using a high concentration of the polymer leads to increase the effective refractive index of the waveguide of the film, leading to reduce the amplified spontaneous emission threshold [100-104].

Unfortunately there are two reasons that prevented us from getting laser from the Red-F nanocavity structure. First is the degradation of the PL signal from the thin film of the Red- F polymer caused by gradual photo oxidation. Second, using a high power resulted in the polymer burning as shown in Figure 5.32 (d). This did not allow us to reach the lasing regime.

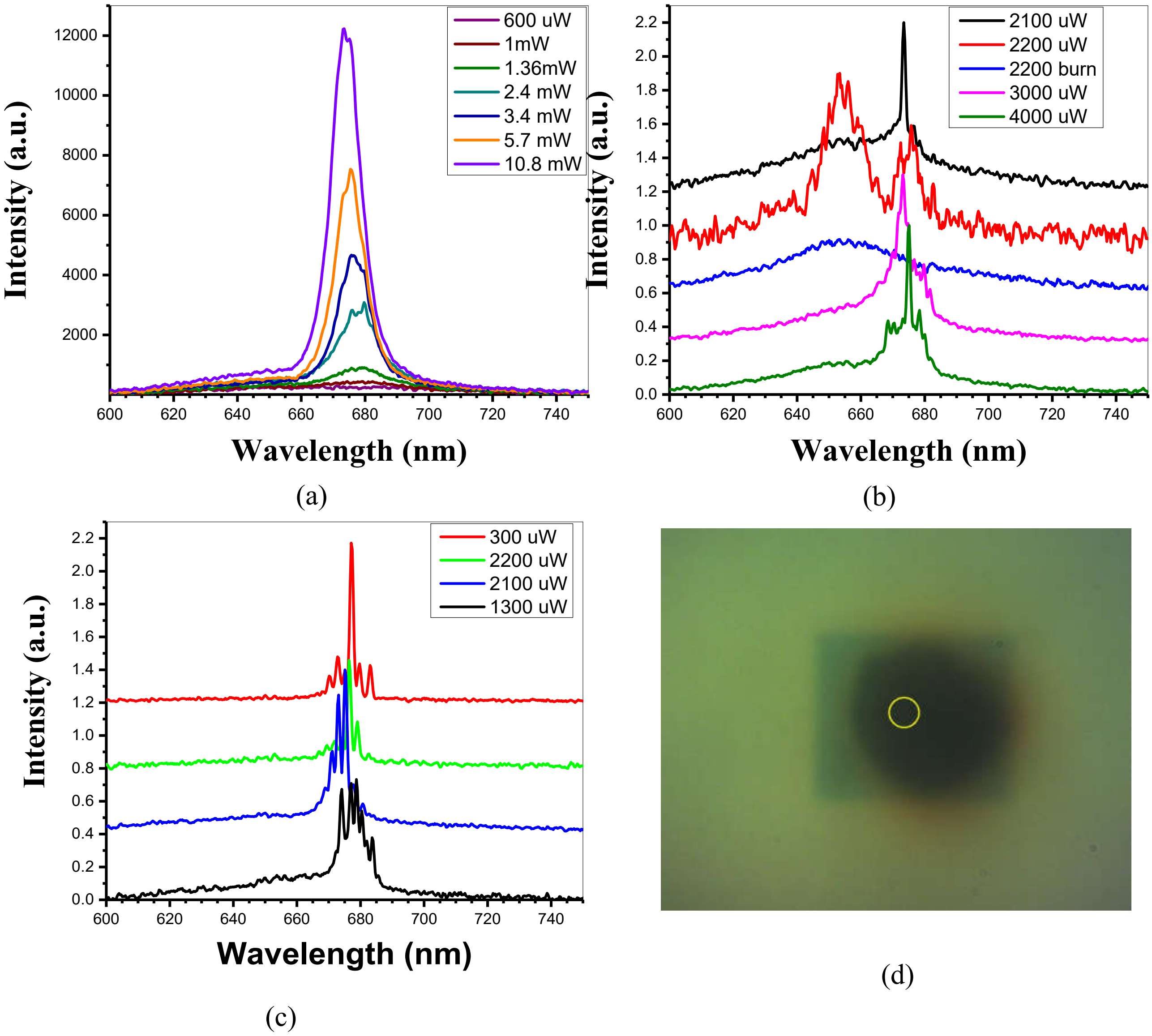

(a)

(b)

(c)

(d)

Figure 5.32: Shows the PL spectra of different thickness of Red- F films as a function of excitation energy, (a) 200 nm, (b) 400 nm, (c) 500 nm and (d) an image of a modified L3 nanocavity after coated with thin film of Red-F After exposure to high excitation energy.

5.9 Summary and Conclusion

In this chapter, I have explored the optical properties of SiN membrane based L3 nanocavities before and after coating with a thin film of Red-F conjugated polymer. Three different designs were explored; an unmodified structure, a cavity with one shifted hole and a cavity with three shifted holes. Theoretical calculations using FDTD simulation and experiments have investigated the influence of shifting the side and surrounding holes on the Q factor and the peak position of the fundamental mode.

Experimental showed that the first modified SiN, one shifted hole, nanocavities had a high Q factor for the fundamental mode of 645 was obtained as a result of using a modified structure. Here, the effect of shift in the edge holes of the cavity on the Q factor was explored and the Q factor is increase from 645 at wavelength of 671 nm for S=0a to 838 for S=20a at wavelength of 673 nm. Then, a Red- F solution was coated on the top surface of the nanocavity. The experimental results showed that the first modified structure got a higher Q factor for the fundamental mode of 942 at the fundamental mode at the wavelength of 707 nm after coating a red-emitting conjugated polymer film.

Moreover, the experimental results showed that the second modified SiN, three shifted hole, based a modified L3 nanocavity had a higher Q factor for the fundamental mode of 710 is obtained as a result of using such structure. Here, the effect of shift in the edge holes of the cavity on the Q factor was explored and the Q factor was increase from 710 at wavelength of 640 nm for S=0a to 931 for S=26a at wavelength of 652 nm. Again, a Red- F solution was used to coat the top surface of the nanocavity. The experimental results illustrated that the Q factor for the fundamental mode increased to reach at 1100 after coating a red-emitting conjugated polymer film. The PL emission was recorded as a function of polarisation mode with a good agreement with FDTD calculations in both perpendicular and parallel polarised modes. The PL emission intensity of the fundamental mode was enhanced by factor of 6 for the first design and by factor of 3 in the second design.

Different thicknesses of thin films of the Red-F conjugated polymer were explored in order to study the amplified spontaneous emission process. However, when such films were place on the cavity, lasing was not achieved, and instead the cavity surface was burnt by the pulsed laser excitation source. This indicating in the structures studied, the threshold for lasing is higher than the damage threshold.

References

[1] Benmerkhi, A., Bouchemat, M. and Bouchemat, T., ‘‘Design of high-Q cavities in 2D photonic crystals air holes filled with polymer’’. Optik, 125, 6223-6226, (2014).

[2] Wang, Z., Zhang, J., Xie, J., Yin, Y., Wang, Z., Shen, H., Li, Y., Li, J., Liang, S., Cui, L. and Zhang, L., ‘‘Patterning organic/inorganic hybrid bragg stacks by integrating one-dimensional photonic crystals and macrocavities through photolithography: toward tunable colorful patterns as highly selective sensors’’. ACS Applied Materials & Interfaces, 4, 1397-1403, (2012).

[3] Noda, S. and Baba, T. eds., ‘‘Roadmap on photonic crystals’’ Springer Science & Business Media, (2013).

[4] Sun, L., Lin, H., Kohlstedt, K.L., Schatz, G.C. and Mirkin, C.A., ‘‘Design principles for photonic crystals based on plasmonic nanoparticle superlattices’’ Proceedings of the National Academy of Sciences, 115, 7242-7247, (2018).

[5] Avoine, A., Vion, C., Laverdant, J., Bonnefont, S., Gauthier-Lafaye, O., Coolen, L. and Maître, A., ‘‘Photonic crystal cavity modes in the visible range characterized by scattering spectroscopy’’. Physical Review A, 82, 063809, (2010).

[6] Saker, K., Bouchemat, T., Lahoubi, M., Bouchemat, M. and Pu, S., ‘‘ Magnetic field sensor based on a magnetic-fluid-infiltrated photonic crystal L4 nanocavity and broadband W1 waveguide’’. Journal of Computational Electronics, 18, 619-627, (2019).

[7] Rivoire, K., Kinkhabwala, A., Hatami, F., Masselink, W.T., Avlasevich, Y., Müllen, K., Moerner, W.E. and Vučković, J., ‘‘Lithographic positioning of fluorescent molecules on high-Q photonic crystal cavities’’. Applied Physics Letters, 95, 123113, (2009).

[8] Vučković, J. and Yamamoto, Y., ‘‘Photonic crystal microcavities for cavity quantum electrodynamics with a single quantum dot’’. Applied Physics Letters, 82, 2374-2376, (2003).

[9] Notomi, Á., ‘‘Theory of light propagation in strongly modulated photonic crystals: Refractionlike behavior in the vicinity of the photonic band gap’’ Physical Review B, 62, 10696, (2000).

[10] Bernard, S., Reinhardt, C., Dumont, V., Peter, Y.A. and Sankey, J.C., ‘‘Precision resonance tuning and design of SiN photonic crystal reflectors’’ Optics Letters, 41, 5624-5627, (2016).

[11] Akahane, Y., Asano, T., Song, B.S. and Noda, S., ‘‘High-Q photonic nanocavity in a two-dimensional photonic crystal’’ Nature, 425, 944, (2003).

[12] Akahane, Y., Asano, T., Song, B.S. and Noda, S., ‘‘Fine-tuned high-Q photonic-crystal nanocavity’’ Optics Express, 13, 1202-1214, (2005).

[13] Tanaka, Y., Asano, T., Akahane, Y., Song, B.S. and Noda, S., 2003. Theoretical investigation of a two-dimensional photonic crystal slab with truncated cone air holes. Applied Physics Letters, 82, 1661-1663, (2003).

[14] Chan, Y.S., Chan, C.T. and Liu, Z.Y., ‘‘Photonic band gaps in two dimensional photonic quasicrystals’’ Physical Review Letters, 80, 956, (1998).

[15] Tandaechanurat, A., Iwamoto, S., Nomura, M., Kumagai, N. and Arakawa, Y., ‘‘Increase of Q-factor in photonic crystal H1-defect nanocavities after closing of photonic bandgap with optimal slab thickness’’ Optics Express, 16, 448-455, (2008).

[16] Liu, Q., Ouyang, Z. and Albin, S., ‘‘Photonic crystal nano-cavities for enhancing zero-phonon line emission from nitrogen-vacancy centers in diamond’’ Optics & Laser Technology, 48, 128-134, (2013).

[17] Gan, L. and Li, Z., ‘‘Photonic crystal cavities and integrated optical devices’’ Science China Physics, Mechanics & Astronomy, 58, 114203, (2015).

[18] Vučković, J., Lončar, M., Mabuchi, H. and Scherer, A., ‘‘Design of photonic crystal microcavities for cavity QED’’. Physical Review E, 65, 016608, (2001).

[19] Riedrich-Möller, J., Kipfstuhl, L., Hepp, C., Neu, E., Pauly, C., Mücklich, F., Baur, A., Wandt, M., Wolff, S., Fischer, M. and Gsell, S., ‘‘One-and two-dimensional photonic crystal microcavities in single crystal diamond’’. Nature Nanotechnology, 7, 69, (2012).

[20] Sreekanth, K.V., Krishna, K.H., De Luca, A. and Strangi, G., 2014. ‘‘Large spontaneous emission rate enhancement in grating coupled hyperbolic metamaterials’’. Scientific Reports, 4, 6340, (2014)

[21] Murshidy, M.M., Adawi, A.M., Fry, P.W. and Lidzey, D.G., ‘‘A one-dimensional photonic-crystal nanocavity incorporating a fluorescent molecular dye’’. Applied Physics Letters, 97, 224, (2010).

[22] Wang, Z., Lu, Z., Mahoney, C., Yan, J., Ferebee, R., Luo, D., Matyjaszewski, K. and Bockstaller, M.R., ‘‘Transparent and high refractive index thermoplastic polymer glasses using evaporative ligand exchange of hybrid particle fillers’’ ACS Applied Materials & Interfaces, 9, 7515-7522, (2017).

[23] Makarova, M., Vuckovic, J., Sanda, H. and Nishi, Y., ‘‘Silicon-based photonic crystal nanocavity light emitters’’. Applied Physics Letters, 89, 221101, (2006).

[24] Barbillon, G., Gourdon, F., Cambril, E., Fabre, N., Yacomotti, A.M. and Bouchoule, S., ‘‘SiNx/organic photonic crystal microcavity optimization for the fabrication of thin-film micro-laser’’. Optics Communications, 325, 15-22, (2014).

[25] Barth, M., Kouba, J., Stingl, J., Loechel, B. and Benson, O., ‘‘SiN photonic crystal cavities: promising tools for the manipulation of light in the visible’’ In Nanoengineering: Fabrication, Properties, Optics, and Devices, International Society for Optics and Photonics IV, 6645, 664503, (2007).

[26] Gritsenko, V.A., ‘‘Electronic structure of silicon nitride’’. Physics-Uspekhi, 55, 498, (2012).

[27] Wang, C.M., Pan, X., Rühle, M., Riley, F.L. and Mitomo, M., ‘‘Silicon nitride crystal structure and observations of lattice defects’’ Journal of Materials Science, 31, 5281-5298, (1996).

[28] Gan, Z., Wang, C. and Chen, Z., ''Material Structure and Mechanical Properties of Silicon Nitride and Silicon Oxynitride Thin Films Deposited by Plasma Enhanced Chemical Vapor Deposition'' Surfaces, 1, 59-72, (2018).

[29] Hammadi, O.A., Khalaf, M.K. and Kadhim, F.J., ''Fabrication and characterization of ultraviolet photodetectors based on silicon nitride nanostructures prepared by magnetron sputtering'' Journal of Nanomaterials, Nanoengineering and Nanosystems, 230, 32-36, (2016).

[30] Kassa-Baghdouche, L., Boumaza, T., Cassan, E. and Bouchemat, M., '' Enhancement of Q-factor in SiN-based planar photonic crystal L3 nanocavity for integrated photonics in the visible-wavelength range'' Optik, 126, 3467-3471, (2015).

[31] Melchiorri, M., Daldosso, N., Sbrana, F., Pavesi, L., Pucker, G., Kompocholis, C., Bellutti, P. and Lui, A., ''Propagation losses of silicon nitride waveguides in the near-infrared range''. Applied Physics Letters, 86, 121111, (2005).

[32] Hosneara, M., Hasnat, A. and Bhuyan, A.H., 2012. Structural and Electrical Properties of Silicon Nitride Ceramic. Daffodil International University Journal of Science and Technology, 7, 50-59, (2012).

[33] Hampshire, S., ''Silicon nitride ceramics–review of structure, processing and properties'' Journal of Achievements in Materials and Manufacturing Engineering, 24, 43-50, (2007).

[34] Nietubyć, R., Sobczak, E., Šipr, O., Vackář, J. and Šimůnek, A., ''Electronic structure of silicon nitride'' Journal of Alloys and Compounds, 286, 148-152, (1999).

[35] Deshpande, S.V., Gulari, E., Brown, S.W. and Rand, S.C., ''Optical properties of silicon nitride films deposited by hot filament chemical vapor deposition'' Journal of Applied Physics, 77, 6534-6541, (1995).

[36] Yashima, M., Ando, Y. and Tabira, Y., ''Crystal structure and electron density of α-silicon nitride: experimental and theoretical evidence for the covalent bonding and charge transfer'' The Journal of Physical Chemistry B, 111, 3609-3613, (2007).

[37] Pernice, W.H.P., Li, M., Gallagher, D.F.G. and Tang, H.X., 2009. Silicon nitride membrane photonics. Journal of Optics A: Pure and Applied Optics, 11(11), p.114017.

[38] Dong, Y., Zhao, H., Song, J., Gao, F., Cheng, C., Chang, Y., Du, G., Yu, M.B. and Lo, G.Q., ''Low threshold two-dimensional organic photonic crystal distributed feedback laser with hexagonal symmetry based on SiN'' Applied Physics Letters, 92, 202, (2008).

[39] Li, D., Wang, F., Ren, C. and Yang, D., ''Improved electroluminescence from silicon nitride light emitting devices by localized surface plasmons'' Optical Materials Express, 2, 872-877, (2012)

[40] Lončar, M., Doll, T., Vučković, J. and Scherer, A., ''Design and fabrication of silicon photonic crystal optical waveguides'' Journal of Light wave Technology, 18, 1402, (2000).

[41] Grande, M., Calo, G., Petruzzelli, V. and D'Orazio, A., ''High-Q photonic crystal nanobeam cavity based on a silicon nitride membrane incorporating fabrication imperfections and a low-index material layer'' Progress In Electromagnetics Research, 37, 191-204, (2012).

[42] Asano, T., Song, B.S. and Noda, S., ‘‘Analysis of the experimental Q factors (~ 1 million) of photonic crystal nanocavities’’ Optics Express, 14, 1996-2002, (2006).

[43] Williamson, I.A., Mousavi, S.H. and Wang, Z., ‘‘Extraordinary wavelength reduction in terahertz graphene-cladded photonic crystal slabs’’ Scientific Reports, 6, 25301, (2016).

[44] Grudinin, I.S., Ilchenko, V.S. and Maleki, L., 2006. ‘‘Ultrahigh optical Q factors of crystalline resonators in the linear regime’’. Physical Review A, 74, 063806, (2006).

[45] Netti, M.C., Charlton, M.D.B., Parker, G.J. and Baumberg, J.J., ‘‘Visible photonic band gap engineering in silicon nitride waveguides’’ Applied Physics Letters, 76, 991-993, (2000).

[46] Y. Akahane, T. Asano, B. S. Song, S. Noda, ‘‘High-Q photonic nanocavity in two-dimensional photonic crystal’’ Nature, 425, 944 (2003).

[47] Makarova, M., Vuckovic, J., Sanda, H. and Nishi, Y., ‘‘Silicon-based photonic crystal nanocavity light emitters’’ Applied Physics Letters, 89, 221101, (2006).

[48] Adawi, A.M., Chalcraft, A.R.A., Whittaker, D.M. and Lidzey, D.G., ‘‘Refractive index dependence of L3 photonic crystal nano-cavities’’. Optics Express, 15, 14299-14305, (2007).

[49] Adawi, A.M., Murshidy, M.M., Fry, P.W. and Lidzey, D.G., ‘‘An optical nanocavity incorporating a fluorescent organic dye having a high quality factor’’ ACS Nano, 4, 3039-3044, (2010).

[50] Gong, Q. and Hu, X., ‘‘Photonic crystals: principles and applications’’. Jenny Stanford Publishing, (2014).

[51] Park, S.Y., Kim, H. and Song, B.S., ‘‘Design of thin-film photonic crystals with complete photonic bandgap’’ Optics Express, 26, 29521-29526, (2018).

[52] Johnson, S.G., Fan, S., Villeneuve, P.R., Joannopoulos, J.D. and Kolodziejski, L.A., ‘‘Guided modes in photonic crystal slabs’’ Physical Review B, 60, 5751, (1999).

[53] Cartar, W., Mørk, J. and Hughes, S., ‘‘Self-consistent Maxwell-Bloch model of quantum-dot photonic-crystal-cavity lasers’’ Physical Review A, 96, 023859, (2017).

[54] Pisanello, F., Qualtieri, A., Stomeo, T., Martiradonna, L., Cingolani, R., Bramati, A. and De Vittorio, M., ‘‘High-Purcell-factor dipolelike modes at visible wavelengths in H1 photonic crystal cavity’’ Optics Letters, 35, 1509-1511, (2010).

[55] https://www.filmetrics.com/reflectance-calculator.

[56] Yoshie, T., Vučković, J., Scherer, A., Chen, H. and Deppe, D., ‘‘High quality two-dimensional photonic crystal slab cavities’’ Applied Physics Letters, 79, 4289-4291, (2001).

[57] Peng, Y.S., Yao, M.H., Li, R.C. and Wang, Z.G., ‘‘Study of modes for two-dimensional L3 photonic crystal nanocavities’’ Optics Communications, 285, 1510-1513, (2012).

[58] Chalcraft, A.R.A., Lam, S., O'Brien, D., Krauss, T.F., Sahin, M., Szymanski, D., Sanvitto, D., Oulton, R., Skolnick, M.S., Fox, A.M. and Whittaker, D.M., ‘‘Mode structure of the L 3 photonic crystal cavity’’ Applied Physics Letters, 90, 241117, (2007).

[59] Lai, Y., Pirotta, S., Urbinati, G., Gerace, D., Minkov, M., Savona, V., Badolato, A. and Galli, M., ‘‘Genetically designed L3 photonic crystal nanocavities with measured quality factor exceeding one million’’. Applied Physics Letters, 104, 241101, (2014)

[60] Barth, M., Kouba, J., Stingl, J., Löchel, B. and Benson, O., ‘‘Modification of visible spontaneous emission with silicon nitride photonic crystal nanocavities’’. Optics Express, 15, 17231-17240, (2007).

[61] Yang, J.K., Kim, C.Y. and Lee, M., ‘‘High-Sensitive TM Modes in Photonic Crystal Nanobeam Cavity with Horizontal Air Gap for Refractive Index Sensing’’ Applied Sciences, 9, 967, (2019).

[62] Aneja, S. and Kumar, M., ‘‘Design of a three-hole defect photonic crystal nanocavity with high-quality and enhanced Purcell factor’’ Optical Engineering, 54, 017106, (2015).

[63] Makarova, M., Vuckovic, J., Sanda, H. and Nishi, Y., ‘‘Silicon-based photonic crystal nanocavity light emitters’’ Applied Physics Letters, 89, 221101, (2006).

[64] Peng, Y.S., Yao, M.H., Li, R.C. and Wang, Z.G., ‘‘Study of modes for two-dimensional L3 photonic crystal nanocavities’’ Optics Communications, 285, 1510-1513, (2012).

[65] Chalcraft, A.R.A., Lam, S., O’Brien, D., Krauss, T.F., Sahin, M., Szymanski, D., Sanvitto, D., Oulton, R., Skolnick, M.S., Fox, A.M. and Whittaker, D.M., ‘‘Mode structure of the L 3 photonic crystal cavity’’ Applied Physics Letters, 90, 241117, (2007).

[66] Deasy, K., Sediq, K.N., Brittle, S., Wang, T., Davis, F., Richardson, T.H. and Lidzey, D.G., ‘‘A chemical sensor based on a photonic-crystal L3 nanocavity defined in a silicon-nitride membrane’’ Journal of Materials Chemistry C, 2, 8700-8706, (2014).

[67] El Kurdi, M., Checoury, X., David, S., Ngo, T.P., Zerounian, N., Boucaud, P., Kermarrec, O., Campidelli, Y. and Bensahel, D., ‘‘Quality factor of Si-based photonic crystal L3 nanocavities probed with an internal source’’ Optics Express, 16, 8780-8791, (2008).

[68] Wang, C.F., Hanson, R., Awschalom, D.D., Hu, E.L., Feygelson, T., Yang, J. and Butler, J.E., ‘‘Fabrication and characterization of two-dimensional photonic crystal microcavities in nanocrystalline diamond’’ Applied Physics Letters, 91, 201112, (2007).

[69] Makarova, M., Vuckovic, J., Sanda, H. and Nishi, Y., ‘‘Silicon-based photonic crystal nanocavity light emitters’’ Applied Physics Letters, 89, 221101, (2006).

[70] Atlasov, K.A., Calic, M., Karlsson, K.F., Gallo, P., Rudra, A., Dwir, B. and Kapon, E., ‘‘Photonic-crystal microcavity laser with site-controlled quantum-wire active medium. Optics Express, 17, 18178-18183, (2009).

[71] Akahane, Y., Asano, T., Song, B.S. and Noda, S., 2003. ‘‘High-Q photonic nanocavity in a two-dimensional photonic crystal’’ Nature, 425, 944, (2003).

[72] Shirane, M., Kono, S., Ushida, J., Ohkouchi, S., Ikeda, N., Sugimoto, Y. and Tomita, A., 2007. Mode identification of high-quality-factor single-defect nanocavities in quantum dot-embedded photonic crystals. Journal of Applied Physics, 101, 073107, (2007).

[73] Sediq, K.N., Coles, D., Fry, P.W. and Lidzey, D.G., ‘‘Plasmonic gold nanodiscs fabricated into a photonic-crystal nanocavity’’ Nanotechnology, 27, 225203, (2016).

[74] Chen, C.J., Zheng, J., Gu, T., McMillan, J.F., Yu, M., Lo, G.Q., Kwong, D.L. and Wong, C.W., ‘‘Selective tuning of high-Q silicon photonic crystal nanocavities via laser-assisted local oxidation’’ Optics Express, 19, 12480-12489, (2011).

[75] Krauss, T.F., O'Faolain, L., Schulz, S., Beggs, D.M., Morichetti, F., Canciamilla, A., Torregiani, M., Melloni, A., Mazoyer, S., Lalanne, P. and Samarelli, A., 2010, February. ‘‘Understanding the rich physics of light propagation in slow photonic crystal waveguides’’ In Advances in Slow and Fast Light III, International Society for Optics and Photonics, 7612, 76120L, (2010).

[76] Riboli, F., Caselli, N., Vignolini, S., Intonti, F., Vynck, K., Barthelemy, P., Gerardino, A., Balet, L., Li, L.H., Fiore, A. and Gurioli, M., 2014. ‘‘Engineering of light confinement in strongly scattering disordered media’’ Nature Materials, 13, 720, (2014).

[77] Fu, Y.J., Lee, Y.S. and Lin, S.D., ‘‘Design and demonstration of high quality-factor H1-cavity in two-dimensional photonic crystal’’ Optics Letters, 38, 4915-4918, (2013).

[78] Tanabe, T., Shinya, A., Kuramochi, E., Kondo, S., Taniyama, H. and Notomi, M., ‘‘Single point defect photonic crystal nanocavity with ultrahigh quality factor achieved by using hexapole mode’’ Applied Physics Letters, 91, 021110, (2007).

[79] Y. Lai, S. Pirotta, G. Urbinati, D. Gerace, M. Minkov, V. Savona, A. Badolato, and M. Galli, “Genetically designed L3 photonic crystal nanocavities with measured quality factor exceeding one million” Applied Physics Letters, 104, 241101 (2014).

[80] Sekoguchi, H., Takahashi, Y., Asano, T. and Noda, S., 2014. Photonic crystal nanocavity with a Q-factor of~ 9 million. Optics Express, 22(1), pp.916-924, (2014).

[81] Bulović, V., Kozlov, V.G., Khalfin, V.B. and Forrest, S.R., ‘‘Transform-limited, narrow-linewidth lasing action in organic semiconductor microcavities’’. Science, 279, 553-555, (1998).

[82] Ostroverkhova, O. ed., ‘‘Handbook of organic materials for optical and (opto) electronic devices’’: Properties and Applications. Elsevier, (2013).

[83] Liu, C., Li, Y., Minari, T., Takimiya, K. and Tsukagoshi, K., ‘‘Forming semiconductor/dielectric double layers by one-step spin-coating for enhancing the performance of organic field-effect transistors’’. Organic Electronics, 13, 1146-1151, (2012).

[84] Tsutsumi, N. and Ishibashi, T., ‘‘Organic dye lasers with distributed Bragg reflector grating and distributed feedback resonator’’. Optics Express, 17, 21698-21703, (2009).

[85] Samuel, I.D.W. and Turnbull, G.A., ‘‘Organic semiconductor lasers’’. Chemical reviews, 107, 1272-1295, (2007).

[86] Huang, Y., Paloczi, G.T., Scheuer, J. and Yariv, A., ‘‘Soft lithography replication of polymeric microring optical resonators’’. Optics Express, 11, 2452-2458, (2003).

[87] Hu, Y., Wang, C.W., Zhu, C., Gu, F. and Lin, S.H., , ‘‘Franck–Condon simulation for unraveling vibronic origin in solvent enhanced absorption and fluorescence spectra of rubrene’’. RSC Advances, 7, 12407-12418, (2017).

[88] Baumann, K., Stöferle, T., Moll, N., Raino, G., Mahrt, R.F., Wahlbrink, T., Bolten, J. and Scherf, U., ‘‘Design and optical characterization of photonic crystal lasers with organic gain material’’ Journal of Optics, 12, 065003, (2010).

[89] Clark, J. and Lanzani, G., ‘‘Organic photonics for communications’’ Nature photonics, 4,438, (2010).

[90] Nguyen, D.T.T., Au, T.H., Tong, Q.C., Luong, M.H., Pelissier, A., Montes, K., Ngo, H.M., Do, M.T., Do, D.B., Trinh, D.T. and Nguyen, T.H., 2016. ‘‘Coupling of a single active nanoparticle to a polymer-based photonic structure’’ Journal of Science: Advanced Materials and Devices, 1, 18-30, (2016).

[91] De Stefano, L., Rotiroti, L., De Tommasi, E., Rea, I., Rendina, I., Canciello, M., Maglio, G. and Palumbo, R., ‘‘Hybrid polymer-porous silicon photonic crystals for optical sensing’’ Journal of Applied Physics, 106, 023109, (2009).

[92] Gan, X., Clevenson, H., Tsai, C.C., Li, L. and Englund, D., ‘‘Nanophotonic filters and integrated networks in flexible 2D polymer photonic crystals’’ Scientific Reports, 3, 2145, (2013).

[93] Heliotis, G., Stavrinou, P.N., Bradley, D.D.C., Gu, E., Griffin, C., Jeon, C.W. and Dawson, M.D., ‘‘Spectral conversion of InGaN ultraviolet microarray light-emitting diodes using fluorene-based red-, green-, blue-, and white-light-emitting polymer overlayer films’’Applied Physics Letters, 87, 103505, (2005).

[94] Heliotis, G., Xia, R., Bradley, D.D.C., Turnbull, G.A., Samuel, I.D.W., Andrew, P. and Barnes, W.L., ‘‘Two-dimensional distributed feedback lasers using a broadband, red polyfluorene gain medium’’ Journal of Applied Physics, 96, 6959-6965, (2004).

[95] Barth, M., Kouba, J., Stingl, J., Löchel, B. and Benson, O., ‘‘Modification of visible spontaneous emission with silicon nitride photonic crystal nanocavities. Optics Express, 15, 17231-17240, (2007).

[96] Murshidy, M.M., Adawi, A.M., Fry, P.W., Whittaker, D.M. and Lidzey, D.G., 2010. The optical properties of hybrid organic-inorganic L3 nanocavities. JOSA B, 27(2), pp.215-221.

[97] Reboud, V., Romero-Vivas, J., Lovera, P., Kehagias, N., Kehoe, T., Redmond, G. and Sotomayor Torres, C.M., ‘‘Lasing in nanoimprinted two-dimensional photonic crystal band-edge lasers’’ Applied Physics Letters, 102, 073101, (2013).

[98] Droulias, S., Fietz, C., Zhang, P., Koschny, T. and Soukoulis, C.M., 2014. ‘‘Lasing threshold control in two-dimensional photonic crystals with gain’’ Optics Express, 22, 19242-19251, (2014).

[99] Di Stasio, F., Berti, L., Burger, M., Marabelli, F., Gardin, S., Dainese, T., Signorini, R., Bozio, R. and Comoretto, D., 2009. ‘‘Amplified spontaneous emission from opal photonic crystals engineered with structural defects’’ Physical Chemistry Chemical Physics, 11, 11515-11519, (2009).

[100] Hvam, J. M. ‘‘Direct recording of optical-gain spectra from ZnO’’. J. Appl. Phys. 49, 3124–3126, (1978).

[101] Calzado, E. M., Villalvilla, J. M., Boj, P. G., Quintana, J. A. & Diaz-Garcia, M. A. ‘‘uneability of amplified spontaneous emission through control of the thickness in organic-based waveguides’’. J. Appl. Phys. 97, 93103, (2005).

[102] Park, J.H., Jeon, O.Y., Cha, M., Park, S. and Park, S.Y., 2005, May. ‘‘Amplified spontaneous emission and two-photon fluorescence in an organic single crystal composed of excited-state intramolecular proton transfer molecules’’. In Quantum Electronics and Laser Science Conference, Optical Society of America, JWB37, (2005).

[102] Calzado, E. M., Villalvilla, J. M., Boj, P. G., Quintana, J. a. & Díaz-García, M. A. ‘‘Concentration dependence of amplified spontaneous emission in organicbased waveguides’’. Org. Electron. Physics, Mater. Appl. 7, 319–329, (2006).

[103] Costela, A., García, O., Cerdán, L., García-Moreno, I. and Sastre, R., ‘‘Amplified spontaneous emission and optical gain measurements from pyrromethene 567-doped polymer waveguides and quasi-waveguides’’. Optics Express, 16, 7023-7036, (2008).

[104] Kazlauskas, K. et al. ‘‘Concentration effects on spontaneous and amplified emission in benzo[c]fluorenes’’. Phys. Chem. Chem. Phys. 9–11, (2015).

Chapter 6
Conclusions and Suggestions for Further Work

6.1 Conclusion

In this thesis, I introduced and demonstrated two major topics. Firstly, the optical properties of optical microcavity micropillars containing an organic emitter were explored. These structures result in a three dimensional confinement of light in a small volume of the order of few wavelengths of the confined light, and provide a considerable opportunity to study the light-matter interaction and control radiative dynamics of emissive molecular materials. Secondly, the optical properties of two dimensional photonic crystal L3 nanocavities were investigated. Significant effort has been made to develop these structures to create structures having high quality factor. Indeed, we discuss process techniques that result in high Q factor photonic crystal nanocavities.

In Chapter 4, I have fabricated and explored the light emission from a series of micropillar microcavities containing a thin fluorescent, red-emitting conjugated polymer film. The fabrication of such structures was based on the use of electron-beam evaporation to prepare the DBR layers and focussed ion-beam to create the micropillars microcavities. The optical modes structure of such pillars are characterised using combined white-light reflectance and photoluminescence emission using both far-field and Fourier-space imaging techniques. It was found that cavities having a maximum Q-factor of 520 were obtained in structures having a diameter of 4 μm.

Optical modelling of the pillar emission was used to describe the distribution of the cavity modes with modes localised towards the centre of the pillar dominating the emission. Finally, it was shown that the wavelength of the emitted light depended on the diameter of the micropillars, with a gradual blue-shift of the energy of all cavity modes occurring as the pillar diameter was reduced. A series of emission peaks suggestive of whispering gallery modes were observed as a result of smooth sidewalls of the micropillars. A FDTD model was used to simulate the experimental results and a good agreement was obtained.

In Chapter 5, I investigated the influence of a number of parameters such as the size of air holes, hole shift and the lattice constant on the photoluminescence (PL) emission from a SiN based L3 two dimensional photonic crystal nanocavity. The advantage of using SiN membranes in this application comes from its transparency at visible wavelengths, allowing it to be combined with organic materials as the emitting source. Here, it was observed that the cavity fundamental mode can be shifted toward longer wavelengths by increasing the lattice constant (a) and reducing the size of the air holes (r) of the two dimensional photonic crystal. These results were supported by theoretical calculations performed using FDTD simulation. Experiments explored the effect of shifting the position of the edge holes around the cavity on the Q factor. It was found that the Q factor increased from 645 at wavelength of 671nm in the control structure to 838 for a side-hole shift of 52 nm at wavelength of 673nm. A Red- F conjugated polymer was then coated onto the top surface of the nanocavity. This was shown to increase the cavity Q factor of the fundamental mode to 942. Moreover, by combining a three side hole shift structure and a Red-F polymer, a cavity having a high Q-factor was realised.

Finally, to compare between the merits of the two dimensional nanocavities and three dimensional micropillar microcavities photonic crystals we should summarize the following:

Firstly, thin film membranes of silicon nitride (Si_3N_4) having refractive index of ($n \approx 2.1$) were used to fabricate *L*3 photonic crystal nanocavity. Such structure is transparent at visible wavelengths. Si_3N_4 also has favourable mechanical properties such as high strength, high hardness, chemical corrosion resistance and a high chemical stability. This is useful properties as it allows established etching processes to be used with designs being easy to transfer from the SCAR e-beam resist to the SiN membrane. Here, *L*3 photonic crystal nanocavity emits light at visible wavelengths as a result of having band gaps in the wavelength range between 500 nm and 875 nm. A cavity with a high quality factor was obtained as a result of modifying the size and location of the air holes around the nanocavity; to reduce the leaky components, thereby maintaining the small V of a cavity a value that is 6 times higher in comparison with an unmodified structure.

Lithography process (EBL) was used to transfer a desired pattern or design into a sensitive thin film of a resist material. The feature size of a design of interest determines the appropriate radiation source. For this reason, an electron beam source was used to create patterns having a feature size of sub-ten nanometers, with very high resolution of a 50 Ȧ precision possible. Then, reactive ion beam etching (RIE) and an inductively coupled plasma (ICP) technique dry etching techniques was used to transfer a desired pattern from the resist material to the SiN membrane. The main advantage of this technique is the ability to control sidewall through anisotropic etching.

Secondly, a micropillar microcavity is a structure in which an active semiconductor layer is placed between two distributed Bragg reflectors (DBRs). The optical structure of a micropillar containing a thin film of a highly fluorescent red-emitting conjugated polymer. To create such structures, a dielectric mirror (Distributed Bragg Reflector [DBR]) consisting of a number of quarter-wave pairs of TiO_2 and SiO_2 ($n = 2.135$ and 1.452 respectively) was used. The TiO_2 was used because it has a high refractive index, lower optical absorption which is ten times less than silicon, small thermal expansion coefficient and a high degree of transparency over the visible spectrum.

Here, a focused ion beam (FIB) technique was used to fabricate three dimensional photonic structures such as micropillar microcavities. The focused beam of Gallium ions was used to etch a specific area from a planar microcavity. A gallium liquid metal ion source (LMIS) was used in the melting (etching) process without using e-beam resist, with the Ga ions having a much greater momentum than electrons used in EBL. Using this technique, a series of circular trenches three dimensional micropillar microcavities of depth 5 μm having diameters between 4 and 11 μm were created.

A thin and thick film of the polymer PFR was used with the nanocavities and micropillar microcavities structures because it has high fluorescence quantum efficiency and emits luminescence that peaks around 660 nm. Confinement of light in the both structures occurs through both total internal reflection (TIR) and Distributed Bragg Reflector (DBR) mechanisms.

6.2 Future work

In this study, the physics and applications of two different kinds of PC have been investigated. The high Q factor obtained from such structures either microcavities micropillars or two dimensional photonic crystal based L3 modified nanocavities suggest a promising potential for further work.

I believe that using such designs with more accurate etching will result in structure with reduced sidewall roughness and decreased the taper angle. This will enhance light confinement inside such structures and will result in further increases in cavity Q-factor. I think the use of a low current beam in the FIB etching process will be useful to decrease the sidewall roughness to create micropillars having a diameter of less than one μm. Here, decreasing the mode volume will lead to an increase in the strength of light confinement in both micropillars and the two dimensional photonic crystals. Such high Q-factor cavities containing organic materials will be of significant interest in the creation of a range of devices including high efficiency organic nanoscale light sources and integrated nanoscale organic-lasers.

Appendix A

The solution of equation 4.3 in Chapter 4

$$E_{n_x,\ n_y} = \sqrt{E\,{}_0^2 \ + \frac{\hbar^2 c^2}{n^2}\left(\frac{x^2{}_{n_{x\theta},\ n_r,}}{R^2} \right)}$$

λ_o= 670.9 nm
E_o= 1.86 eV , E_o^2= 3.46 eV = 8.85 × 10^{-38} J^2
$\hbar^2$= 1.1121×10^{-68} $J^2.s^2$
C^2= 9×10^{16} m^2/s^2
n^2= 2.3
R^2= 4×10^{-12} m^2
$\frac{\hbar^2 c^2}{nR^2}$ = 1.01630×10^{-40} J^2= Cons.

E_1^2= 8.85 × 10^{-38}+ (1.01630×10^{-40}*5.783)= 8.85 × 10^{-38}+0.058772629× 10^{-38}
E_1^2= 8.91× 10^{-38} J^2
E_1= 2.985×10^{-19} J= 1.8625 eV
λ_1= 665.7 nm

Publications and presentations

Publications

1- Al-Jashaam, F.L., Jayaprakash, R., Coles, D.M., Musser, A.J., Georgiou, K. and Lidzey, D.G., ‘‘Optical-Mode Structure of Micropillar Microcavities Containing a Fluorescent Conjugated Polymer’’. Advanced Quantum Technologies, (2019).

Presentations

1- UK Semiconductors 2018/TMD conference at Sheffield Hallam University, attendance.
2- European Optical Society Biennial Meeting (EOSAM) 2018, poster presentation.